Surface Modified Titanium Anodes for Electroplating of Manganese Dioxide

A dissertation submitted to meet the requirement for the degree of

Magister Scientiae

In the

Department of Physics

Faculty of Natural and Agricultural Sciences

At the

University of the Free State

By

Arnoldus Jacobus Jonker

Supervisor

Dr. J.J. Terblans

Co-Supervisors

Dr. J.J.C. Erasmus

Prof. H.C. Swart

March 2005

Preface

With a great deal of time and effort required on literature research and a stupendous amount of experimental work and data analyses, it is inevitable that no work in science could be attributed to a single person. It is therefore that I am indebted to a number of persons whose names deserve mentioning. Dr. J.J.C. Erasmus initiated the original idea for this study. His enduring optimism and belief in a positive outcome of the study ensured that the work continued in the most difficult times. A great deal of planning and administrative duties were also in the devoted hands of Dr. J.J.C. Erasmus and are acknowledged. His insight into the electrochemistry experiments revealed new concepts in science to me for which I am thankful. I am greatly obliged to Dr. J.J. Terblans for his ideas and interest in the study. His patient and kind assistance was of inestimable value during the experimental surface analyses. I owe a huge debt to Prof. H.C. Swart for associating me with the Physics department at the University of the Free State (UFS) as well as for his encouragement. His patience and acceptance of delay in progress at times made it possible for me to continue this study amid other responsibilities at Delta E.M.D. (Pty) Ltd. This study would also not have come into being if not for the approval and financial assistance of the management of Delta E.M.D. (Pty) Ltd. The latter entity was represented by Dr. J.C.S. Malan and I owe an incalculable amount to him for making possible an unprecedented research project at Delta E.M.D. (Pty) Ltd. I have learned a great deal in the company of Prof. W.D. Roos and his assistance with preparation of TiC samples as well as his help during difficulties with Auger measurements significantly expedited progress during my work at the Physics department. I received the most pleasant and professional assistance from the Instrumentation department at the UFS regarding the design and construction of components for the electrochemical cell. It is with special reference to Mr. P.D.S. Botes that I acknowledge their efforts. I am indebted to Mrs. R. le Grange at the SASOL library for always being helpful and prompt to supply me with requests regarding literature.

Furthermore, it is with sincerity that I acknowledge every family member, friend, fellow student, teacher, colleague and employer who has inspired, encouraged and led me through all my years of study. It is also with great admiration and appreciation that I recognise all relevant lecturers at the UFS who contributed to endear science in my hart and mind. Finally, it is with humble intentions that I would like to express my eternal gratefulness to the Creator.

Abstract

Keywords: Dimensionally stable anodes, electrolytic manganese dioxide, electrocatalysts, titanium, ruthenium, electrolysis, voltammetry, Auger electron spectroscopy, X-ray diffraction.

The valve metal characteristic of Ti provides, together with a number of other physical properties, the appropriate anode material for the production of battery grade electrolytic MnO_2 (EMD). However, electro-oxidation of Mn(II) to Mn(IV) in an acidic medium creates conditions for anodic oxidation of the surface of a Ti metal electrode. The ohmic potential drop in an interelectrode gap, ΔV_Ω, is *inter alia* a function of the extent of anodic oxidation on an electrode's surface. The magnitude of electrical currents in large-scale electrolysis cells compels attention to ΔV_Ω since it equates to power consumption that has large economic incentives. Electrocatalytic transition metal oxide electrodes, termed dimensionally stable anodes (DSA's), not only provide high electrical conductivity, but it also has the added advantage of lowering electrode polarization *via* catalytic considerations. DSA's have numerous other applications, but it is last mentioned properties that draw attention to these electrodes as substrates for MnO_2 electroformation. The basic construction of a DSA is a mixture of a transition metal oxide (more than often a Pt group metal) and a valve metal oxide that adheres to a valve metal substrate.

The primary objective of preparing and evaluating DSA's using different precursor solutions in a thermal decomposition technique is combined with an electrosynthesis method to grow $RuO_x.nH_2O$ films. Interpretation of X-ray diffraction (XRD) measurements demonstrated the ability of a higher calcination temperature to form larger quantities of RuO_2 on Ti. It was also conclusive that an increase in the Ru metal concentration in a precursor solution results in a measurable increase in intensity of the (1 1 0) reflection from RuO_2. Electrolysis experiments in conjunction with Auger electron spectroscopy (AES) depth profiling and AES surface spectra vividly illustrated the dominance of the surface concentration of Ru over the total depth distribution of Ru in lowering electrode polarization in the current density range between $155A.m^{-2}$ and $170A.m^{-2}$. The parameter referred to as polarization slope were derived from electrolysis measurements and a value of $1.63 \pm 0.03mV/A.m^{-2}$ places the DSA prepared with a 0.8wt/wt% Ru precursor solution at the top of the rankings in terms of

preparation cost and electrocatalytic properties. Repetitive potential cycling between –200mV and 1000mV *vs*. Ag/AgCl in 5mM $RuCl_3.3H_2O$ was used to electroform $RuO_x.nH_2O$ films. Cyclic voltammetry yielded results that indicate that the growth of $RuO_x.nH_2O$ is inextricably associated with a complex redox process, while it was furthermore observed that the peak current density of the cyclic voltammogram increases with cycle number. This suggests another complicating factor that most likely results from the electrocatalytic property of the growing oxide film. XRD conclusively showed that subsequent annealing results in a phase transformation of the hydrous Ru oxide that affects its behaviour when used as a DSA for MnO_2 electroplating. AES depth profiling was used to arrive at the conclusion that an unannealed $RuO_x.nH_2O$ film is most probably porous, but electrochemistry showed that it lacks stability under anodic load. With a polarization slope of $1.590 \pm 0.006 mV/A.m^{-2}$, an annealed $Ti/RuO_x.nH_2O$ electrode (30min at 600°C) is the most advantageous in terms of MnO_2 electroplating of all $RuO_x.nH_2O$ films studied.

Electrode polarization measurements on Ti/TiC electrodes as well as commercial Ti-Mn and Ti-Pb electrodes showed promising results, but none of these materials are in contention when compared with said DSA's.

The study was complemented with an investigation into the effect of an acidic $MnSO_4$ solution on Ti metal. The reactivity of Ti towards atmospheric O_2 gives stability to the metal in the form of a superficial oxide film. Dissolution of this passive film can occur under appropriate conditions. Single electrode potential measurements were employed to observe metal activation that is accompanied by H_2 evolution at temperatures above 52°C. An activation potential of $–0.67 \pm 0.01$V *vs*. Ag/AgCl has proven to remain constant at room temperature after activation was induced *via* temperature perturbation to 86 ± 2°C. A hypothesis is presented that describes spontaneous H_2 evolution as a supporting reduction half reaction to the reduction of TiO_2. Electroplating of MnO_2 onto Ti substrates that were subjected to spontaneous H_2 evolution shows a linear increase in electrode polarization (at $100.5 A.m^{-2}$) as a function of exposure time with a slope of $0.19 \pm 0.02 V.hr^{-1}$ *vs*. Ag/AgCl. This attests existing theories that the change in free energy for the formation of TiO_2 from TiH_2 is more negative than for oxidation from Ti metal or that unrecombined hydrogen is present on the Ti surface at the onset of electrolysis.

Opsomming

Tesame met ‘n aantal ander fisiese eienskappe voorsien die “valve” metaal eienskap van Ti die geskikte anode materiaal vir die produksie van battery-graad elektrolitiese MnO_2 (EMD). Tydens oksidasie van Mn(II) na Mn(IV) in ‘n suur medium word kondisies egter geskep wat anodiese oksidasie van die oppervlak van ‘n Ti metaal elektrode bevorder. Die ohmiese potensiaal verskil oor ‘n inter-elektrode gaping, ΔV_Ω, is onder andere ‘n funksie van die mate van anodiese oksidasie op ‘n elektrode-oppervlak. Die grootte van elektriese stroom in kommersiële elektrolitiese selle veroorsaak dat aandag gevestig word op ΔV_Ω aangesien die produk van laasgenoemde twee veranderlikes gelykstaande is aan elektriese drywing wat groot ekonomiese implikasies inhou. Elektrokatalitiese oorgangsmetaaloksied elektrodes wat bekend staan as “dimensionally stable anodes” (DSA’s) voorsien hoë elektriese geleidingsvermoë en is ook instaat om elektrode-polarisasie te verlaag deur middel van katalitiese eienskappe. DSA’s het verskeie toepassings, maar dit is die katalitiese- en geleidings-eienskappe wat dit van belang maak vir die toepassing as anode-substrate vir MnO_2 elektroplatering. Die basiese konstruksie van ‘n DSA is ‘n mengsel van ‘n oorgangsmetaaloksied (gewoonlik ‘n Pt-groep metaal) en ‘n “valve” metaaloksied in die vaste toestand op ‘n “valve” metaal substraat.

Die hoof doelwit van voorbereiding en evaluering van DSA’s met behulp van verskillende voorloper oplossings in ‘n termiese ontbindings tegniek is gekombineer met ‘n elektrosintetiese roete om $RuO_x.nH_2O$ films te groei. Die moontlikheid om groter hoeveelhede RuO_2 met die substraat oppervlak te kombineer by hoër uitgloei temperature is bevestig d.m.v. X-straal diffraksie (XRD) metings. Daar is verder bewys dat ‘n toename in Ru konsentrasie in die voorloper oplossing veroorsaak dat die (1 1 0) refleksie van RuO_2 beduidend toeneem. Elektroliese eksperimente tesame met Auger elektronspektroskopie (AES) diepteprofiele en oppervlakspektra het duidelik aangetoon dat die oppervlakkonsentrasie van Ru baie belangriker is vir die verlaging van elektrode polarisasie tussen stroomdigthede van $155A.m^{-2}$ en $170A.m^{-2}$, eerder as die totale diepte verspreiding van Ru. ‘n Veranderlike wat bekend staan as “polarisasie helling” is afgelei uit elektroliese resultate en ‘n waarde van $1.63 \pm 0.03mV/A.m^{-2}$ vir die DSA wat berei is met ‘n 0.8massa/massa% Ru voorloper oplossing maak hierdie elektrode aanloklik in terme van voorbereidingskoste en elektrokatalitiese vermoë. $RuO_x.nH_2O$ films is gegroei deur middel

van herhaaldelike potensiaal skanderings tussen –200mV en 1000mV *vs*. Ag/AgCl in 5mM $RuCl_3.3H_2O$. Sikliese voltammetrie het resultate gelewer wat aandui dat die groeiproses van $RuO_x.nH_2O$ geassosieer word met ‘n komplekse redoksproses. Daar is ook gevind dat die piek stroomdigtheid van die sikliese voltammogram toeneem met siklus nommer. Dit dui op ‘n verdere komplekserende faktor wat heel waarskynlik die gevolg is van die elektrokatalitiese eienskap van die groeiende oksiedfilm. XRD het oortuigende bewys gelewer dat ‘n fase-transformasie van die gegroeide oksiedfilm plaasvind tydens hitte-behandeling, wat verder ook die DSA se gedrag beïnvloed tydens MnO_2 elektroplatering. AES diepteprofiele is aangewend om aan te toon dat ‘n onverhitte $RuO_x.nH_2O$ film heel waarskynlik poreus is, maar elektrochemie het aangedui dat sodanige film onstabiel is wanneer ‘n anodiese spanning daaroor aangewend word. ‘n Uitgegloeide $Ti/RuO_x.nH_2O$ elektrode (30min by 600°C) met ‘n polarisasie helling van $1.590 \pm 0.006 mV/A.m^{-2}$ hou die meeste potensiaal in van al die bestudeerde $RuO_x.nH_2O$ films, spesifiek ten opsigte van die toepassing daarvan vir elektroplatering van MnO_2.

Gemete polarisasie hellings vir Ti/TiC elektrodes sowel as kommersiële Ti-Mn en Ti-Pb elektrodes het belowende resultate getoon, maar kan nie in hierdie toepassing met DSA’s kompeteer nie.

Die studie is verder uitgebrei met ‘n ondersoek aangaande die effek van ‘n suur $MnSO_4$ oplossing op Ti metaal. Die reaktiwiteit van Ti t.o.v. atmosferiese O_2 maak die metaal stabiel *via* die vorming van ‘n oksied film op die metaal-oppervlak. Laasgenoemde film kan egter oplos onder geskikte omstandighede. Enkel-elektrode potensiaal metings is aangewend om metaal aktivering waar te neem soos vergesel word deur H_2 ontwikkeling by temperature bokant 52°C. Daar is gevind dat ‘n aktiveringspotensiaal van $–0.67 \pm 0.01V$ *vs*. Ag/AgCl konstant bly by kamertemperatuur nadat aktivering geïnduseer is *via* temperatuur versteuring tot 86 ± 2°C. ‘n Teorie is voorgestel wat H_2 ontwikkeling beskryf as a sekondêre reduksie halfreaksie wat kompeteer met die reduksie van TiO_2. MnO_2 elektroplatering op Ti elektrodes wat vooraf blootgestel is aan H_2 ontwikkeling toon ‘n lineêre elektrode-polarisasie toename van $0.19 \pm 0.02 V.hr^{-1}$ *vs*. Ag/AgCl teenoor tyd by $100.5 A.m^{-2}$. Hierdie waarneming ondersteun bestaande teorië dat die vrye energie verandering vir vorming van TiO_2 vanaf TiH_2 meer negatief is as vanaf Ti metaal of dat geadsorbeerde H-radikale Ti metaal teenwoordig is wat na H^+ geoksideer word sodra ‘n anodiese potensiaal aangewend word.

Contents

Chapter 1

An overview on the use of Ti based anodes for the electrolytic production of MnO_2.

1.1 Introduction to the electroplating of MnO_2.

Manganese dioxides are frequently utilised as cathode materials in primary alkaline battery applications. γ-MnO_2 exists as an imperfect crystalline form consisting of an intergrowth of ramsdellite (R-MnO_2), pyrolusite (β-MnO_2) and ε-MnO_2 phases [1, 2] and yields better battery performance than other forms of the chemical. γ-MnO_2 can be produced by anodic oxidation of Mn^{2+} in hot dilute H_2SO_4 solutions at current densities ranging from 50 to 250$A.m^{-2}$ [3]. It is further reported that the precursor for the production of electrolytic MnO_2 (EMD) has a $MnSO_4$ (source of Mn^{2+}) concentration ranging from 0.5M to 0.7M while the H_2SO_4 concentration varies between 0.2M to 0.7M [4]. The concentrations of both these species are important operational parameters in industrial EMD production plants. This can be exemplified by a result in reference [4] where it was concluded that the anodic peak in a cyclic voltammogram for a $MnSO_4/H_2SO_4$ solution increases with +200mV *vs*. mercury sulphate electrode (2M H_2SO_4) when the acid concentration is increased from 0.5M to 6M. Except for solution concentration and current density, temperature (at which the electrolysis takes place) is another important variable that determines the properties of the solid state EMD. Although it was observed that electroplating of γ-MnO_2 could take place at room temperature, it was found that the material is much more crystalline when oxidation takes place at 90-98°C [5]. Except for the latter as a reason for energy expenditure to produce EMD at high temperatures, it was furthermore determined that oxidation of Mn(II) to Mn(IV) is mass transfer controlled [4] and that high temperatures enhance the oxidation rate of Mn(II) to Mn(IV). Nijjer *et. al*. [4] used cyclic voltammetry to conclude that the oxidation potential for the Mn(II)/Mn(IV) couple decreases with an increase in temperature. As an illustration of the effect of temperature on the oxidation of Mn(II) to Mn(IV), it was reported that a temperature increase from 21°C to 35°C decreases the oxidation potential *vs*. a mercury sulphate electrode (2M H_2SO_4) with 50mV. Another practical reason for the use of

high temperatures in commercial electrolytic baths is to eliminate precipitation of impurity species.

The overall reaction for electroplating of EMD is:

$MnSO_4 + 2H_2O \rightarrow MnO_2 + H_2SO_4 + H_2$ .....(1.1),

or in terms of the anodic and cathodic half reactions:

$Mn^{2+} + 2H_2O \rightarrow MnO_2 + 4H^+ + 2e^-$ .....(1.2)

$2H^+ + 2e^- \rightarrow H_2$ .....(1.3).

Cyclic voltammetry experiments provide evidence that reaction 1.2 does not occur in one step, but it has been suggested that a Mn^{3+} state forms prior to Mn^{4+} [6, 7] in accordance with equation 1.4.

$Mn^{2+} \rightarrow Mn^{3+} + e^-$ .....(1.4)

Two pathways are now possible for the formation of the +4 valence state. The first possibility suggest that Mn^{3+} disproportionates as in equation 1.5. This was reported to prevail at low acid concentrations [8].

$2Mn^{3+} \rightarrow Mn^{2+} + Mn^{4+}$ .....(1.5)

Alternatively, Mn^{3+} may hydrolyse to form an insulating MnOOH compound as follows [9 - 11]:

$Mn^{3+} + 2H_2O \rightarrow MnOOH + 3H^+$ .....(1.6)

Subsequent oxidation in equation 1.7 yields the required MnO_2.

$MnOOH \rightarrow MnO_2 + H^+ + e^-$ .....(1.7)

The findings of Rodrigues *et. al*. [6] can be used to further describe, not only the mechanism of oxidation of Mn^{2+} to MnO_2 during electrolysis, but also the reduction of the electroplated EMD. These authors employed cyclic voltammetry on a Pt working electrode to probe a variety of phenomena during MnO_2 electroplating. A voltammogram that was recorded between 0.0V and 1.6V *vs*. saturated calomel in 0.5M $MnSO_4$ + 0.4M H_2SO_4 is illustrated in figure 1.1. It was determined that both the anodic and cathodic peak potentials are dependent on scan rate, rendering the electro-oxidation reaction irreversible. It was however conclusive from their study that P_a and $P_{c,1}$ (anodic and cathodic peak currents) increase linearly with (scan rate)$^{1/2}$ giving evidence that the reactions that govern these peaks are diffusion controlled. The fact that two cathodic peaks were present was used to describe the reduction of MnO_2 under these conditions using the reactions:

$MnO_2 + H^+ + e^- \rightarrow MnOOH$ .....(1.8)

$MnOOH + 3H^+ + e^- \rightarrow Mn^{2+} + 2H_2O$ .....(1.9)

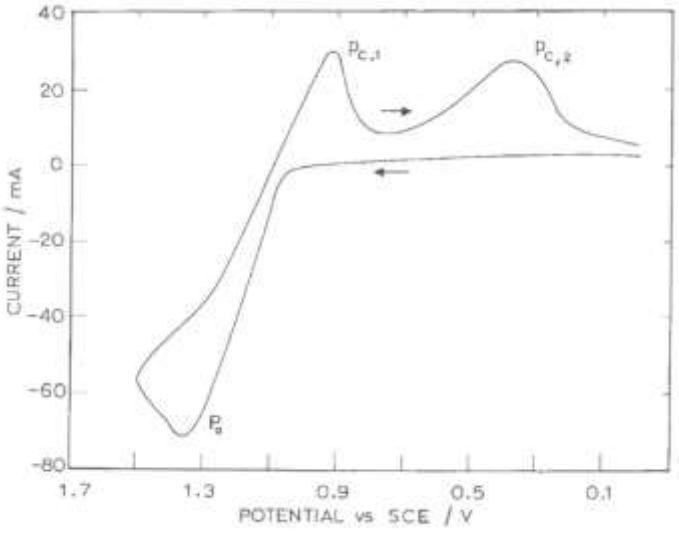

Figure 1.1: Cyclic voltammogram in 0.5M $MnSO_4$ + 0.4M H_2SO_4 on a Pt electrode at 80°C. Scan rate = 200mV.s^{-1}.

Protons (H^+) and e^- are prominent in these reactions and these subatomic particles are also of importance for MnO_2 reduction during discharge of EMD in battery applications. The following multistep mechanism for MnO_2 electrodeposition is presented as a final point on the research of Rodrigues *et. al*. [6].

step 1: $Mn^{2+}_{bulk} \rightarrow Mn^{2+}_{surface}$ .....(1.10)

step 2: $Mn^{2+}_{surface} \rightarrow Mn^{3+}_{ads} + e^-$ .....(1.11)

step 3: $H_2O \rightarrow OH_{ads} + H^+ + e^-$ .....(1.12)

step 4: $2Mn^{3+}_{ads} \rightarrow Mn^{2+}_{ads} + Mn^{4+}_{ads}$ .....(1.13)

step 5: $Mn^{2+}_{ads} + 2OH_{ads} \rightarrow MnO_2 + 2H^+$ .....(1.14)

step 6: $Mn^{4+}_{ads} + 2H_2O \rightarrow MnO_2 + 4H^+$ .....(1.15)

Duarte *et. al.* [12] studied electro-oxidation of Mn^{2+} to MnO_2 on graphite electrodes using stationary potentiostatic polarization and cyclic voltammetry techniques. Figure 1.2 shows separate recordings of cyclic voltammograms on glassy carbon electrodes in solutions of 0.5M H_2SO_4 and 0.2M $MnSO_4$ + 0.5M H_2SO_4. Oxygen evolution at potentials > 1.9V *vs*. standard hydrogen electrode (SHE) is the only reaction that occurs in the H_2SO_4 solution. In the presence of 0.2M $MnSO_4$, a peak centered at 1.45V *vs*. SHE is realised as MnO_2 electroplating by the authors in ref [12]. Although only one oxidation peak, with the exception of H_2O decomposition, is present, the formation of MnO_2 is again described as a multistep reaction. Reaction paths similar to equations 1.4 to 1.7 were presented in reference [12]. A shoulder can be identified at 1.8V *vs*. SHE on the O_2 evolution peak for the voltammogram in the Mn^{2+} containing solution. This shoulder was attributed to electro-oxidation of the plated MnO_2 to MnO_4^- ions. A deplorable situation is therefore unavoidable in a production facility if the applied potential to an anode is significantly above the required value for oxidation of Mn^{2+} to Mn^{4+}. Formation of soluble MnO_4^- species partially coincides with O_2 evolution. This means that costly electrical power is not only wasted in the

production of O_2 gas, but faradaic charge transfer is furthermore used to dissolve and consequently cause the formation of a thinner MnO_2 deposit, resulting in poor overall current efficiencies.

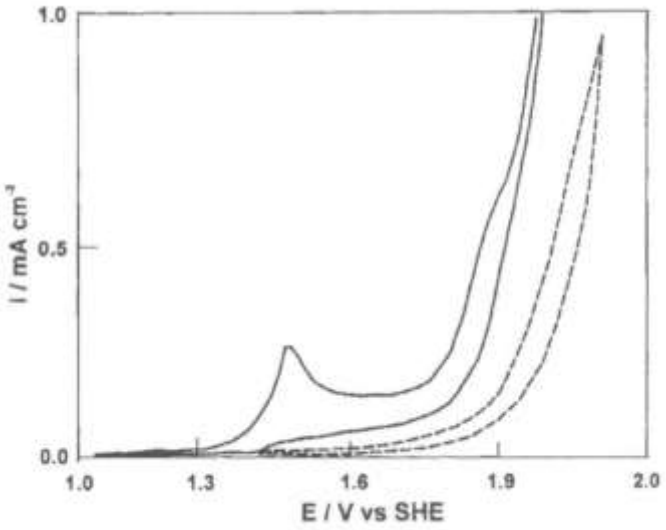

Figure 1.2: Cyclic voltammogram in 0.5M H_2SO_4 (-----) and 0.2M $MnSO_4$ + 0.5M H_2SO_4 (—) on glassy carbon at room temperature. Scan rate = $1mV.s^{-1}$.

1.2 Application of MnO_2 as an electrochemically active battery cathode.

The application of EMD as the positive active material in Leclanche and primary alkaline batteries appears to be based exclusively on reaction 1.8 [13 - 15]. The importance of H^+ ions during discharge of a galvanic cell of the type under discussion can therefore not be over-emphasised. The first step during discharge is the insertion of protons into the γ-MnO_2 crystal structure. This proton insertion initially causes an expansion of the lattice without any other changes. Moreover, the mechanism of lattice expansion involves two steps. Expansion is firstly isotropic, i.e. dependent on the crystallographic orientation, then anisotropic [16 - 18]. It is also worth reporting that this initial increase in lattice volume is a reversible process [19]. Hereafter, the γ-MnO_2 structure starts to transform into a spinel structure once the degree of proton-insertion exceeds 1 proton per Mn atom. The phase of the spinel structure is usually Mn_3O_4 (Hausmanite) or γ-Mn_2O_3 [20]. These reduced states of the initial Mn^{4+} form are made possible by the e^- in equation 1.8. The source of these e^- is plentiful since it originates from the oxidation of the anode material. Urfer *et. al.* [13] used the term "proton-e^-

pair" to describe the discharge process. The proton-e^- pair is visualised as diffusing away form the MnO_2 surface towards the interior of the chemical during discharge and the rate at which this diffusion takes place has obvious implications in terms of the performance of the battery. Brouillet *et. al*. [21] assumed proton diffusion to be the rate-limiting step during MnO_2 reduction. Except for the obvious influence of crystallography on the diffusion coefficient of H^+ in EMD, the rate of diffusion is also a function of, *inter alia*, the EMD's chemical, physical and electrochemical properties. These properties are in turn dependent on the four major electroplating parameters namely temperature, current density, $MnSO_4$ concentration and H_2SO_4 concentration (it has already been mentioned that a high temperature leads to a more crystalline γ-MnO_2 structure). Further insight into the discharge mechanism of MnO_2 in a battery setup was obtained from the work of Rodrigues *et. al.* [15]. Recognition was not given to free accessible protons by the latter authors and reactions 1.8 and 1.9 were interpreted as follows:

$$MnO_2 + H_2O + e^- \rightarrow MnOOH + OH^- \quad \text{.....(1.16)}$$

$$MnOOH + H_2O + e^- \rightarrow Mn(OH)_2 + OH^- \quad \text{.....(1.17)}$$

Reaction 1.16 is described as a reduction in the solid state and is homogeneous. The availability of "structural" H_2O and e^- in the MnO_2 crystal structure can therefore be appreciated. Reaction 1.17 involves a heterogeneous process in which Mn^{3+} ions are required to be in solution (electrolyte).

1.3 Technological requirements for electrodes in the MnO_2 electrolysis process.

It follows from half reactions 1.2 and 1.3 that the EMD is plated on the anode (+ electrode) with hydrogen gas evolution taking place on the cathode (- electrode). The electroplating environment, as well as the nature of the EMD deposit place restrictions on the material that will suffice as an anode.

Obvious requirements for industrial anode materials are:

(i) EMD must adhere to the electrode surface, but must also be readily removable.

(ii) The anode material must not contaminate the product.

(iii) Good overall mechanical and chemical stability.

(iv) An anode should have a service lifetime that represents a cost that is justifiable against the value of the produced EMD.

(v) The anode, as well as its preparation technique, must be environmentally friendly [22].

Other technological demands will transpire from a description of an equation that renders electrical potential parameters to the electrolysis process:

$$\Delta V = \Delta E + \Sigma\eta + \Delta V_{\Omega} \quad \text{.....(1.18)}$$

It is imperative for any profitable industrial electroplating facility to minimise the applied potential, ΔV, to an electrolysis cell. Applied voltage is a direct measure of the energy requirement for electroplating at a constant current density and an increase in ΔV will result in an increase in power consumption and financial expenditure. Whereas the anodic and cathodic overpotentials, $\Sigma\eta$, and the ohmic potential drop in the interelectrode gap, ΔV_{Ω}, are *inter alia* subjected to the electrode material, the thermodynamic potential difference, ΔE, depends on the electrode reactions and has no technological implications. $\Sigma\eta$ depends on both the electrode material and the state of its surface and possibilities exist to minimize this variable. The requirement that (vi) the electrode should have catalytic properties towards the reaction of interest, is directly addressing $\Sigma\eta$. Furthermore, the demands of (vii) dimensional stability and (viii) high electrical conductivity are the embodiment of ΔV_{Ω}.

Currents in production cells are usually large and internal ohmic losses are not only inevitable, as is the case for any other circuit, but it represents a significant percentage of the overall applied potential. Points (vii) and (viii) can therefore have large economic incentives since it represent ohmic resistance and enumerate directly to energy consumption in the form of electricity. Although it is usually irrelevant to MnO_2 electrodeposition, the lack of dimensional stability does culminate in a penalty in terms of power consumption in certain electrochemical cells, of which the chlor-alkali industry represents a classic example.

Lead, lead alloys and graphite in the various shapes of plates or blades were used in the early days of EMD production, but these materials did not suffice in terms of the requirements set above. Graphite, for example, tends to undergo mechanical failure during an automated EMD-removal operation, while hardened lead alloys cause contamination of the product under high current densities. Titanium in the field of EMD technology was one of the most important innovations and was pioneered by the Japanese company, Tosoh. Ti metal fulfills the basic requirements (i) to (v) and is used as anode or electrode-substrate for more advanced anodes in most EMD manufacturing plants around the world. An example of a modified Ti anode includes application of a lead dioxide film to the Ti substrate. This can be done using an electrolytic solution containing 350g/l $Pb(NO_3)_2$ and 5g/l $Cu(NO_3)_2$ at 70°C with the application of a current density of $1A.m^{-2}$ and increasing it to $20A.m^{-2}$ over a duration of 18hours [23]. In a recent patent [3], anodes were constructed that consisted of a Ti core and a titanium-lead active surface layer. The following possible combinations for the active layer are claimed:

(a) 32wt% Ti and 68wt% Pb,
(b) 51wt% Ti, 2wt% ZrC and 47wt% Pb,
(c) 39wt% Ti, 1wt% TiC and 60wt% Pb-Ca-Sn,
(d) 30wt% TiAl6V4 and 69.5wt% Pb,
(e) 40wt% Ti and 60wt% Pb,
(f) 15wt% Ti and 85wt% Pb and
(g) 70wt% Ti and 30wt% Pb.

All the above forms of anodes have limited scope for commercial application due to high cost of manufacturing, while some have also shown failure of the coatings during operation.

The most recent development known to the author is a Ti-Mn alloy that was initiated by a Chinese metal manufacturing company.

1.4 Anodic oxidation of Ti.

The required conditions for MnO_2 electroplating, especially solution composition (pH) and a positive electrode potential, are suitable for anodic oxidation of a valve metal electrode to occur according to the reaction [24]:

$$M + 2H_2O \leftrightarrow MO_2 + 4H^+ + 4e^- \quad \text{.....(1.19)}$$

M = Ti, Zr, Hf, V, Nb, Ta, Cr, etc.

The process of Ti surface oxidation is regarded as being inextricably associated with EMD production. It is therefore justified to give a short description on this phenomenon as well as to elaborate somewhat on techniques that can be employed to study anodic oxidation in the absence of MnO_2 electroplating.

It is general knowledge in physics that the relationship between potential difference, ΔV, and the electric field strength, E, that sustains this potential difference, is given by:

$$\Delta V = \int_{P_i}^{P_f} E \cdot dl \quad \text{.....(1.20),}$$

with P_i and P_f being the respective positions over which ΔV is measured. If dV is taken as the potential difference over the infinitesimal distance, dl, then equation 1.20 can be rewritten as:

$$\int dV = -\int E \cdot dl \quad \text{.....(1.21).}$$

If the electric field is taken as constant over distance, d, and only scalar quantities are considered, the result is:

$$V = Ed \quad \text{.....(1.22), or}$$

$$E = \frac{V}{d} \quad \text{.....(1.23).}$$

The high field model (HFM) makes use of equation 1.23 to describe passive film growth under potentiostatic conditions. It is apparent that the electric field strength will decrease as the film grows thicker, leading to a diminution of the ionic current with progressive film growth. The ionic current for film growth according to the HFM is given by the following equation [25]:

$$i = Ae^{BE} \quad \text{.....(1.24),}$$

with A and B being temperature dependent constants. An alternative to equation 1.24 is:

$$i = Ae^{B/d} \quad \text{.....(1.25).}$$

An introduction to the HFM can also be found in the work of Oliveira *et. al.* [26], while equation 1.24 is also mentioned in reference [24]. Valuable insight could be obtained from the HFM, but the model has some drawbacks. One of the most concerning shortcomings is that the model does not place a limit on the magnitude of the electric field. Equation 1.23 makes it possible to calculate physically unrealistic high values for E. This aberration is, however, rectified by the point defect model (PDM). It follows from this model that E is independent of both applied voltage and film thickness. A mathematical description and physical interpretation of the PDM is involved and will not be attempted in this study. Nonetheless, it goes to show that the theory behind anodic oxidation and film growth does have a theoretical background and is a complicated field of study.

1.4.1 Electrochemical preparation and characterisation of anodic oxide films on Ti.

The electrochemical oxidation of Ti and TiN has been extensively studied with voltammetric methods [24, 27 - 39] in various electrolytes including H_2SO_4, Na_2SO_4, NaCl, NaOH, H_2PO_4, HCl, $KClO_4$ and $HClO_4$, as well as non-aqueous electrolytes such as Na_2HPO_4 and $C_3H_9O_4P$ dissolved in ethylene glycol [30]. The electrolyte that is used for anodic oxidation is important since it determines the oxidation state of Ti in the oxide film e.g. TiO, TiO_2, Ti_2O_3

and Ti_3O_5 [24]. Anodic oxidation of a metal can be carried out in a conventional thermostated electrochemical cell. The working electrode consists of the valve metal to be oxidised (e.g. Ti). As a requirement for the coulometric estimation of oxide film thickness, the working electrode should have a known surface area. Platinum wire or gauze as an auxiliary electrode has the obvious advantage, but transition metals will also suffice for this purpose if only cathodic potentials are applied to the auxiliary electrode. Depending on the electrolyte in which oxidation is to take place, various reference electrodes can be used for measuring the working potential. By merely scanning the working potential between the extremes of the hydrogen evolution potential and oxidation of H_2O, anodic oxidation of Ti is initiated at a point well beneath the O_2 evolution potential. Scan rates ranging from $1mV.s^{-1}$ to $1000mV.s^{-1}$ have been employed in previous studies on oxidation of valve metals. Together with variables such as temperature, electrolyte composition and final anodic potential, it was also concluded that the solid state properties of the oxide film strongly depend on the initial growth rate of the oxide film (e.g. the initial scan rate) [35, 36].

An example of potentiodynamic oxidation of a 250Å Ti thin film in 1N $HClO_4$ is illustrated in the voltammogram in figure 1.3 [29]. Potentials were measured against a saturated calomel electrode (SCE) and oxide films were grown at a scan rate of $5mV.s^{-1}$. The faradaic current peak at +0.498V vs. SCE is reported to be most probably due to an initial ionisation of the surface atoms of the Ti metal. Beyond this first anodic peak, the current decayed to a near constant value of 30-40μA. This current/voltage behavior is consistent with a theory in which the growth of the oxide layer is rate limited by the field assisted migration of ions across the metal/oxide interface and not by the oxide/solution interfacial charge transfer. Armstrong and Quinn [29] stated that propagation of the oxide layer is exclusively rate limited by the transport of Ti ions across the metal/oxide interface. It is however known that anodic oxide films on valve metals such as Al, Bi, Nb and Ta grow at both the oxide/electrolyte and metal/oxide interfaces *via* outward migration of metal cations and inward migration of O^{2-}/OH^- ions across the oxide film, respectively [40]. The concept of transport number can be applied to the migration of ionic species across a metallic oxide film. Transport number is defined as the fraction of ionic current carried by a specific species [31]. The transport number for a cation is thus:

$$\text{Cation transport nr} = \frac{\text{cation current}}{\text{total ionic current}} \quad \text{.....(1.26)}$$

As an example, the transport numbers for a few relevant cations are 0.4 for alumina [41, 42], 0.24 for niobia and tantala [40, 43], 0.13 for bismuth oxide [42] and 0.35 for anodic oxides on titanium [44].

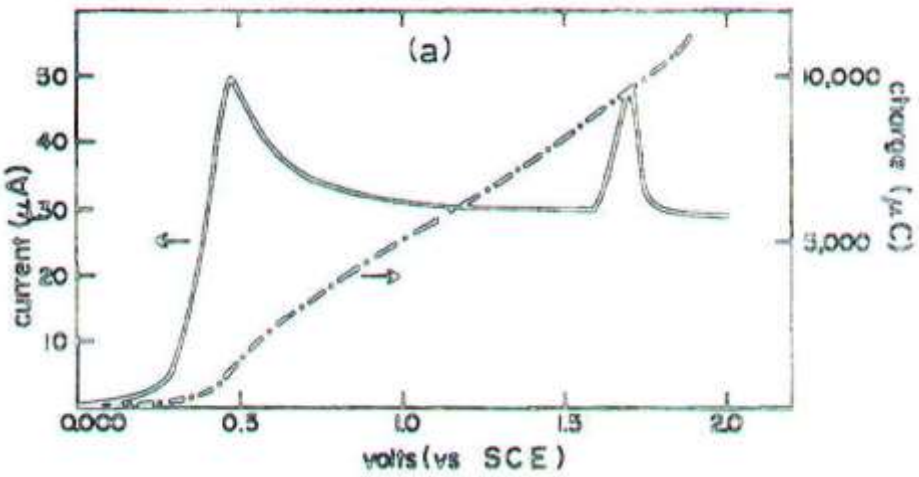

Figure 1.3: Voltammogram illustrating anodic oxidation of a 250Å Ti film in 1N $HClO_4$. Scan rate = $5mV.s^{-1}$.

Habazaki *et. al*. [31] devised an experimental method to determine the transport numbers for Ti^{4+} ions in amorphous anodic TiO_2. A Ti-6at%Si alloy was used for anodisation to obtain an oxide film with a thickness of 183±3nm. The Si atoms in the Ti served a dual purpose. It was firstly used to stabilise the amorphous oxide film, i.e. to eliminate an amorphous-to-crystalline transition. Secondly, it acted as a marker plane due to the Si being immobile as a result of the high Si^{4+}-O bond energy. The transport number for Ti^{4+} was obtained by rationing the number of Ti ions above the Si marker plane to the total number of ions in the oxide film using Rutherford backscattering spectroscopy (RBS) as analysis method. A value of 0.39±0.03 was obtained in this way corresponding with the value published by Wood *et. al*. [44].

The second peak current at +1.72V vs. SCE in figure 1.3 was not definitely associated with a certain reaction by Armstrong and Quinn [29]. It was however proposed by more than one author [24, 29] that the origin of this peak lies in a phase transformation of the oxide film.

Regardless of the mechanism and kinetics of the formation of an anodic oxide film on Ti or any other valve metal, once it is formed, a number of questions related to the physical properties of the oxide film arise. Properties such as film resistivity, dielectric constant, refraction index, crystal structure, topography etc. have been the endeavour of scientific knowledge in the field of anodic oxide films. However, the property that usually first attracts attention is simply the film thickness. The following methods have been developed to determine film thickness:

(a) Coulometric method
(b) Light reflection method
(c) Ellipsometric method
(d) Capacitance method
(e) Hunter method

The coulometric method makes use of Faraday's equation to convert the amount of charge transferred for film formation to its thickness, d.

$$d = d_0 + \frac{M_r}{zFAr\rho}\int_0^t Idt \quad \text{.....(1.27),}$$

where d_0 is the thickness of the air formed oxide film, M_r is the molar mass of the oxide, the number of e^- transferred is given by z, F represents Faraday's constant, A is the electrode area, r is a quantity known as the surface roughness factor and ρ introduces the density of the oxide film in equation 1.27. The quantity $\int_0^t Idt$ indicates the amount of charge involved. It is clear that the coulometric method does not allow accurate determination of film thickness. As a first problem, a reaction is required to indicate the number of e^- applicable or alternatively, the initial and final oxidation state of the Ti is required. Reaction 1.19 allows assuming a value of 4 for z (Ti^0 to Ti^{4+}) and the value of M_r is now also known, although this assumption of TiO_2 being the only form of oxide may be over-simplified. Finally, TiO_2 may exist in one of three different crystal structures, namely rutile, anatase and brookite. Each of these crystal structures has its own characteristic density and if X-ray diffraction is able to determine

which of the above structure covers the bulk of the metal surface, then ρ is known in equation 1.27. The density, as well as other relevant properties of the different crystal structures of TiO_2 is summarised in table 1.1.

Crystallographic phase	*Bravais lattice*	*Reference*
Anatase	Tetragonal	[45]
Brookite	Orthorombic	[45]
Rutile	Tetragonal	[45]
Crystallographic phase	*Band gap (nm)*	*Reference*
Anatase	377	[46]
Rutile	397	[46]
-	413	[47]
Crystallographic phase	*Density ($g.cm^{-3}$)*	*Reference*
Anatase	3.9	[45]
Brookite	4.13	[45]
Rutile	4.23	[45]
Amorphous	2.86 tot 3.04	[45]
Crystallographic phase	*Refraction index*	*Reference*
Anatase	2.5246	[45]
Brookite	2.6226	[45]
Rutile	2.7545	[45]

Table 1.1: Summary of properties of different polymorphs of TiO_2.

A physical quantity that may give insight into the effects of anode oxidation during electroplating of MnO_2 is the oxide film's dielectric constant. The dielectric constant is indicative of a substance's insulating behaviour; if the dielectric constant increases, the material is more insulating. An oxide film on a valve metal has a capacitance that is a function of the film's thickness. The relationship between capacitance and film thickness can be used to calculate a film's dielectric constant. Bacarella *et. al*. [28] proposed a fundamentally simple method to determine the capacitance of an oxide film on an electrode in an electrochemical cell. This method is known as the galvanostatic pulse technique and places severely strict requirements on instrumentation. A current density of about $2x10^{-3}A.cm^{-2}$ is to be pulsed through the working electrode for 3ms and the voltage-time trace for the first 20-50μs is recorded. The definition of capacitance, C, can now be used to calculate its magnitude as follows:

$$C = \frac{dQ}{dV} \quad \text{.....(1.28)}$$

$$= \frac{Idt}{dV} \quad \text{.....(1.29)}$$

$$= \frac{I}{dV/dt} \quad \text{.....(1.30)}$$

with $\frac{dV}{dt}$ the slope of the measured voltage *vs.* time curve. Capacitance values should be determined for a range of film thickness to use the parallel plate capacitor to determine the dielectric constant [27]:

$$d = \frac{DA}{(4\pi C)(9x10^{9})} \quad \text{.....(1.31),}$$

where d represents the film thickness, D is the dielectric constant of the oxide and A is the electrode area. It follows readily from equation 1.31 that D can be calculated from the slope of a graph of film thickness vs. capacitance. Rahim [27] used potentiodynamic anodisation at a scan rate of $1mV.s^{-1}$ to oxidise Ti in a solution of 0.5M Na_2SO_4 + 0.01M H_2SO_4. A dielectric constant of 18.2 was obtained for an oxide film that was grown at potentials beneath the O_2 evolution reaction, while a higher value (39.7) was obtained for films grown within the O_2 evolution reaction.

1.4.2 Disadvantages of anode passivation during electroplating of MnO_2.

It is the tendency of Ti to be anodically oxidised that makes it useful as an anode in an electrolysis process such as EMD production from an acidic Mn^{2+} containing solution. Common metals such as Cu or Zn will dissolve when used as anodes in electrolysis processes and the advantage of a valve metal is evident from a commercial production perspective. Except for the obvious advantage, the extent of anode oxidation should be limited during EMD production [48 - 53], or else it can severely increase ΔV_{Ω} and could consequently also affect EMD quality. Passivation is the general term used to describe the slowing down of any process, action or reaction. Passivation, as applicable to metals in academic circles, denotes improved corrosion resistance of a metal in an electrolyte (or air), whatever the cause. This description of passivation makes it possible to state that the term “passivation”, as used to

describe a kind of detrimental effect during MnO_2 electroplating, is equivalent to oxidation of the metal anode. An anode is regarded as passivated from a commercial perspective when anode oxidation has reached a stage to increase ΔV to a value that is higher than typical for electroplating of EMD. The financial implication of an increase in ΔV can be illustrated with the following elementary example. Consider a 500mV increase in ΔV for 50 electrolysis cells in series. This equates to a 475kW increase in power consumption at a constant current of 19000A. If the cells are to be operated for 360days over the duration of a year at 0.09 S.A. Rand per kW.h, the increase in expenditure equates to (360days x 24h/day) x (0.09R/kW.h) x (475kW) = R369 360.

Only two theories have been found in literature sources that were proposed to explain the increase in cell voltage due to an oxide layer on the surface of a Ti anode during electroplating. Swinkels [49] stated that a thin ($\approx$ 10nm) semiconducting layer of oxide is formed on a Ti surface under oxidising conditions. During plating of EMD, current flows through this layer and the process of electrolysis can continue unhindered, but under severely oxidising conditions, the oxide film becomes thicker. Current now has to pass through a thicker layer of oxide and to maintain a constant current, a higher voltage drop across the oxide layer is required and this leads to even more severe oxidising conditions and a still higher voltage drop is required for a constant current to flow. A snowball effect is thus experienced and at this point it is stated that the anode has become passivated. This description is however incomprehensible if the oxide layer on the metal surface is a semiconductor. This discrepancy can be explained by looking at the possible increase in cell voltage. At initiation, EMD plating on Ti can start at voltages in the order of 2.4V over the cell (ΔV) using a Pb cathode and the appropriate set of experimental conditions e.g. current density, $MnSO_4$ concentration, H_2SO_4 concentration and temperature. By varying one or more of the latter parameters, it is possible to induce an increase in cell voltage, and values of up to 7V is measurable to maintain the desired current density. Assuming that the oxide layer (passivation) is exclusively the source of the increase in cell voltage, a simple calculation can be used to calculate the thickness of such oxide layer. For a current density of $100A.m^{-2}$, the unit RA can be introduced as a measure of resistance, R, associated with a certain area, A. From Ohm's law:

$V = IR$ .....(1.32), and therefore:

$$RA = \frac{V}{i} \quad \text{.....(1.33),}$$

where V represents the cell voltage and

$$i = \frac{I}{A} \quad \text{.....(1.34),}$$

is the current density. For an increase of 4.6V in V at a current density of $100A.m^{-2}$, a resistance quantity of $RA = 0.046\Omega.m^2$ is calculated. The definition of resistivity, ρ, relates resistance with the dimensions of the material namely its length, L and area, A:

$$R = \rho\frac{L}{A} \quad \text{.....(1.35).}$$

The resistance of an intrinsic semiconductor has a typical value of 1Ω.m [54], leading to a value for L of:

$$L = \frac{RA}{\rho} = \frac{0.046\,\Omega.m^2}{1\Omega.m} = 46mm \quad \text{.....(1.36),}$$

a value that is highly unlikely to represent the thickness of the oxide layer.

A theory that was used to describe electrolytic rectification behavior of an anodic film on aluminum [55], can also be employed to possibly correlate voltage increase with passivation. It was found that an anodic oxide film might exhibit rectification as a diode due to an n-i-p junction that forms on the metal surface. The inner layer of the oxide film that is directly in contact with the metal substrate has an excess of metal ions and, as a consequence, is a defect semiconductor containing an excess of cations to produce an n-type semiconductor. The outer layer, on the other hand is exposed to an excess of anions in the form of oxygen ions and forms a p-type semiconductor. The middle layer might consist of a stoichiometric semiconductor compound e.g. TiO_2 in the case of a Ti anode, to represent an intrinsic semiconductor. If a positive polarity is placed on the metal substrate, the n-i-p junction is connected in reverse bias and a depletion region develops as a result of diffusion of free

carriers across the junction. In the case of a true solid state diode, no electronic current will flow in the reverse bias configuration until reverse breakdown occurs. This is, however, not observed during the electroplating of EMD, where other complexing factors in conjunction with the rectification theory may explain the observed current at high cell voltages.

Another aspect that needs to be addressed to resolve the question of increase in cell voltage as possibly related to passivation, is how it is possible for an oxide film to grow underneath an already deposited layer of MnO_2. Authors [48 - 50, 52 - 53] in the field of anode passivation during electroplating of MnO_2 have ignored any explanations of this nature, except for Preisler [51] who presented an explanation based on the semiconducting properties of MnO_2. This author proposed that it is actually the layer of MnO_2 which separates the Ti from the ionic environment of the aqueous solution that limits the extent of passivation. When exposed to the solution, the current will be carried by ions and this would enhance oxidation of the metal at sufficient voltages. The MnO_2 behaves as an n-type semiconductor, making it possible for the current to be carried through the MnO_2 deposit to the $MnO_2/TiO_x/Ti$ interface by means of the e- in the conduction band of the MnO_2. It was found in experimental trials at various industrial plants associated with the production of EMD, that an increase in cell voltage takes place predominantly at high current densities and low temperatures, i.e. lower than the conventional 95°C - 98°C. Preisler's hypothesis explains last mentioned observations as follows: when the current density exceeds a value that can be maintained by the e^- in the conduction band of the MnO_2, ions provide means for the extra current to be carried. Oxygen ions are now able to migrate to the Ti metal where oxidation can take place. The same explanation goes for a voltage increase at lower temperatures: a decrease in temperature causes the e^- in the conduction band of the n-type semiconductor to decrease and additional current is carried by ions.

Whatever the explanation for the observed increase in cell voltage under passivating conditions, it also appears to be affecting the MnO_2 quality under certain conditions of the electroplating onto a Ti anode. Miyazaki *et. al*. [52] compared the EMD crystallites that were electroplated under normal conditions with material that was produced under "increased voltage" conditions using secondary electron microscopy (SEM). The results are illustrated in figures 1.4 and 1.5. Under normal conditions the crystallites grew in a bamboo sprout-like manner, while it had a sharp knife edge-like topography under increased voltage conditions.

They also found EMD that was produced under normal conditions to have a larger discharge capacity in wet alkaline test cells. These test cells served as a simulation of Zn/MnO_2 alkaline battery cathodes. Armacanqui and Ekern [48] in turn stated that the passivation of titanium leads to increased microporosity and decreased consistence of the typical γ crystallographic structure, which then causes a degradation of the EMD electrochemical performance.

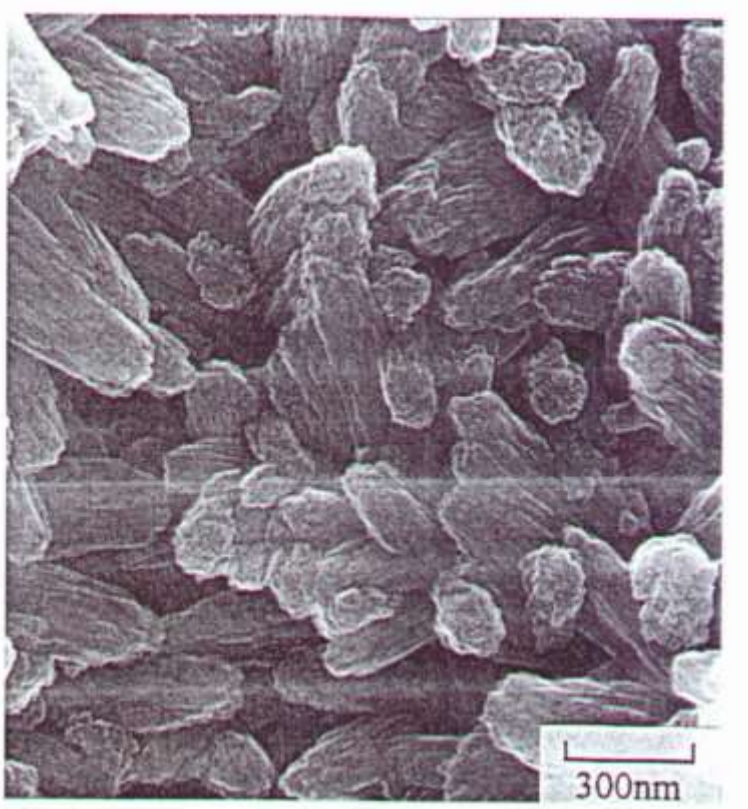

Figure 1.4: SEM image of EMD electroplated on Ti at a "normal" cell voltage.

1.5 Motivation and objective of study.

Except for being a veritable fact, it cannot be over-emphasised that anode passivation is the main cause for the already mentioned deleterious effects of high ΔV and consequent degradation of EMD quality. Furthermore, it has been mentioned that oxidation of MnO_2 to soluble MnO_4^- is a possibility at sufficiently elevated anodic potentials. It is so obvious as to be hardly worth mentioning that these three deviations pose a pernicious threat to production costs and product quality and the fact that it should be averted cannot be obscured. The present study is therefore devoted to further development and understanding of existing technology in the form of Ti based anode materials to elude the mentioned deficiencies of a

pure valve metal. This objective is to be obtained by preparing electrode specimens using different techniques, followed by evaluating the structural, electrochemical and compositional properties of these electrode materials.

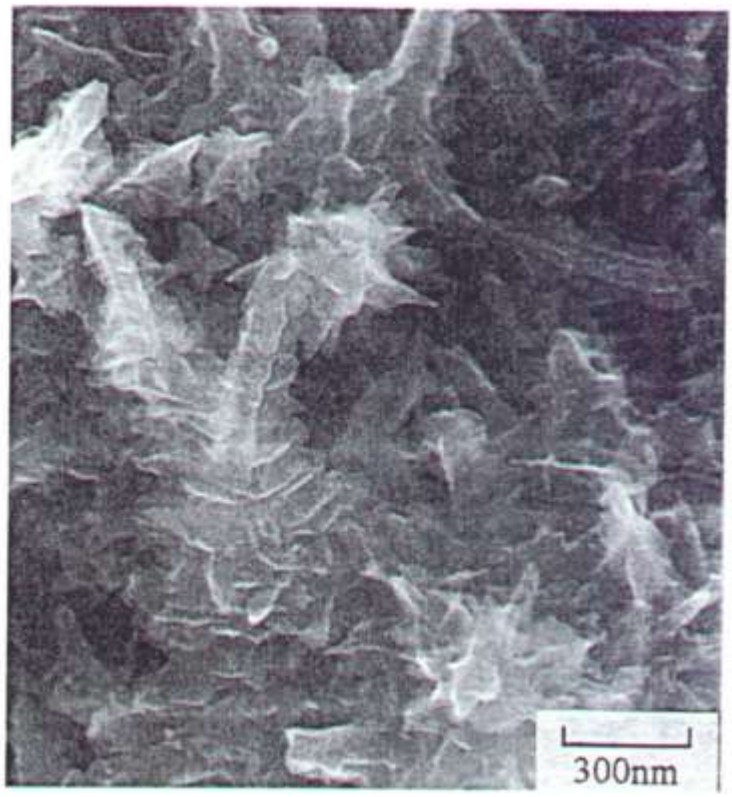

Figure 1.5: SEM image of EMD electroplated on Ti at "increased" cell voltage.

1.6 Layout of dissertation.

The following categorisation serves as a concise description of the contents of this dissertation:

(a) An introduction to electrocatalysts is presented in the literature study in chapter 2.
(b) The different experimental techniques are described in chapter 3 with reference to the theory of the methods as well as its specific application in this investigation.
(c) The electrochemistry of Ti metal in an acidic medium is discussed in chapter 4.
(d) Results and discussions on the electrochemistry and structural properties of a variety of electrode materials can be comprehended from chapter 5.
(e) Surface analyses and compositional depth profiling of the anode materials from chapter 5 is presented in chapter 6.

Chapter 2

Literature study on the preparation, properties and characterisation of electrocatalytic transition metal oxide electrodes.

2.1 Introduction to dimensionally stable anodes and electrocatalysis.

As far as is known, the first reports that hinted at the term electrocatalysts are dated prior to World War II. Even before this, it was realised that the electrolytic reduction of aqueous solutions to yield molecular hydrogen could be manipulated by two catalytic effects [56]. The first is the specific action or behaviour of the cathode material in the electrolytic cell and secondly, the process can be affected *via* addition of certain salts to the electrolyte in which the electrolysis is taking place. The fact that certain metal electrodes e.g. Pt (platinised), Au, Ag, etc. showed lower overvoltage for the reduction of protons compared to metals such as Zn, Pb, etc. was realised to be the result of the catalytic activity of the former metals. The phenomenon was merely referred to as catalysis in electrochemistry and the metals of interest were not referred to as catalysts or electrocatalysts for that matter.

Reports indicate that mixed Ru based oxides have been studied since the late 1950's due to electrocatalytic behaviour of these oxides [57], but the first electrocatalyst was prepared and officially patented by H.B. Beer in 1966. The initial objective of Beer was not an attempt to lower overvoltages during electrolysis processes, but was devoted to improvements in chlorine gas production. Frequent reference will be made to anode technology that is relevant to the chlor-alkali industry in the following paragraphs. This is, however, just to describe the origin and historic trend of development of industrial electrodes known as dimensionally stable anodes (DSA's) which have a much greater diversity of applications at the present time. Graphite anodes in chlor-alkali cells are subjected to wear that leads to the production of less pure chlorine gas. A diminution in the dimension of a graphite anode has also proven inevitable, which in turn leads to an increase in the inter-electrode gap. These restrictions could in principle be overcome by using any valve metal as an anode in aqueous media. Although it is the passivity of a valve metal that renders it appropriate for use as an anode with a constant dimension, progressive anodic oxidation of the electrode could however cause a failure in the form of a catastrophic increase in ΣV_{Ω}. The surface of a valve metal

like Ti therefore needs to remain activated and this was obtained by Beer using a precious metal oxide. The first electrode in this form was prepared *via* thermal decomposition of a Ru precursor solution on a Ti substrate to form a thin layer of a RuO_2 + TiO_2 mixed oxide. This presented a prototype dimensionally stable anode and with this composition, the oxide acts as an electrocatalyst towards the electrode reaction of interest. Since it correctly serves two of its purposes, the name "DSA" is not just a contigency, but it does elude one of its more impressive and extraordinary properties, namely that of electrocatalysis. It is fair to state that it is actually this property that has sparked the use of DSA's in electrolytic plants other than the chlor-alkali industry. As a final point on terminology, it should be noted that although the initial definition of a catalysed process in general stated that it is limited to thermodynamically spontaneous reaction, this has changed [58]. Processes with an increase in free energy can indeed be catalysed and is also relevant for industrial applications where the reagents are not always expected to be fully converted. This is frequently true for electrocatalysts since these materials mainly find applications as electrodes in electrolysis processes. Hence, electrocatalytic DSA's have grown to be of significant value and are worthy of its nomenclature.

Since the replacement of graphite anodes in chlor-alkali cells, numerous papers have appeared on the subject of DSA's [22, 57, 59 - 64]. Initial investigations concentrated on industrial applications of a binary mixed oxide of a valve metal and a platinum group metal on a valve metal substrate. The initial and most common applications of electrocatalytic DSA's are for the mentioned Cl_2 gas production and O_2 evolution. Today, a typical DSA for chlorine production is a ternary oxide system of RuO_2-IrO_2-TiO_2. Except for the latter, DSA's can also be designed to render itself for numerous other industrial and scientific applications of which a complete list can be found in table 2.1, which was taken from the book of Trasatti [59]. Among these is the electrolytic production of MnO_2. The application of an electrocatalyst as a substrate for MnO_2 electrodeposition is therefore not a novelty, but studies on this specific application of electrocatalysts are very scanty. The only report that the author is aware of is that of Matsuki and Sugawara [50]. An extensive study on this subject therefore needs no further justification.

DSA applications	
1. Chlorate electrosynthesis	15. pH sensors and actuators
2. Bromate electrosynthesis	16. Detectors for liquid chromatography
3. Persulfate electrosynthesis	17. Electronics
4. Sodium peroxyborate electrosynthesis	18. Resistors
5. Chlorine dioxide electrosynthesis	19. Double layer capacitors
6. Electrolytic MnO_2	20. Photocatalysis
7. CO_2 reduction	21. Photo-electrolysis
8. Molten salt electrolysis	22. Photovoltaics
9. Ozone production	23. Electroless redox catalysis
10. Wastewater treatment	24. Lead-acid batteries
11. Cathodic protection	25. Li batteries
12. Metal electrowinning	26. Hydrogen cathodes
13. Gold electroplating	27. Oxygen cathodes
14. Chromium electroplating	28. Organic electrosynthesis

Table 2.1: A list of applications of electrocatalytic electrodes other than for Cl_2 and O_2 evolution reactions.

2.2 Preparation techniques of DSA's.

Although any valve metal should in principle suffice as a DSA substrate, Ti appears to be the industrial support metal of choice, while Ru has played a dominant role as the platinum group metal. One reason for the widespread choice of Ti and Ru is the fact that TiO_2 and RuO_2 form isomorphous crystal structures that facilitate a solid solution [60]. Other platinum group metals, especially Ir, have also been mentioned [64 – 66], while it is even possible to use metals outside the platinum group [59, 64] to form a ternary mixed oxide that increases the service life of an anode [60]. The basic construction of a DSA however remains the same, i.e. a platinum group metal oxide on a valve metal substrate. The general perception is that the method of preparation is capable of dramatically influencing a variety of properties of the formed electrocatalytic oxide. Only two methods can effectively be employed for DSA preparation in the industrial environment namely (a) thermal decomposition of a suitable precursor solution on the parent metal and (b) electrosynthesis. A few oxide electrodes and

their most common precursor solutions are illustrated in table 2.2. Other techniques to deposit a metal oxide include plasma-spray, reactive sputtering and chemical vapour transport. These methods are not suitable for large-scale applications since it requires strict control. Last mentioned techniques are nonetheless valuable in fundamental research e.g. chemical vapour transport can be controlled to grow single crystals of RuO_2 [67]. The principles of these techniques will however not be discussed, but a summary of the former two methods will be given.

Oxide	Precursor
RuO_2	$RuCl_3.nH_2O$
IrO_2	$IrCl_3.nH_2O$, $H_2IrCl_6.6H_2O$
MnO_2	$Mn(NO_3)_2.4H_2O$
Co_3O_4	$Co(NO_3)_2.6H_2O$
NiO_x	$Ni(NO_3)_2.6H_2O$
SnO_2	$SnCl_2.2H_2O$, $SnCl_4$
PdO_x	$PdCl_2$
Cr_2O_3	$CrCl_3.6H_2O$, $Cr(NO_3)_3.9H_2O$

Table 2.2: A list of precursors used for preparing oxide electrodes. [59].

2.2.1 Thermal decomposition technique.

It should be emphasised that the thermal decomposition (TD) technique traditionally involved a rudimentary method of application of a precursor solution onto the valve metal substrate after which calcination will decompose the precursor to form the electrocatalytic oxide film. More advanced methods have recently also been employed as a TD technique e.g. spraying of the precursor on the heated substrate [68]. Although the principle of the TD technique is simple, a diversity of parameters can influence the properties of the resulting film. As an example, RuO_2 can be formed *via* decomposition of an acidic $RuCl_3.3H_2O$ precursor between 300°C and 500°C. This is also the optimum temperature for preparation of oxides such as Co_3O_4 and $NiCo_2O_4$, which also find applications as DSA's. At too high temperatures, the Ti support can become oxidised to such extent that it is to the detriment of the applied potential during operation of the DSA. Oxidation of the Ti substrate is always expected since the formation of TiO_2 (ΔG^0 = -890kJ.mol^{-1}) is thermodynamically favoured

over that of RuO_2 (ΔG^0 = -255kJ.mol^{-1}) [57], but a solid solution of RuO_2 and TiO_2 will form at 400°C [69, 70]. Other problems involved with high calcinating temperatures are a decrease in the effective surface area of the oxide and contact problems between the support and oxide film [71]. An advantageous temperature effect is the decrease in resistivity of RuO_2 and IrO_2 films with annealing temperature. A too low firing temperature will however result in the presence of undecomposed material and instability of the DSA under anodic load. Borresen *et. al.* [57] indicated that the catalytic activity of $Ru_{0.04}Ti_{0.96}O_2$ electrodes decrease with an increase in annealing temperature. The temperature effect also extends to the crystal structure of oxide films. For some oxides, X-ray diffraction showed a change in the size of the unit cell as a function of annealing temperature [72]. The crystallite size also changes as a function of temperature. The preparation of a certain precious metal oxide is furthermore not limited to a single precursor. A nitrate solution of Ru is an alternative to the chloride compound to prepare RuO_2. Since the mechanism by which an oxide film forms is dependent on the precursor, the characteristics of the film will also differ for different precursors. Ardizzone *et. al*. [73] found RuO_2 crystallites to be more finely dispersed when prepared from the nitrate solution than the chloride. This can possibly lead to an increase in electronic resistance of the film, since it is expected that intergrain resistance will increase due to an increase in the number of grains. Except for varying the precursor compound to alter the film characteristics, the solvent in which the precursor is dissolved can also have an effect on the oxide. Fairly common alternatives to an aqueous solvent are isopropanol [65] or ethylene glycol [61]. The possibilities of the TD method can further be exemplified with the work of Fang *et. al.* [68]. An organic precursor was utilised to prepare a RuO_2 DSA. A ruthenium ethoxide species, $Ru(OC_2H_5)_3$, was prepared in an ethanol solution according to the reaction:

$$RuCl_3 + 3Na(OC_2H_5) \rightarrow Ru(OC_2H_5)_3 + 3NaCl \quad .....(2.1).$$

This reaction took place in ethanol as solvent at boiling point (78°C), after which the NaCl precipitated and the $Ru(OC_2H_5)_3$ remained in solution. Using this TD method, it was found that the RuO_2 had an amorphous composition for decomposition temperatures below 200°C, while a crystalline phase appeared at 250°C and above. The authors of reference [68] also concluded that the surface morphology of the films is dependent on annealing temperature. Scanning electron microscopy results revealed the presence of much greater extent of

porosity in the particles for films prepared at low temperatures (<200°C). Another example illustrating the effect of the solvent on film properties is the preparation of mixed RuO_2 + IrO_2 electrodes. By using the same precursor compound but different solvents, a definite difference in electrocatalytic response is evident. When isopropanol is used as the solvent, a simple additive behaviour of $\%IrO_2$ is observed as a function of the electrode's electrocatalytic behaviour. If water is used, indications are that intimate mixing occurs on an atomic level [74].

2.2.2 Electrosynthesis.

Besides the use of RuO_2 as part of an electrocatalyst in large scale electrochemical production processes, its large surface area also finds application in electrochemical capacitors [61, 68, 75], while metallic resistivity (35μΩ.cm) and high thermal stability makes it a sought after material to act as a thermal diffusion barrier in integrated circuits [75]. The net result of the above versatility of RuO_2 is that research in the field of electrocatalysts and electrochemical capacitors has led to the discovery of electrochemical methods for the growth of electrocatalytic oxide films on valve metal surfaces [60, 62, 66, 76]. Potentiostatic and galvanostatic methods are possibilities to obtain thin oxide films, while potential cycling in a cyclic voltammetry (CV) method can yield a greater quantity of the electrocatalytic material on a parent metal. Electrodeposition of electro-active RuO_2 films is however not a very widely studied subject. Fabrication of hydrous Ru oxide films for studies on electrochemical capacitors was done using cyclic voltammetry to coat a Ti substrate with the oxide [76]. A plating electrolyte consisting of 5mM $RuCl_3.nH_2O$ and 0.01M HCl in a 0.1M KCl supporting electrolyte was used to grow the Ru based oxide at a temperature of 50°C. A scan rate of $50mV.s^{-1}$ was employed and the potential was repetitively cycled between –200mV and 1000mV *vs*. Ag/AgCl. The authors of reference [77] used the same method as the latter, but used a solution of 2mM $RuCl_3.nH_2O$ in 0.1M $NaNO_3$ and scanned the potential between -100mV and 900mV *vs*. saturated calomel at a rate of $20mV.s^{-1}$ on an Au electrode. Although it is reported [76] to be difficult to electroform ruthenium oxide from aqueous solutions using galvanostatic methods, these methods were utilised by Zhitomirsky [62] and Vukovic [60]. Vukovic used galvanostatic deposition on a Ti wire as working electrode in a stirred solution of 2.9mM $(NH_4)_2RuCl_6$ and 0.1M HCl. A current density of $400A.m^{-2}$ was controlled for 15min at ambient temperature. Zhitomirsky found it possible to prepare TiO_2,

RuO_2 and composite RuO_2-TiO_2 films on Pt substrates using thermal treatment subsequent to cathodic electrosynthesis. 5mM $RuCl_3.nH_2O$ in H_2O was used as the electrolyte for the Ru based oxide preparation. Since inorganic salts of Ti^{4+} are readily hydrolysed in H_2O to form titanium hydroxide precipitates, a peroxocomplex of Ti was used for oxide loading. This Ti complex can be prepared by dissolving $TiCl_4$ salt in H_2O_2 in a methyl alcohol solvent. In the mentioned study, the concentrations were 0.005M $TiCl_4$ and 0.01M H_2O_2 respectively. Cathodic polarization was done at a constant current density of $200A.m^{-2}$ for 20min at 1°C. The influence of pH, electrolyte composition, solubility of the oxide as well as its ability to adhere to the substrate and the growth rate was recognised in last mentioned study.

Indications are that there exists a disparity between the structure and overall composition of electroformed and thermal oxides. Mo *et. al*. [77] stated that electrodeposited Ru based oxide films are not similar to crystalline RuO_2 films prepared *via* chemical vapour deposition. Electroformed oxides are "hydrous" and have a $RuO_x.nH_2O$ or $Ru(OH)_4$ composition as suggested by Hu and Huang [76] and Zhitomirsky [62]. Whilst thermal oxides are expected to be a solid solution of TiO_2 and RuO_2, with chains of RuO_2 providing conductivity in a TiO_2 matrix, a definite junction between superficial TiO_2 and the $RuO_x.nH_2O$ is envisaged for hydrous oxides. Borresen *et. al*. [57] reported that an improvement in both the stability of the oxide film, as well as its electrocatalytic response would result from alloying the RuO_2 with TiO_2 in the TD method. This is in contrast with electrodeposited films. Experimental evidence is given in reference [60] that annealing of a hydrous ruthenium oxide film leads to a decrease in effective surface area and electrochemical activity. Although the binary oxide is in effect absent for electroformed oxides, it has been reported that annealing of a hydrous oxide will result in a "dry" oxide similar to a thermal oxide. It will however differ from other thermal oxides only in the sense that the precursor is different [78, 79]. Thus, the electrochemically grown hydrous film acts in principle as a solid state precursor.

2.3 Properties of electro-active oxide electrodes.

The foregoing discussions on preparation techniques already contain a prolific description of the properties of DSA's and specifically RuO_2. Although emphasis will be given to Ru based oxides in the following discussion, the essential properties of a DSA in general are worth listing again: (a) A conductive metal oxide should limit film resistivity to $1 \times 10^{-2} \Omega.m$,

(b) the oxide should have a high surface area that can be modified e.g. thermal treatment, (c) mechanical and chemical stability is required for a realistic service life, (d) environmental friendliness is another requisite for the applicable materials [22] and (e) most importantly, the electrode must show electrocatalytic behaviour towards the reaction of interest. A point to note on the general character of the oxide films under discussion is that it is reported that the oxides are of perfect stoichiometry, e.g. RuO_2, TiO_2 etc., but this is not necessarily the case. RuO_2, as an example, is an oxygen-deficient compound that contains residual chlorine when $RuCl_3.nH_2O$ is used as a precursor solution. One of the greatest virtues of a DSA is the conductivity of the oxide film. In a RuO_2 – TiO_2 mixed oxide system, a low resistivity is brought about by chains or clusters of RuO_2 that possess metallic conductivity in the TiO_2 matrix. To maintain the required conductivity as defined above, the quantity RuO_2 in the oxide mix should remain above 25-30mol% [69, 80, 81]. It was described in reference [57] that the RuO_2 clusters originate from oxide particles of 5-30nm in size. Film conductivity as a function of mol% RuO_2 is illustrated in figure 2.1 [59]. Another variable that has already been mentioned and that impacts on the conductivity of RuO_2 films is the annealing temperature in the TD technique. The resistivity of RuO_2 and IrO_2 as a function of annealing temperature is presented in figure 2.2 [82, 83]. Contrary to the provision of metallic conductivity by RuO_2, films of Co_3O_4 and $NiCo_2O_4$ are semiconductors and conductivity of these oxides results from nonstoichiometry that increases conductivity due to doping. These oxides however severely lack the advantageous properties of RuO_2 and IrO_2. Except for a higher electronic resistivity, two additional shortcomings are that (a) Co_3O_4 and $NiCo_2O_4$ are much less porous than RuO_2 and IrO_2 and (b) a solid solution with TiO_2 is not possible [84].

Regarding the effective surface area of precious metal oxides, it should be emphasised that it is actually the latter property, together with the chemical and electrochemical stability that renders these oxides as DSA's rather than the metal itself, because the activity of the oxides are not better than that of the pure noble metals [85]. Another advantage of the oxides over the noble metals is that bubbles that form during gas evolution reactions are more readily released from the electrode surface.

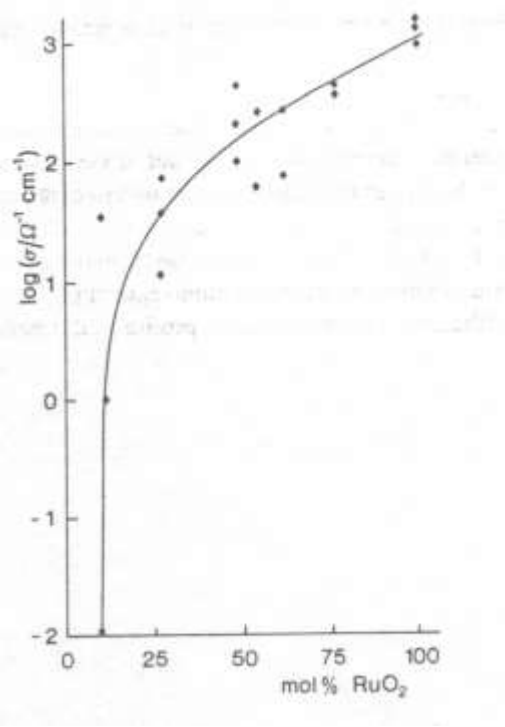

Figure 2.1: Conductivity of RuO_2-TiO_2 mixed oxide films as a function of mol% RuO_2.

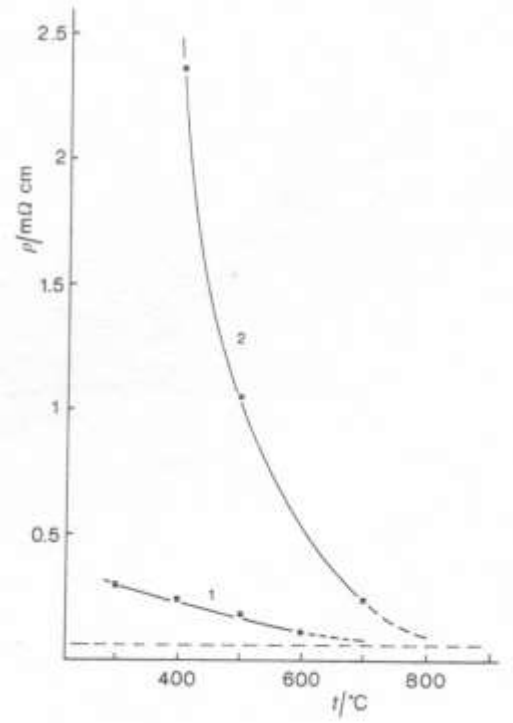

Figure 2.2: Resistivity of RuO_2 (1) and IrO_2 (2) as a function of firing temperature.

The cost of precious metal oxides requires for these oxides to have chemical and electrochemical stability during operation to maximise the service life of a DSA. Hydrous

electroformed Ru based oxides are prone to anodic corrosion [60, 86, 87]. The general rule is that the more hydrated the oxide, the greater the extent of corrosion. This degradation of the electro-active oxide is however not an instantaneous event, but progresses at a rate determined by the conditions of application. The net effect is that the TiO_2 substrate is eventually exposed as the RuO_2 is preferentially oxidised to soluble species. Thermal treatment stabilises such films, but to the disadvantage of electro-activity. Thermally prepared films however present the prospect of greater improvement in stability *via* alloying with a third element to form ternary mixed oxides. Three elements have been reported as suitable for improving stability namely Sn, Zr and Ir [59 – 61, 64 – 66, 88]. The anodic corrosion rate (v_c) is found to decrease exponentially with the mol% IrO_2 in RuO_2 [74]. These results are presented in figure 2.3. Similar results on the effect of SnO_2 are illustrated in figure 2.4 [88].

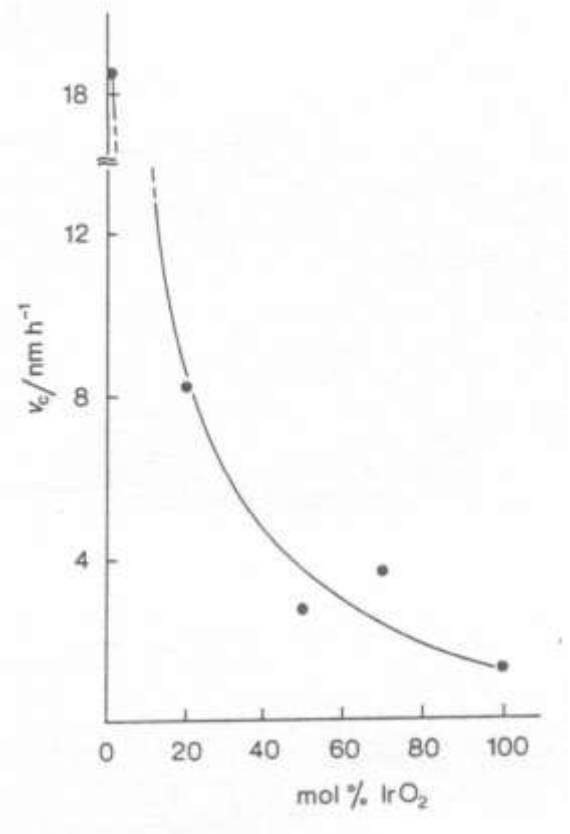

Figure 2.3: Decrease in corrosion rate as a function of IrO_2 in a RuO_2 - IrO_2 mixed oxide. Anodic polarization was done on electrodes in 0.5M H_2SO_4 at 1 x 10^4A.m^{-2}.

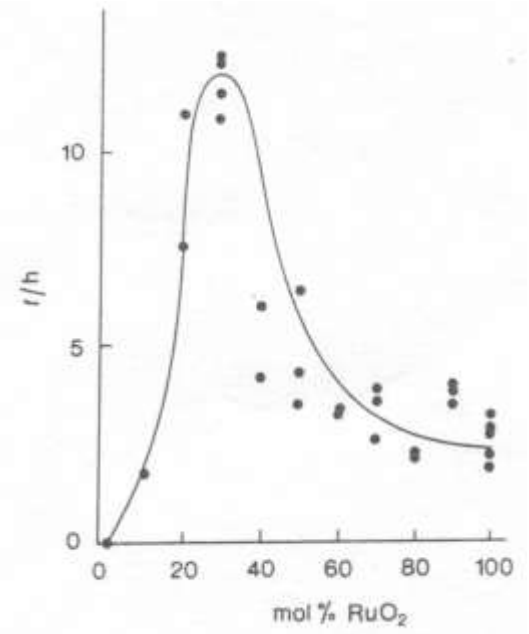

Figure 2.4: Electrode lifetime as a function of mol% RuO_2 in RuO_2 - SnO_2 mixed oxides. Anodic polarization was done on electrodes in 0.5M H_2SO_4 at 5 x 10^3A.m^{-2}.

For industrial applications, there is usually not much interest in distinguishing between the measurable enhanced activity of an electrocatalyst as determined by the effects of the oxide's effective surface area and electronic properties. It is however important for fundamental studies to have a description of electrocatalytic activity. Although literature on catalysis in general is readily available, it appears as if a paucity exists on the availability of literature sources that deal with the essence of electrocatalytic theory. Trasatti [59] introduced the term "electron-transfer relays" and described it as the surface-active sites on the electrode material that are responsible for catalysis of the induced redox transition *via* a chemical interaction. It has also been proposed that an electrode is more active towards a certain redox reaction that is taking place on its surface if the electrocatalyst has a redox transition close to the reversible potential of the reaction being induced on its surface.

2.4 Electrochemical characterisation of DSA's.

2.4.1 Voltammetry.

Several workers in the field of oxide electrodes have made use of cyclic voltammetry as a characterisation technique [57, 60, 61, 64, 65, 68, 76]. This consists of scanning the electrode

potential in acid or alkaline solutions in ranges where no permanent changes of the electrode occur. Examples of electrolytes are H_2SO_4, $HClO_4$ and HCl, but it is 0.5M H_2SO_4 that is predominantly being used. The obtained voltammograms are usually unique for each electrode material and is appropriately referred to as the electrochemical spectrum of a specific material. Although such a spectrum is indeed unique, it is subjected to experimental conditions e.g. sweep rate [57]. Data obtainable from voltammetric results include the voltammetric charge, q*. This variable is calculated from a part in the voltammogram where no peaks are present and it gives a relative indication of the electrochemical active surface area of an electrode, i.e. a larger q* is representative of an electrode with a greater surface area. The reaction responsible for q* in an acidic medium is the intercalation of protons in the oxide:

$$-MO_x(OH)_y + \gamma H^+ + \gamma e^- \rightarrow -MO_{x-\gamma}(OH)_{y+\gamma} \quad \text{.....(2.2),}$$

where M represents the metal in the oxide under discussion and the surface is assumed to be terminated by –OH groups. This exchange process of protons was determined to be relevant up to 50nm below the surface of thermally prepared RuO_2 [90]. It should be emphasised that q* is only a relative indication and it cannot necessarily be converted to the actual surface area of the electrode. Nonetheless, q* can be used as a variable to compare electrodes that were differently prepared. This is illustrated in figure 2.5 for electroformed ruthenium oxide films that were annealed at different temperatures [59]. The results are as expected, namely the current response decreases with annealing temperature, which is an indication of a decrease in surface area and/or electrocatalytic behaviour with annealing temperature. The fact that q* is dependent on scan rate and originates from H^+ migration, provides scope to investigate the porosity of oxide electrodes. By using a very fast scan rate, v, it can be assumed that the total charge is limited to the outer surface and a quantity $q^*_{(v=\infty)}$ defines an external surface charge quantity. By sweeping the potential very slow, it is assumed that the total porous surface is accessible to proton intercalation and the sum of the external and internal surface charge can be represented by $q^*_{(v=0)}$. If q^*_i is defined as:

$$q^*_i = q^*_{(v=0)} - q^*_{(v=\infty)} \quad \text{.....(2.3),}$$

it is acceptable that $q_i^* \approx 0$ for non-porous oxides, while $q_i^* > 0$ for porous films [91].

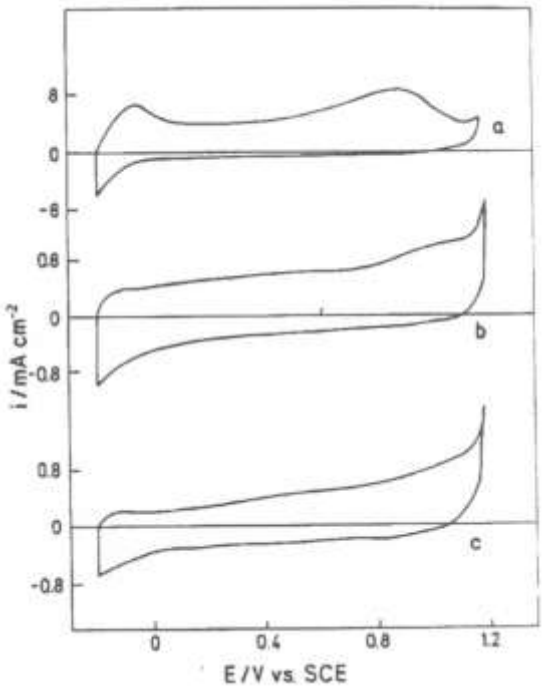

Figure 2.5: Cyclic voltammograms of electrodeposited Ru oxide films on Ti that were subjected to different thermal treatments. (a) 200°C, (b) 450°C, (c) 600°C. Scan rate = 50mV.s^{-1}, 0.5M H_2SO_4.

A relative indication of the capacitance of the oxide-electrolyte interface can also be experimentally determined by scanning the potential in an area where voltammetric peaks are absent [92]. This region of a voltammogram is sometimes referred to as a capacitive wave [57]. A plot of residual current (I) at a certain potential (E) *vs*. scan rate (v) yields information on capacitance. The slope of the latter curve is:

$$m = \frac{I}{v} \quad \text{.....(2.4)}$$

$$= \frac{dI}{dv} \quad \text{.....(2.5),}$$

but from the definition of electric current follows that:

$$I = \frac{Q}{t} \quad \text{.....(2.6),}$$

and from the definition of sweep rate:

$$v = \frac{E}{t} \quad \text{.....(2.7).}$$

Substitution of (2.6) and (2.7) into equation (2.5) gives:

$$m = \frac{dQ/dt}{dE/dt} \quad \text{.....(2.8)}$$

$$= \frac{dQ}{dE} \quad \text{.....(2.9)}$$

$$= C \quad \text{.....(2.10).}$$

Another effective method for a comparative evaluation of DSA's is by means of determining the Tafel slope in a potentiostatic polarization curve. A Tafel plot is obtained by maintaining a fixed potential on an electrode for a duration that is required to obtain a constant current. This procedure is repeated for the same duration at each potential. A plot of electrode potential *vs.* current results in the Tafel plot. The value of the Tafel slope contains information on the electrocatalytic property of an electrode. A lower value suggests better electrocatalytic ability and a value <30mV/decade is regarded to be within the electrocatalytic range. It is usually required that the applied electrode potential should extend into a current response region, i.e. a potential that induces a redox transition. One such reaction for the mentioned electrolytes is O_2 evolution. Figure 2.6 is an example where an annealed electrode was compared with an electrodeposited Ru oxide film [60]. Another advantage of this technique is that it is applicable at potentials where permanent changes of the electrode can take place. This is also illustrated in figure 2.6 where the decrease in the current density at 1.220V *vs*. SCE is due to anodic corrosion. Stationary potentiostatic polarization curves in the form of a plot of current density (i) vs. E could also yield information on the properties of a working electrode. Figure 2.7 is an example taken from the work of Duarte *et. al*. [12]. Polarization curves on electrodes of glassy carbon, Pb/PbO_2, Ti

and graphite fibre electrodes showed that Ti requires the lowest overpotential of all the above to facilitate reaction 1.2, but that graphite fibre electrodes allow the highest current densities at specified potentials.

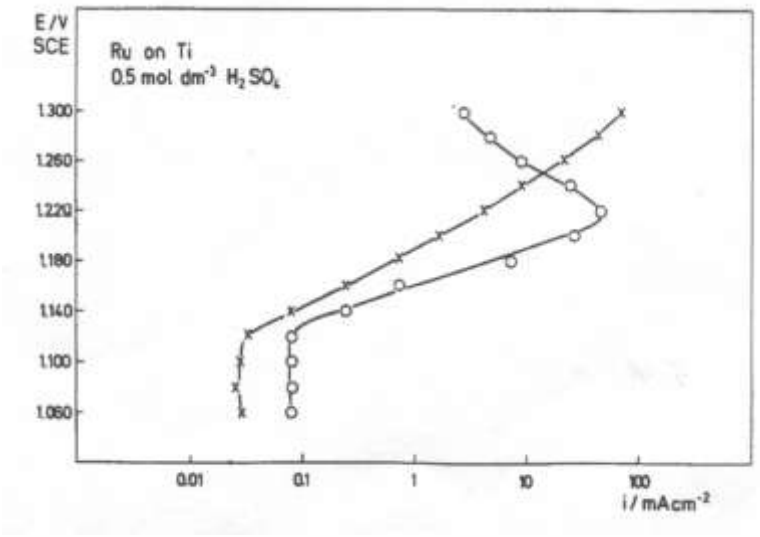

Figure 2.6: Potentiostatic polarization curves for O_2 evolution in 0.5M H_2SO_4: (o) hydrous Ru oxide film on Ti, (x) hydrous film with annealing.

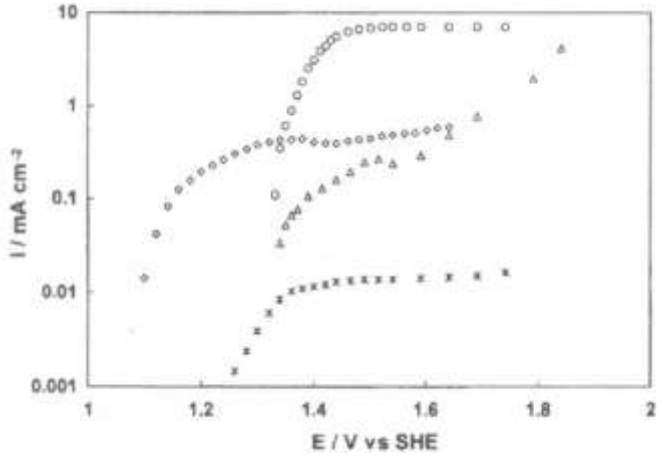

Figure 2.7: Potentiostatic polarization curves for electro-oxidation of Mn^{2+} onto different electrodes in a 0.2M $MnSO_4$ + 0.5M H_2SO_4 solution. (x) glassy carbon, (Δ) Pb/PbO_2, ($\Diamond$) Ti, (o) graphite fibre electrode.

2.4.2 Electrolysis.

With the exception of the potenstiostatic polarization curves, the discussed voltammetric methods have the shortcoming of not being specific towards a defined reaction. Polarization measurements are envisaged to directly evaluate DSA's for the electroplating of MnO_2. This method comprises measurement of the total anode polarization, i.e. concentration polarization and overvoltage as a function of geometrical anode current density during electrodeposition of MnO_2 onto the electrode's surface. To have an unambiguous understanding of what is actually being measured, it will be advantageous to give a description of polarization in terms of the process of MnO_2 electroplating. The term polarization is generally known as the phenomenon where the applied potential to carry out a non-spontaneous reaction (electrolysis) will equate to electrical energy that is greater than the increase in free energy for the process. The difference between the theoretical minimum and the applied voltage is defined as the polarization potential. Given that industrial scale electrolysis is always done in excess of the infinitely small current density that is required to represent a reversible process, polarization is unavoidable. During MnO_2 production there are also changes taking place on the electrodes, as well as changes of the electrodes itself that render the electrodes to be irreversible. An example of the latter process is the oxidation of an electrode's surface if a valve metal is used as an anode. The prospect here is to be able to isolate the contribution of the oxidation of the anode from that of normal electrode polarization which facilitate electrolysis. This can be done by keeping all variables constant and by perturbing polarization *via* an increase in the anodic current density. The overall contribution of the anodic processes to cell polarization can be measured against a suitable half reaction in the form of a reference electrode. The reference electrode's half reaction is effectively an outsider to the electrolysis process and an isolated measurement of anode polarization is thus possible. Although the measured polarization includes several variables e.g. EMD deposit, concentration polarization etc., it is known that during EMD production anode passivation is largely responsible for the observed increase in polarization at high current densities [49, 51]. This makes polarization measurements at least a qualitative method to determine the electrocatalytic response of a DSA towards MnO_2 electroplating, as well as the DSA's ability to delay passivation of the Ti substrate.

2.5 Surface analysis techniques.

2.5.1 Auger electron spectroscopy as a method to study oxide films on Ti.

It is clear from the previous description of thermally prepared DSA's that TiO_2 is inevitably a component of an electrocatalytic film if Ti metal is used as the substrate. A report on various aspects of the application of Auger electron spectroscopy (AES) to study oxides of Ti is therefore justified.

The following three transitions are considered to be most significant for Ti:

(a) $LM_{2,3}M_{2,3}$ (390eV)
(b) $LM_{2,3}M_{4,5}$ (421eV)
(c) $LM_{4,5}M_{4,5}$ (451eV)

The LMV transition at 421eV represents the strongest intensity peak for Ti. The Auger electron for this transition originates from a valence band with the consequence that the relative intensity of this peak is not only dependent on Ti concentration, but the metal's oxidation state also influences the measured intensity. A reduction in intensity is the consequence of transference of electrons from the Ti valence band to oxygen atoms during oxidation [93]. The same applies to the LVV transition at 451eV; a definite decrease in intensity is observed from Ti to TiO and TiO_2 [94]. This dependence of the LMV transition can be employed to estimate the oxidation state of Ti. The intensity ratio of the Ti (LMM) to the Ti (LMV) in a differentiated spectrum varies from 2 in TiO_2 to 0.7 in Ti metal. It is furthermore possible to estimate the oxidation state of Ti by considering the fine structure of the Ti (LMM) and Ti (LMV) transitions [29, 94 – 97]. If a fair amount of attention is paid to the AES spectral shapes, it is possible to differentiate between Ti in the following three formal valence states: Ti metal, TiO and TiO_2. The EdN(E)/dE and N(E) spectra for TiO and TiO_2 are reproduced in figure 2.8 [95]. The Ti LMV transition at 421eV can be deconvoluted into three spectral components namely A, F and B as indicated in the N(E) spectrum in figure 2.9. The relative magnitude of each of these components is dependent on the chemical state of the Ti. For Ti metal, component B was found to be overwhelming whereas the relative

intensities of A, F and B for TiO are as indicated in figure 2.9. In the case of TiO_2, component A was found to be the main constituent.

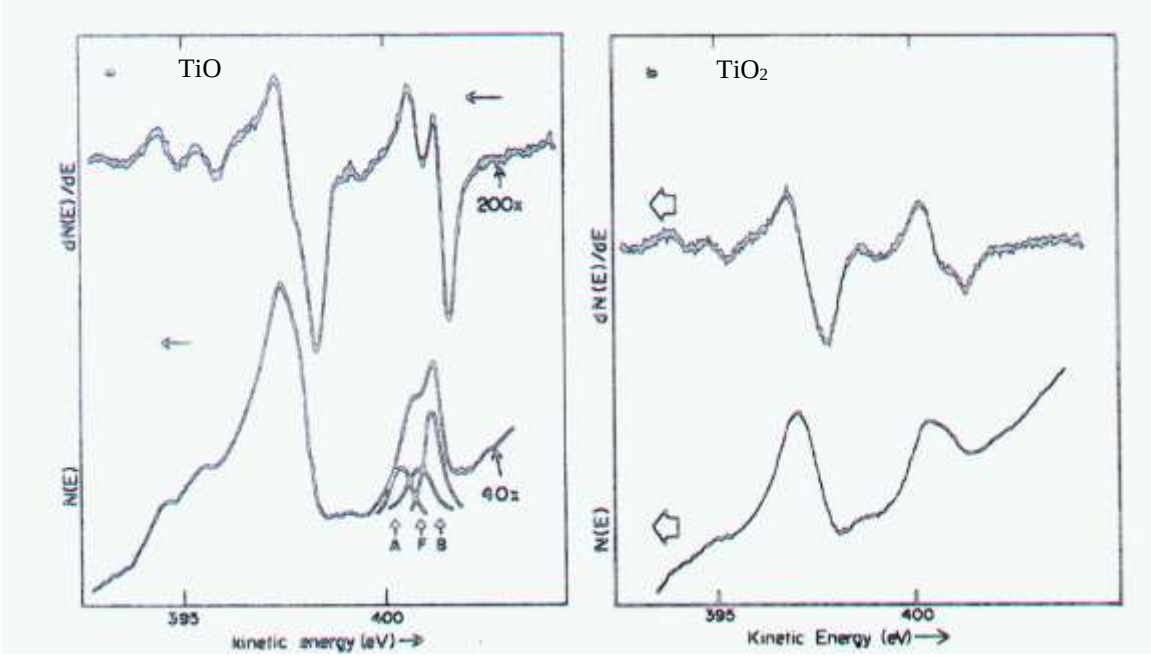

Figure 2.8: N(E) and EdN(E)/dE Auger spectra for TiO and TiO_2.

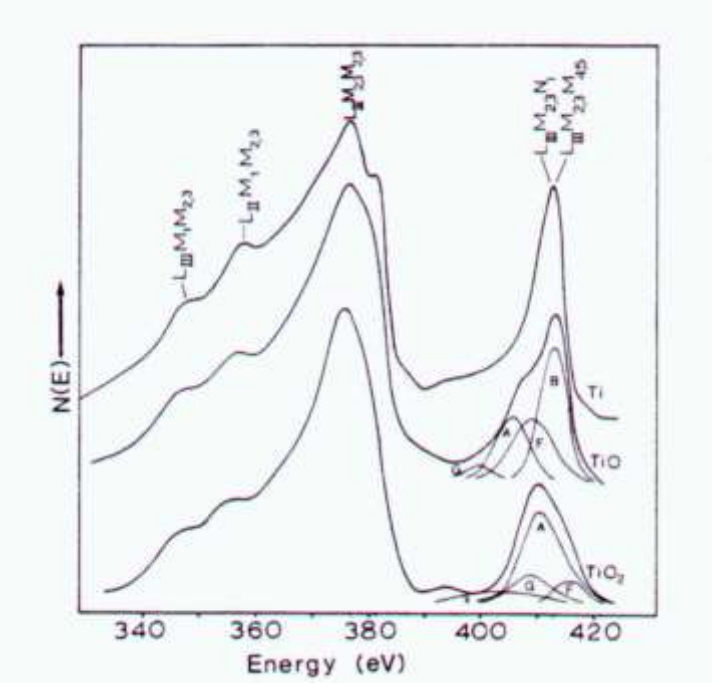

Figure 2.9: Ti $L_3M_{2,3}M_{2,3}$ and Ti $L_3M_{2,3}M_{4,5}$ spectra for pure Ti, TiO and TiO_2.

In a study to specifically investigate the changes that occur in the Auger spectrum of clean titanium metal upon exposure to oxygen and subsequent oxidation, Basset and Gallon [96] was able to grow oxygen free Ti thin films on tantalum substrates *via* the sublimation of a Ti filament in a UHV system at a base pressure of $5x10^{-5}$ Torr. An AES spectrum of the clean Ti metal in the energy range 260eV to 520eV is presented in figure 2.10.

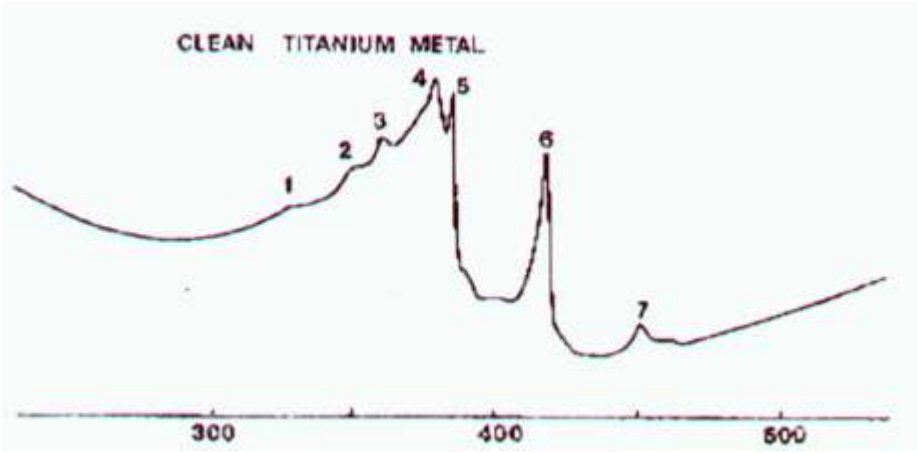

Figure 2.10: The Auger spectrum for pure Ti in the kinetic energy range of 260eV to 520eV.

The absence of the O KLL transition at 510eV in figure 2.10 proves the integrity of the clean metal. The peaks present in the spectrum are assigned according to table 2.3. All the measured peak energies correspond well with calculated values as mentioned in reference [96]. Peak 2 can be regarded as a plasmon loss peak with a certain degree of certainty. It is however peak 5 that has led to much controversy. Coad and Riviere [97] regarded peak 5 as spin-orbital splitting of the $L_3M_{2,3}M_{2,3}$ transition, while other workers in the field [96] concluded this to be highly unlikely due to the behaviour of this peak during oxidation. Another possible explanation for this peak at 385eV is the $L_3M_1M_{4,5}$ transition that has a calculated value of 390eV. Although not visible in the spectra of figure 2.10, a small peak at exactly 390eV was observed and this discarded the $L_3M_1M_{4,5}$ transition as the origin of peak 5. The explanation that is probably nearest to the truth is that the 385eV peak is a shake-up satellite originating from the $L_3M_{2,3}M_{4,5}$ transition at 418eV. Just as the case for shake-up satellites associated with core electron emission during X-ray photoelectron spectroscopy (XPS), the shake-up peak in this case is the result of re-organisation of the valence electrons that involves excitation of one electron to a higher unfilled level. In XPS the energy required for this reshuffling of an electron is obtained from the primary photoelectron and as a result, the shake-up peak is at lower kinetic energy than its associated peak of origin. A realistic

explanation in the case of an Auger transition is that the electron, which undertakes the transition to the core level, is not able to release all its energy to the Auger electron since a fraction is needed for the excitation of an electron to a higher unfilled level. If this is true, the Auger transition would appear at a lower kinetic energy than expected. Peak 5 is found at an energy of 31eV below that of the $L_3M_{2,3}M_{4,5}$ transition and it was reported that a 3p electron is excited into a vacant band state above the Fermi level [96]. The observed difference of 31eV is of the expected magnitude for the above-mentioned process, since it is known that the 3p level in Ti lies 34eV below the Fermi level [98].

Peak no.	Transition	Energy (eV)		Spectroscopic Level		
		Calculated	Observed	Core e^-	Transition e^-	Auger e^-
1	$L_3M_1M_1$	330	332	$2p_{3/2}$	$3s_{1/2}$	$3s_{1/2}$
2	Plasmon	-	352	-	-	-
3	$L_3M_1M_{2,3}$	358	361	$2p_{3/2}$	$3s_{1/2}$	$3p_{1/2}$; $3p_{3/2}$
4	$L_3M_{2,3}M_{2,3}$	383	380	$2p_{3/2}$	$3p_{1/2}$; $3p_{3/2}$	$3p_{1/2}$; $3p_{3/2}$
5	See text	-	385	-	-	-
6	$L_3M_{2,3}M_{4,5}$	418	416	$2p_{3/2}$	$3p_{1/2}$; $3p_{3/2}$	$3d_{3/2}$; $3d_{5/2}$
7	$L_3M_{4,5}M_{4,5}$	449	448	$2p_{3/2}$	$3d_{3/2}$; $3d_{5/2}$	$3d_{3/2}$; $3d_{5/2}$

Table 2.3: Assignment of Auger transitions for Ti metal, using the peak numbers from figure 2.10.

To measure the effect of oxidation on the AES spectrum, Basset and Gallon [96] carried out oxidation at pressures between $1x10^{-5}$ Torr and $1x10^{-4}$ Torr. Various exposure times were used to present different degrees of oxidation and the unit Torr.sec was devised as a quantification of exposure. The exposure before each spectrum was taken as indicated in figure 2.11. When comparing figure 2.11(a) with figure 2.10, it is obvious that peak 5 is the most sensitive to oxygen exposure. At $5x10^{-6}$ Torr.sec the magnitude of peak 5 has already started to ebb away, while the other peaks remained unaffected. After $50x10^{-6}$ Torr.sec, peak 5 has completely disappeared, while peak 6 has started to change shape and peak 7 is reduced in size. After $5x10^5$ Torr.sec, peak 6 is a double peak with peak 7 completely absent. The changes in peaks 6 and 7 can be understood in a qualitative way using the assignments of these transitions as in table 2.3. For peak 7, both the Auger and transition electrons are from the $M_{4,5}$ X-ray level which are the $3d_{3/2}$ or $3d_{5/2}$ spectroscopic levels, which in turn are the

valence electrons for Ti. These electrons are removed from the valence band during the formation of the oxide and the disappearance of peak 7 *via* oxidation is thus explained. The same argument goes for peak 6 where the Auger electron originates from the valence band and its removal causes the observed change in the spectrum during oxidation. Peaks 1 to 4 are related to core level transitions and are therefore not influenced by oxidation.

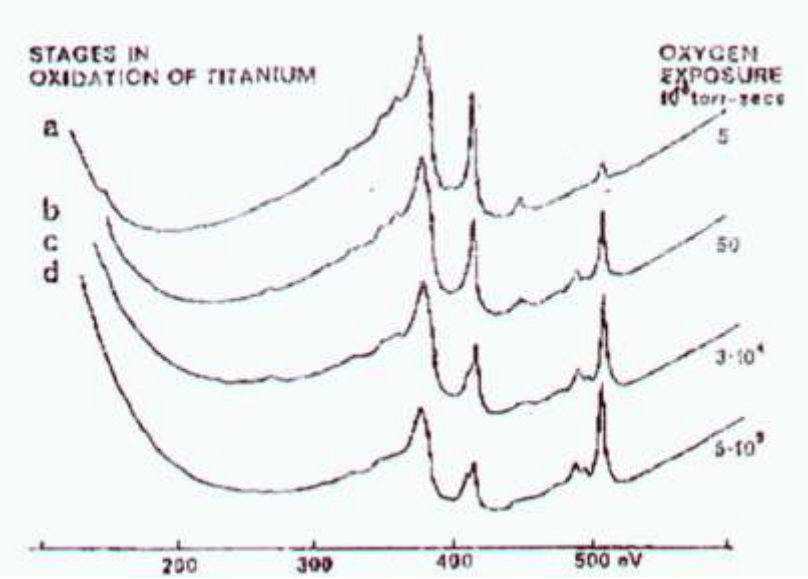

Figure 2.11: AES spectra that were taken after various stages of oxidation of a Ti film.

As an alternative way of distinguishing between Ti, TiO and TiO_2, the EdN(E)/dE spectra reveal significant differences in the fine structure of the LMM and LMV transitions between the mentioned oxidation states of Ti. An elegant comparison between the Ti LMM and LMV Auger derivative spectra of the metal, oxide and dioxide is illustrated in figure 2.12 [94]. Ti metal can be recognised using the transition at 390eV that differs from both TiO and TiO_2. The shoulder peak on the high-energy side of the $L_3M_{2,3}M_{2,3}$ transition is prominent on the Ti Auger spectrum and completely absent in the TiO and TiO_2 spectra. This is the same peak as peak 5 in figure 2.10. Figure 2.13 shows the results of an experiment by Armstrong and Quinn [29] where the oxidation charge (i.e. the Ti was anodically oxidised) was incrementally increased and AES spectra of the applicable samples recorded. The LMV transition's fine structure shows contribution primarily from TiO, but the pattern changes with increasing charge, suggesting a change towards a TiO_2 character.

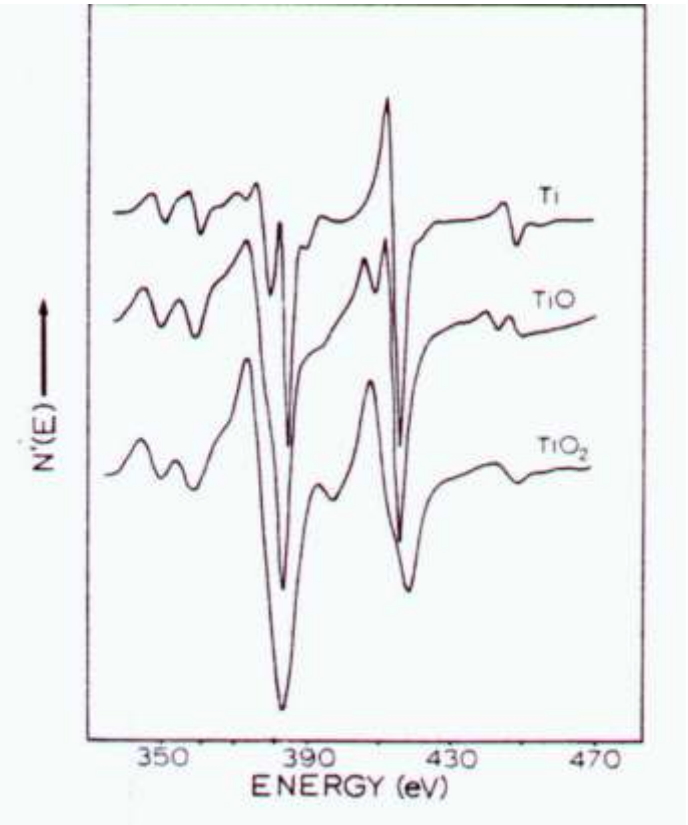

Figure 2.12: Comparison between the Auger derivative spectra of Ti, TiO and TiO_2.

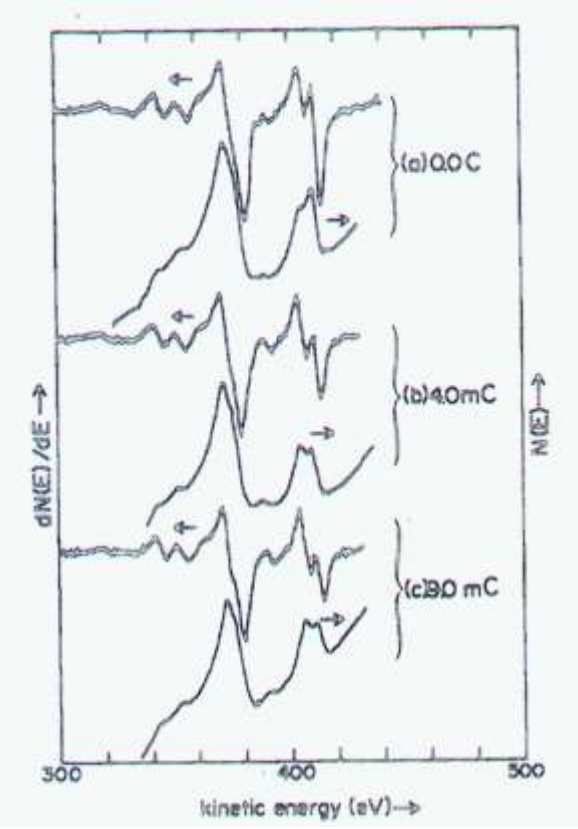

Figure 2.13: Auger spectra of a Ti surface after incremental oxidation in an electrochemical experiment.

Also realising that the features of the Auger fine structure can be employed to interpret the chemical environment of a metal atom, Solomon and Baun [94] attempted to explain the differences in the Ti LMV Auger transitions of Ti, TiO and TiO_2 using Fischer's [99, 100] molecular orbital diagram for a transition metal that is octahedrally coordinated to oxygen. An example of an octahedral coordination compound is shown in figure 2.14 for rutile.

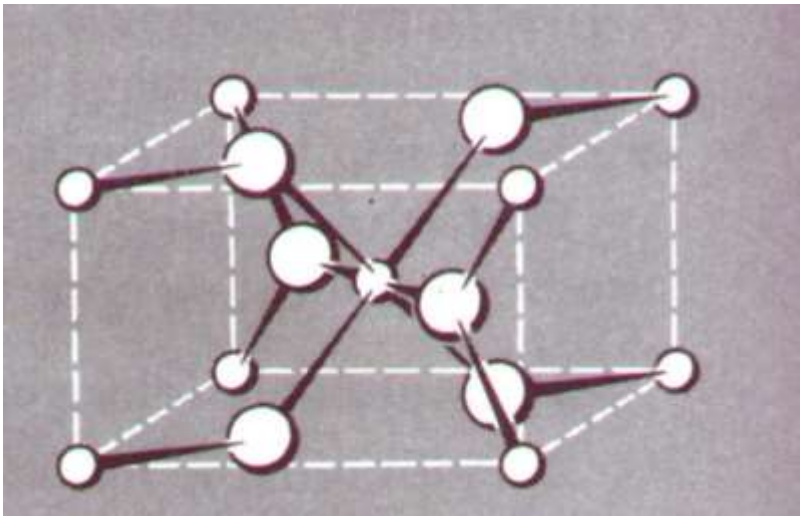

Figure 2.14: Octahedral coordination structure of rutile. Small circles denote metal cations and large circles represent oxygen anions.

This octahedral coordination gives rise to a splitting in the d orbitals of the transition metal. The crystal field approach is a special case of the ligand field theory that satisfactorily explains this d orbital splitting. Imagine a metal ion, M^{m+}, situated at the center of an octahedral set of negative point charges as in figure 2.15. Assume for a while the metal ion to be Ti^{3+} which has a closed shell configuration except for one valence electron outside in a 3d orbital. For a free ion of Ti^{3+}, this valence electron will have an equal probability of occupying any one of the five d orbitals. The electrostatic perturbations shown in figure 2.15 however cause the d orbitals to be energetically different for the occupation of the valence electron. The orientation of the electron density of the five d orbitals relative to the negative point charges is illustrated in figure 2.16. It is clear from this illustration that the d_{xy}, d_{yz} and d_{xz} orbitals have electron density probability concentrated in the spaces between the octahedral arrangement of point charges, while the d_{z^2} and $d_{x^2-y^2}$ orbitals have their electron density concentrated directly in the direction of the point charges. This leads to a situation where the valence electron of Ti^{3+} will prefer to be either in a d_{xy}, d_{yz} or d_{xz} orbital where it can reside further away from a point charge. The d_{xy}, d_{yz} and d_{xz} orbitals are therefore

energetically equivalent, while it can be shown that the d_{z^2} and $d_{x^2-y^2}$ orbitals are equivalent, but at a higher energy than the other three orbitals.

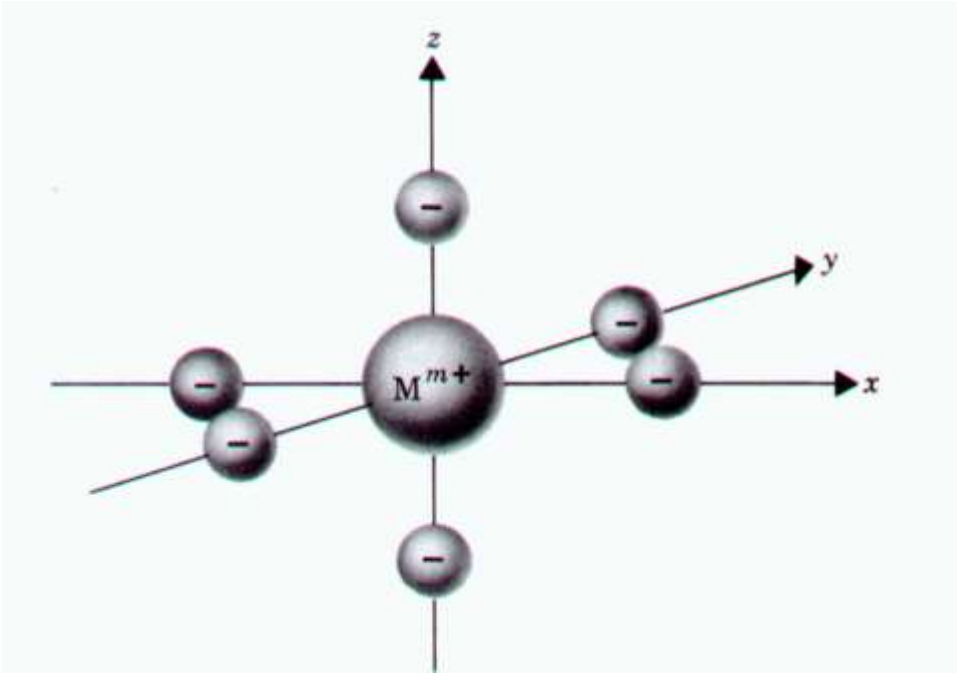

Figure 2.15: Six negative point charges in an octahedral coordination around a metal ion.

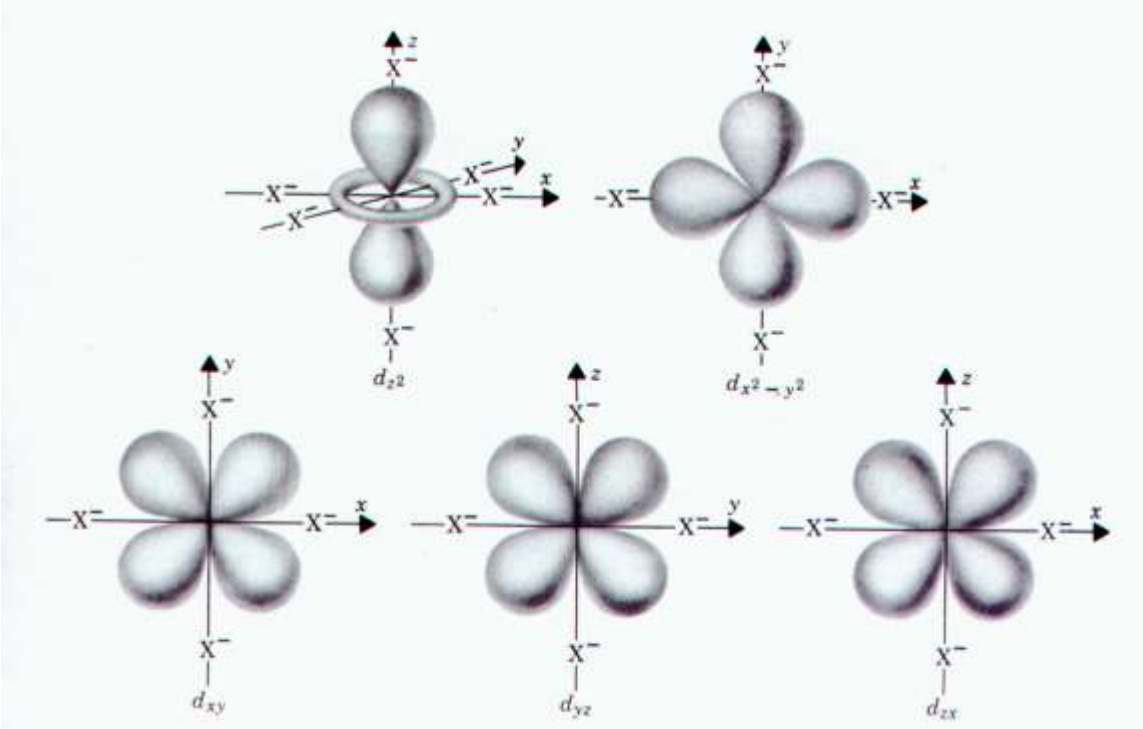

Figure 2.16: Electron density distribution of the five d orbitals of a transition metal. The Cartesian axes can be used as a reference to determine the orientation of the lobes relative to the point charges in figure 2.15.

The d orbital splitting follows clearly from the above description and t_{2g} is a notation to represent the d_{xy}, d_{yz} and d_{xz} orbitals while e_g represents the d_{z^2} and $d_{x^2-y^2}$ orbitals. The respective energy positions of the t_{2g} and e_g orbitals relative to the unsplit d orbital are illustrated in figure 2.17. It is the correspondence between the t_{2g} Ti atomic orbital and an atomic orbital from oxygen that gives rise to the $2t_{2g}$ molecular orbital that plays an important role in describing the LMV Auger transitions of titanium oxides. All the other relevant atomic and molecular orbitals are described in figure 2.18. The deconvoluted $L_3M_{2,3}M_{4,5}$ peak in figure 2.9 was described using the molecular orbitals in this diagram. Ti in the TiO compound is in the 2+ valence state, while it is tetravalent (Ti^{4+}) in TiO_2. This results in a $2t_{2g}$ molecular orbital that accomodates two electrons in the case of TiO and none in case of TiO_2. A $2t_{2g}$ to $2p_{3/2}$ or $2p_{5/2}$ transition is therefore possible for TiO, resulting in the B component of the $L_3M_{2,3}M_{4,5}$ transition being prominent. The A peak of the $L_3M_{2,3}M_{4,5}$ transition arises from the $2e_g$ to $2p_{3/2}$ or $2p_{5/2}$ transition, which is consequently applicable to TiO_2. It is therefore the difference in occupancy of the $2t_{2g}$ molecular orbital that describes the difference in fine structure of the $L_3M_{2,3}M_{4,5}$ transition for TiO and TiO_2.

Similar to Basset and Gallon [96], Solomon and Baun [94] also described the shoulder peak of the $L_3M_{2,3}M_{2,3}$ transition as being a shake-up peak that is sensitive to the number of states at the Fermi surface. Last mentioned states are influenced by the presence of oxygen and this results in the sensitivity of the shake-up satellite to oxide formation.

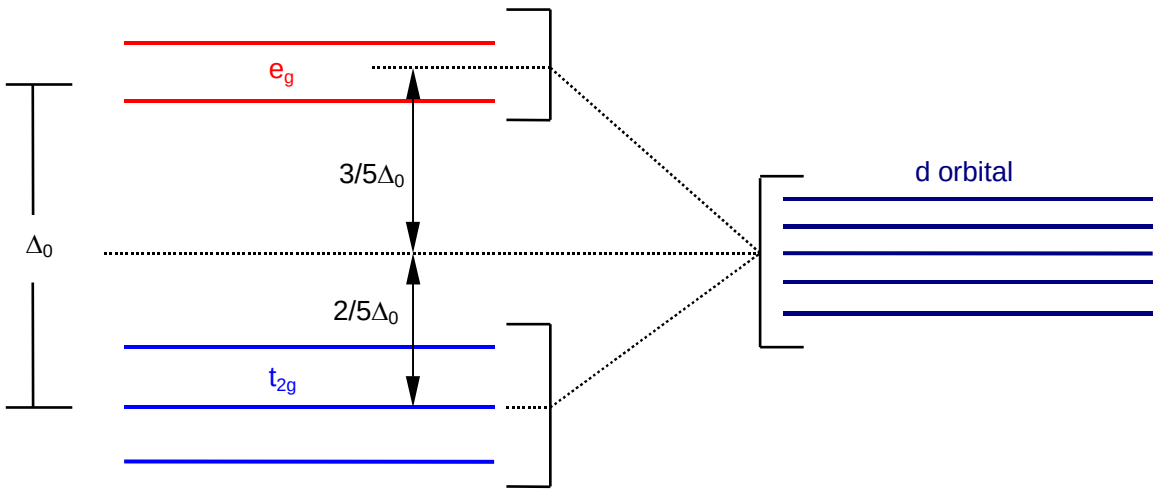

Figure 2.17: Energy-level diagram of the t_{2g} and e_g orbitals relative to an unsplit d orbital.

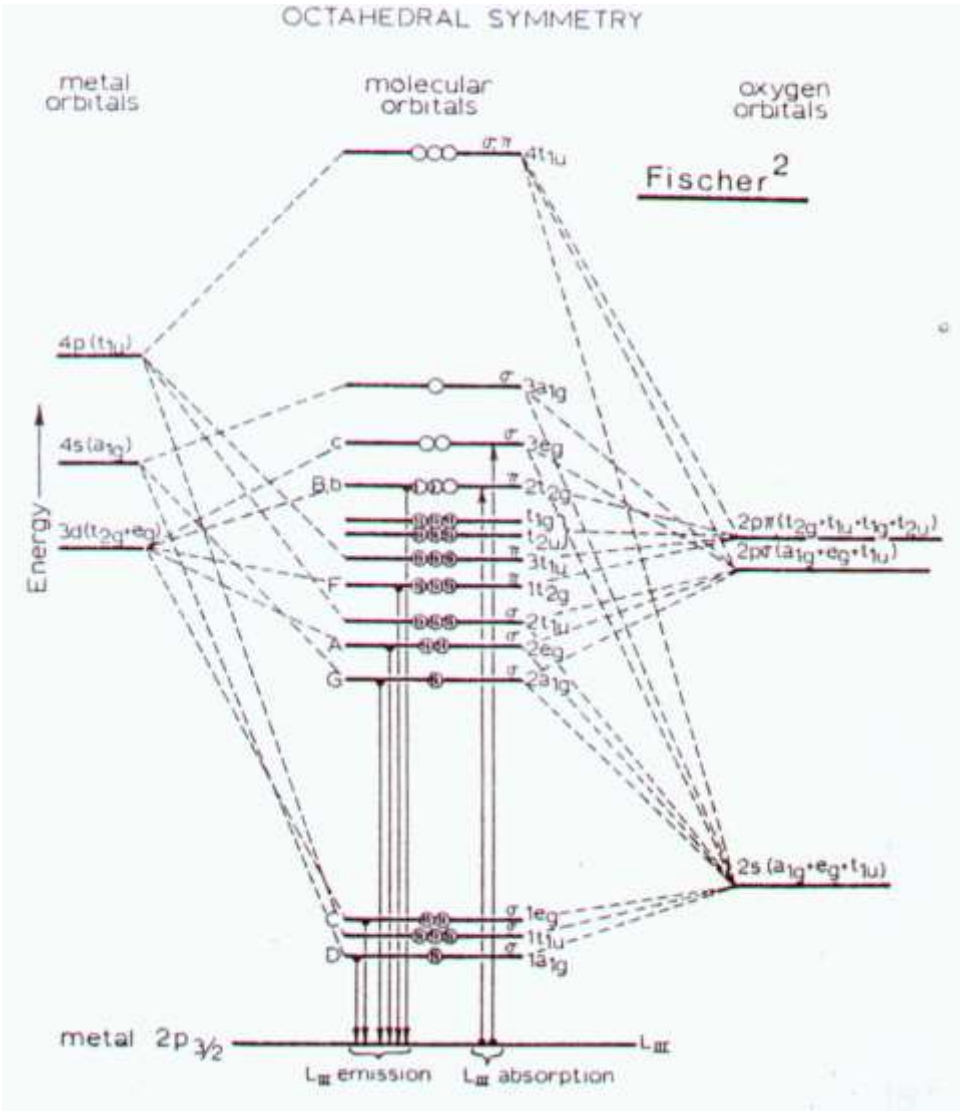

Figure 2.18: Molecular orbital diagram for Ti coordinated to oxygen as proposed by Fischer.

Apart from the work of Armstrong and Quinn [29], three more experimental papers [36, 37, 101] were found in which AES was used in conjunction with electrochemical methods to investigate the oxidation of the surface of Ti and TiN working electrodes. Massiani *et. al*. [36] used TiN films, which were prepared *via* reactive sputtering onto glass substrates, as working electrodes in 0.5M H_2SO_4. AES depth profiles were recorded for an untreated sample as well as anodised samples. An increase in oxygen concentration on the surfaces of anodised samples was clearly evident from the latter depth profile.

2.5.2 Auger electron spectroscopy to study RuO_2.

The transitions that require attention during an Auger study of Ru containing films are as follows:

(a) MNN (200eV)
(b) $MN_{2,3}N_{4,5}$ (235eV)
(c) $MN_{4,5}N_{4,5}$ (277eV)

Similar to the oxides of Ti, the intensity ratios of applicable Auger-peak-to-peak-height (APPH) values can be used as a means to resolve the oxidation state in which the Ru exists. The APPH ratio of I_{277eV} : I_{235eV} is 2.4 for metallic Ru and decreases to 1.6 for stoichiometric RuO_2 [93]. This concept could be readily applied to depth profiles to obtain the Ru oxidation state as a function of sputter time.

One concerning factor that should be taken into consideration during AES measurements on Ru oxide compounds is the fact that the C KLL transition at 275eV coincides with the Ru $MN_{4,5}N_{4,5}$ transition. Ru could however be distinguished from the C transition due to the symmetry of the differentiated Ru $MN_{4,5}N_{4,5}$ transition. Atanasoka *et. al*. [102] indicated that a ratio of 0.75 to 0.77 for the positive to negative excursion of last mentioned Ru transition a reliable indication is of the absence of C.

2.6 Conclusion on literature study.

A literature study was presented in the preceding paragraphs on electrocatalytic dimensionally stable anodes. Discussions were devoted to a concise summary on aspects such as the history and origin of DSA's, methods to prepare metal oxide electrodes, properties of the latter as well as characterisation techniques. An in-depth survey on the application of AES to study TiO_2 and RuO_2 was also considered. It should be emphasised that an enormous amount of information is still available on the DSA concept, but it will be an arduous enterprise to present everything in detail in one study. Nonetheless, it followed from a description of the uses of DSA's that its application as an anode in MnO_2 electroplating exists as academic and industrial knowledge. It can thus be appreciated that a

study on DSA's to decrease electrode polarization during EMD plating as well as to alleviate passivation has a prospect of success.

2.7 Layout of forthcoming experimental study.

An overview of the procedure with which the experimental study is approached is as follows. Two methods for DSA preparation are used namely (a) thermal decomposition and (b) electrosynthesis *via* cyclic voltammetry. A trivial method of thermal decomposition of an aqueous $RuCl_3.3H_2O$ precursor solution on a Ti substrate is used to prepare test samples. These samples are all regarded as having a surface composition of a binary mixed oxide of Ru and Ti and can be denoted as $Ti/TiO_y/RuO_x$ samples. In order to attempt different ratios of Ru:Ti in the electrocatalytic films, different Ru concentration precursor solutions are used as well as mixed $RuCl_3.3H_2O$ and $TiCl_3$ precursors. The response of different DSA's towards reaction 1.2 is evaluated in an electrochemical cell under conditions selected to simulate an accelerated life test of an anode. Crystallographic interpretations are performed using X-ray diffraction (XRD) and the relative atomic density of Ru and Ti in the electrocatalysts is determined with AES. The advantages of such information in terms of an industrial MnO_2 production facility are obvious. Production cost of a DSA is directly proportional to the concentration of the Pt group metal in the precursor solution. An assessment of the implications of a varying content of Ru in the precursor on subsequent DSA film composition and electrochemical behaviour is therefore a prerequisite for financial considerations regarding the cost of electrode preparation and energy consumption during electrolysis.

The second section concerns DSA samples prepared *via* the CV electrosynthesis technique that are occasionally termed as $Ti/RuO_x.nH_2O$ specimens in this study. An investigation into the effect of thermal treatment on structural changes of the hydrous oxide films was done with XRD. The same electrolysis method as for the thermally prepared DSA samples is also used to compare electrochemical performance during MnO_2 electroplating as a function of duration of annealing. AES follows to observe the surface composition of the prepared films, as well as for depth profiling.

The study was complimented with electrochemical and structural studies on Ti-Pb and Ti-Al composite electrodes as well as a Ti/TiC system. The former two electrodes are commercially available materials, while the latter was prepared using an electron beam evaporation technique followed by vacuum annealing.

An investigation into pure Ti metal for MnO_2 electrodeposition is regarded as an inherent part of the current objective. Experimental results and conclusions on Ti metal as an anode was found to contribute significantly to fundamental knowledge on this metal's behaviour in typical EMD production solutions.

Chapter 3

Experimental.

3.1 Experimental techniques.

The theory and application of the experimental techniques utilised in the current study are well documented. The underlying principles of the applicable techniques will therefore only be briefly discussed for the sake of completeness.

3.1.1 Cyclic voltammetry.

The foundation of a cyclic voltammetry experiment is the measurement of current (response signal) that develops due to application of a varying electrical potential (excitation signal) to a working electrode (WE). A WE is defined as the electrode at which the active analyte species is oxidised or reduced. Application of potential to a working electrode is facilitated by a reference electrode (RE) of which the potential is constant by definition. The RE has a resistance of $>10^{11}\Omega$ and the electrical circuit that comprises the RE has a high impedance that facilitates the condition of zero current flowing through the RE. Thus, the RE is regarded as being non-polarizable. An auxiliary electrode (AE) that is connected to the WE carries the current generated at the WE. A simplified schematic of a three-electrode setup is shown in figure 3.1.

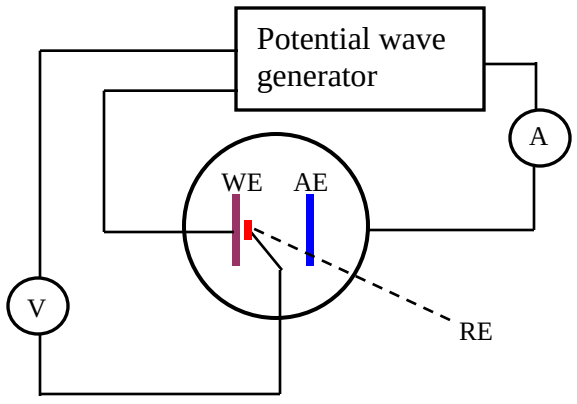

Figure 3.1: Simplified circuit diagram of a three-electrode electrochemical system.

The excitation signal measured and controlled between the WE and RE takes on the form of a triangular potential wave. The potential is linearly scanned from an initial value of E_i to a switching potential $E_{\lambda 1}$. The direction of the scan is reversed at $E_{\lambda 1}$ and scanned to $E_{\lambda 2}$ that is more than often predetermined to be at the same value as E_i. The combination of a forward and reverse scan as described above represents one cycle. An example of one cycle of a triangular wave as applied to a glassy carbon WE in a solution containing 20mM $K_4Fe(CN)_6.3H_2O$ as the electro-active species in an aqueous supporting electrolyte of 3M NaCl is illustrated in figure 3.2. The resulting current *vs*. potential curve is termed a voltammogram and is plotted in figure 3.3.

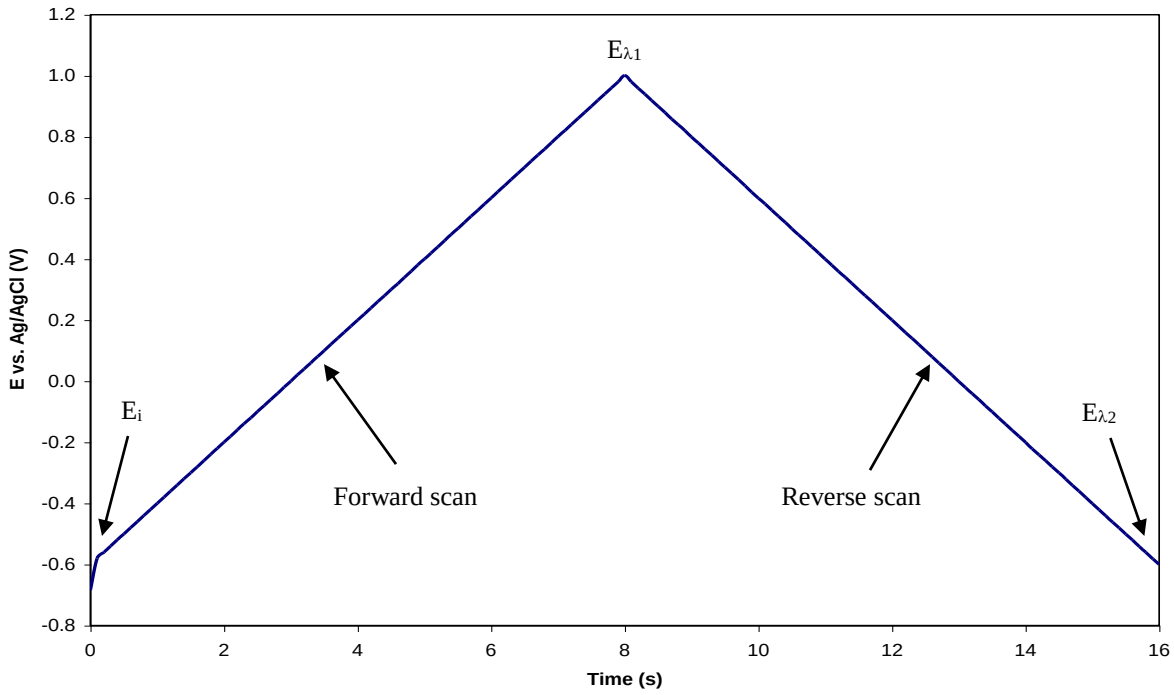

Figure 3.2: Excitation signal in the form of a triangular wave. Scan rate = 200mV.s^{-1}.

During the forward scan, the WE is made increasingly positive *vs*. the RE (Ag/AgCl in this example), i.e. the WE is made more anodic as a function of time. At point A in the voltammogram the surface of the WE is a sufficiently strong oxidant to cause oxidation of the $Fe^{II}(CN)_6^{4-}$ species. The applicable reaction is:

$$Fe^{II}(CN)_6^{4-} \rightarrow Fe^{III}(CN)_6^{3-} + e^- \quad \text{.....(3.1)}$$

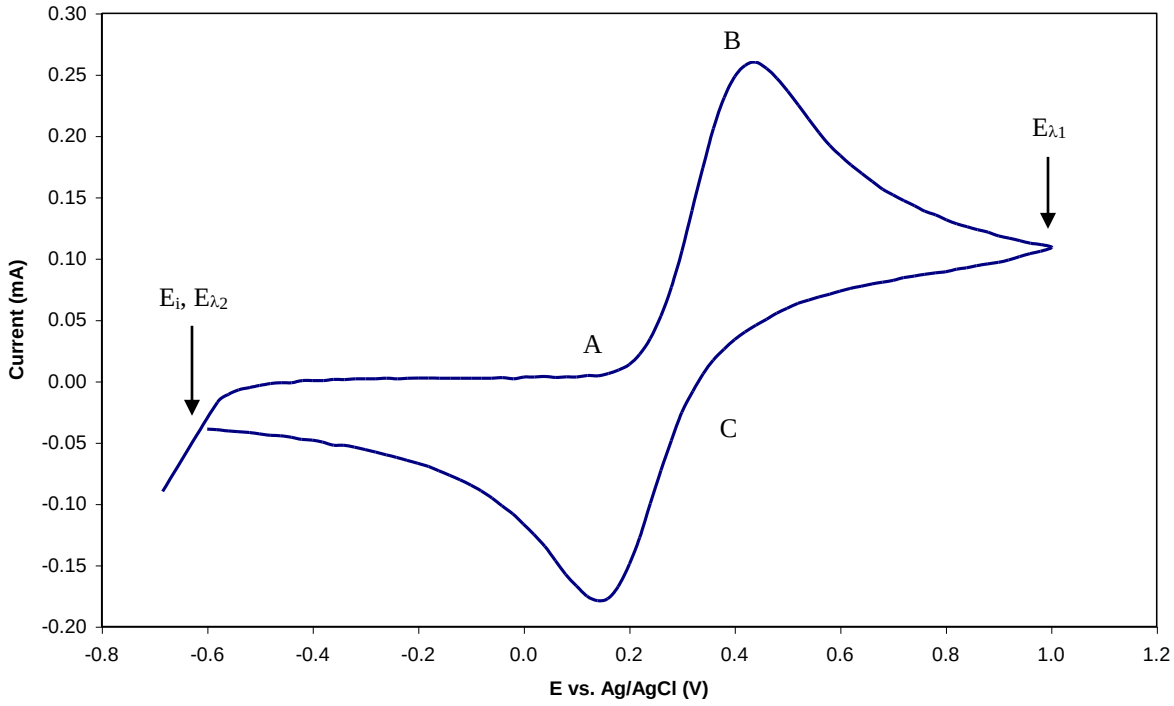

Figure 3.3: Voltammogram of 20mM $K_4Fe(CN)_6.3H_2O$ in 3M NaCl. Glassy carbon WE, Pt wire AE, Ag/AgCl (3M NaCl) as the RE.

It is important to understand that "e-" in equation 3.1 represents the measured current. This means that a redox reaction causes electrical current and that the reaction rate is directly proportional to absolute current. From point A onward the anodic current increases rapidly as reaction 3.1 takes place until the $Fe^{II}(CN)_6^{4-}$ concentration at the electrode's surface has decreased to a value that is insufficient to maintain an increase in oxidation rate. The current consequently peaks at point B where the rate of oxidation equals the rate of mass transfer, and then starts to decrease. After the switching potential, the WE is made increasingly negative with cathodic current being generated from point C onwards, i.e. the WE is now a reducing agent. The applicable reaction that generates current in the reverse scan is:

$$Fe^{III}(CN)_6^{3-} + e^- \rightarrow Fe^{II}(CN)_6^{4-} \quad \text{.....(3.2)}$$

The $Fe^{III}(CN)_6^{3-}$ species that was formed in the forward scan remains adjacent to the WE's surface and is reduced back to the initial state in reaction 3.2.

3.1.2 X-ray diffraction.

The physical basis for diffraction originates from interference patterns that are produced by phase differences between waves that are elastically scattered from objects in a periodic array. A prerequisite for this phenomenon to occur is that the wavelength of the scattered waves should be comparable to the distance between the objects in the array. For X-ray diffraction (XRD), the mentioned waves are monochromatic X-rays with a wavelength in the order of 1Å, while the source of scattering (periodic array) is the atoms in a crystal. The diffraction pattern produced in this way allows for the determination of crystal structures of solid state elements and compounds. To understand the basic principle of diffraction phenomena, it usually suffices to derive the Bragg equation using a simplified diagram of two crystallographic planes, known as Miller indices (h k l).

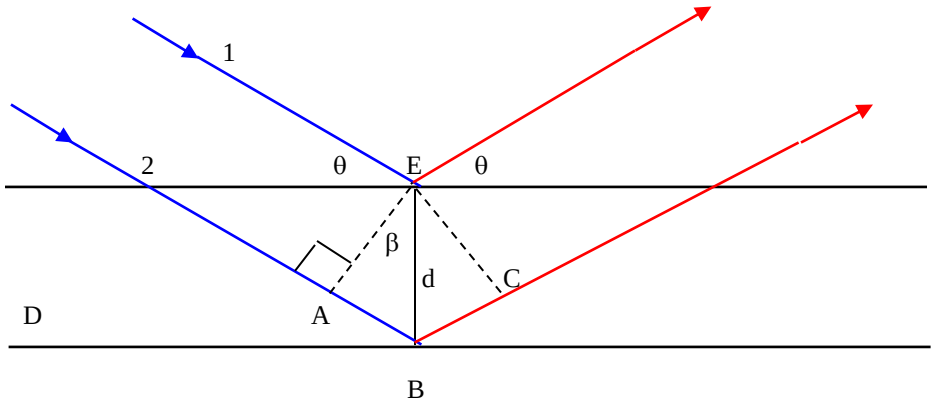

Figure 3.4: Illustration of reflection of X-radiation waves from two Miller planes.

Regard radiation with wavelength λ in figure 3.4 as incoming from the left to be reflected by the family of (h k l) planes. It can be appreciated from Snell's law that the angle of incidence θ, must equal the angle of reflection as indicated in figure 3.4. Assume now a simplistic situation where waves 1 and 2 result in constructive interference. For this to be true, wave 2 must be phase retarded by an integral multiple of λ. In mathematical terms:

ABC = nλ, n ε N .....(3.3);

From geometry follows that:

$\angle ABD = \theta$ ..... (3.4), thus

$\angle ABE = 90° - \theta$ ..... (3.5), and this results in:

$\beta = 180° - [90° + (90° - \theta)] = \theta$ ..... (3.6), but basic trigonometry gives:

$\sin\beta = AB/d$ ..... (3.7),

with d being the interplanar spacing.

If equation 3.6 is substituted into 3.7, the result is obviously:

$\sin\theta = AB/d$ ..... (3.8).

From symmetry follows that ABC = 2AB, thus:

$\sin\theta = ABC/2d$ ..... (3.9).

The Bragg equation follows from substituting equation 3.3 into 3.9:

$n\lambda = 2d\sin\theta$ ..... (3.10).

Note that the Bragg equation was derived here for a specific case of constructive interference from only one family of planes with the assumption that the incoming waves are in phase. A general derivation of equation 3.10 is illustrated in the book of H.P. Myers [103].

An illustration of the geometry of a goniometer and the experimental position of the θ and 2θ angles is summarised in figure 3.5.

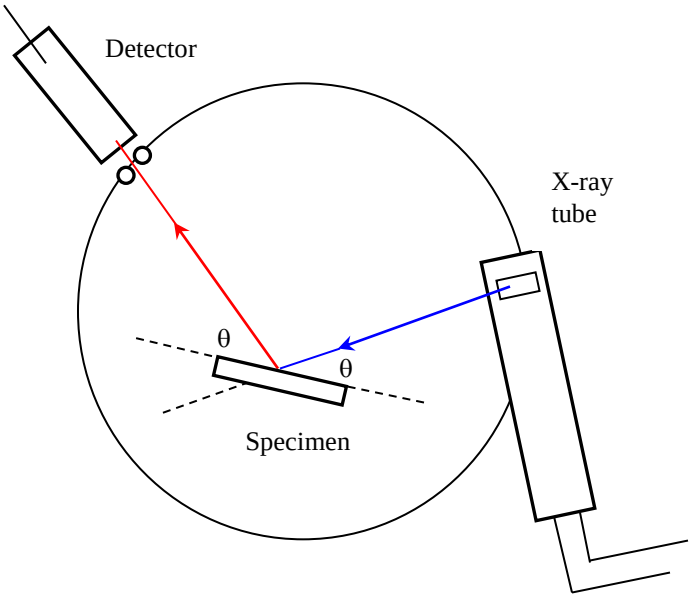

Figure 3.5: Illustration of a typical experimental setup for XRD measurements.

3.1.3 Auger electron spectroscopy.

3.1.3.1 Principle of AES.

The Auger effect can be described on an atomic scale as follows. A primary electron beam is used to cause core level ionisation of an atom. Hereafter, relaxation to a lower energy state takes place through rearrangement of electrons. The ionised core level is filled with an electron from a higher level. To compensate for the energy release of the electron that undergoes the transition, an electron is ejected from the atom with a kinetic energy E_A according to equation 3.11.

$$E_A = E_1 - E_2 - E_3' \quad \text{.....(3.11),}$$

with E_1 and E_2 the binding energies of the atom in the singly ionised state and E_3' in the doubly ionised state. The relevance of E_1, E_2 and E_3' is also defined by the sequential description in figure 3.6. The Auger effect is a non-radiative phenomenon and measurement of the number of ejected electrons as function of kinetic energy is the practical consideration of the technique. Each element in the periodic table has characteristic Auger peaks and AES is therefore classified as a surface analytical technique.

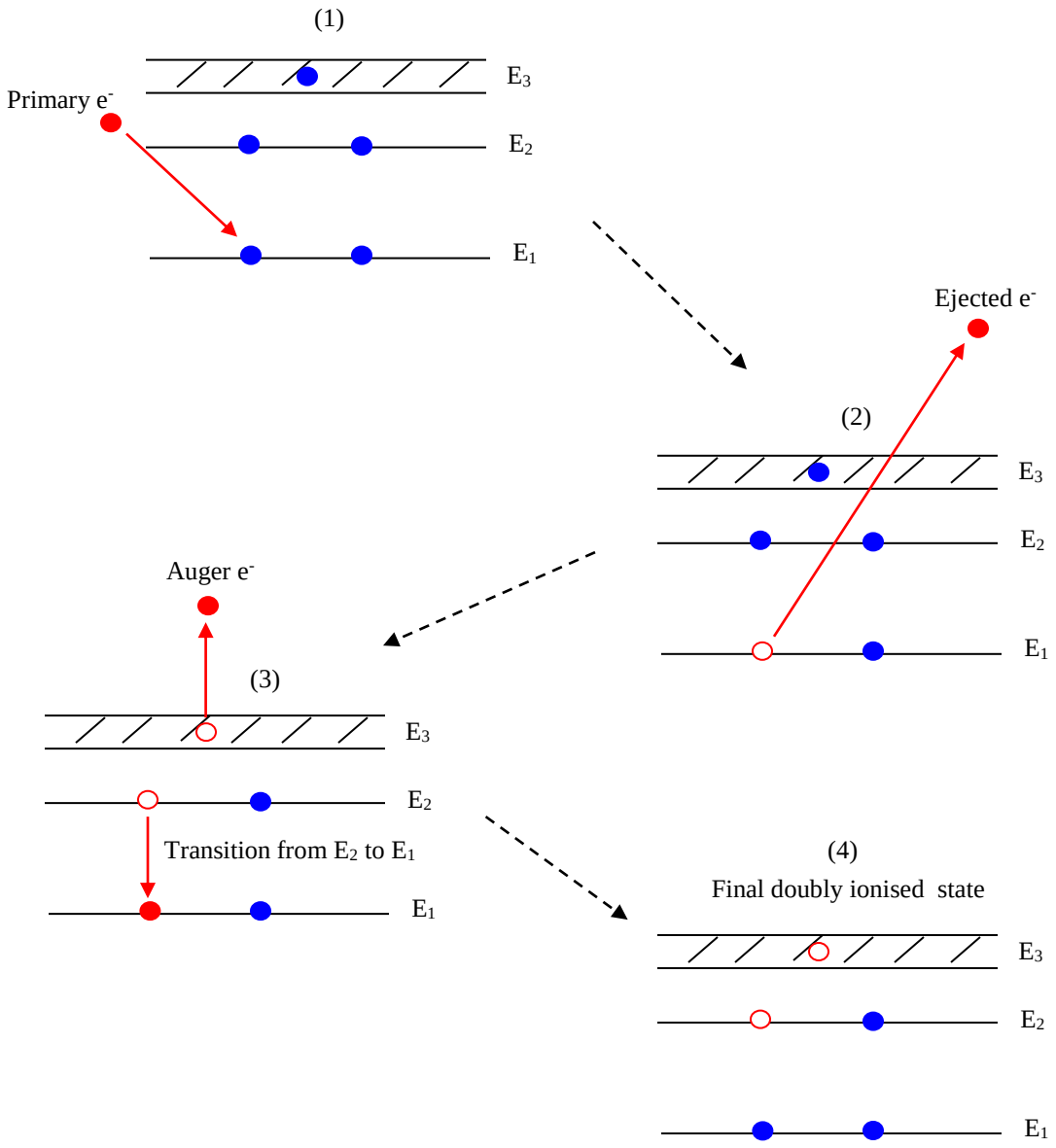

Figure 3.6: Energy level diagram to illustrate the Auger process.

The basic experimental construction of an AES system is depicted in figure 3.7. Ultra high vacuum (UHV) is a requirement for high temperature filaments, constant energy electron beam and avoiding changes in the surface composition of a specimen. An electron gun that operates in the 1keV to 20keV range is usually employed. Two types of energy analysers are possibilities in an AES spectrometer namely (a) cylindrical mirror analysers or (b) spherical sector analysers. Various types of ion guns can be utilised for cleaning of the sample surface and for compositional depth profiling. A secondary electron detector is optional for measurements of surface topography.

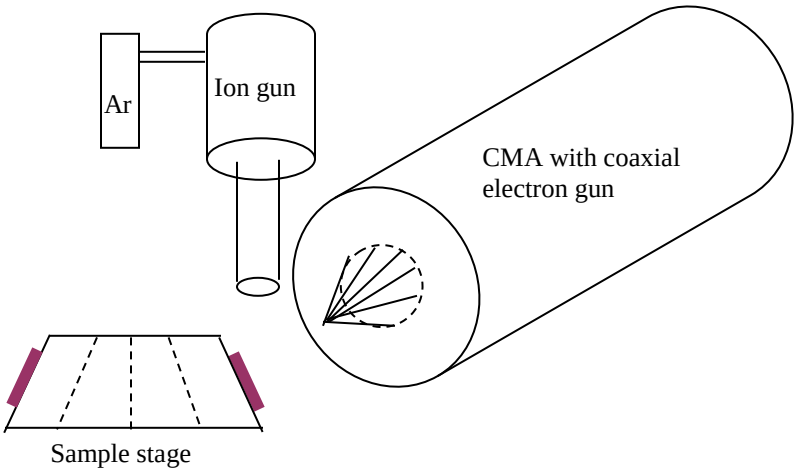

Figure 3.7: Basic components of an Auger spectrometer.

3.1.3.2 Notation.

Electron energy levels in quantum mechanics are each associated with a value of the principle quantum number, *n*. States with *n* = 1, 2, 3, 4……. are traditionally designated with letter names namely K, L, M, N……. A combination of these principle quantum numbers are usually given in conjunction with Auger electron energies to describe a certain Auger transition. As an example, the 421eV Auger transition in a derivative spectrum for Ti is termed as an LMM transition. The first letter ("L") represents the level or shell (shell is a group of states with the same *n*) from which an electron is ejected by a primary electron to cause an initial excited ionised atom. The second letter (first "M") denotes the origin of the electron that underwent the transition and the third letter (second "M") is the shell from which the Auger electron originates. Although this nomenclature is universally applied in AES, it was originally used as an X-ray notation. The above example means that both the Auger electron and the electron that underwent the transition are from the same shell. This however does not mean that the electrons originate from the same orbital or subshell and the consequence is that it is possible for Auger electron energies to have the same transition designation [104]. This is indeed the case for Ti, since the transitions at 390eV, 421eV and 451eV are all LMM transitions. To accommodate this discrepancy, a suffix is used to acknowledge the involved subshells and possibilities for electron spin. The orbital angular momentum quantum number, *l* = 0, 1, 2, ……*n*-1 (or *l* = s, p, d, f….), is used to describe a subshell, i.e. a subshell is a group of electron states with the same *n* and *l* values. Furthermore, electron spin is quantified by the spin angular momentum quantum number, *s* =

+/- ½. The total angular momentum can now be characterised by the quantum number *j*, with $j = l + s$. The mentioned suffix originates from the value of *j* and correlation between the two numbers is listed in table 3.1. As an example, consider the $LM_{2,3}M_{2,3}$ and $LM_{2,3}M_{4,5}$ transitions for Ti at 390eV and 421eV respectively. The suffix 2 means $l = 1$ and $j = ½$. Thus $s = -½$. The suffix 3 gives $l = 1$ and $j = {}^3/_2$, and *s* is now equal to + ½. It is now clear that two suffixes are used just to take into account that two possibilities exist for electron spin. The same goes for the 4 and 5 suffixes, both indicate that $l = 2$ with both possibilities for *s*. It is however important to realise that $M_{2,3}$ represents an electron (any spin) in the p subshell ($l = 1$) and $M_{4,5}$ indicates the d ($l = 2$) subshell.

Quantum numbers					
n	*l*	*j*	X-ray suffix	X-ray level	Spectroscopic level
1	0	½	1	K_1	$1s_{1/2}$
2	0	½	1	L_1	$2s_{1/2}$
2	1	½	2	L_2	$2p_{1/2}$
2	1	${}^3/_2$	3	L_3	$2p_{3/2}$
3	0	½	1	M_1	$3s_{1/2}$
3	1	½	2	M_2	$3p_{1/2}$
3	1	${}^3/_2$	3	M_3	$3p_{3/2}$
3	2	${}^3/_2$	4	M_4	$3d_{3/2}$
3	2	${}^5/_2$	5	M_4	$3d_{5/2}$
etc.	etc.	etc.	etc.	etc.	etc.

Table 3.1: X-ray and spectroscopic notation.

3.1.3.3 Quantification in AES.

The identification of elements in a differentiated Auger spectrum is straightforward if plasmon and ionization loss peaks are taken into account. A chart of principle Auger electron energies of the elements can be used to identify peaks in a spectrum. If overlapping of peaks is present, the measured energy values in more than one Auger transition usually confirm an element when compared with tabulated transitions.

The first question that is usually raised in terms of quantitative AES analysis, is how to relate the number of Auger electrons collected by an analyser with the actual atomic density, N_i, of

a certain species in a sample. A relation, based on first principles, between the latter parameter and the measured Auger intensity, I_i, is given by equation 3.12 [104].

$$I_i = I_p N_i \sigma_i \gamma_i (1+r) \lambda (\cos\theta) K \quad \text{.....(3.12)}$$

with:

I_i = Auger intensity for the ABC transition of element i

I_p = Primary electron beam current

N_i = Number of atoms of element i per unit volume

σ_i = Ionization cross section for the A level of element i

γ_i = Auger transition probability for the ABC transition of element i

r = Secondary ionization for the A level of element i by scattered electrons (backscatter effect)

λ = Inelastic mean free path

θ = Angle between Auger electron and surface normal

K = Experimental constant that is dependant upon the analyser's angle of acceptance and transmission function, as well as the detector efficiency and the surface roughness factor.

The atomic concentration of element i, X_i, follows from the equation:

$$N_i = \rho X_i \quad \text{.....(3.13)}$$

with ρ indicating the total atomic density.

It is thus clear that this approach takes into account experimental differences that may exist between measurements, but it does also present many theoretical and experimental complications. Two parameters in equation 3.12 that have drawn attention in literature are γ_i and λ [104 - 106]. Muller [105] assumed Auger transition probability to be unity at low energy ranges due to low photon emission probability at low energy, while it is regarded as a difficult variable to calculate in reference [104]. An experimental method to determine inelastic mean free paths is presented by Seah [106]. The method is based on the deposition of one material onto another material that acts as the substrate, while the Auger spectra are

measured after each deposition step. The quantity of material deposited is monitored with a quartz crystal oscillator. Inelastic mean free path is then determined according to the rate of decrease of the Auger signal of the substrate material.

A method is however presented that eliminates involvement of the matrix effects. From equation 3.10 follows that:

$N_i = I_i / I_p\sigma_i\gamma_i(1+r)\lambda(\cos\theta)K$ .....(3.14),

and substitution of equation 3.13 into 3.14 gives:

$\rho X_i = I_i / I_p\sigma_i\gamma_i(1+r)\lambda(\cos\theta)K$ .....(3.15),

thus:

$X_i = I_i / \rho I_p\sigma_i\gamma_i(1+r)\lambda(\cos\theta)K$ .....(3.16),

or if S_i denotes $I_p\sigma_i\gamma_i(1+r)\lambda(\cos\theta)K$,

then $X_i = I_i / \rho S_i$ .....(3.17).

For a pure element follows that X = 1, therefore for two pure elements:

$$\frac{I_1}{\rho_1 S_1} = \frac{I_2}{\rho_2 S_2} \quad \text{.....(3.18).}$$

Rearrangement of the terms in equation 3.18 gives:

$$S_1 = \left(\frac{\rho_2}{\rho_1}\right)\left(\frac{I_1}{I_2}\right)S_2 \quad \text{.....(3.19).}$$

S_1 is now defined as an atomic sensitivity factor and equation 3.19 gives scope to relate one element's sensitivity factor to that of any other element. An appropriate reference material can therefore be chosen to represent a reference sensitivity factor. Equation 3.19 can then be expressed as:

$$S_1 = \left(\frac{\rho_{ref}}{\rho_1}\right)\left(\frac{I_1}{I_{ref}}\right)S_{ref} \quad \text{.....(3.20),}$$

where S_{ref} represents an arbitrarily chosen, but appropriate element to serve as reference sensitivity factor. The LMM transition of Cu at 922eV is used in the Physical Electronics handbook of Auger electron spectroscopy [104] as the reference sample. S_{ref} for this specific transition is set at unity and with the use of equation 3.20, all other transitions can be normalised against S_{ref}. It should be stressed that I_i and I_{ref} must be obtained under exactly the same set of experimental conditions. This includes sample tilt, primary electron beam energy, primary electron beam current, energy resolution and detection mode. A list of sensitivity factors can be found in reference [104] together with the system used and the experimental settings. Sensitivity factors can now be used directly in the Palmberg method to determine the relative atomic concentration, X_A, of a species A in a homogeneous matrix consisting of i elements:

$$X_A = \frac{N_A}{\sum N_i} = \frac{I_A / S_A}{\sum I_i / S_i} \quad \text{.....(3.21).}$$

It should be realised that the method described above is only a semi-quantitative approach since it does not take the following matrix effects into account [107]:

(a) Differences in peak shape between sample and standard.
(b) Differences in surface topography between sample and standard.
(c) Backscattering effects.
(d) Variation in sampling depth due to different electron escape depths.

Significant errors may therefore result from analyses and conclusions should be drawn with vigilance. One way to improve the accuracy of the described technique is to determine sensitivity factors for the instrument and elements that are envisaged in a certain analysis. Only the applicable transitions and a reference e.g. Cu are required to calculate the S_i values from equation 3.20.

3.2 Sample preparation using thermal decomposition of aqueous precursor solutions.

ASME SB 265-90 grade 2 Ti from Multi-Alloys was used as the substrate for the preparation of all DSA samples to represent a parent metal similar to that used in industrial production facilities.

3.2.1 Samples for electrolysis and structural measurements.

Rectangular electrodes were cut from the 1.3mm thick Ti sheet to have an average two-sided working surface area of 1.744 x $10^{-3}m^2$ with an extended shaft. An illustration of the Ti sample's dimensions is sketched in figure 3.8. The shaft could be insulated with a tight fitting teflon cylinder, protruding through a teflon lid on top of the electrochemical cell to make external electrical contact possible during experiments. This setup also allowed for accurate determination of the geometrical exposed surface area of the working electrode and thus for calculation of the applied current density during electrolysis.

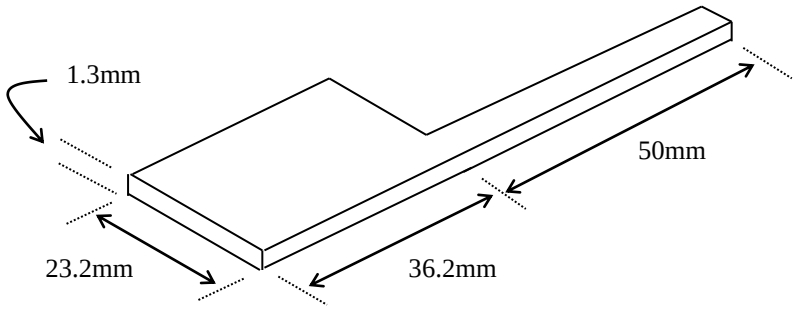

Figure 3.8: Dimensions of a typical Ti substrate specimen.

Both sides of the working surface of the samples that were destined for electrolysis were sandblasted to ensure adherence of the MnO_2 layers on the DSA's. After ultrasonic degreasing of the samples in hexane, the roughened surfaces were chemically etched in 2M H_2SO_4 at 80 ± 2°C for 60min after which it was rinsed with acetone to expedite a clean

surface for application of the Ru and/or Ti containing precursor solution. Two concentrations of $RuCl_3.3H_2O$ were obtained from Next Chimica, namely 3.21wt/wt% as Ru and 19.89wt/wt% as Ru. The solutions were used as obtained and concentrations of 0.8wt/wt% Ru, 7.5wt/wt% Ru and 10wt/wt% Ru were prepared from the respective higher concentration solutions using deionised water. A range of aqueous precursors with different Ru concentrations was therefore available for preparation of the intended different DSA's. Mixed component precursor solutions were prepared from the 19.89wt/wt% Ru and a 20.44wt/wt% $TiCl_3$ in HCl solution from Alfa Aesar. The objective was to have three solutions with different Ru:Ti compositional ratios, but to limit the total metal (Ru and Ti) in solution to a single value. The result was solutions with a total metal concentration of 7.5wt/wt% each, but with Ru concentrations of 2.25wt/wt%, 3.75wt/wt% and 7.5wt/wt%.

Application of the various precursor solutions on the Ti pieces was done by immersing a sample in an excess volume of the applicable solution to ensure total coverage of the working surface. Thereafter the sample was placed in an upright vertical position, i.e. the orientation in which the electrode would operate in the electrochemical cell, thus facilitating gravitational removal of excess precursor solution. This was done at atmospheric pressure and ambient temperature for a constant duration of 7min for each sample. The sample was then fired at 400 ± 10°C for a duration of 30min in a type RM4 Labcon muffle furnace. After reaching room temperature the sample was ultrasonically treated in deionised water to remove all particles that did not adhere to the metal surface as part of the electrocatalytic film. This whole process, starting from immersion in the precursor solution, was done in triplicate for each sample. All the DSA samples for electrolysis and XRD measurements are listed in table 3.2.

Except for the crystallographic characterisation of the eight samples in table 3.2, the effect of annealing temperature on the lattice parameters of RuO_2 as well as the effect of elevated temperature on oxidation of the Ti substrate was also investigated. With the exception of not being sandblasted, the Ti test samples for these measurements were prepared in exactly the same manner as the samples for electrolysis outlined in table 3.2. Annealing was done in a Lindberg tube furnace at temperatures of 400°C, 500°C and 600°C for each of the following precursor solutions: 3.21wt/wt% Ru, 10wt/wt% Ru, 19.89wt/wt% Ru and 10wt/wt% Ru in an O_2 atmosphere. The O_2 atmosphere was maintained by a flow of the gas through the quartz

tube at approximately 4.5l/min using an Ashcroft regulator. Oxygen flow was only initiated after the first 2min of annealing to prevent removal of the “wet” precursor from the Ti surface. The samples described above are summarised in table 3.3.

Total metal in precursor (wt/wt%)	Ru in precorsor (wt/wt%)	Ti in precursor (wt/wt%)	Ru : total metal mass ratio	Annealing temperature (°C)
7.5	2.25	5.25	0.3	400
7.5	3.75	3.75	0.5	400
7.5	5.25	2.25	0.7	400
0.8	0.8	0	1.0	400
3.21	3.21	0	1.0	400
7.5	7.5	0	1.0	400
10	10	0	1.0	400
19.89	19.89	0	1.0	400

Table 3.2: List of DSA specimens used for electrolysis and XRD measurements.

Ru in precursor (wt/wt%)	Annealing temperature (°C)	Atmosphere
3.21	400	Air
3.21	500	Air
3.21	600	Air
10	400	Air
10	500	Air
10	600	Air
19.89	400	Air
19.89	500	Air
19.89	600	Air
10	400	O_2
10	500	O_2
10	600	O_2

Table 3.3: List of DSA specimens used in the temperature study.

3.2.2 Samples for surface analyses.

A list of the DSA samples that were subjected to depth profiling is summarised in table 3.4. The substrate preparation was again done in accordance to the method already described for as-received Ti, i.e. non-sandblasted surfaces, in contrast to the Ti used for electrolysis experiments.

Total metal in precursor (wt/wt%)	Ru in precursor (wt/wt%)	Ti in precursor (wt/wt%)	Ru : total metal mass ratio	Annealing temperature (°C)
7.5	2.25	5.25	0.3	400
7.5	3.75	3.75	0.5	400
7.5	5.25	2.25	0.7	400
0.8	0.8	0	1.0	400
3.21	3.21	0	1.0	400
10	10	0	1.0	400

Table 3.4: List of DSA specimens used for AES depth profiling.

A photograph of a prepared DSA specimen is included in figure 3.9 as an example.

Figure 3.9: Photograph of a DSA specimen prepared with a 3.21wt/wt% Ru precursor, 400°C, 30min x 3.

3.3 Electrochemical setup and instrumentation.

3.3.1 Setup and procedure for electrolysis experiments.

Electrolysis experiments were done in a thermostatic, single-compartment glass cell of volume 300cm^3. Since Pb cathodes are an option for H_2 evolution in commercial EMD cells, it was used as counter electrodes in these experiments to further mimic an industrial environment. Pb foil of 1.5mm thickness was obtained from Alfa Aesar and was cut into rectangular pieces of dimensions just larger than the Ti pieces. Before being used, the lead electrodes were polished with 1000 grit SiC paper from 3M and etched in boiling HNO_3 for a few seconds. Two counter electrodes were positioned in the teflon lid of the cell on both sides of the centered DSA. The counter electrodes were parallel to the working electrode with an inter-electrode spacing of 16 ± 1mm on each side to attempt a uniform electric field on the surface of the latter electrode during electrolysis. All electrode potentials are referenced against an Ag/AgCl (3M NaCl) electrode from Bioanalytical Systems. The latter electrode was placed in a 3M NaCl liquid junction that was in turn inserted at the top end of a 100mm Liebig condenser. The condenser was sealed at its bottom with a capillary tube and glass frit and was filled with cell electrolyte. The capillary tube protruded through the lid of the cell and the frit was positioned at a distance of 2mm from the top of the working electrode. This setup allowed for the electrolyte in the liquid junction directly above the working electrode to be the same as that of the electrolysis solution. This prevented any possible current oscillations as previously observed by An *et. al.* [108]. The purpose of the condenser was to keep the reference electrode at a constant temperature of 18 ± 2°C. A Davies double surface condenser was additionally used to eliminate evaporation from the sealed electrochemical cell. The experimental setup is graphically illustrated in figure 3.10 with photographs of the actual electrochemical cell and system in figures 3.11 to 3.13.

The cell electrolyte consisted of volumetrically prepared 74g/l $MnSO_4$ and 40g/l H_2SO_4. AR grade $MnSO_4$ and H_2SO_4 from Merck were dissolved in deionised water in Erlenmeyer flasks and cooled to room temperature. Hereafter, dilution was made in volumetric flasks to protect the integrity of latter flasks' calibration from the exothermic nature of the dissolution reactions. Temperature in the electrochemical cell itself was controlled at 86 ± 2°C *via* circulation of a low viscosity oil from a Labcon waterbath and circulator. Linear current

scans ranging from 100A.m^{-2} to 170A.m^{-2}, scanned at a rate of 10mA.m^{-2}.s^{-1} on the working electrode, were used as excitation signals and were generated by an Autolab PGSTAT30 potentiostat/galvanostat from Eco Chemie, set in galvanostat mode. Electrode polarization was measured as the response signal and data accumulation was done with GPES software from the same manufacturer.

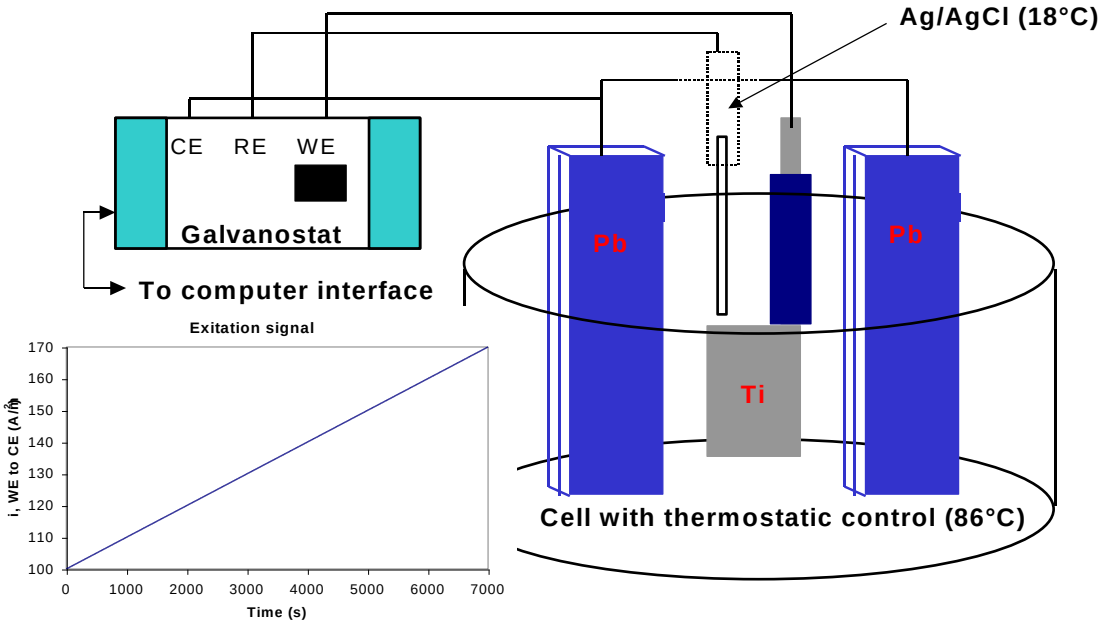

Figure 3.10: Experimental setup for electrolysis.

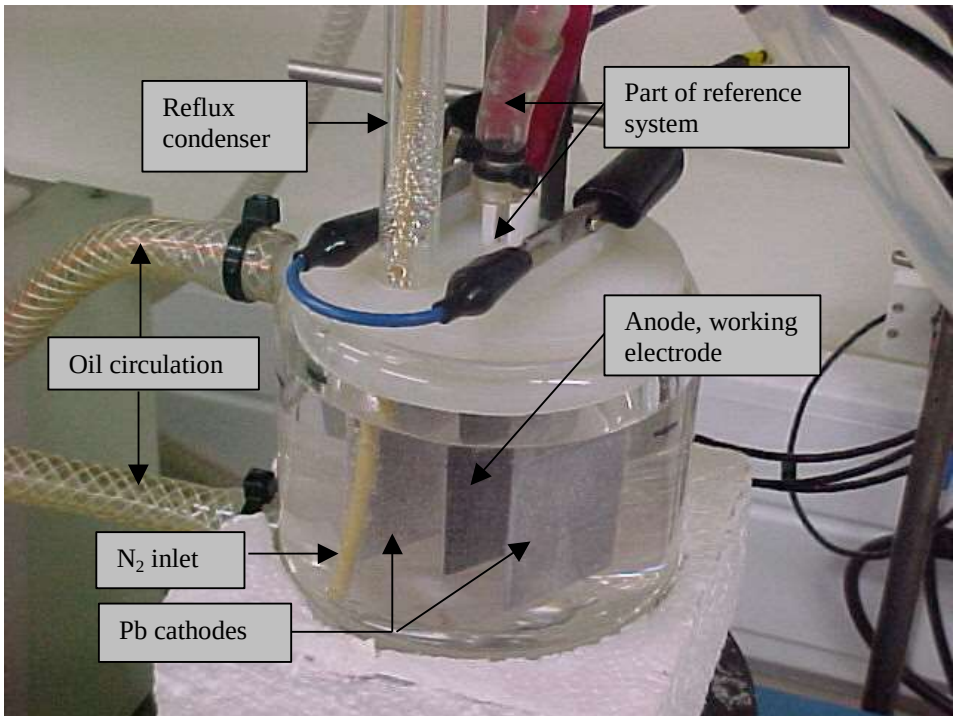

Figure 3.11: Photograph of the electrochemical cell.

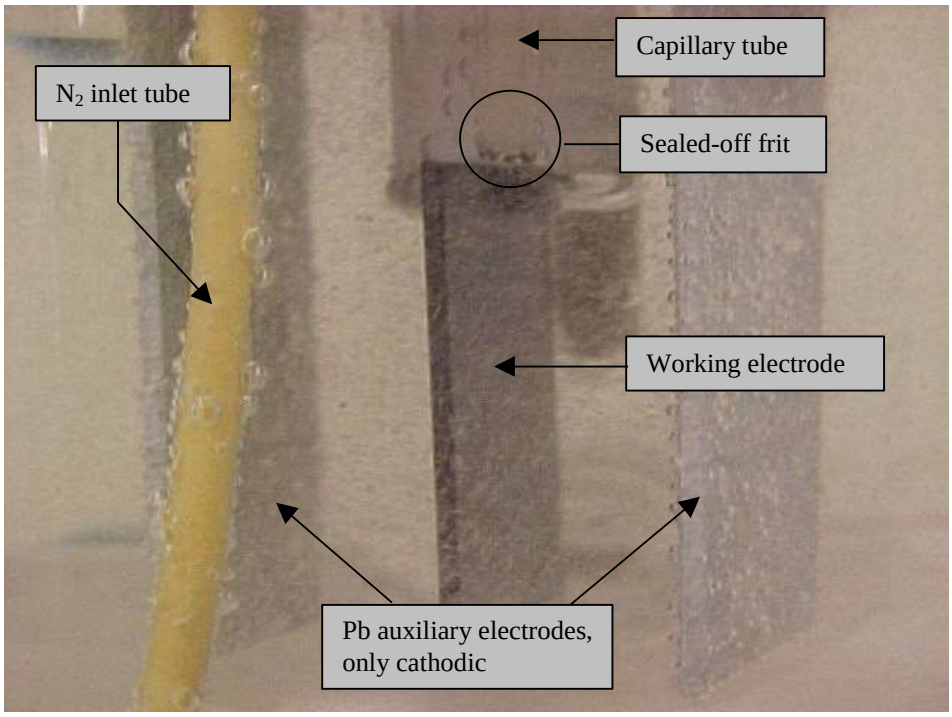

Figure 3.12: Photograph of the electrodes positioned in the electrochemical cell.

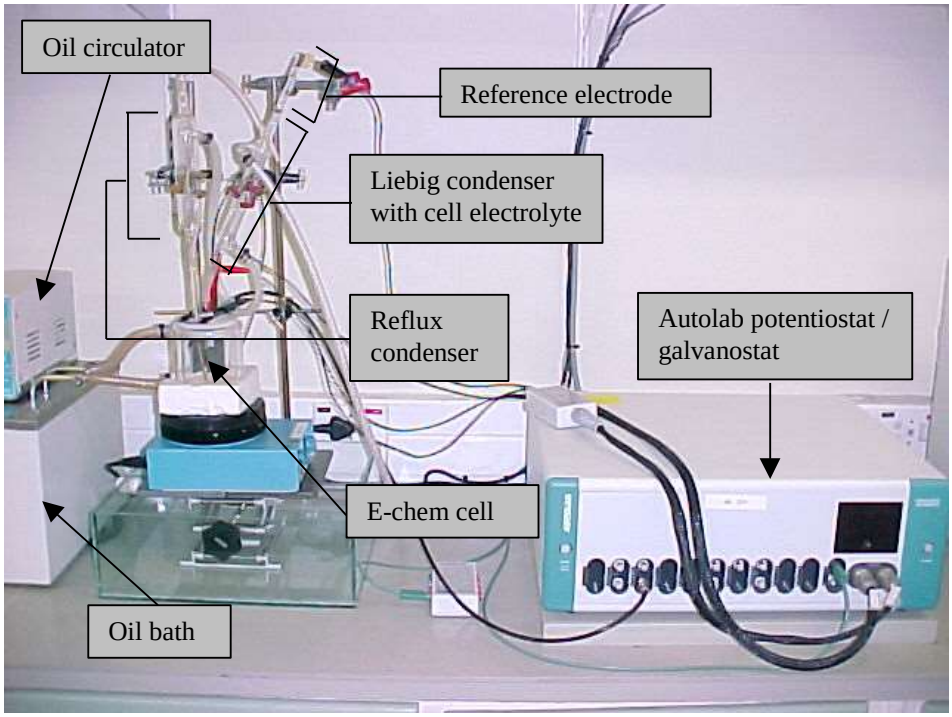

Figure 3.13: Photograph of the complete electrochemical system.

3.3.2 Setup and procedure for the electrochemical growth of hydrous $RuO_x.nH_2O$ films.

With the exception of the auxiliary electrodes and the reference system, the experimental setup for the growth of electrocatalytic films on sandblasted Ti was exactly the same as for electrolysis as described in section 3.3.1. Ni mesh was used as counter electrodes in the positions of the Pb foil. The Liebig condenser was filled with 3M NaCl and the Ag/AgCl electrode was placed directly in this solution. The experimental setup is illustrated in figure 3.14. Water circulation through the Liebig again ensured a reference electrode at 18 ± 2°C. The cell electrolyte was maintained at isothermal conditions of 50 ± 2°C during cyclic voltammetry. The active species in the electrolyte was 5mM $RuCl_3.3H_2O$ and was prepared from a concentrated solution as supplied by Next Chimica. 0.1M KCl served as the supporting electrolyte and was volumetrically prepared from AR grade (Merck) chemicals and distilled water. Electrosynthesis was done similar to the method of Hu and Huang [76] by scanning the potential on the working electrode between –200mV and 1000mV at a rate of 50mV.s^{-1} for 85 cycles in the absence of agitation. The same instrumentation as for electrolysis was used to generate the required potential waves and to capture the data.

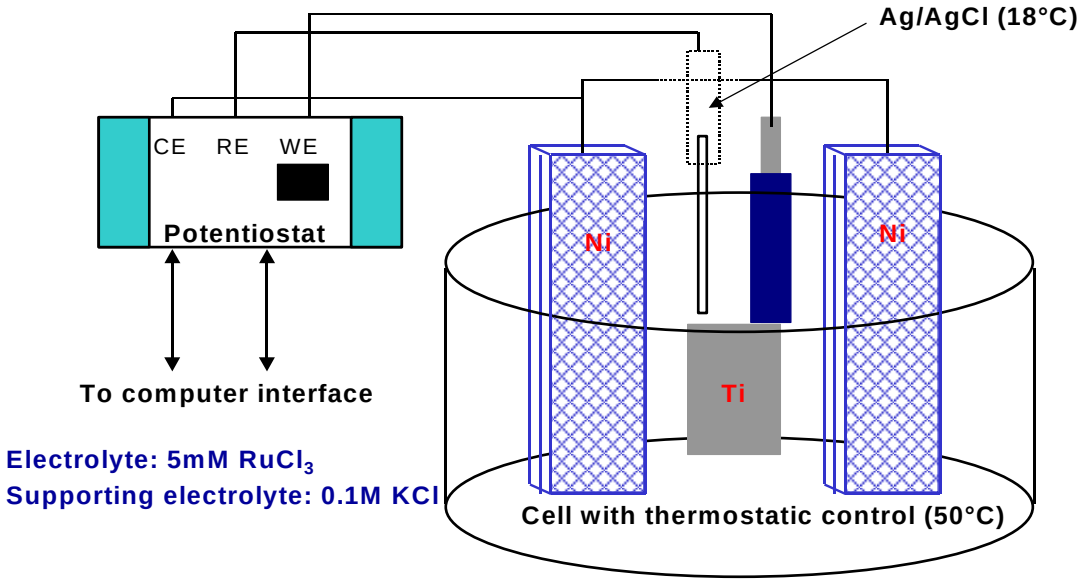

Figure 3.14: Experimental setup for electrosynthesis of $RuO_x.nH_2O$ films.

3.4 Sample preparation using cyclic voltammetry.

All samples were again prepared from ASME SB 265-90 grade 2 Ti with the same geometrical dimensions as the specimens in the thermal decomposition technique. Sandblasted surfaces were ultrasonically degreased in hexane to promote film adherence and to ensure clean substrates respectively. Electroformation of the $RuO_x.nH_2O$ films was done as described in section 3.3.2. Figure 3.15 depicts a voltammetrically prepared film. The homogeneity of the latter oxide film is a striking improvement when compared to the thermally prepared DSA in figure 3.9. After oxide loading, the various samples were calcinated for different durations at 600°C in air at atmospheric pressure.

3.4.1 Samples for electrolysis and structural measurements.

Thermal treatment of samples in this section was done with a type RM4 Labcon muffle furnace. The applicable information is summarised in table 3.5.

Calcinating T (°C)	Duration (min)	Application	
		XRD	Electrolysis
Unannealed	Unannealed	•	•
600	15	•	
600	30	•	•
600	60	•	•
600	120	•	•
600	240	•	•
600	480	•	

Figure 3.5: List of electrochemically prepared specimens for XRD and electrolysis studies.

3.4.2 Samples for surface analyses.

Annealing of voltammetrically prepared samples for AES measurements was done at 600°C in a Lindberg furnace fitted with a quartz tube. The effect of the durations of 30min, 60min, 120 min and 240min was investigated.

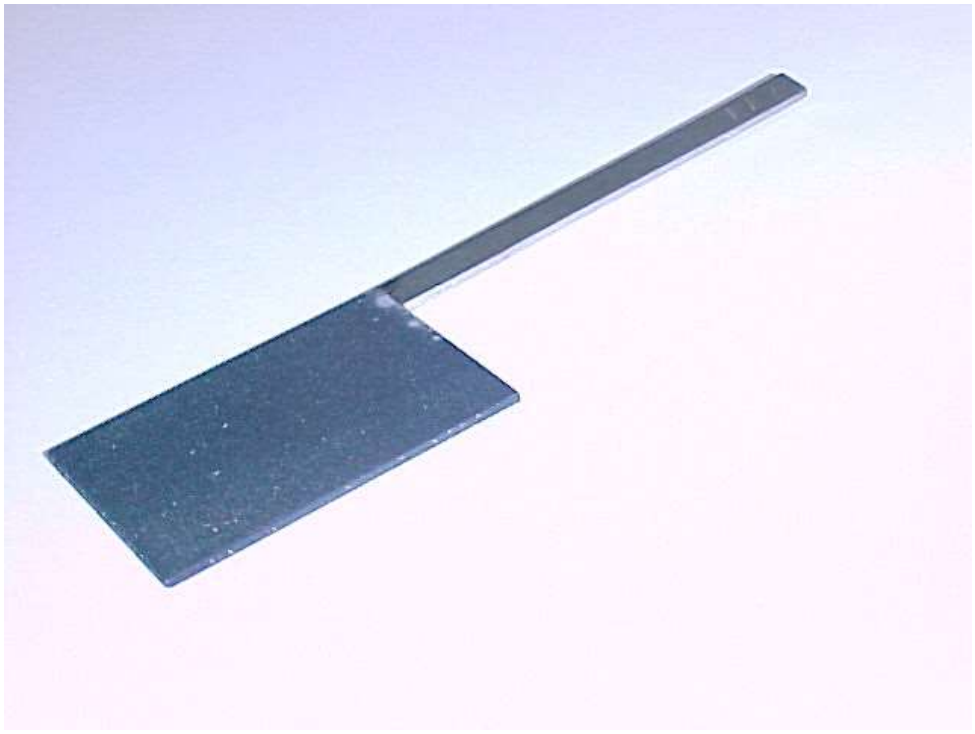

Figure 3.15: Photograph of an electroformed $RuO_x.nH_2O$ film on Ti metal.

3.5 Instrumentation and settings for physical characterisation.

3.5.1 X-ray diffraction.

All samples, except for the samples in the study regarding the effect of temperature on RuO_2 lattice parameters, were subjected to diffraction measurements in a Siemens D5000 Matic powder diffractometer that was adapted to accommodate the electrodes. Spectra were taken using Cu Kα radiation (λ = 1.54Å) that was generated using a voltage of 40kV between the filament and anode, while the beam current was maintained at 35mA. The goniometer was controlled to yield step sizes of 0.02° and intensity measurements were averaged using a time/step value of 2sec. The signal from the instrument's scintillation counter was directly converted to a data file during each measurement using software as supplied by Siemens. Crystallographic changes on the DSA samples in the temperature study were probed using a Philips PW 1130/00 diffractometer. All spectra were taken at 2° 2θ/min, while the attenuation factor on the detector's control system was manipulated to yield the best possible signal-to-noise ratio for each spectrum. The absolute value of the measured intensities were

not considered in the data analyses since the peak positions render information on the lattice parameters.

3.5.2 AES system.

All Auger measurements were carried out in a Physical Electronics model PHI 590 Auger/ESCA ultrahigh vacuum (UHV) system. A photograph of the vacuum system is shown in figure 3.16. The base pressure in the system was below 8 x 10^{-9}Torr. Emission of Auger electrons was initiated by a 2keV primary electron wave that was generated from a 10keV co-axial electron gun inside a cylindrical mirror analyser (CMA). The relative low primary beam energy of 2keV was regarded as imperative from the work of Armstrong and Quinn [29] as well as Atanasoska *et. al*. [102] to prevent reduction of TiO_2 and RuO_2. The average e^- beam current was 4.5μA as measured in a Faraday cup using an electrometer. A modulation voltage of 2V was applied to the CMA to ensure that differentiated spectra were recorded, while a multiplier voltage of 1.6kV was kept constant for all measurements. The settings on the system's lock-in amplifier were at 2eV/s and 0.3s for the scan rate and time constant respectively.

Figure 3.16: Physical Electronics AES system.

Prior to each depth profile, the alignment of the electron and ion beams was optimised using the Faraday cup. A 135nA ion beam consisting of 2keV Ar^+ ions was generated by an electron impact source. With the emission current in the ion gun constant at 25mA it was found that the Ar pressure could vary between 11 x 10^{-3}Pa and 20 x 10^{-3}Pa without changing the current. The pressure inside the ion gun was however kept between 14 x 10^{-3}Pa and 15 x 10^{-3}Pa for depth profiles on all specimens. The ion beam was raster-scanned over an area of 3mm x 3mm to give a square etch pit on the sample surface. During depth profiling, the energy scans on the CMA was under computer control and Auger peak-to-peak height (APPH) vs. time was measured for Ru (125 – 305eV), Ti (315 – 465eV) and O (460 – 535eV). One of the objectives of the AES measurements on the DSA specimens was to compare the samples, at least semi-quantitatively, regarding the Ru concentration on the surface as well as the relative thickness of the electrocatalytic films. Slight changes in the primary beam current between different depth profiles are inevitable and this could cause precarious interpretations when using the measured APPH values to represent concentration. To prevent such an aberration, an AES spectrum of a sputter cleaned Cu standard was taken before each depth profile. Changes in the APPH of the 922eV transition of Cu were used to calculate a factor with which the e^- yield changes between measurements. This factor was used to normalise APPH measurements in the various depth profiles in order to have a direct comparison between profiles using APPH values. A sputter-scaling factor was also experimentally determined by doing a depth profile on a Ti thin film of known thickness after analyses on each electrocatalyst. Electron beam evaporation was employed to prepare Ti thin films on <100> Si wafers at a pressure below 10^{-6}Torr in a bell jar evaporation system. A calibrated Inficon thickness monitor was used to measure the thickness of the deposited Ti during evaporation.

3.6 Titanium composite electrodes and preparation of Ti/TiC.

Ti-20% Pb and Ti-35% Pb electrodes were obtained from Advanced Materials Products Inc. (USA). The 20% Pb sample was sandblasted before electrolysis, but the anode containing 35% Pb had a very rough surface and was only ultrasonically degreased in hexane before being used in EMD plating experiments under the exact same conditions as for all the electrocatalysts. A Ti-Mn composite material, designed by the Beijing General Research Institute for Non-ferrous Metals (China) for the specific purpose of EMD production was

also ultrasonically degreased and a test piece was used in an electrochemical experiment. AES measurements were utilised to assess the composition of this metal composite. A specimen of the metal was polished on 400grit SiC paper using distilled H_2O as lubricant. This was complemented with a polish on microcloth using 6μm Buehler diamond compound. Standards of Ti and Mn were subjected to the same preparation for AES measurements. AES measurements were also done as for the electrocatalysts, but with a primary electron energy of 3keV as the only difference. To prepare Ti/TiC electrodes, graphite was deposited onto both surfaces of sandblasted ASME SB 265-90 grade 2 Ti samples by means of electron beam evaporation under vacuum conditions (<10^{-6}Torr). The samples were thereafter annealed in the quartz tube of a Lindberg furnace at a base pressure of 2.2 x 10^{-7}Torr. The annealing temperature, T, was kept constant at 750°C and the time, t, to give a sufficient diffusion distance, x, was calculated from equation 3.22.

$$x = \sqrt{4Dt} \quad \text{.....(3.22)}$$

The diffusion coefficient, D, at 750°C was calculated from the Arrhenius type equation 3.23.

$$D = D_0 e^{-Q/RT} \quad \text{.....(3.23)}$$

Values for the activation energy, Q, and the pre-exponential factor, D_0, were taken from the work of H.C. Swart *et. al.* [109] as 207kJ/mol and 4.1 x $10^{-8}m^2.s^{-1}$ respectively. The evaporated carbon thickness and the calculated annealing times are summarised in table 3.6. These Ti/TiC samples were consequently used in electrochemical evaluation and AES depth profiling. The experimental conditions for both electrolysis and depth profiling were as previously explained.

Experiment	Thickness of evaporated C (Å)	D at 750°C ($m^2.s^{-1}$)	Calculated time (seconds)	Annealing time (min)
AES	918 & 916	1.1 x 10^{-18}	1915	64
E-chem	780 & 664	1.1 x 10^{-18}	1383	46

Table 3.6: Conditions for preparation of TiC films on Ti. Two thickness values are specified for each sample due to both sides being coated with graphite in different experiments. The calculated time was doubled and used as the duration for annealing.

Chapter 4

Results and discussion: Spontaneous H_2 evolution reaction on Ti in an acidic medium and its effect on subsequent electrode polarization during MnO_2 electrodeposition.

4.1 Sandblasted Ti for EMD production.

Although Ti metal does not possess electrocatalytic properties and although its surface is susceptible to anodic oxidation that diminishes its metallic conductivity, it is nonetheless an acceptable anode material under appropriate conditions of temperature, current density and $MnSO_4$ & H_2SO_4 concentrations. A sandblasted Ti surface satisfies requirements i to v as described in section 1.3. For these reasons, sandblasted Ti (without any chemical or physical modifications) finds application in industrial MnO_2 electroplating facilities. An investigation into Ti as an electrode is therefore justified to be part of the concept to develop improved anodes for EMD production.

The results to follow are however not a conventional study on the application of Ti as an anode material. It is rather a study in which emphasis is placed on the effects of exposure of Ti metal to the electroplating precursor solution on its subsequent behaviour during electroplating. The results will present new insight into the vigilance with which unmodified Ti metal should be employed to facilitate electroplating in an acidic environment.

4.1.1 Introduction and theoretical survey.

Unfilled d electron energy levels give Ti metal the capability of reacting with atmospheric oxygen to form a tenuous, but stable surface oxide film that renders the element as a valve metal. Depending on environmental conditions, the thickness of the oxide film ranges from 1 to 10nm [27, 28, 48, 49, 110 - 113] and is responsible for Ti metal's passivity. A classic example to describe passivity is the corrosion resistance of a metal in an aqueous acidic or basic medium. The higher the degree of passivity, the better the resistance to dissolution. Brusic [114] mentioned that a shift of single electrode potential in a positive direction (more noble value) always accompanies improved corrosion resistance. This suggests that the value

of the electrode potential is representative of the metal's surface. Several authors [34, 48, 115 - 117] have used the rest potential of a metal electrode in solution as an indication of its surface condition. The same is true for Ti metal and irrespective of its passivity, breakdown of the passive film does occur when subjected to certain conditions. "Depassivation" usually takes place with a rapid change in electrode potential to a much less noble value than for its passivated counterpart. A steady state potential is reached that designates uniform dissolution of the oxide film and/or metal. This steady state potential is referred to as the activation potential and the whole transition process is referred to as activation. The required time to undergo activation is referred to as the breakdown period, τ_b, and several variables are known to influence τ_b. The breakdown period for an oxide film on Ti in an acidic medium generally decreases with an increase in solution concentration and temperature. Certain ions in solution also affect τ_b e.g. Ti^{3+} and Ti^{4+} retards activation whereas fluoride ions have an enhanced effect on film dissolution [32, 118]. Another parameter, worth mentioning, that influences the stability of an electrochemically formed oxide film on Ti is the scan rate at which the film is originally grown in a linear sweep voltammetry method. Blackwood [34] reported that a significantly more stable anodic oxide film is obtainable at a lower sweep rate. The authors in reference [34] explained last mentioned findings as the result of an oxide film with a more dense crystal structure due to the lower initial formation rate. If film dissolution rate is dependent on ion diffusion through the oxide film, then the latter theory holds due to an increase in barrier height caused by the close packed structure. Another variable that contributes to the complication of the activation process is an aging process of passive electrodes in H_2O at elevated temperatures. Allard *et. al*. [119] kept passive electrodes in H_2O at 65°C for a period of days after which they found the oxide to be more stable in the activation solution and resolved this due to a slow change in the film structure.

The foregoing discussion makes it obvious that activation of a metal electrode is an intricate process and two suggestions that address the activation mechanism can be found in references [32], [34] and [45]. A spontaneous redox reaction on the oxide surface could cause reduction of TiO_2 to form a soluble TiOOH species. The reduction is balanced by oxidation of Ti to TiO_2 to give an overall disproportionation reaction of the form:

$$Ti + 3TiO_2 + 2H_2O \rightarrow 4TiOOH \quad \text{.....(4.1)}$$

A more simplistic approach is that TiO_2 dissolves chemically to yield Ti(IV) species in solution resulting in metal activation. In a study conducted by Blackwood *et. al.* [34], the oxide-thinning rate at open circuit was determined as a function of H^+ concentration in H_2SO_4 solutions and a first order relation was inferred between the two variables. The suggested dissolution reaction is of the form:

$$TiO_2 + H_2O + H^+ \rightarrow Ti(OH)_3^+ \quad \text{.....(4.2)}$$

with the product forming a $Ti(OH)_3HSO_4$ species in solution.

The current endeavour is to monitor the open circuit voltage (OCV) behaviour of a Ti electrode in an acidic Mn^{2+} containing solution that is employed for the preparation of EMD. Since open circuit decay is effectively a removal of the oxide film, this phenomenon should in principle provide means of rejuvenating a passivated electrode without any energy expense. Except for displaying a steady state OCV, an activated Ti electrode also evolves H_2 gas in certain acidic media [48, 117]. A proposed mechanism by which H_2 spontaneously evolves from the electrode's surface will also be presented in section 4.1.3. Ti is well known to absorb H_2 [115, 116, 120], and the effect of hydrogen-charged Ti on subsequent oxidation in alkaline solutions has been studied with electrochemical methods [115, 116] to indicate an enhancement of TiO_2 formation due to TiH_2 on the electrode's surface. It will therefore also be attempted to establish a link between H_2 exposure to the anode at OCV and subsequent electrode oxidation at the initial stages of MnO_2 electrodeposition. This is necessary seeing that Ti can be activated to be the embodiment of a clean metal surface without any passive film and lower polarization during electrolysis is therefore possible. The initial oxidation rate at the onset of electroplating could however increase due to TiH_2 on the surface, resulting in a drastic increase in power dissipation to maintain a set current density.

4.1.2 Experimental considerations.

All experiments are of electrochemical nature and were done employing the setup and instrumentation as described in section 3.3.1.

4.1.3 Discussion.

A classical illustration of activation presents itself in figure 4.1. Before going into a discussion on this result, it should be mentioned that the measurement was started with the electrode immersed in a solution containing the cell electrolyte (74g/l $MnSO_4$ and 40g/l H_2SO_4) at room temperature. A temperature gradient was induced at t = 0sec as illustrated in the graph and the electrode potential was thus measured as a combined function of time and temperature. The sudden decrease in potential at approximately 900sec (52°C) is accompanied with H_2 gas evolution at a slow rate on certain spots on the metal's surface. This rapidly transforms, within 200sec, into uniform gas formation over the entire surface at an increased rate. A steady increase in H_2 evolution rate is maintained up to 2300sec (78°C) after which it remains constant. The activation potential is constant at a value of -0.67 ± 0.01V *vs*. Ag/AgCl. This value compares well with –0.8 ± 0.05V *vs*. Ag/AgCl for Ti in 1M $MnSO_4$ and 0.3M H_2SO_4 at 90 ± 2°C in the studies of Armacanqui and Ekern [48, 117]. It is also in the same order of magnitude of –1.2V *vs*. Hg/Hg_2SO_4 for activated Ti in 0.1M H_2SO_4 at 65°C [34].

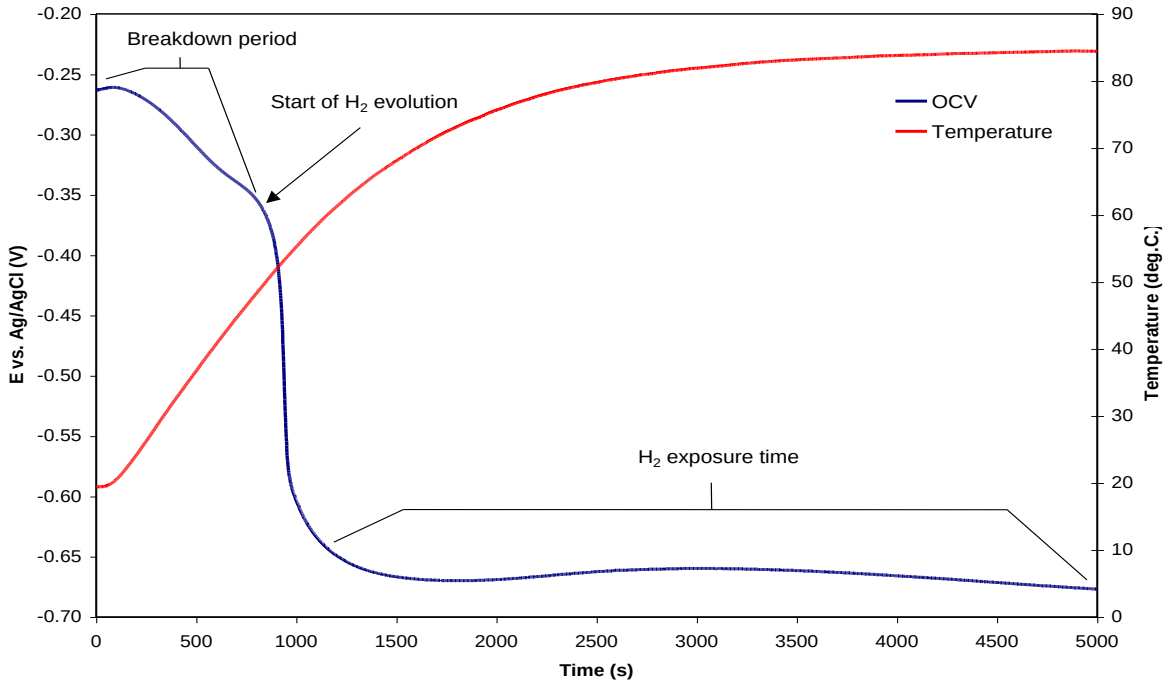

Figure 4.1: Open circuit decay profile to illustrate activation of Ti metal in 74g/l $MnSO_4$ & 40g/l H_2SO_4.

The phenomenon of H_2 evolution requires charge transfer as well as recombination of hydrogen at the solution-electrode interface and is thus a process of importance. A tenable theory for this process can be attempted by resolving reaction 4.1 into its two half reactions:

$4TiO_2 + 4H^+ + 4e^- \leftrightarrow 4TiOOH$ (reduction) .....(4.3)

$\underline{Ti + 2H_2O \leftrightarrow TiO_2 + 4H^+ + 4e^- \text{ (oxidation)}}$ .....(4.4)

$3TiO_2 + Ti + 2H_2O \leftrightarrow 4TiOOH$ (net reaction) .....(4.1)

This shows that 4mol of TiO_2 dissolves (reduced to TiOOH) for every 1mol of Ti being oxidised back to TiO_2. This description of film breakdown is acceptable when the surface is still in a passive state, i.e. TiO_2 is still available, because a sufficient amount of TiO_2 is available for the reduction process. Once the electrode is activated, TiO_2 is assumed to be depleted from the surface and although the spontaneous oxidation of Ti is still providing TiO_2, 4mol of TiO_2 is required for every 1mol Ti oxidised to balance the charge in the redox process (reactions 4.3 and 4.4). The redox process would therefore come to a definite stop because the oxidation process is supplying an excess of electrons that cannot be consumed by the reduction half reaction (of which the oxidation half reaction is also the supplier of the species to be reduced) in equation 4.3. This shortcoming in the redox process now provides scope for an explanation of H_2 evolution. A perennial supply of H^+ ions is available in solution adjacent to the activated metal surface and the electrons from reaction 4.4 are now being used in a reduction reaction of the form:

$2H^+ + 2e^- \rightarrow H_2(g)$ .....(4.5)

It is believed that the TiO_2 formed in reaction 4.4 will still be reduced to soluble TiOOH, since a once activated electrode does not show passivation behaviour at a constant temperature. The H^+ reduction is therefore a supporting half reaction to equation 4.3. A more general form of equation 4.5 is presented in equations 4.6 and 4.7 where the hydrogen is believed to be adsorbed onto the Ti surface before being discharged as a gaseous product:

$Ti + H_2O + e^- \leftrightarrow TiH_{ad} + OH^-$ .....(4.6)

$TiH_{ad} + H_2O + e^- \leftrightarrow Ti + H_{2(g)} + OH^-$ .....(4.7)

An extension of the results described in figure 4.1 follows in figure 4.2.

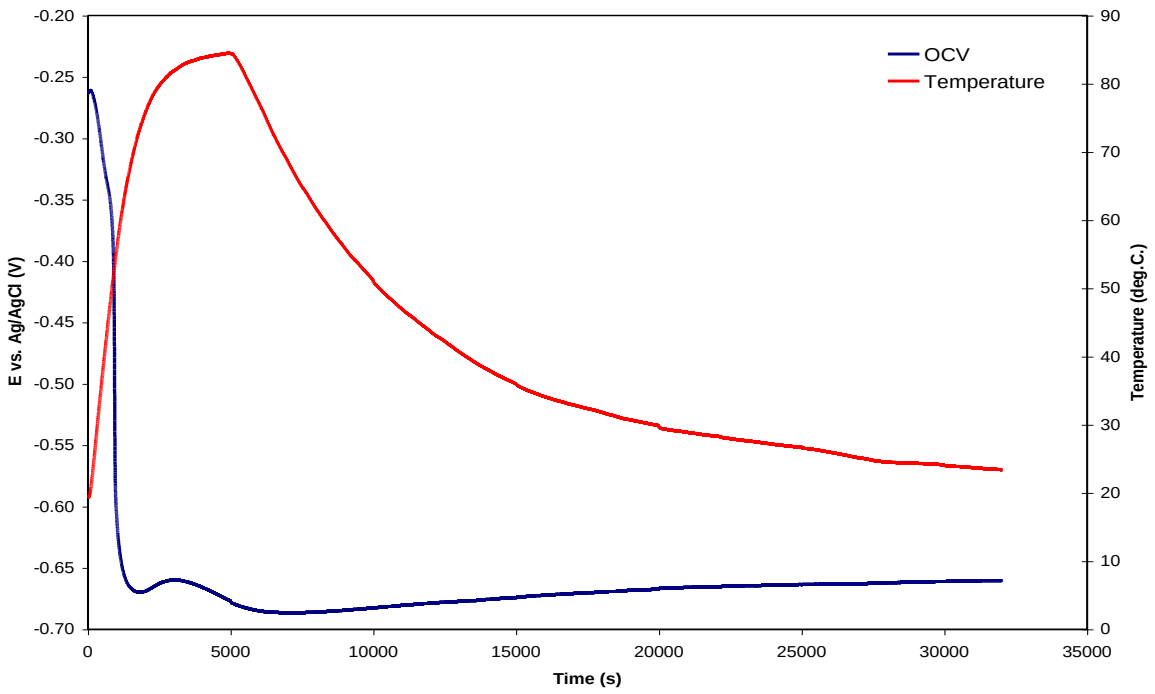

Figure 4.2: Graph of electrode potential *vs*. time to illustrate the effect of a negative temperature slope on activated Ti.

The proceeding in figure 4.2 was a planned loss in temperature control at 5000sec. The loss in thermal energy of the system due to normal air conductance and radiation is reflected in the temperature behavior as a function of time. The following visual observations were made during the cool down period. A decrease in H_2 evolution rate compared to the peak temperature is definite at 9000sec (56°C). Gas formation is only visible on certain areas of the electrode at a very reduced rate at 14300sec (37°C) and has completely ceased at 17000sec (33°C). These changes in electrolyte temperature and H_2 formation rate are however innocuous to the state of the electrode's surface as can be gathered from the measured electrode potential. Although indications are that elevated temperature is a requirement to induce activation, the results in figure 4.2 show that an activated Ti surface does not necessitate thermal energy to remain in this condition, neither is H_2 evolution a requisite for Ti to be classified as activated. At 32000sec, the electrode potential measures an exposed, oxide free metal surface in an acid medium at room temperature. It is nonetheless believed that the surface is not completely metallic, since adsorbed hydrogen should be present and TiH_2 is also expected to terminate the dangling bonds.

In a series of experiments to quantify the effect of H_2 exposure to an activated Ti anode on subsequent anodic oxidation during MnO_2 electroplating, electrodes were subjected to H_2 evolution for different periods of time. This was done by starting with each electrode at OCV in the acidic $MnSO_4$ electrolyte at room temperature after which a temperature gradient similar to that in figure 4.1 was initiated. The H_2 exposure time was manipulated by varying either the heating rate of the system or the OCV duration before electrolysis was initiated at $100A.m^{-2}$ for the various samples. Visual discretion was used in conjunction with OCV measurements to identify the onset of H_2 evolution. The principle of this method is illustrated in figure 4.3 for two samples. A different rate of temperature increase was used here and the open circuit breakdown follows a trend of being dependent on temperature. Also note the difference in the initial surface condition of the two electrodes as reflected by the respective potentials at 1sec, but with similar activation potentials. This emphasize the value of an electrode's rest potential; it is immediately concluded from the more noble potential *vs.* Ag/AgCl of electrode B that, initially, its surface is oxidised to a greater extent than that of electrode A.

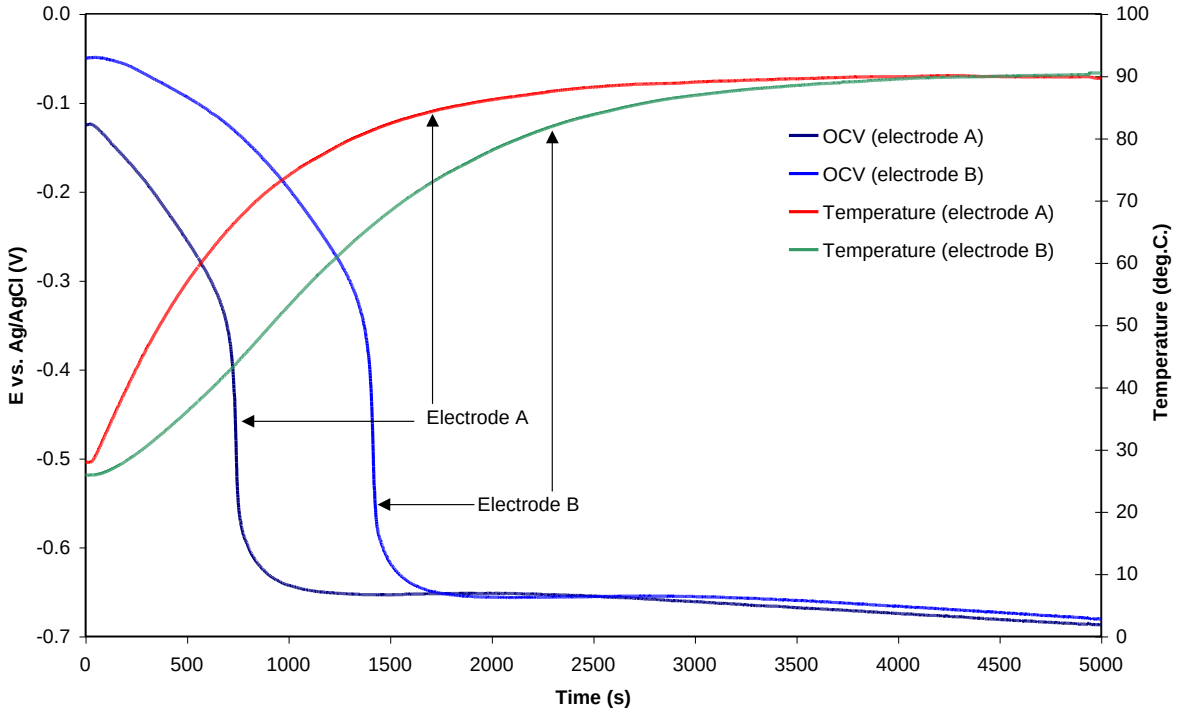

Figure 4.3: OCV decay curves for electrodes that were exposed to different rates of temperature increase.

Electroplating on activated Ti surfaces were subsequently done by scanning the anode current density from 100A.m^{-2} to 170A.m^{-2}. During electrolysis, the total anode polarization was measured *vs*. Ag/AgCl (3M NaCl) without any corrections. Anode polarization values were taken at the onset of electrowinning, just as the potential became stable at 100.5A.m^{-2} and the values are plotted as a function of hydrogen exposure time in figure 4.4 with the values summarised in table 4.1.

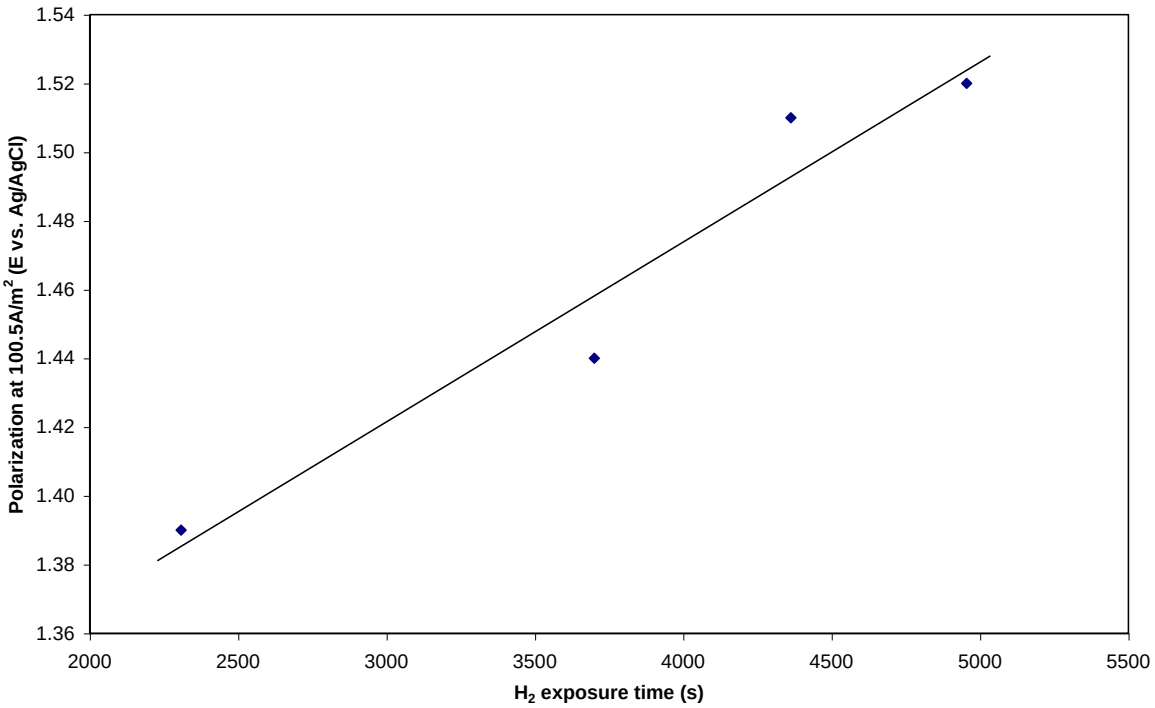

Figure 4.4: Effect of hydrogen exposure time on anode polarization at 100.5A.m^{-2} during MnO_2 electroplating.

t (s)	E at 100.5A.m^{-2} (V)
2308	1.39
3700	1.44
4363	1.51
4955	1.52

Table 4.1: Values of anode polarization at 100.5A.m^{-2} for different H_2 exposure durations.

This result gives undisputed evidence that H_2 exposure is to the detriment of electrode polarization. A linear relation between the parameters in figure 4.4 results in a slope of 0.188 ± 0.02V.hr^{-1} for the applicable H_2 exposure time range. The hypothesis presented here is

taken from the work of Tanaka [115, 116] where it is stated that TiH_2 enhances TiO_2 formation. TiH_2 formation occurs on the Ti surface during activation to an extent that is dependent on H_2 exposure time. Figure 4.4 therefore shows that the value of the free energy of formation of TiO_2 from TiH_2 must be more negative than the reported $-890kJ.mol^{-1}$ [121] for formation from Ti metal. Reaction 4.9 is thus thermodynamically favoured over reaction 4.8.

$$Ti + 2H_2O \rightarrow TiO_2 + 4H^+ + 4e^- \quad .....(4.8) \qquad (\Delta G^o_{Ti-TiO2} = -890kJ.\,mol^{-1})$$

$$TiH_2 + 2H_2O \rightarrow TiO_2 + 6H^+ + 6e^- \quad .....(4.9) \qquad (\Delta G^o_{TiH-TiO2} < -890kJ.\,mol^{-1})$$

An alternative theory to the above can be found in reference [117] where the findings were contradictory to the present results. Armacanqui and Ekern found non-activated Ti to passivate faster than activated Ti and proposed reaction 4.10 as an explanation:

$$H_{ad} \rightarrow H^+_{(aq)} + e^- \quad .....(4.10)$$

During activation, not all the adsorbed H recombines to form H_2 gas. When the anodic potential is applied for electroplating, the adsorbed hydrogen is oxidised to protons according to equation 4.10 before oxidation of Ti starts. It is suggested that reaction 4.10 is in competition with Ti oxidation resulting in a situation where initial passivation of an activated Ti substrate is less than for a non-activated metal due to the absence of H_{ad} and reaction 4.10 for non-activated Ti. Reaction 4.10 can however also be used to explain an increase in polarization (passivation) for a hydrogen exposed Ti electrode. Reaction 4.10 causes a surge in H^+ concentration adjacent to the Ti surface and this is known to facilitate passivation during EMD production [49, 51].

Significant differences are evident in the polarization curves as a function of current density during electrowinning as presented in figure 4.5. Polarization of the electrode with a H_2 exposure time of 4363sec rises within $1A.m^{-2}$ to the electrode with the next highest H_2 exposure time, but a wide gap between these two electrodes is again manifested at higher current densities. A linear relation between polarization at $100.5A.m^{-2}$ and H_2 exposure time may therefore be a precarious assumption, but it is nonetheless a vivid illustration that H_2 exposure of a Ti anode would lead to a deplorable situation in terms of power dissipation

during electroplating. Possible methods that are used in the EMD electroplating industry to renew the surface of passivated Ti metal anodes are (a) cathodic treatment and (b) sandblasting, while (c) open circuit decay has been proven less effective [122]. In an industrial facility, cathodic treatment could potentially be done by using an anode as a cathode in which case H_2 evolution will take place at a significantly higher rate than on an activated electrode at open circuit at the same temperature. The knowledge acquired here prevents the use of cathodic treatment as a method for anode regeneration and the only possibility to obtain a clean metal surface remains sandblasting.

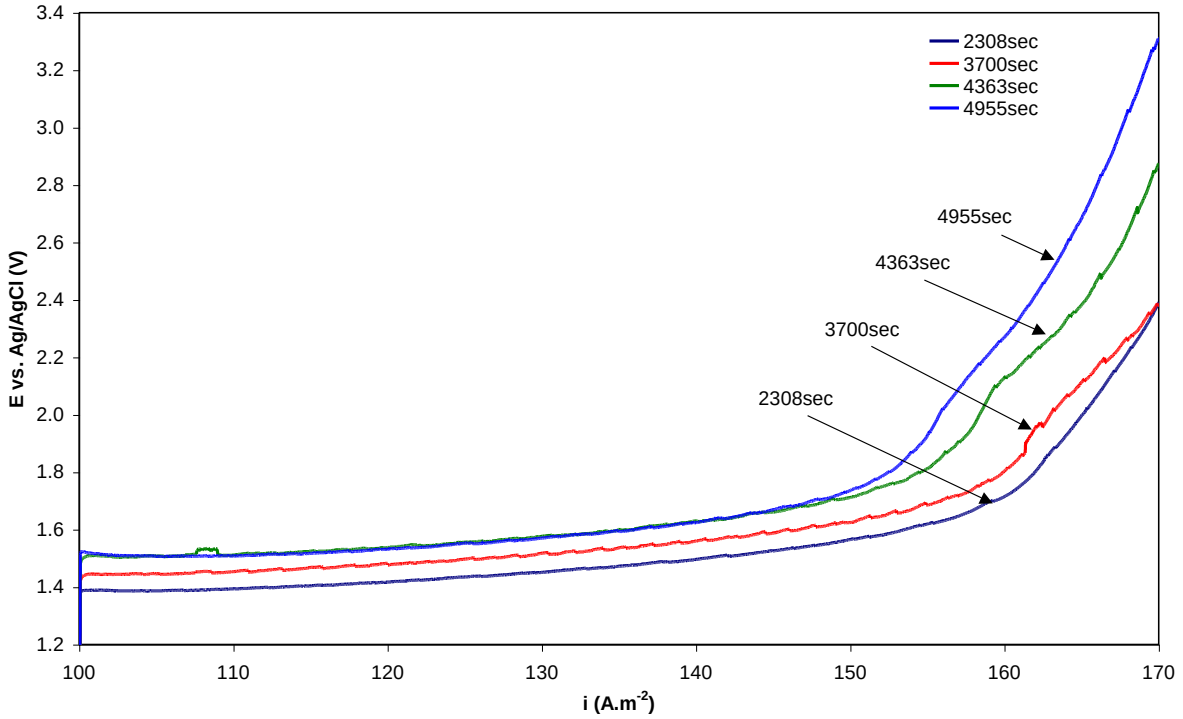

Figure 4.5: Polarization curves for MnO_2 electroplating onto anodes that experienced different H_2 exposure times.

4.1.4 Conclusion

Open circuit decay of Ti metal in an electrolyte of $MnSO_4$ in aqueous H_2SO_4 was studied using rest potential measurements during a temperature gradient to 86 ± 2°C. H_2 evolution originated at 52°C and an activation potential presented itself at -0.67 ± 0.01V *vs.* Ag/AgCl. A spontaneous redox system was resolved and used to explain H_2 evolution as a supporting reduction half reaction. New insight into the behaviour of activated Ti at room temperature

shows that an oxide free metal surface is possible without H_2 evolution. It can be claimed that H_2 evolution causes permanent changes to the surface of a Ti electrode that in turn enhances anode passivation at the onset of EMD production. The use of open circuit decay or cathodic treatment to rejuvenate a passivated anode for MnO_2 electroplating is therefore not a viable option.

Chapter 5

Results and discussion:
Electrochemistry and structural analyses of DSA and Ti composite electrodes.

5.1 Binary mixed oxide DSA's for MnO_2 electroplating.

5.1.1 Polarization slopes.

The result that benchmarks the validity and possible success of employing the electrochemical technique of MnO_2 electroplating in evaluating differently prepared DSA's (refer to table 3.2) is given in figure 5.1.

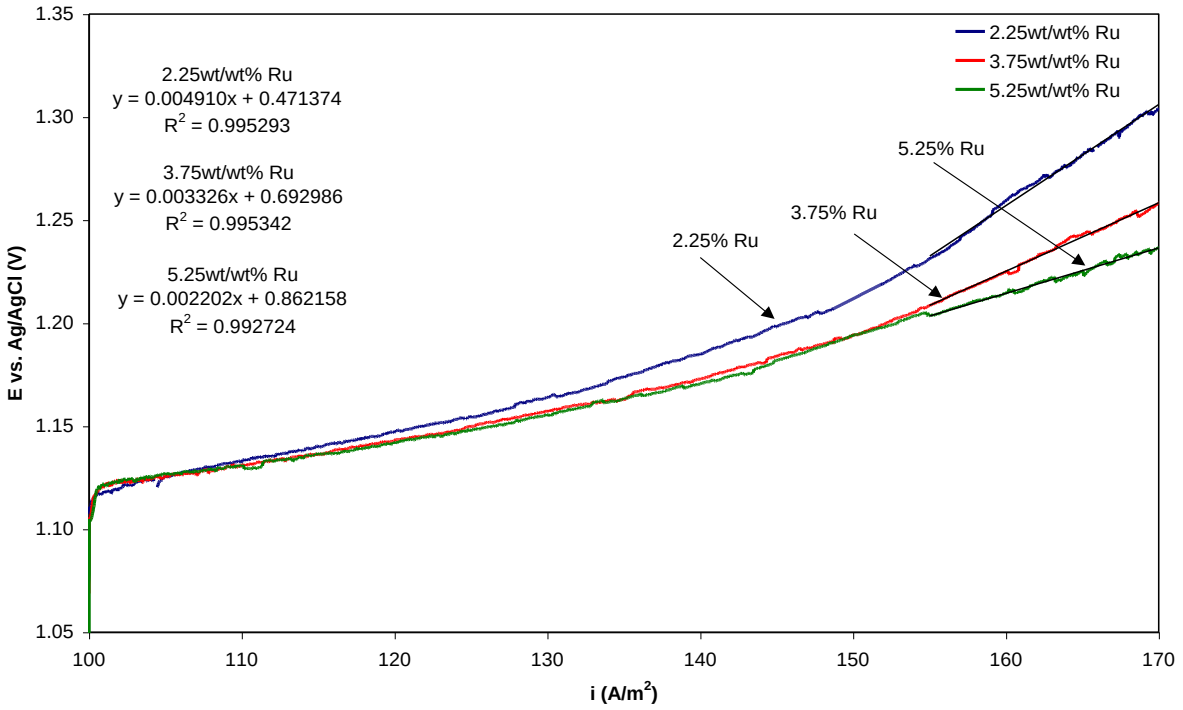

Figure 5.1: Polarization curves for MnO_2 electroplating on electrodes that were prepared with different Ru concentrations in Ru/Ti mixed precursor solutions. Total metal concentration was kept constant at 7.5wt/wt%.

In this figure the total anode polarization was merely measured against the Ag/AgCl reference system as the current density was linearly increased for each of the electrodes. It is clear from the figure that the initial electrode behaviour up to $120A.m^{-2}$ is independent of the

Ru concentration in the Ru/Ti mixed precursor. Thus, the measurement method does not discriminate between electrodes regarding their electrocatalytic capabilities or the conductivity of the oxide films at these current densities. The potential values at 100.5A.m^{-2} are included in table 5.1 and the variation is assumed to be within experimental error. The characteristics of the plots in figure 5.1 were used to introduce the parameter referred to as polarization slope. This quantity is merely a measure of the rate of increase in electrode potential as a function of current density. The polarization slopes were calculated from 155A.m^{-2} to 170A.m^{-2} for the three experiments in figure 5.1 and plotted *vs*. the Ru concentration in the precursor in figure 5.2. These results are also summarised in table 5.1.

Ru in precursor (wt/wt%)	Ti in precursor (wt/wt%)	E *vs*. Ag/AgCl at 100.5A.m^{-2} (V)	Polarization slope (mV/A.m^{-2})	XRD peak intensity at 28° 2θ
2.25	5.25	1.116	4.9 ± 1.6	59
3.75	3.75	1.118	3.326 ± 0.002	88
5.25	2.25	1.119	2.202 ± 0.008	130

Table 5.1: Summary of data used in figures 5.2 and 5.4.

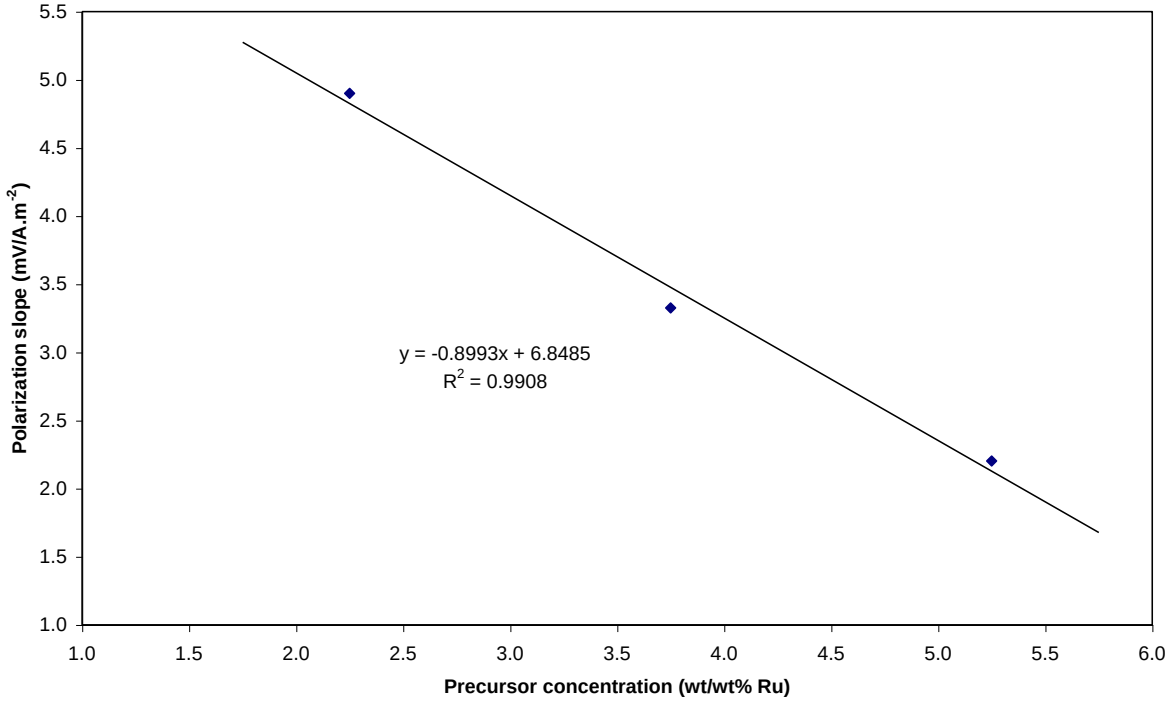

Figure 5.2: Polarization slopes as a function of Ru concentration in the precursor solution. Slopes were calculated from 155A.m^{-2} to 170A.m^{-2} for the curves in figure 5.1.

It is therefore not just an assumption to state that the precursor solution influences the behaviour and character of the prepared electrocatalytic film. Furthermore, the resistance of the anodes to increased polarization is linearly dependent on the precursor's Ru concentration in this particular set of experiments. The XRD results, as an initial measure of the quantity of RuO_2, are shown in figure 5.3. The positions of the Ti and RuO_2 peaks were taken from the Powder Diffraction Files (PDF) of the International Centre for Diffraction Data (ICDD) and indicated in figure 5.3. The fact that Ti contributes significantly to the diffraction pattern already gives an indication of the thickness of the RuO_2 films since the incident X-rays yield information to a depth in the order of microns. The measured intensity of the peak at 28° 2θ was used to categorise the DSA's regarding the quantity of RuO_2 in the films. These peak intensities are plotted in figure 5.4 as a function of the polarization slopes to yield a conclusion that a higher content of RuO_2 in the electrocatalytic film diminishes the extent of electrode polarization at high current densities.

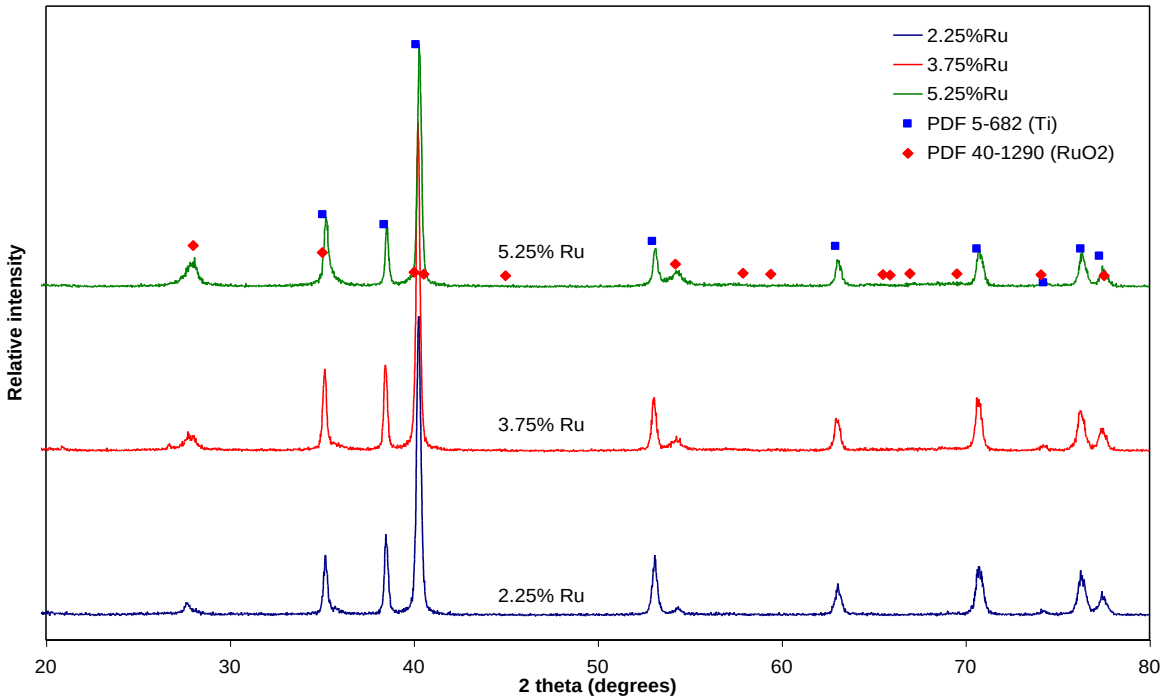

Figure 5.3: X-ray diffraction spectra of RuO_2 electrodes as prepared on sandblasted Ti with mixed Ru : Ti precursor solutions. Total metal concentration was kept constant at 7.5wt/wt%.

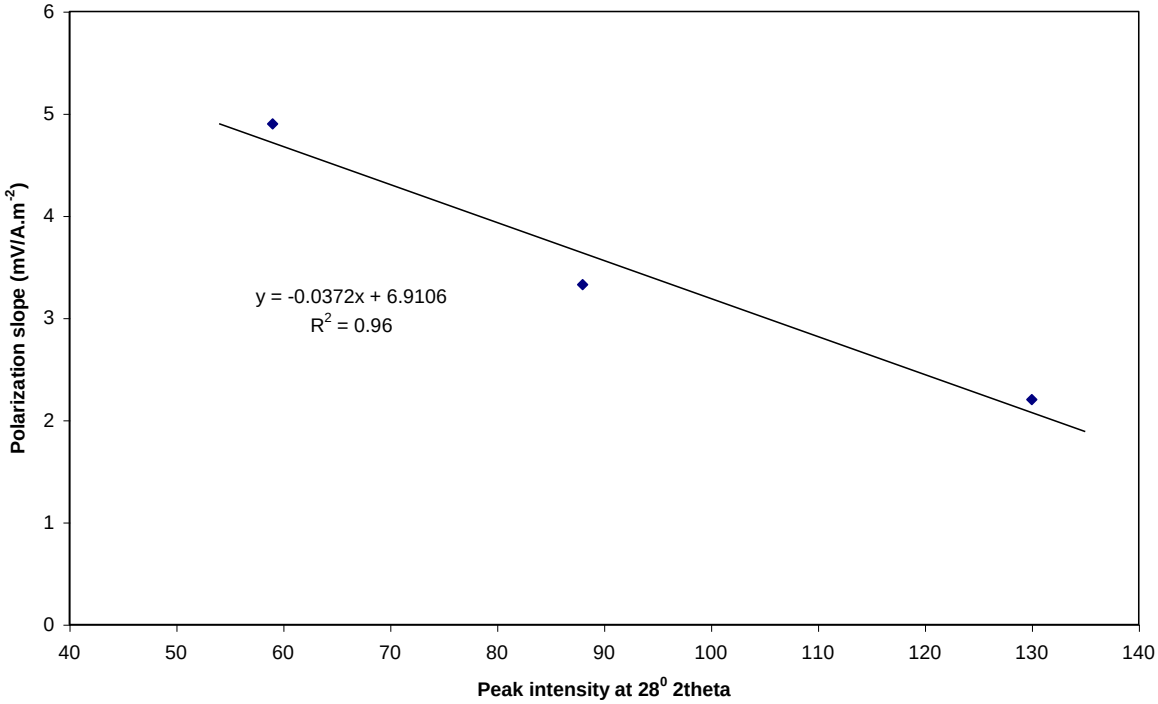

Figure 5.4: Correlation between the rate of electrode polarization and the intensity of the XRD peak of RuO_2 at 28° 2θ. DSA samples were prepared from mixed Ru : Ti precursor solutions.

The XRD spectra of DSA's as prepared with single component Ru precursor solutions are combined in figure 5.5. The PDF's for Ti, RuO_2 and TiO_2 are again included in the graph to illustrate, *via* the 28° 2θ peak, the increased concentration of RuO_2 on the Ti substrate as the Ru concentration in the solution is increased. Note the absence of peaks for TiO_2 in the measured spectra. The same holds for the films that were prepared with the mixed precursors in figure 5.3. Broadening of the 28° 2θ peaks in figure 5.5 however suggests that TiO_2 crystals has indeed formed due to the fact that the highest reflection for rutile TiO_2 occurs at 27.4° 2θ. Broadening of the mentioned peak is absent in the mixed precursor-films. This implies that even less TiO_2 is present in the latter films or that the TiO_2 is amorphous. Whatever the case, it is expected that significant amounts of TiO_2 should have formed during annealing of the $TiCl_3$ containing precursor. It is therefore not yet concluded from the XRD results that the oxides of Ru and Ti are not in a binary mixed form in films from both the single component and mixed component precursors.

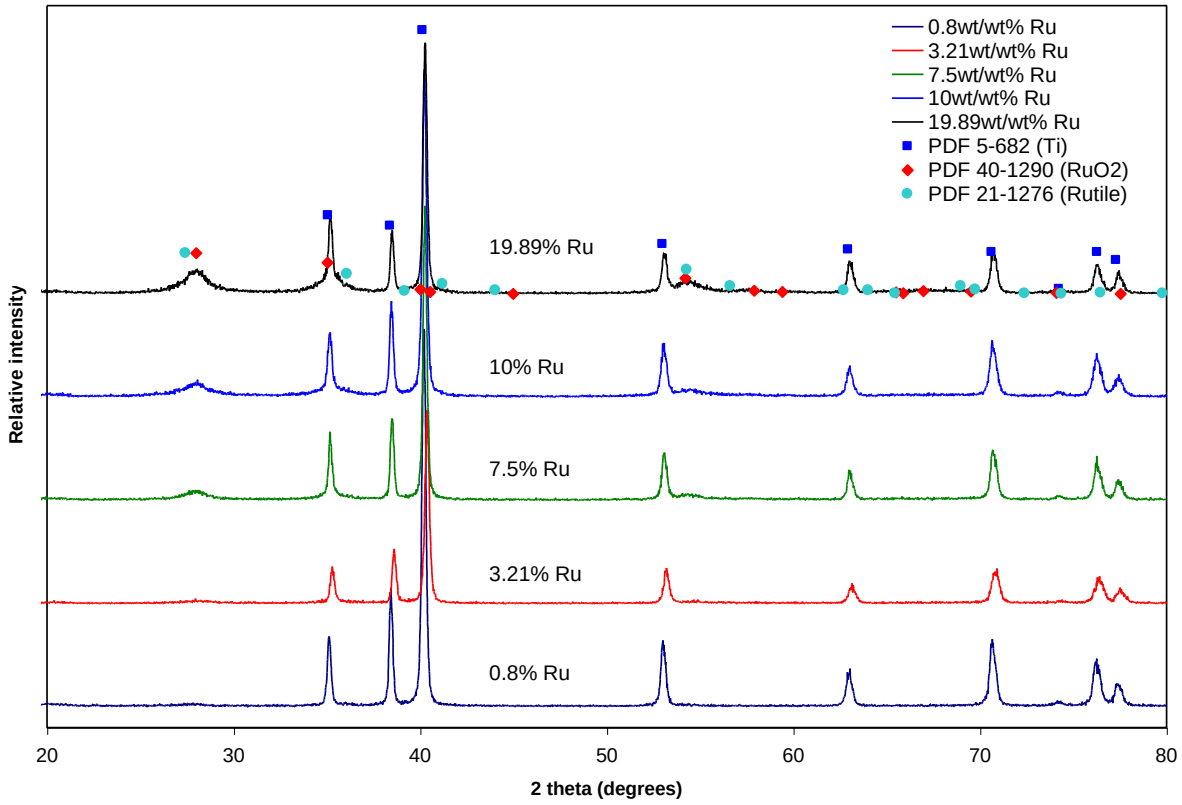

Figure 5.5: X-ray diffraction spectra of RuO_2 electrodes as prepared on sandblasted Ti with different Ru concentrations in single component aqueous $RuCl_3$.

As was the case for the electrocatalytic films from mixed Ru/Ti precursors, the electrode polarization at 100.5A.m^{-2} is also practically independent of the Ru concentration in the single precursor solution (all potentials are within 8mV). The values are listed in table 5.2. It is furthermore also regarded as equivalent to the values reported in table 5.1 for the mixed precursor-DSA's.

Ru in precursor (wt/wt%)	E *vs.* Ag/AgCl at 100.5A.m^{-2} (V)		Average E *vs.* Ag/AgCl at 100.5A.m^{-2} (V)
0.8	1.118	1.118	1.118
3.21	1.116	1.118	1.117
7.5	1.114	-	1.114
10	1.116	1.119	1.118
19.89	1.122	1.122	1.122

Table 5.2: Effect of precursor concentration on electrode polarization at 100.5A.m^{-2}.

A first assessment of the polarization curves for the DSA's, as prepared from the different precursors, showed an unexpected and peculiar trend. As a result, all the electroplating experiments, with the exception of the 7.5wt/wt% precursor DSA, were done in duplicate. The polarization curves during MnO_2 plating for one of the samples illustrate the repeatability in figure 5.6. The slopes in the interval from 155A.m^{-2} to 170A.m^{-2} are plotted in figure 5.7 for all the samples with the actual values given in table 5.3.

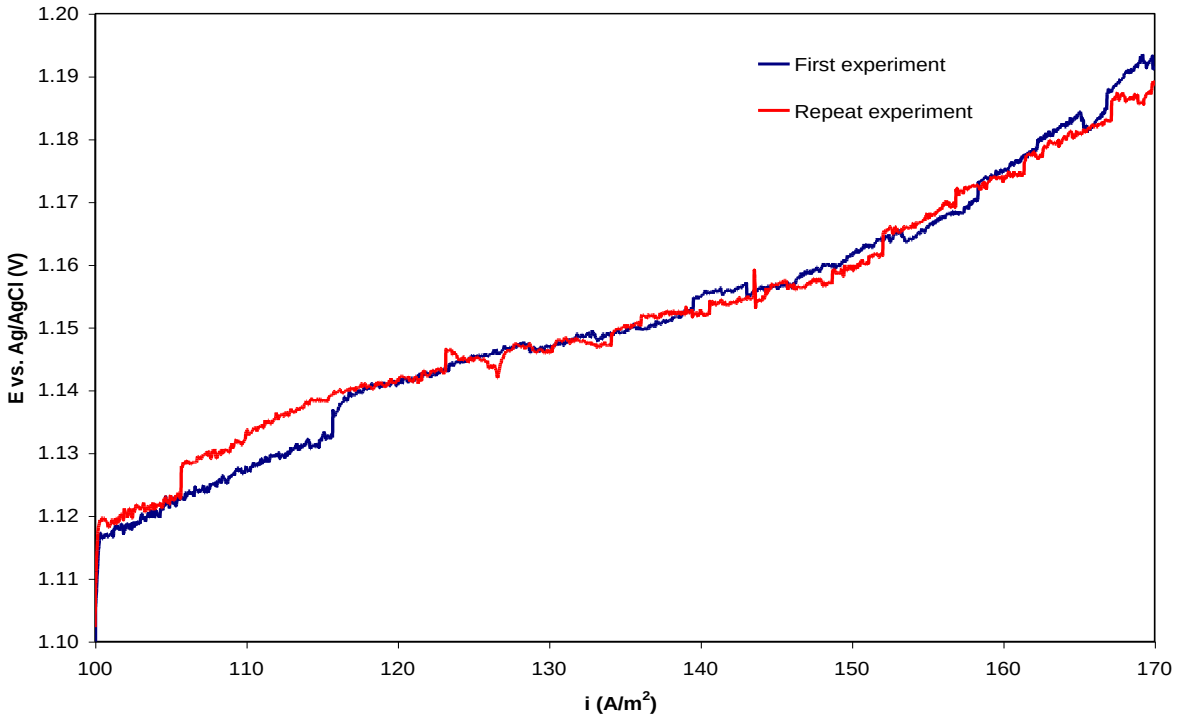

Figure 5.6: Duplicate polarization curves for MnO_2 electroplating on electrodes that were prepared from a 10wt/wt% Ru concentration precursor solution.

Ru in precursor (wt/wt%)	Polarization slope (mV/A.m^{-2})		Average slope (mV/A.m^{-2})
0.8	1.67 ± 0.01	1.59 ± 0.02	1.63 ± 0.03
3.21	1.80 ± 0.01	1.885 ± 0.008	1.84 ± 0.01
7.5	1.65 ± 0.01	-	1.65 ± 0.01
10	1.80 ± 0.03	1.361 ± 0.008	1.58 ± 0.04
19.89	1.03 ± 0.03	1.06 ± 0.02	1.05 ± 0.04

Table 5.3: Summary of electroplating experiments on DSA's that were prepared from single component Ru precursor solutions.

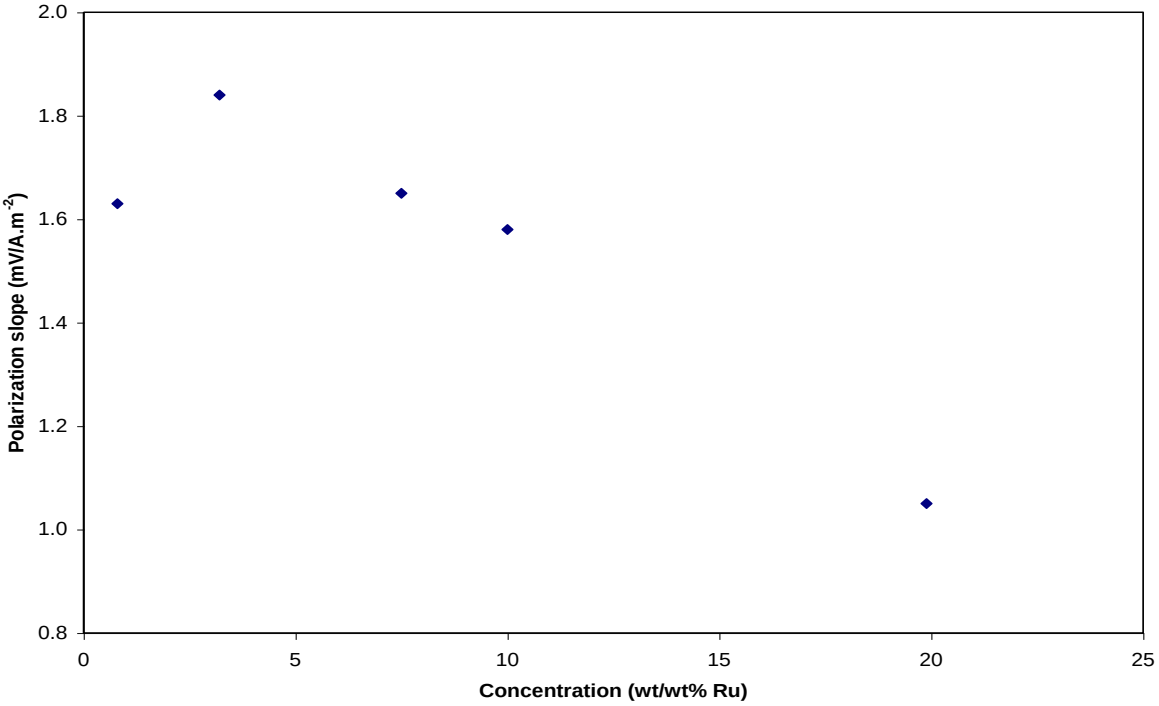

Figure 5.7: Polarization slopes as a function of Ru concentration in the single component precursor solutions.

It is clear that the relation between polarization slope and Ru concentration is not a simple linear trend as was initially discovered for the mixed Ru:Ti precursor DSA's. Nonetheless, a linear relation does exist for Ru concentrations in the mixed precursor ranging from 2.25wt/wt% to 5.25wt/wt% (refer to figure 5.2), but not necessarily for values outside this range. Deviation from linearity for the parameters under discussion only became distinct due to the fact that the Ru concentrations in figure 5.7 extended over a much wider range. However, if the first data point (0.8wt/wt%; 1.63mV/A.m^{-2}) in figure 5.7 is omitted, a linear trend line could be fitted through the remaining points as in figure 5.8 with an R^2 correlation coefficient of 0.9926. In this specific case there is an apparent improvement in electrocatalytic behaviour and/or polarization resistance with a decrease of Ru in the precursor from 3.21wt/wt% to 0.8wt/wt%. No reference was found in the literature that could offer an explanation as to why there exists a decrease in the polarization slope as a result of this decrease in Ru in the precursor solution. It is noteworthy to indicate that the slope for the 0.8wt/wt% precursor DSA equals that of the 7.5wt/wt% precursor DSA. The 28° 2θ peak in figure 5.5 clearly stands out for the film prepared with the 7.5wt/wt% Ru solution, but was not measurable for the sample that was prepared with the low concentration solution. Thus,

the two surfaces definitely differ from one another, but their electrochemical behaviour towards reaction 1.1 is the same. An explanation for this phenomenon can be presented as follows. A low concentration precursor (0.8wt/wt% Ru) results in the formation of a much more intimate mixture between the RuO_2, TiO_2 and Ti substrate. For the higher concentration precursor (3.21wt/wt% Ru), a thicker film forms during annealing, but binding between the substrate and RuO_2 particles is not as perfect as is the case for the low concentration. For still higher precursor concentrations (7.5wt/wt% to 19.89wt/wt%) the deposit becomes progressively thicker during annealing and the electrodes' electrocatalytic properties and resistance to passivation improves considerably. A linear behaviour is envisaged for this as was deduced from figures 5.2 and 5.8.

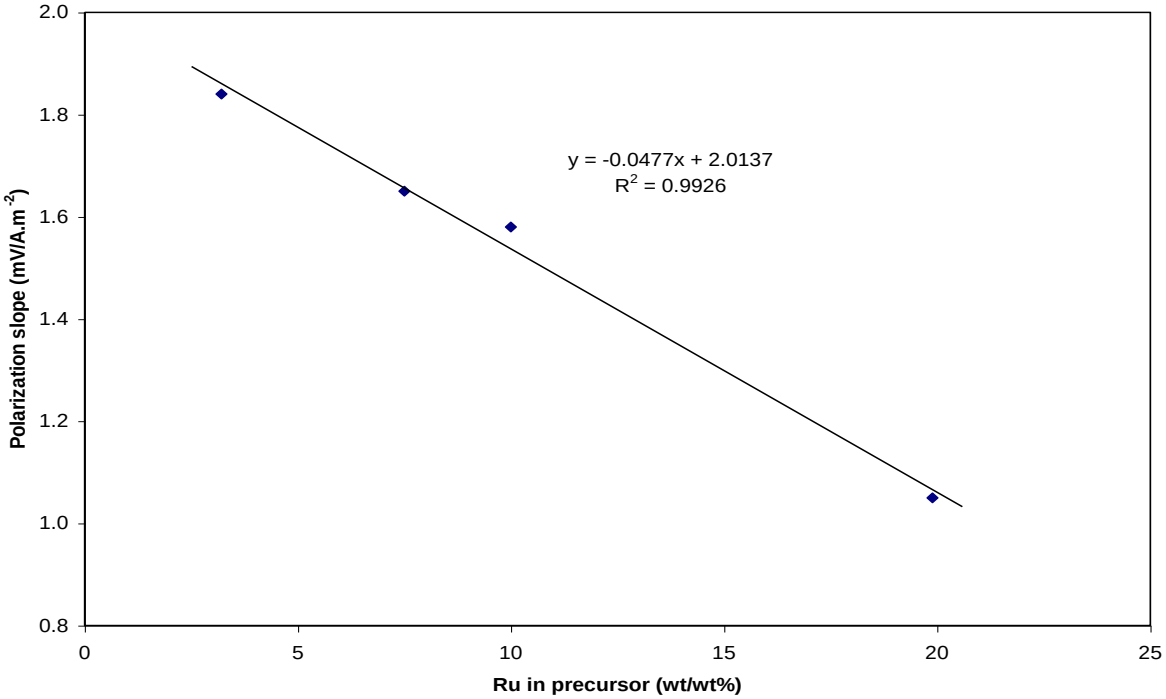

Figure 5.8: Duplicate of figure 5.7 with the first point (0.8wt/wt%) omitted.

If the proposed explanation can be accepted, the DSA sample from the 3.21wt/wt% Ru precursor can be regarded as being at the boundary where the concentration was not sufficient to form enough RuO_2 that would yield electrocatalytic behaviour to transcend that of the intimate association that results from a very low Ru concentration in solution. A salient point that deserves definite attention is a comparison between the values of the polarization slopes of the DSA's from the mixed precursors and that of the single component precursor solutions. Polarization slopes for the latter DSA's are lower than the former for all applicable

Ru concentrations. This fact emphasises the above theory, since it can be appreciated that the $TiCl_3$ in solution could be a source of hindrance to the formation of a RuO_2 film in intimate association with the substrate. Regardless of the source of variation between the DSA's, it is clear that a single component precursor solution will outrank a mixed solution for the purpose of thermal DSA preparation for MnO_2 electroplating, both in terms of preparation cost and performance of the anode under said operating conditions.

5.1.2 Crystallographic interpretation of electrocatalytic films.

The ensuing study on the effect of annealing temperature on the lattice parameters of tetragonal RuO_2 was prompted by the finding that the unit cell dimensions of IrO_2 and RuO_2 are dependent on the calcinating temperature [82, 123]. This variation in the unit cell dimension with annealing temperature has its origin in residual chloride that is present in the RuO_2 structure if an aqueous $RuCl_3$ solution is used as precursor. Other defects have also been reported to be present in oxides at low firing temperatures [59]. In the current study, focus was once again on diffraction intensities of the (1 1 0) crystallographic orientation of RuO_2 at 28° 2θ for the purpose of evaluating the effect of annealing temperature on the RuO_2 lattice parameters. The reason for this is due to the fact that the (1 1 0) reflection is the most prominent and it experiences the least interference from diffraction peaks originating from Ti and TiO_2.

The temperature effect on DSA's prepared with 3.21wt/wt% and 10wt/wt% Ru precursors can be deduced from figures 5.9 and 5.10. No significant peak is observed between 27° 2θ and 28° 2θ for both these DSA's at either 400°C or 500°C, but peaks are present at 27.4° 2θ and 28.0° 2θ for the 600°C samples. This shows that 600°C was sufficient to ensure adherence of enough RuO_2 to make the 28.0° 2θ peak measurable, while the 27.4° 2θ peak reveals that 600°C causes either substrate oxidation or a mixed oxide of RuO_2 and TiO_2 was formed. The (1 1 0), (1 0 1) and (2 1 1) reflections at 28.0° 2θ, 35.0° 2θ and 54.2° 2θ for RuO_2 and at 27.4° 2θ, 36.1° 2θ and 54.3° 2θ for TiO_2 were found to coincide with the PDF Bragg angles in figures 5.9 and 5.10 for the 600°C samples. It can therefore be assumed that the lattice parameters are comparable to that of bulk RuO_2, i.e. the values reported in the PDF's, and that lattice distortion is not present. As a result, all the applicable Bragg angles

smaller than 80° 2θ in the PDF's were used to calculate values for the tetragonal lattice parameters ("a" and "c") in RuO_2 and TiO_2 (figures 5.9 & 5.10) with equation 5.2.

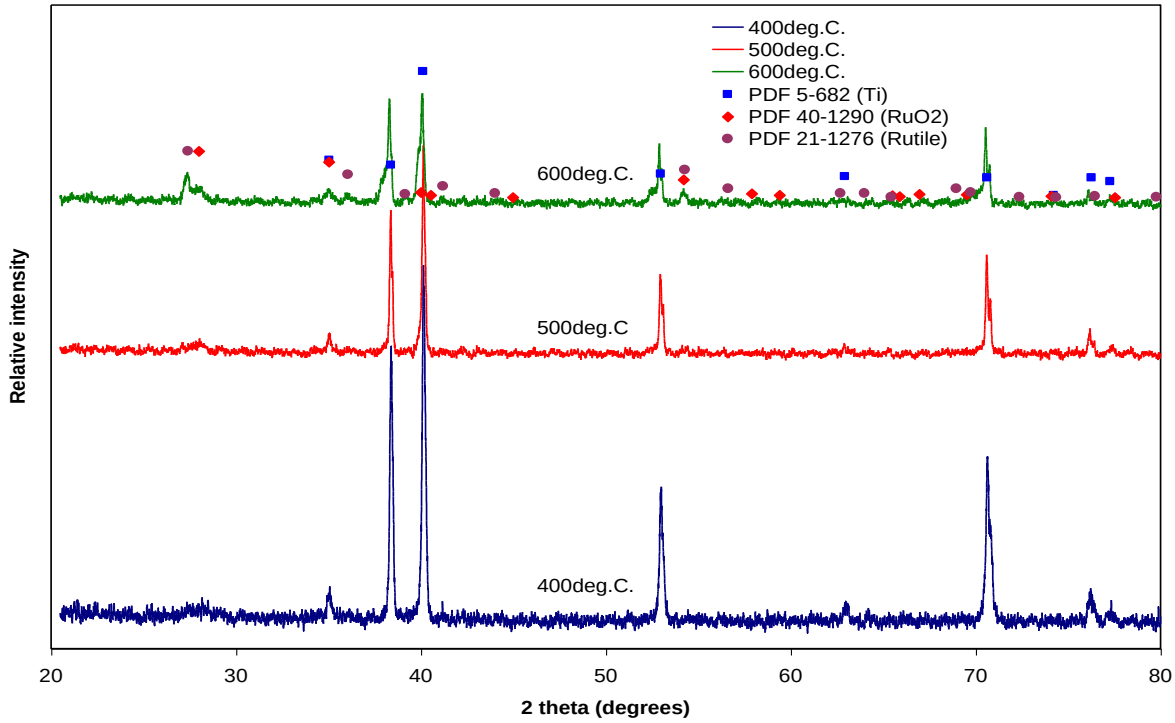

Figure 5.9: X-ray diffraction spectra of thermally prepared DSA's at different temperatures using a 3.21wt/wt% Ru precursor solution.

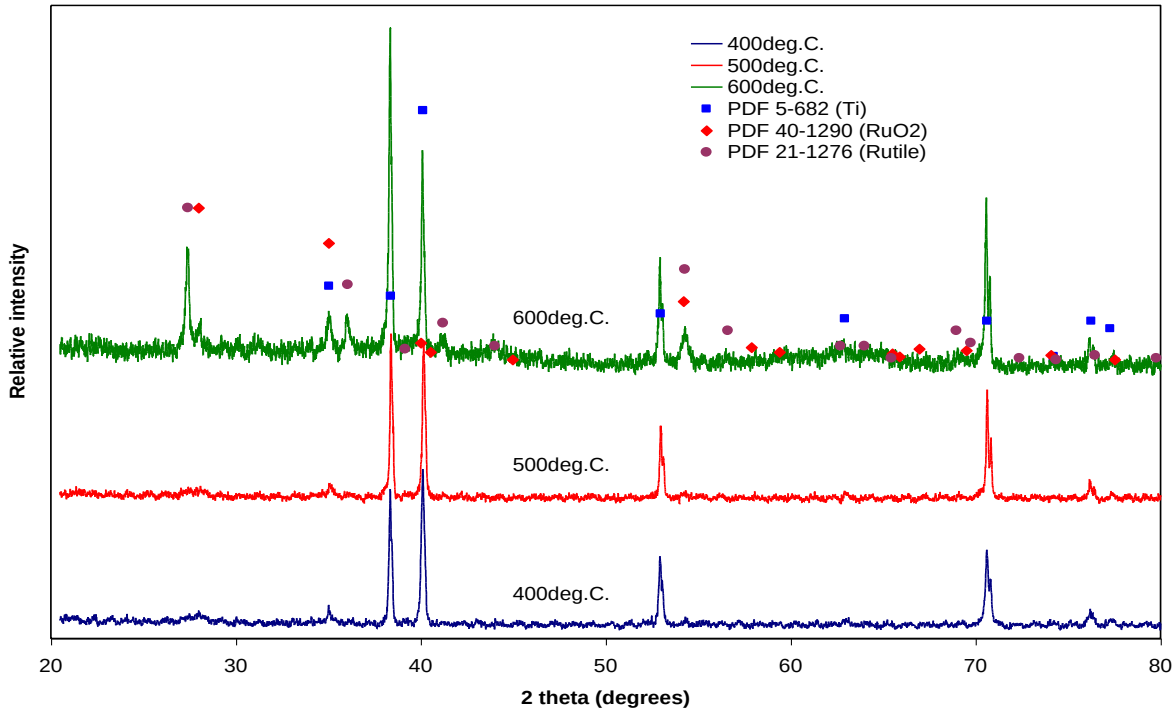

Figure 5.10: X-ray diffraction spectra of thermally prepared DSA's at different temperatures using a 10wt/wt% Ru precursor solution.

Equation 5.2 was derived by combining the Bragg relation (equation 3.10) with the equation that describes interplanar spacing as a function of the unit cell edges (equation 5.1) for a tetragonal system.

$$n\lambda = 2d\sin\theta \quad \text{.....(3.10)}$$

$$\frac{1}{d_{hkl}^2} = \frac{h^2 + k^2}{a^2} + \frac{l^2}{c^2} \quad \text{.....(5.1)}$$

$$\sin^2\theta = \frac{\lambda^2}{4a^2}(h^2 + k^2) + \frac{\lambda^2}{4c^2}(l^2) \quad \text{.....(5.2)}$$

The $\frac{\lambda^2}{4a^2}$ constant was calculated using all the 2θ values were the "l" Miller index was absent as illustrated in tables 5.3 and 5.4 for RuO_2 and TiO_2 respectively.

d (Å)	2θ (degrees)	$\sin^2\theta$	h k l	$h^2 + k^2$	l^2	$\lambda^2/4a^2$
3.1826	28.00	0.0585	1 1 0	2	0	0.02925
2.5584	35.03	0.0906	1 0 1	1	1	-
2.2502	40.02	0.1171	2 0 0	4	0	0.02928
2.2225	40.54	0.1200	1 1 1	2	1	-
2.0128	44.98	0.1463	2 1 0	5	0	0.02926
1.6898	54.22	0.2077	2 1 1	5	1	-
1.5907	57.90	0.2343	2 2 0	8	0	0.02929
1.5539	59.41	0.2456	0 0 2	0	4	-
1.4232	65.51	0.2927	3 1 0	10	0	0.02927
1.4158	65.89	0.2958	2 2 1	8	1	-
					Average	0.02927

Table 5.3: Calculation of the "a" lattice parameter for RuO_2 using the Bragg reflections where l = 0.

d (Å)	2θ (degrees)	$\sin^2\theta$	h k l	$h^2 + k^2$	l^2	$\lambda^2/4a^2$
3.2482	27.43	0.0563	1 1 0	2	0	0.02815
2.4869	36.07	0.0959	1 0 1	1	1	-
2.2973	39.17	0.1124	2 0 0	4	0	0.02810
2.1880	41.21	0.1239	1 1 1	2	1	-
2.0542	44.03	0.1406	2 1 0	5	0	0.02812
1.6877	54.29	0.2082	2 1 1	5	1	-
1.6235	56.63	0.2251	2 2 0	8	0	0.02814
1.4798	62.71	0.2708	0 0 2	0	4	-
1.4530	64.00	0.2808	3 1 0	10	0	0.02808
1.4242	65.46	0.2923	2 2 1	8	1	-
					Average	0.02812

Table 5.4: Calculation of the "a" lattice parameter for TiO_2 using the Bragg reflections where l = 0.

An average of the five $\frac{\lambda^2}{4a^2}$ values was used in tables 5.5 and 5.6 to calculate the $\frac{\lambda^2}{4c^2}$ constant at the relevant Miller indices. The averages of these constants were used to calculate the "a" and "c" lattice parameters. Unit cell measurements of a = 4.504Å and c = 3.108Å for RuO_2 are comparable with the lattice dimensions of TiO_2. The TiO_2 unit cell has a dimension of a = 4.595Å and c = 2.963Å and is slightly more distorted from a cubic nature than RuO_2. Atanasoska *et. al*. [102] used low energy electron diffraction (LEED) to determine the unit cell dimensions of RuO_2, as prepared by a method of chemical vapour transport, to be a = 4.36Å and c = 3.04Å. These values differ somewhat from the results in this study, but Huang *et. al*. [124] also used X-ray diffraction to calculate the size of a unit mesh of RuO_2 as a = 4.49Å and c = 3.11Å. The lattter values are in good agreement with the current results.

d (Å)	2θ (deg)	$\sin^2\theta$	h k l	$h^2 + k^2$	l^2	$\lambda^2/4a^2$	$\lambda^2/4c^2$
3.1826	28.00	0.0585	1 1 0	2	0	0.02927	-
2.5584	35.03	0.0906	1 0 1	1	1	0.02927	0.06133
2.2502	40.02	0.1171	2 0 0	4	0	0.02927	-
2.2225	40.54	0.1200	1 1 1	2	1	0.02927	0.06146
2.0128	44.98	0.1463	2 1 0	5	0	0.02927	-
1.6898	54.22	0.2077	2 1 1	5	1	0.02927	0.06135
1.5907	57.90	0.2343	2 2 0	8	0	0.02927	-
1.5539	59.41	0.2456	0 0 2	0	4	0.02927	0.06164
1.4232	65.51	0.2927	3 1 0	10	0	0.02927	-
1.4158	65.89	0.2958	2 2 1	8	1	0.02927	0.06164
						Average	0.06144

Table 5.5: Calculation of the "c" lattice parameter for RuO_2 using the Bragg reflections where $l \neq 0$ and using an average value of $\frac{\lambda^2}{4a^2} = 0.02927$.

d (Å)	2θ (deg)	$\sin^2\theta$	h k l	$h^2 + k^2$	l^2	$\lambda^2/4a^2$	$\lambda^2/4c^2$
3.2482	27.43	0.0563	1 1 0	2	0	0.02812	-
2.4869	36.07	0.0959	1 0 1	1	1	0.02812	0.06778
2.2973	39.17	0.1124	2 0 0	4	0	0.02812	-
2.1880	41.21	0.1239	1 1 1	2	1	0.02812	0.06766
2.0542	44.03	0.1406	2 1 0	5	0	0.02812	-
1.6877	54.29	0.2082	2 1 1	5	1	0.02812	0.06760
1.6235	56.63	0.2251	2 2 0	8	0	0.02812	-
1.4798	62.71	0.2708	0 0 2	0	4	0.02812	0.06770
1.4530	64.00	0.2808	3 1 0	10	0	0.02812	-
1.4242	65.46	0.2923	2 2 1	8	1	0.02812	0.06734
						Average	0.06762

Table 5.6: Calculation of the "c" lattice parameter for TiO_2 using the Bragg reflections where $l \neq 0$ and using an average value of $\frac{\lambda^2}{4a^2} = 0.02812$.

It is confirmed in figure 5.11 that the 19.89wt/wt% Ru precursor produced enough RuO_2 in the film even at 400°C for the (1 1 0) peak to exist in the spectrum as is expected. The 2θ value of this peak was used to calculate the "a" lattice parameter for each film's spectrum in figure 5.11. The results are summarised in table 5.7. Although the significance of the results in table 5.7 is difficult to ascertain, a contraction of the "a" parameter with an increase in annealing temperature is evident. A shoulder on the left-hand side of the (1 1 0) reflection of the 600°C sample in figure 5.11 again attests of substrate oxidation or formation of a mixed oxide. Except for an apparent completely absent (1 1 0) reflection of RuO_2 for the 600°C specimen in figure 5.12, there is no ascertainable difference between the spectra in figures 5.10 and 5.12. This means that no real measurable crystallographic differences exist between a sample that was annealed in the presence of an O_2 atmosphere and an anode that was calcinated in normal atmosphere.

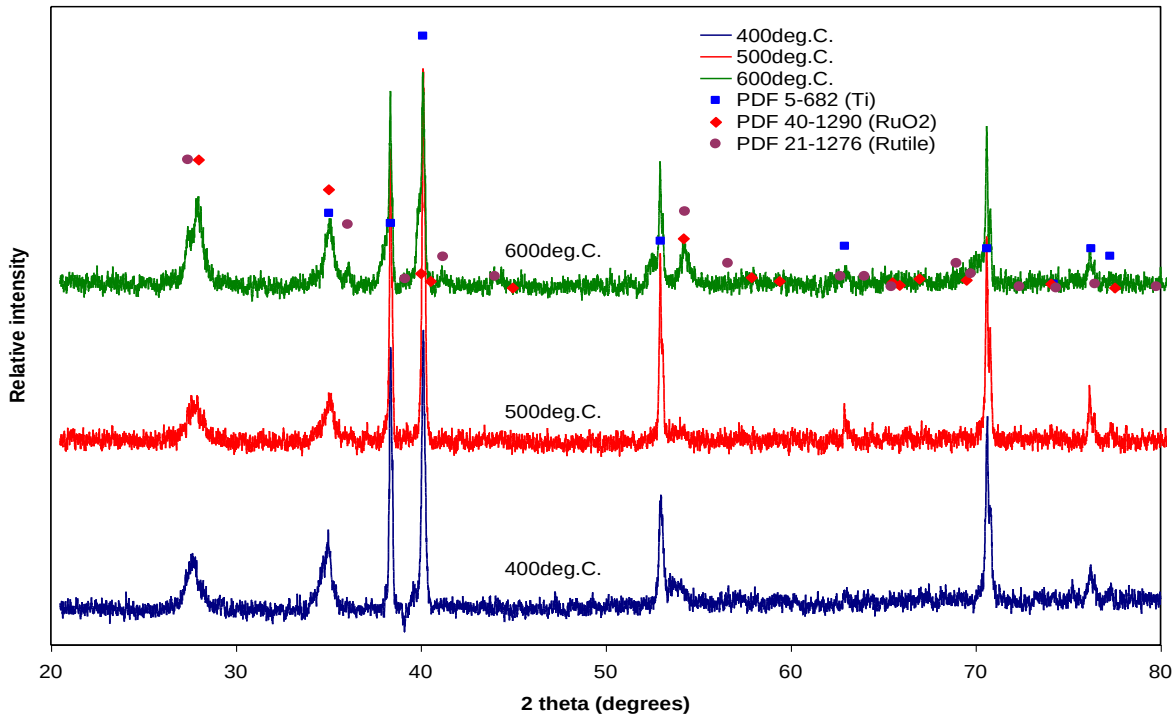

Figure 5.11: X-ray diffraction spectra of thermally prepared DSA's at different temperatures using a 19.89wt/wt% Ru precursor solution.

Annealing temp. (°C)	2θ at max intensity between 27.6° and 29°	$\sin^2\theta$	$h^2 + k^2$	a (Å)
400	27.658	0.05713	2	4.556
500	27.908	0.05815	2	4.516
600	27.994	0.05850	2	4.502

Table 5.7: Experimental data taken from figure 5.11 to determine the effect of annealing temperature on one parameter of the unit cell dimensions of RuO_2.

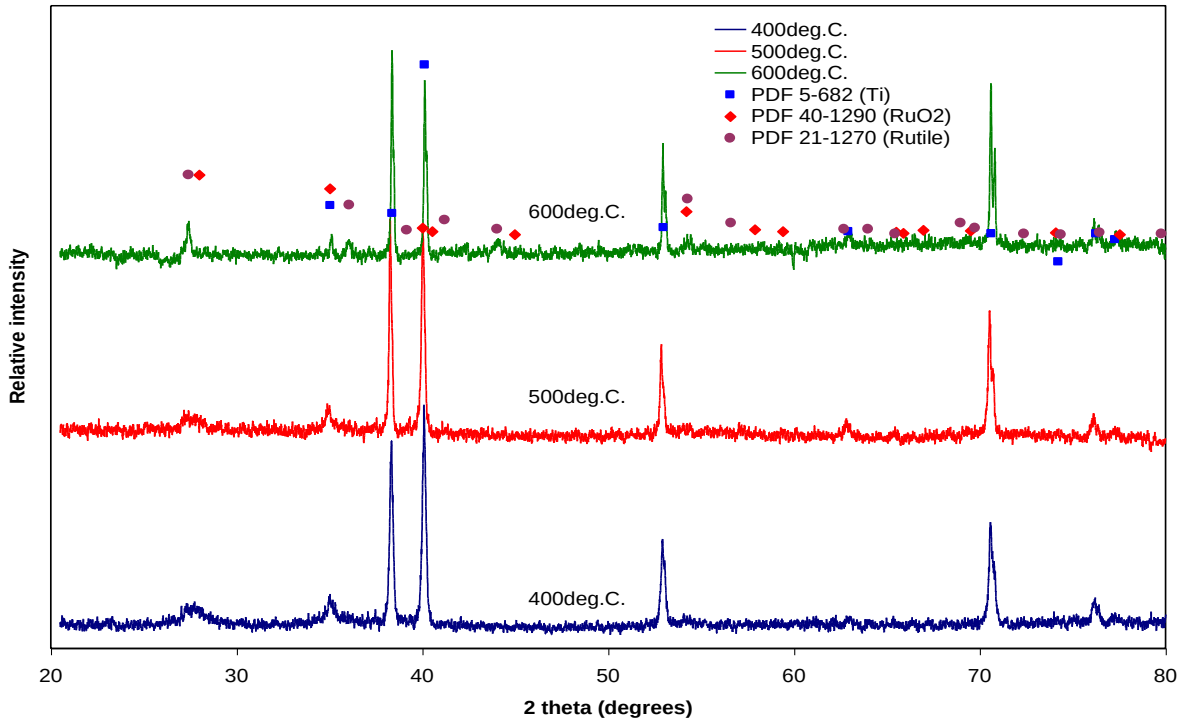

Figure 5.12: X-ray diffraction spectra of thermally prepared DSA's at different temperatures using a 10wt/wt% Ru precursor solution in an O_2 atmosphere.

5.1.3 Structure of the electroplated MnO_2 layers.

Diffraction spectra of the electroplated MnO_2 layers on the various specimens were measured to establish correlations between EMD on the experimental electrodes and commercially produced EMD powder. Figure 5.13 illustrates that all the relevant d-spacings that originate from pyrolusite and ramsdellite phases are present in the electroplated EMD on the DSA's that were thermally prepared from single component precursor solutions. This is confirmed by the spectrum of a commercial powdered EMD sample. Differences in peak widths and relative peak intensities are evident from figure 5.13 and this has certain implications regarding film structure. The main concern however is to illustrate that the plated EMD is in all cases polycrystalline and that all relevant Miller indices exist in the growth direction of the MnO_2 film. The same conclusions can be drawn from figure 5.14 for EMD as plated onto DSA's that were prepared with Ru/Ti mixed precursor solutions. Note that the 3 spectra in figure 5.14 are very much alike.

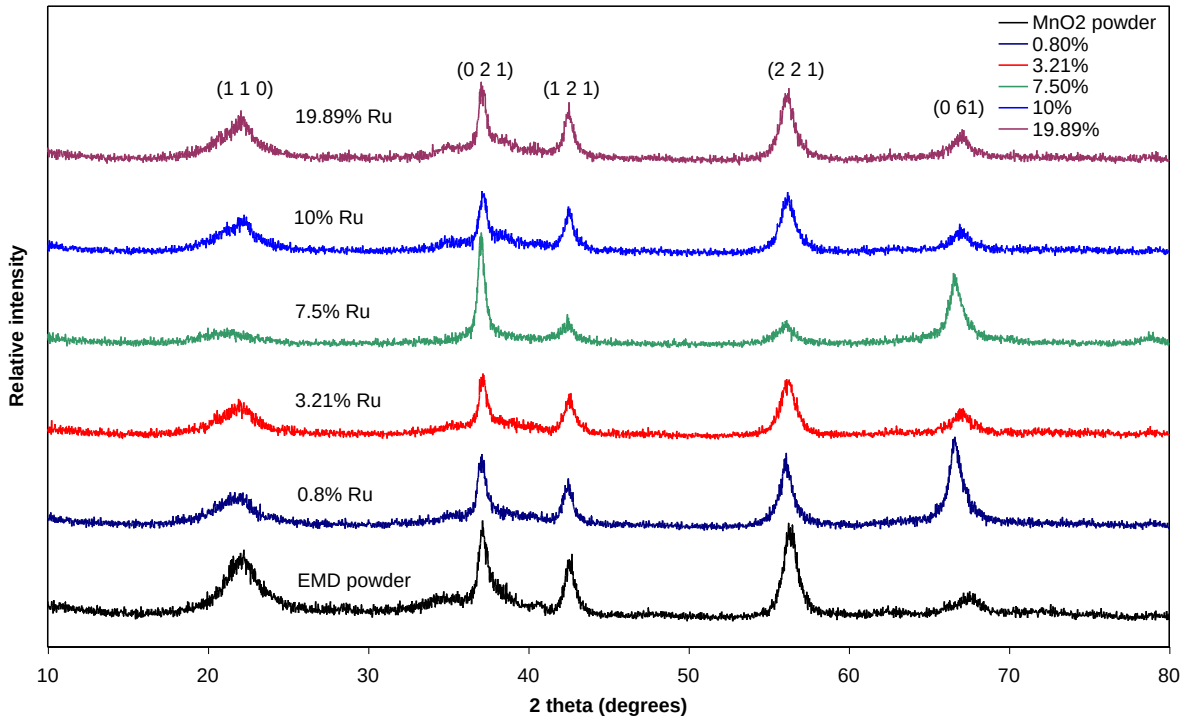

Figure 5.13: X-ray diffraction spectra of electroplated MnO_2 on DSA's that were prepared with different Ru concentrations in single component precursor solutions.

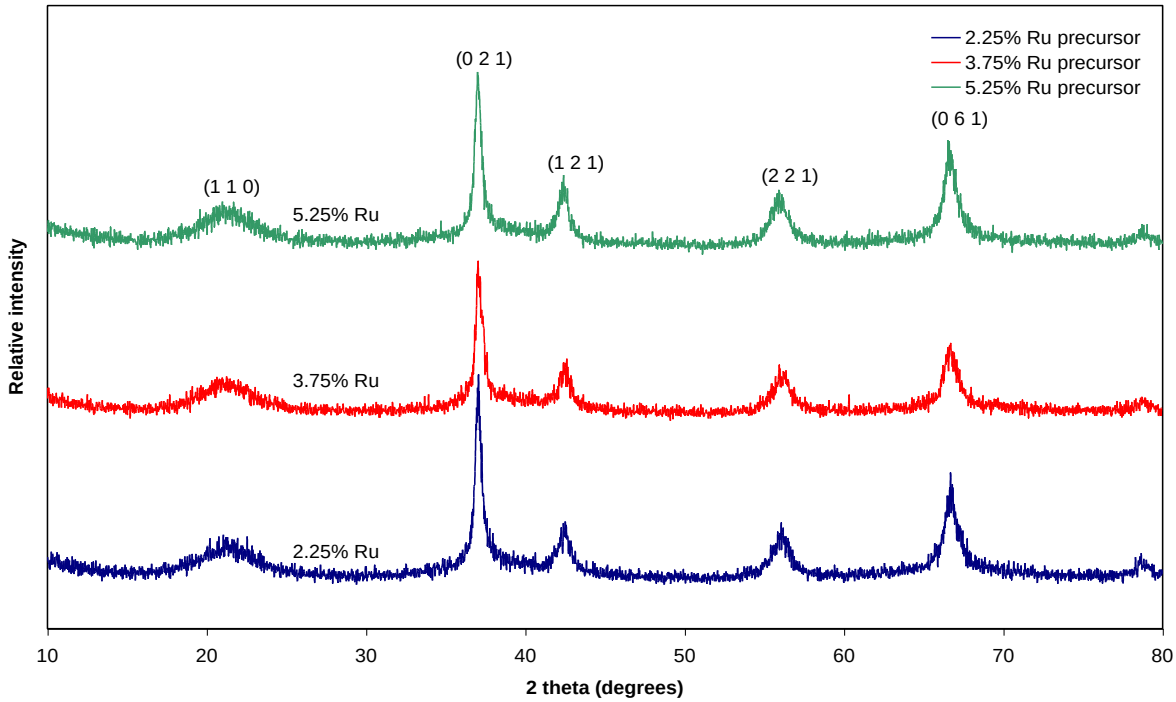

Figure 5.14: XRD spectra of electroplated MnO_2 on DSA's that were prepared with different Ru concentrations in mixed Ti/Ru precursor solutions (7.5wt/wt% total metals).

5.2 Ti/ $RuO_x.nH_2O$ electrocatalysts for MnO_2 electroplating.

5.2.1 Cyclic voltammetric growth.

As a salient point, it can be noted in figure 5.15 that the voltammetric currents are dependent on the cycle number of the voltammograms. The relation between peak current density of the cathodic peaks centered between 600mV and 900mV and the cycle number is shown in figure 5.16 to be of a linear nature. It is clear that two slopes are present. Linear regression through the first 5 cycles gives a slope of 159 ± 9mA.m^{-2}/cycle while from cycle 7 onwards a value of 357.9 ± 0.5mA.m^{-2}/cycle is calculated. Although not as prominent as the latter, the same feature can be deduced for the peak current - to - cycle number dependency of the anodic peaks between 300mV and 600mV, as well as for peaks centered between 0mV and 300mV in the cathodic scans. The applicable values are 336 ± 20mA.m^{-2}/cycle and 455 ± 2mA.m^{-2}/cycle for the first and second slopes respectively for the anodic peaks between 300mV and 600mV. It is also true that the first slope is smaller than the second slope for the cathodic peaks between 0mV and 300mV. Last mentioned slopes are 339.1 ± 0.8mA.m^{-2}/cycle and 427 ± 1mA.m^{-2}/cycle. Even without any quantitative

information, it is clear that the rate of increase in reaction rate between successive cycles is significantly smaller for the first 5 cycles than for the final 79 cycles. This can be a suggestion that the substrate retards the growth of the electrocatalyst for the first 5 cycles, after which the rate of increase in the reaction rate (increasing peak current density with cycle number) is facilitated by a very thin deposited $RuO_x.nH_2O$ layer. The initially grown layer therefore acts as an electrocatalyst for further growth of $RuO_x.nH_2O$.

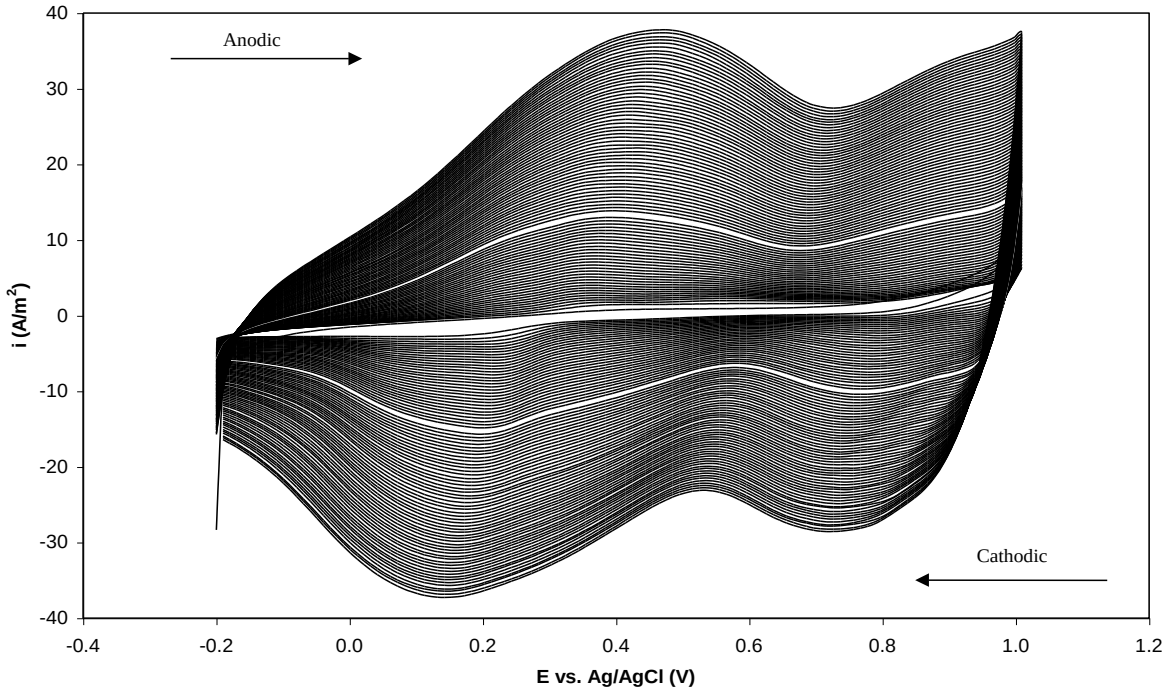

Figure 5.15: 85 Cyclic voltammograms recorded during the growth of $RuO_x.nH_2O$ on Ti metal. Cyclic voltammetry was done in a solution of 5mM $RuCl_3.3H_2O$, scan rate = $50mV.s^{-1}$.

Another point to note is that the anodic excursion from 800mV to 1V in the very first cycle resulted in significantly more charge transfer than for the same process in the next 10 scans. Figure 5.17 gives confirmatory evidence for this. The most probable reaction taking place in the first scan at these potential values is oxidation of Ti metal that is absent in any other scan. An oxidised substrate could further be the cause for the lower rate of increase in peak current density for the first 5 cycles. Assignment of applicable reactions to the various peaks is described in reference [76]. Starting at the cathodic peak between 0mV and 300mV, it is proposed that Ru is deposited as the metal or an oxy-chloro species. When going in the

anodic direction, last mentioned species is oxidised to form $RuO_x.nH_2O$. Beyond 800mV, Ru is further oxidised to a Ru(VI) species, but is again reduced to $RuO_x.nH_2O$ on the return scan.

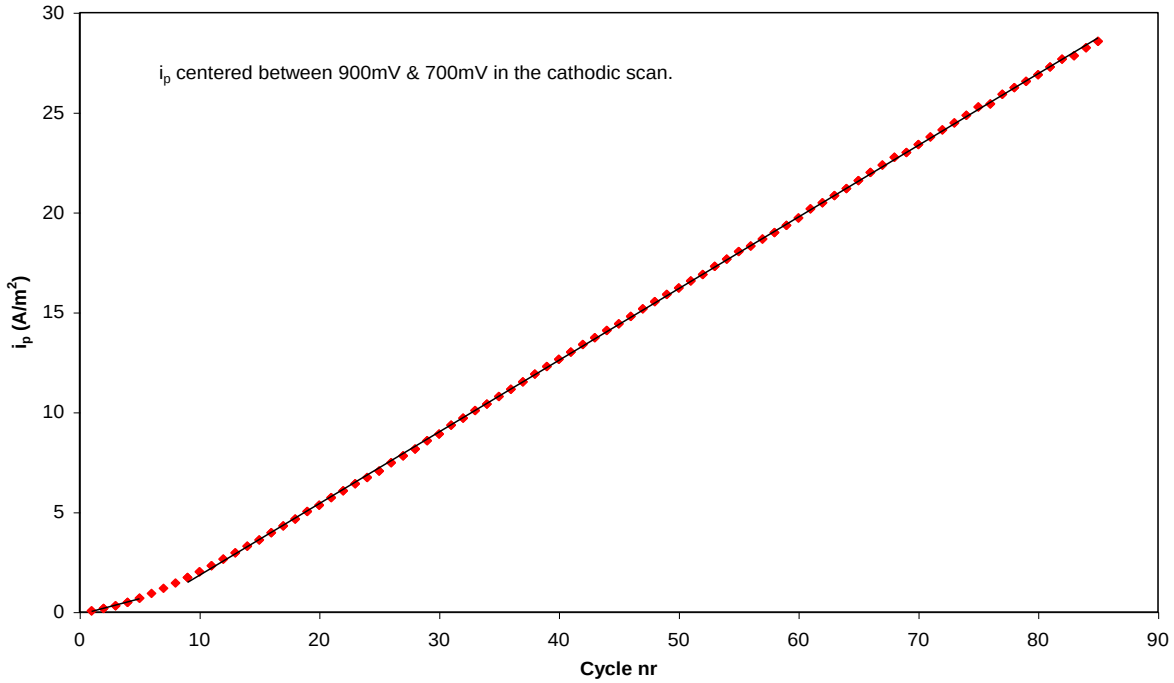

Figure 5.16: Peak current density as a function of cycle number for the peak centered between 700mV and 900mV in the reverse sweep.

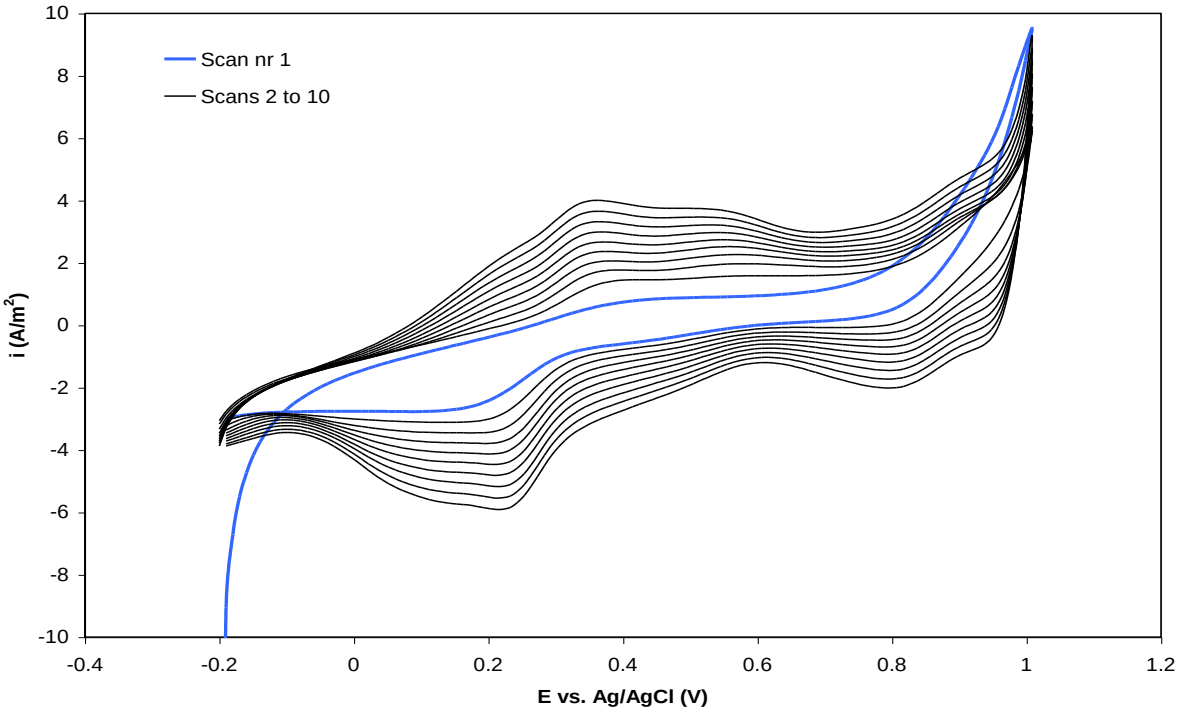

Figure 5.17: First ten cycles of oxide loading, with the first cycle indicative of anodic oxidation of the Ti substrate.

5.2.2 Film structure.

A direct comparison between the diffraction spectra of the annealed samples can be seen in figure 5.18 where the calcination time is also indicated.

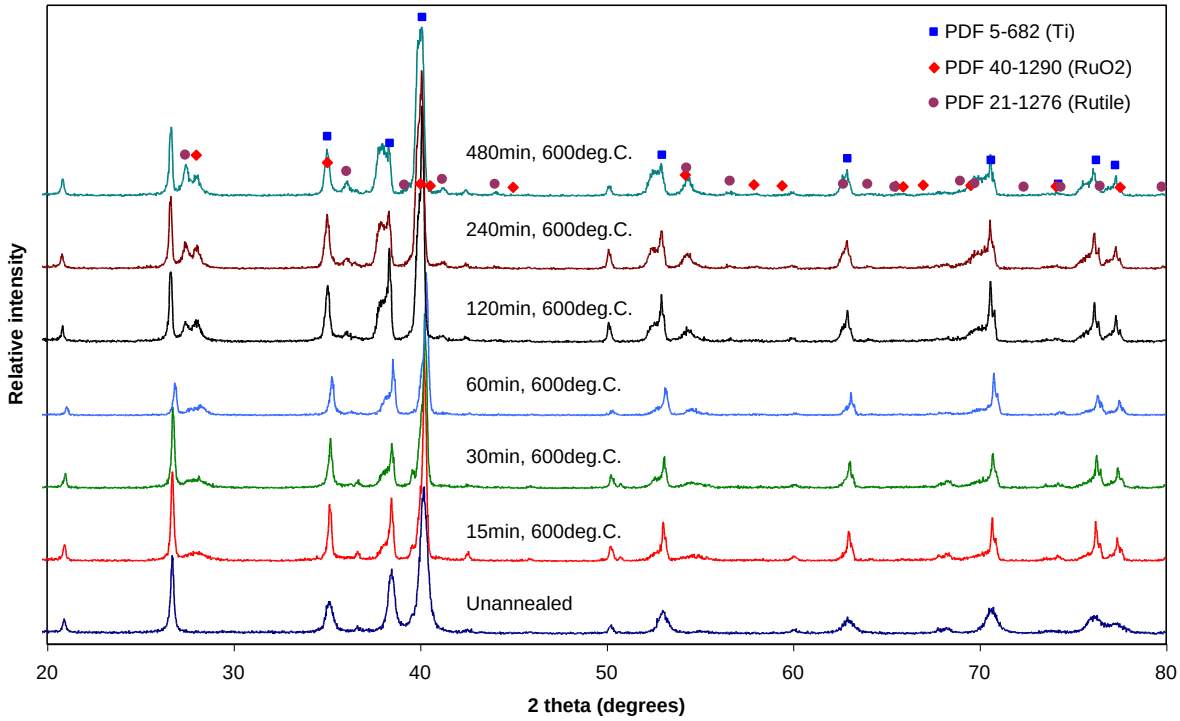

Figure 5.18: XRD spectra of annealed $RuO_x.nH_2O$ layers and one unannealed electrode to show a phase change due to thermal treatment.

The 2θ values for the reflections of Ti, rutile TiO_2 and RuO_2 were again taken from the PDF of the ICDD and are also presented in figure 5.18. A prominent feature in the spectrum of the unannealed sample is the total absence of the strongest reflection for RuO_2 at 28° 2θ, i.e. the reflection from the (1 1 0) plane, but with a high intensity peak situated at 26.7° 2θ. The peak at 28° 2θ originates from Miller indices with an interplanar spacing of 3.18Å whereas the Bragg equation determines a 3.33Å spacing for the peak at 26.7° 2θ. Together with the fact that the 28° 2θ peak appears upon annealing, a hypothesis is proposed that interpret the 3.33Å spacing as an expansion of the lattice in the hkl direction originating from the 3.18Å spacing. This lattice expansion is caused by crystal water in the $RuO_x.nH_2O$ structure of which a fraction is removed upon thermal treatment to yield the 28° 2θ peak associated with RuO_2. The presence of the 26.7° 2θ peak in all the spectra up to an annealing time of 8hr is

indicative of an ever-present 3.33Å spacing in the crystallographic structure of the electrodeposited film. The increase in the intensity of the reflection from the (1 1 0) plane of TiO_2 at 27.4° 2θ is a true reflection of substrate oxidation. A finding from the diffraction spectra that is informative but which will not be discussed in detail here is the effect of annealing time on the ratio of the intensity of the Ti reflection at 53° 2θ and the combined TiO_2/RuO_2 peak intensity at 54.3° 2θ. An amazingly good logarithmic function between the mentioned variables presents itself in figure 5.19.

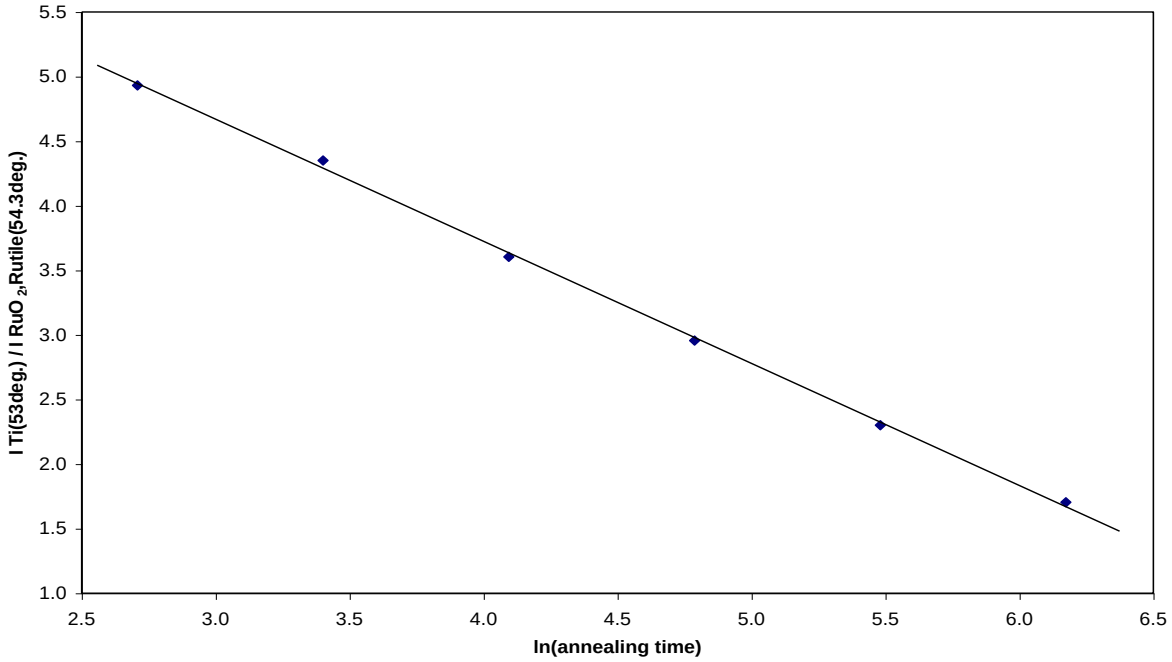

Figure 5.19: Logarithmic relation between an X-ray diffraction parameter and annealing time. XRD intensities were taken from the Ti peak at 53° 2θ and the overlapping RuO_2 and TiO_2 reflections at 54.3° 2θ.

5.2.3 Polarization slopes and the MnO_2 structure.

The purpose of the electrolysis experiments was to categorise the DSA samples on a calcination time scale. The polarization results are presented in figure 5.20. All potential values in figure 5.20 are again reported against Ag/AgCl as it was measured, with no correction for the liquid junction potential or any normalisation to the standard hydrogen electrode. Although figure 5.20 yields a direct comparison between electrodes, the respective polarization rates were calculated from $155A.m^{-2}$ to $170A.m^{-2}$ and reported in figure 5.21 as a function of annealing time. The actual data for figure 5.21 is summarised in table 5.8.

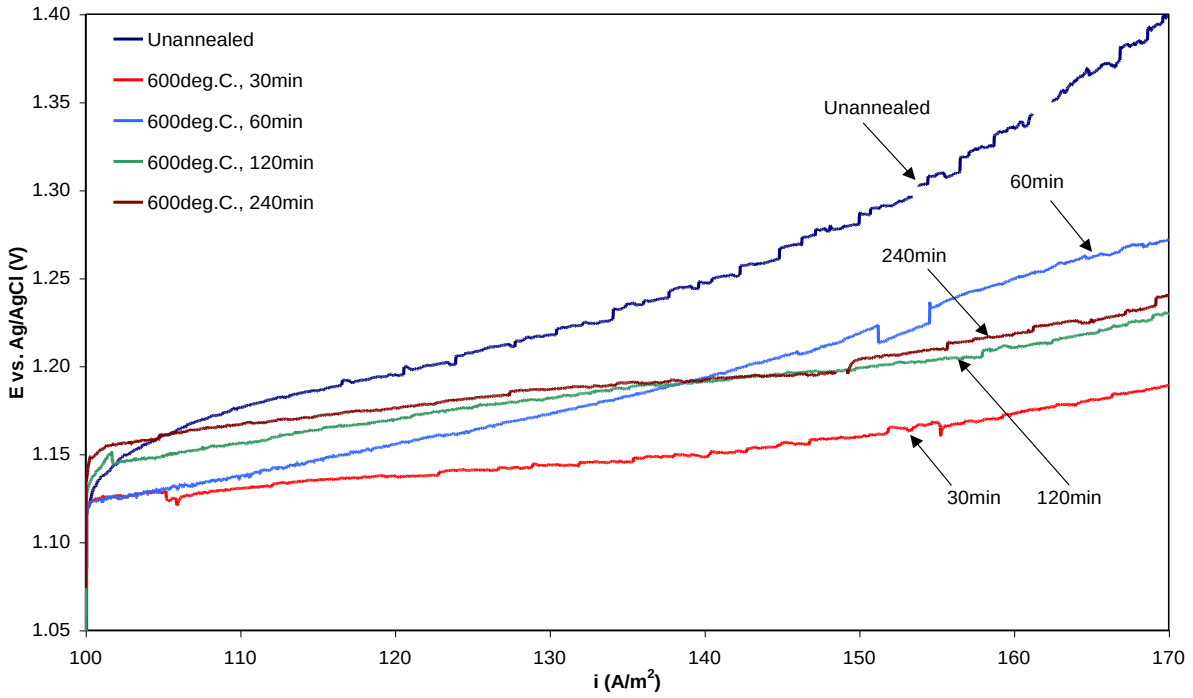

Figure 5.20: Polarization curves for MnO_2 electroplating using different DSA samples to illustrate the effect of annealing time on hydrous electrochemical stability.

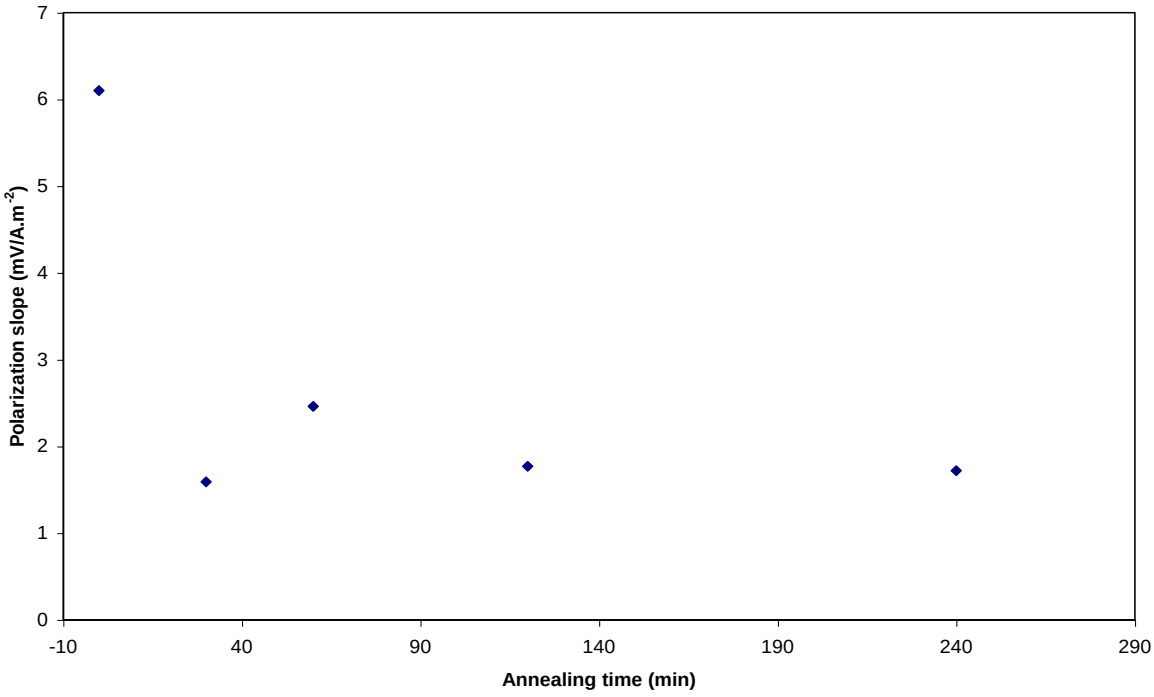

Figure 5.21: Polarization slopes plotted against annealing time. Slopes were calculated from 155A.m^{-2} to 170A.m^{-2} for the curves in figure 5.20.

Annealing T (°C)	Annealing time (min)	Polarization slope ($mV/A.m^{-2}$)
600	0	6.10 ± 0.02
600	30	1.590 ± 0.006
600	60	2.46 ± 0.01
600	120	1.77 ± 0.01
600	240	1.72 ± 0.01

Table 5.8: Summary of the data used in figure 5.21.

The relationship between the polarization slopes and annealing times can be partly explained using visual observation of electrode behaviour during the electrolysis process, as well as what is expected from the effect of annealing on the oxide film. An unannealed sample shows severe anodic corrosion during the first 3sec. of electroplating, while this is absent for all the annealed samples. It has previously been reported that deposited layers of Ru tend to corrode under anodic polarization in H_2SO_4 solutions [86, 87, 125], with the products of corroded RuO_2 being RuO_4 or H_2RuO_5 [87, 126]. Anodic corrosion on the unannealed sample is therefore the cause of a loss in electrocatalytic material resulting in a higher rate of polarization. Anodic oxidation of the exposed Ti substrate may also be considered as a definite possibility that contribute to an increase in the measured part of the polarization slope. The 30min annealed sample represents the best behaviour of the set of DSA's. Here, it is expected that annealing time is at an optimum to stabilise the $RuO_x.nH_2O$ to prevent anodic corrosion, while 1hr annealing resulted in oxidising the Ti substrate to such an extent that an increased resistance results at higher current densities. The annealing times for the remaining two samples probably sufficed to form binary mixed oxides that decreased the contribution of the TiO_2 to polarization at high current densities. Figure 5.20 also shows that the initial polarization of the 2hr and 4hr annealed samples were higher than the 30min and 1hr counterparts. Two possibilities for this is (a) a decrease in active surface area which commonly occurs during thermal annealing of hydrous oxides and (b) a loss in electrochemical activity [60].

The structure of the electroplated MnO_2 layers again reveals to correspond with powdered EMD from an industrial process as described in figure 5.22. Just as the MnO_2 structure from thermally prepared DSA's was independent of the Ru concentration in the precursor, the

duration of calcination is now irrelevant to the EMD film's structure. It should be emphasised that the crystallographic measurements on the MnO_2 films were only intended as a superficial study and although no significant differences are observed between any of the DSA specimens regarding the latter property, it does not render the results as futile. Crystallinity is known as one of several variables to impact on the MnO_2 reduction reaction in a voltaic cell and results in figures 5.13, 5.14 and 5.22 eliminate any potential threat that variation in DSA-preparation may pose to EMD discharge behaviour as far as structure is concerned.

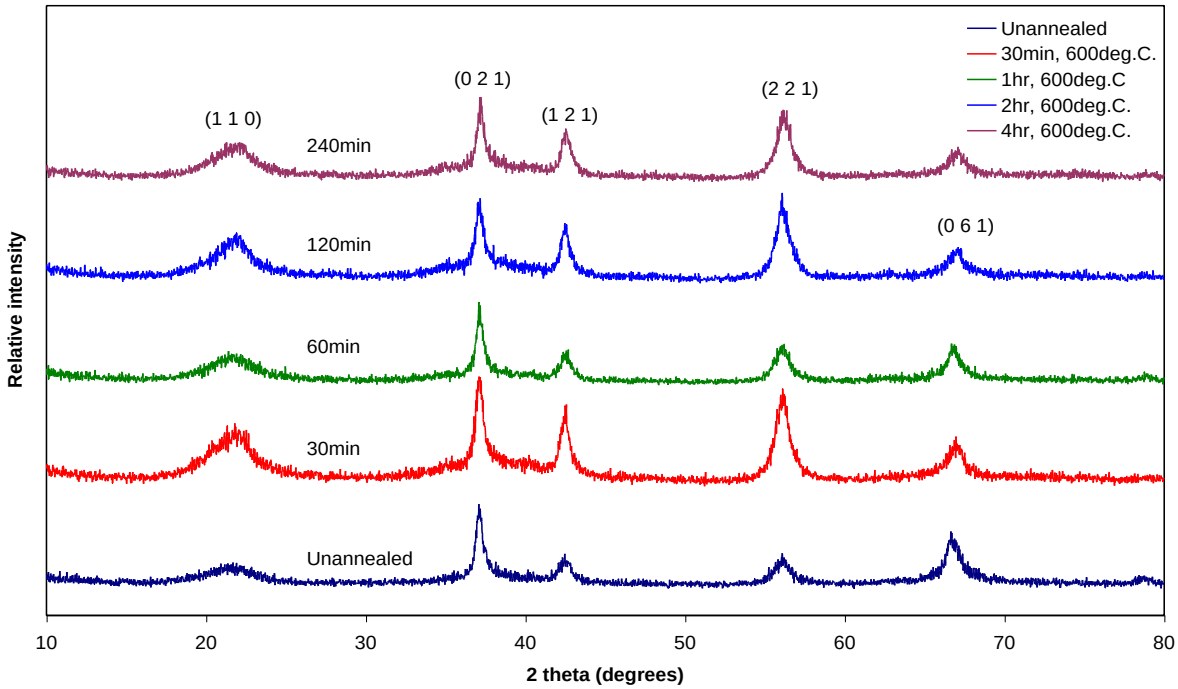

Figure 5.22: X-ray diffraction spectra of electroplated MnO_2 on DSA's that were prepared with cyclic voltammetry and calcinated for different durations at 600°C.

5.3 Polarization behaviour of Ti composite electrodes.

The electrochemical behaviour of the Ti-Mn, Ti-Pb and TiC anodes is illustrated in figures 5.23 and 5.24. The result of a DSA as prepared with a 0.8wt/wt% Ru precursor is included in these figures to have a reference point regarding the performance of the Ti composite and carbide anodes. The polarization behaviour of a Ti anode that was prepared according to the same procedure as the DSA specimens, but in the absence of Ru in a 3% HCl solution, is also plotted in figure 5.24. The result for the latter anode is included as a graphical illustration of the advantages of certain anode materials over Ti.

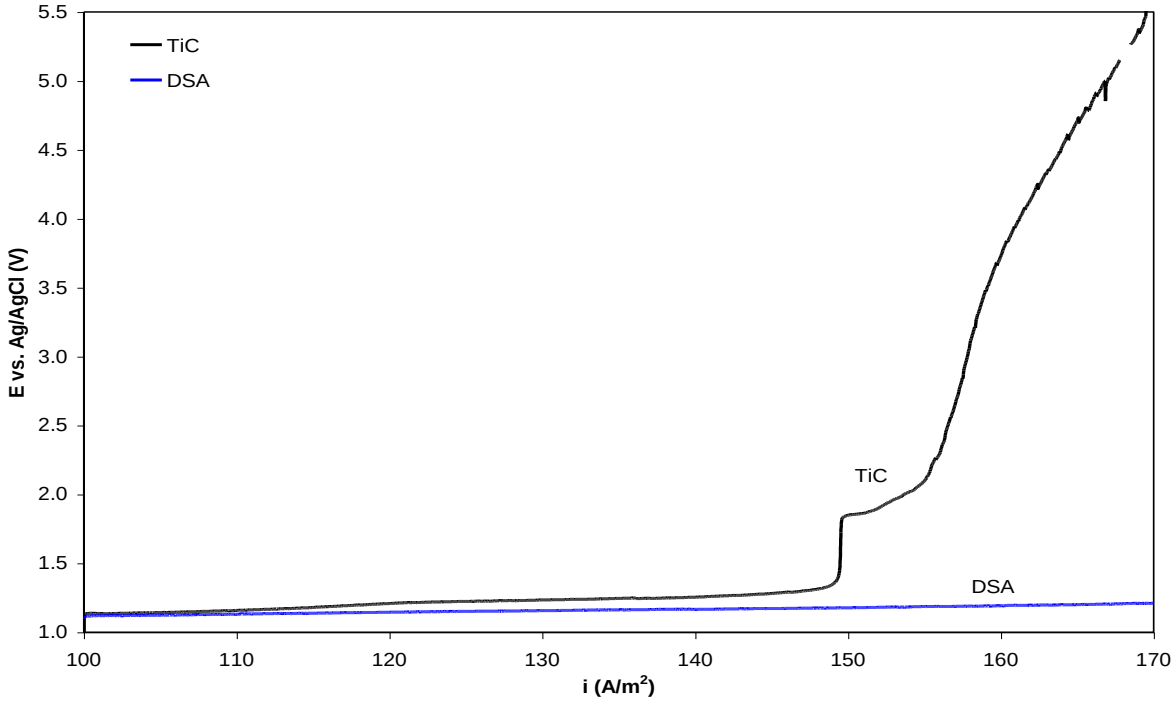

Figure 5.23: A comparison between the polarization behaviour of a TiC anode and a DSA (0.8wt/wt% Ru) under anodic load during MnO_2 electroplating.

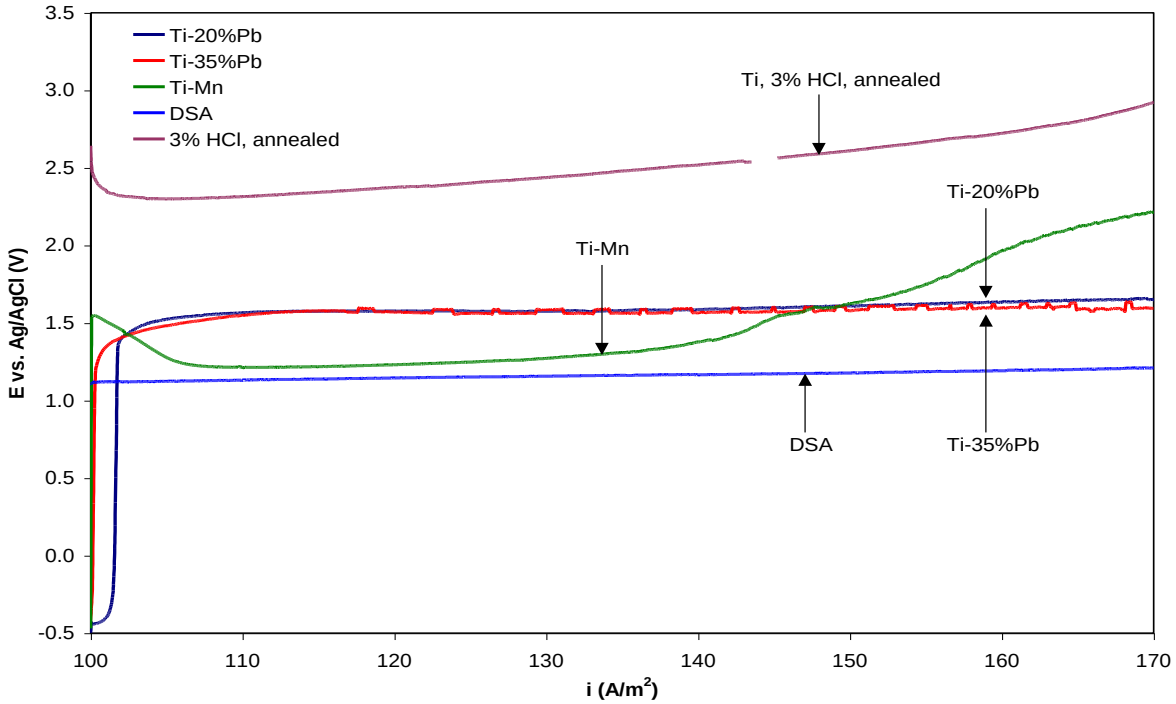

Figure 5.24: A comparison between the polarization behaviour of different anodes under anodic load during MnO_2 electroplating.

Although the curves in figures 5.23 and 5.24 appear to be confusing, it is worthwhile to scrutinise the polarisation behaviour of the different electrodes. Very important conclusions can be obtained from a direct comparison between electrode behaviour in these figures. Before assessing the actual values of the polarization slopes for the various samples, it should be of value to discuss the general trends in figures 5.23 and 5.24. It should firstly be mentioned that the scale of the y-axis prevents any assessment of a polarization slope for the DSA specimen using inspection as was the case in figures 5.1 and 5.20. This already gives a very sinister meaning to some of the other electrode slopes regarding power consumption if such mentioned electrodes should be employed in an industrial facility. At $100A.m^{-2}$ the Ti/TiC electrode started at a potential of 1.14V *vs*. Ag/AgCl. This is very much comparable to the 1.12V *vs*. Ag/AgCl for the electrocatalytic surface of the DSA samples and renders integrity to the TiC surface at this current density. The polarization of the Ti/TiC electrode remained within comparison of the DSA up to $120A.m^{-2}$, i.e. the Ti/TiC electrode was at 1.21V *vs*. Ag/AgCl at this current density and the DSA at 1.15V *vs*. Ag/AgCl. This behaviour of the TiC surface is surprising if the "noble" character of the RuO_2/TiO_2 system is taken into account and the TiC surface can almost be regarded as infringing on the DSA's uniqueness at these current densities. A gap started to develop between the latter two electrodes after $120A.m^{-2}$ and the Ti/TiC electrode underwent a transition at $149.5A.m^{-2}$ to totally unsatisfactory polarization values. Electrode behaviour reminiscent to that of a DSA has therefore mutated into a problematic high polarization that is inferior to all other electrodes in figures 5.23 and 5.24.

Polarization of both the Ti-Pb composite electrodes show a sharp transition to a value in the order of 1.50V *vs*. Ag/AgCl with a slope that appears the same as that of the DSA in the figure. The actual values of the slopes from $155A.m^{-2}$ to $170\ A.m^{-2}$ are $2.07 \pm 0.07A.m^{-2}$ and $0.0 \pm 0.2A.m^{-2}$ for the Ti-20%Pb and Ti-35%Pb electrodes respectively. This proves that a current density up to $170A.m^{-2}$ is innocuous to the Ti-35%Pb electrode in terms of passivation. The overall electrode performance of the latter electrode is however not regarded as an improvement over the DSA since the potential applied to the DSA was lower over the entire current range. The final potential of the DSA at $170A.m^{-2}$ was 1.21V *vs.* Ag/AgCl compared to 1.59V *vs.* Ag/AgCl for the composite electrode. This equates to a difference of 380mV and although actual production of EMD is never done at these current densities, this difference can still be interpreted as realistic in terms of discriminating between electrodes

for industrial processes since the applied current densities were used as an accelerated life test of the anodes as was already mentioned.

The Ti-Mn anode required 1.55V *vs.* Ag/AgCl upon initiation of electrolysis at 100A.m^{-2}. This was followed by a linear decrease of polarization to 1.24V *vs.* Ag/AgCl at 106A.m^{-2} that stayed reasonably constant up to 130A.m^{-2} before a positive polarization slope manifested itself up to 170A.m^{-2}. The negative polarization slope is an interesting phenomenon, yet difficult to explain with the knowledge that is currently available. An explanation can be attempted using the concept as proposed by Tseung and Jasem [127]. The surface of an oxide electrode was described as being more active towards the O_2 evolution reaction if the surface has a redox transition close to the reversible reduction potential of the O_2 evolution reaction. This concept can now be applied to the Ti-Mn electrode. During the initial stages of electrolysis, anodic oxidation of both the Ti and Mn takes place. The formed manganese oxide could be regarded as representative of an oxide material with a formal reduction potential similar to that for reaction 1.2 and the surface acts as an electrocatalyst towards this reaction up to 130A.m^{-2} after which the polarization rate exceeds that of the RuO_2/TiO_2 electrocatalyst. The polarization slopes of the various electrodes at high current densities are compared in table 5.9. The current range in which these slopes were calculated was not kept constant as was the case when comparing the DSA's in tables 5.1 and 5.3. This deviation from a consistent comparison resulted from the curvature of some of the polarization plots in figure 5.24. The slopes were consequently calculated in regions were the linearity of the curves were acceptable. The current density range for each sample is included in table 5.9.

Specimen	Selected range for slope calculation (A.m^{-2})	Polarization slope (mV/A.m^{-2})		Average slope (mV/A.m^{-2})
Ti-20%Pb	155 – 170	2.20 ± 0.02	1.93 ± 0.04	2.07 ± 0.07
Ti-35%Pb	155 – 170	0.0 ± 0.2	-	0.0 ± 0.2
Ti-Mn	165 – 170	19.9 ± 0.1	22.0 ± 0.2	21 ± 2
TiC	160 – 170	179.4 ± 0.6	-	179.4 ± 0.6
DSA (0.8% Ru)	155 – 170	1.67 ± 0.01	1.59 ± 0.02	1.63 ± 0.03
Annealed Ti	165 – 170	24.5 ± 0.1	-	24.5 ± 0.1

Table 5.9: Polarization slopes of anodes, other than DSA's, during electroplating of MnO_2.

The diffraction results of the EMD layers on non-electrocatalytic electrodes in figure 5.25 made the crystallographic investigations of the EMD films worthwhile as far as identification of differences is concerned. Both the Ti-Mn and Ti-20%Pb composite electrodes caused a very high degree of orientation of the (0 6 1) lattice plane. This is evident from the fact that (0 6 1) is the only peak present and the high peak-to-background ratio furthermore confirms this. EMD on the oxidised Ti electrode had a preference for the (0 2 1) plane, but not to such an extent as the EMD on the composite electrodes had for the (0 6 1) plane, since the (1 2 1), (2 2 1) and (0 6 1) indices are also present. It is realised that the crystallographic orientation of the mentioned MnO_2 films will disappear once in the powdered form and it should furthermore be emphasised that the single peak for MnO_2 on the Ti-Mn and Ti-20%Pb electrodes does not substantiate single crystal films. It could nonetheless be appreciated that this crystallographic phenomenon presents a possibility to influence the final crystal structure of EMD after transforming it to a powder.

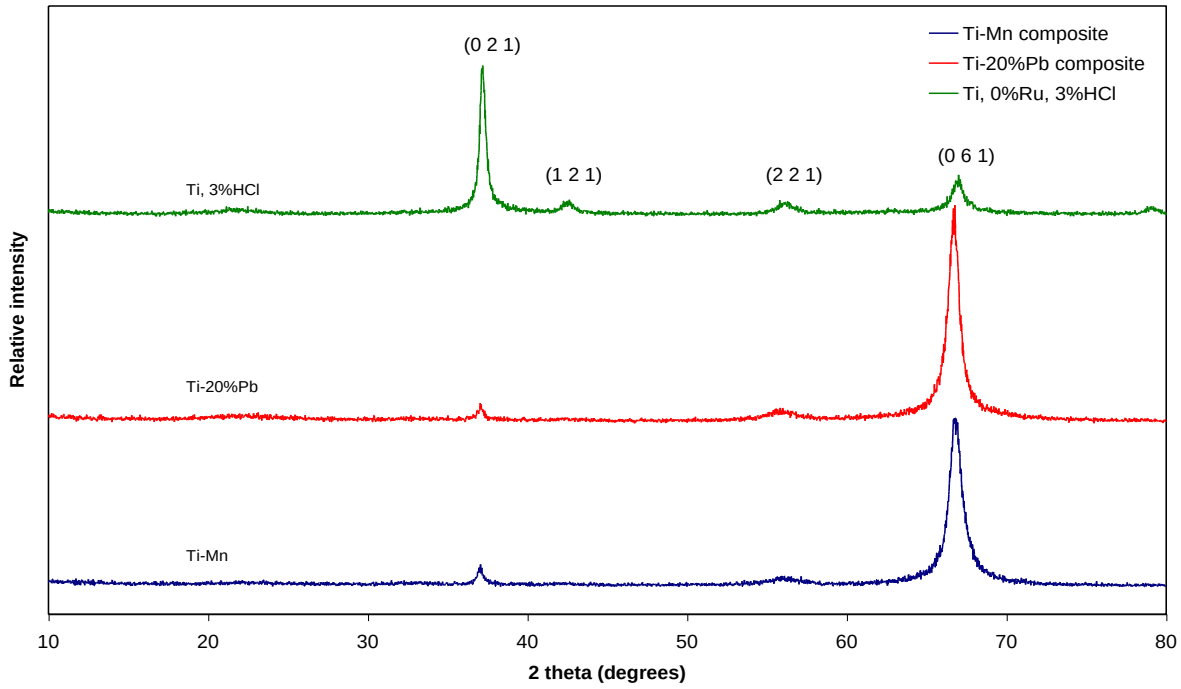

Figure 5.25: X-ray diffraction spectra of electroplated MnO_2 on non-electrocatalytic surfaces.

5.4 Conclusion.

When considering the initial objectives in sections 1.5 and 2.7, it is obvious that this chapter has yielded much of the desired information. Different techniques were effectively employed to prepare $Ti/TiO_y/RuO_x$ and $Ti/RuO_x.nH_2O$ specimens. Interpretations of crystal structures were done with XRD and it was semi-quantitatively shown that an increase in Ru metal concentration in the precursor solutions results in a measurable increase in RuO_2 in the thermal films as reflected by the growth of the (1 1 0) reflection at 28° 2θ (figures 5.3 and 5.5). Definite identification of crystalline TiO_2 in the films that were prepared at 400°C was not possible, but it cannot be over emphasised that an increase in calcination temperature to 600°C causes RuO_2 to adhere more readily to the Ti substrate. The lattice parameters for rutile RuO_2 and TiO_2 were calculated from the PDF of the ICDD.

A theory was proposed to explain crystal water in the $RuO_x.nH_2O$ films to be removed upon firing at 600°C. One of the most remarkable findings is that the initial electrode polarization (at $100.5A.m^{-2}$) is not influenced by the precursor composition. Whether the precursor contains 0.8wt/wt% Ru, 19.89wt/wt% Ru or a mixture of $RuCl_3$ and $TiCl_3$, the polarization value at $100.5A.m^{-2}$ is 1.118V *vs*. Ag/AgCl on average. The polarization resistance of thermally prepared $Ti/TiO_y/RuO_x$ electrodes appears to be a linear function of Ru in the precursor within a certain range. A more complex behaviour was observed for the cyclic voltammetrically prepared films. If the DSA's are to be considered for industrial applications, it is a foregone conclusion that the 0.8wt/wt% Ru precursor-DSA (single component) present unparalleled advantages in terms of a combination of preparation cost and electrocatalytic behaviour during MnO_2 electrodeposition. Findings for the latter electrode include a polarization slope of $1.63 \pm 0.03mV/A.m^{-2}$ and an initial potential value of 1.118V *vs*. Ag/AgCl at $100.5A.m^{-2}$. With a polarization slope of $1.590 \pm 0.006mV/A.m^{-2}$ and initial polarization of 1.124V *vs*. Ag/AgCl at $100.5A.m^{-2}$, the 30min annealed (600°C) $Ti/RuO_x.nH_2O$ electrode is in contention for industrial purposes if the capital cost for the required preparation facility is accepted by a manufacturer.

The Ti composite electrodes presented interesting behaviour, with the Ti/TiC electrode being the most effective to lower electrode polarization comparable to a DSA, but only up to $120A.m^{-2}$.

Chapter 6

Results and discussion: Surface analyses.

6.1 Surface composition of Ti/$RuO_x.nH_2O$ electrocatalysts.

The result of a measurement that is essential to coerce accurate interpretation of elements in the measured Auger spectra is illustratively presented in figure 6.1. This spectrum of Cu was taken after sputter cleaning to give the differentiated MVV and LMM transitions at 65.7eV and 923.2eV respectively. These energy positions are taken at the most negative part of the differentiated spectrum to compare it with 66eV and 922eV as published in reference [104]. Calibration of the AES system in terms of energy position of the transitions between 0eV and 1000eV can therefore be assumed to be acceptable.

Examples of AES spectra of the surface of electroformed $RuO_x.nH_2O$ films are analysed in figures 6.2 and 6.3 for an unannealed and a 240min (600°C) annealed sample. A comparative inspection of figures 6.2 and 6.3 brings 4 facts to the forefront. Firstly, Cl that originates from both the precursor solution and supporting electrolyte is present and leaves a significantly larger trace on the unannealed sample than on the calcinated surface. Secondly, K is also incorporated in the surface during the electrochemical growth process from the KCl supporting electrolyte. The third observation is that the transition at 279eV indicates the presence of C (see section 2.5.2). The fourth point that appears from the two graphs is the discrimination of the Ti APPH between the surfaces of the two samples. It is obvious that the Ti concentration on the outermost surface of the calcinated sample is higher compared to the unannealed sample.

Identification of relevant energy positions for the entire range of heat-treated samples (voltammetrically prepared) is summarised in table 6.1 and spectra for a single point in each of the surfaces are compared in figure 6.4. The spectra in figure 6.4 serves to confirm the 4 conclusions in the previous paragraph and to elaborate on the effect of calcination on the electrocatalysts under discussion. One of the most prominent differences between the spectra is the sudden decrease in the Cl APPH between the unannealed sample and the rest on the surface compositions. This shows that the method of heat treatment caused significant

removal of Cl from the surface with the possibility of a change in Ru oxidation state should it be that reasoned that some of the measured Cl was chemically bonded to this metal centre.

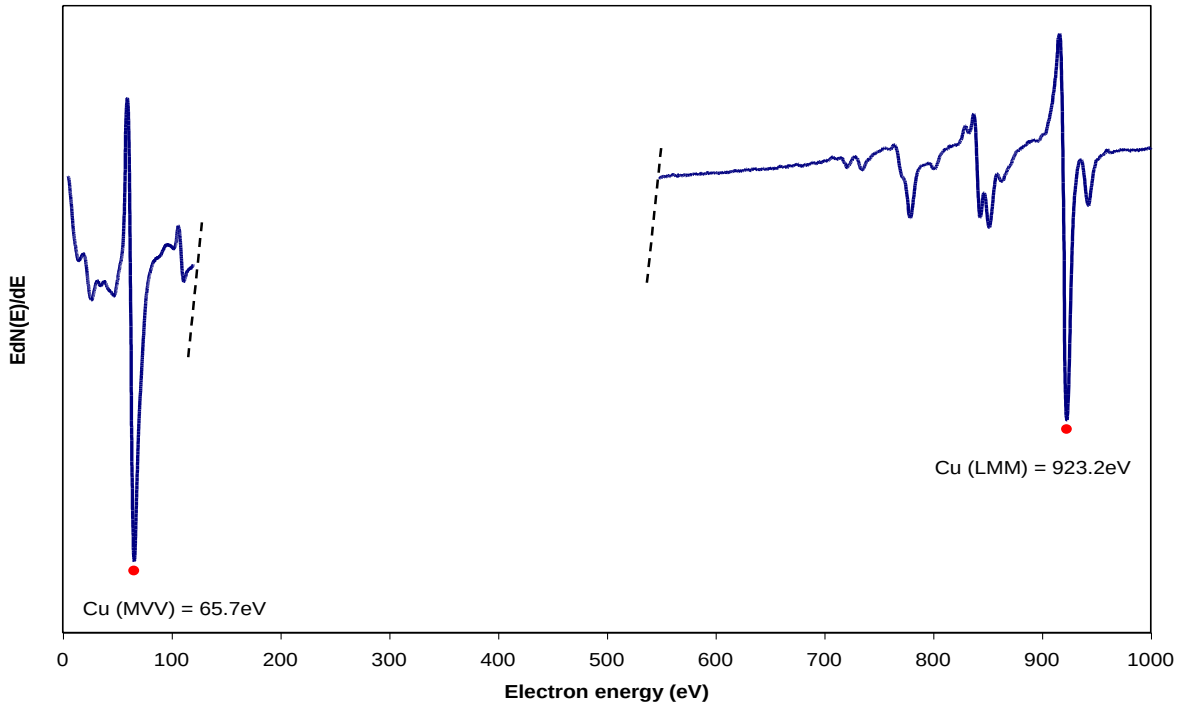

Figure 6.1: AES spectrum of a Cu standard to confirm energy calibration of the Auger system.

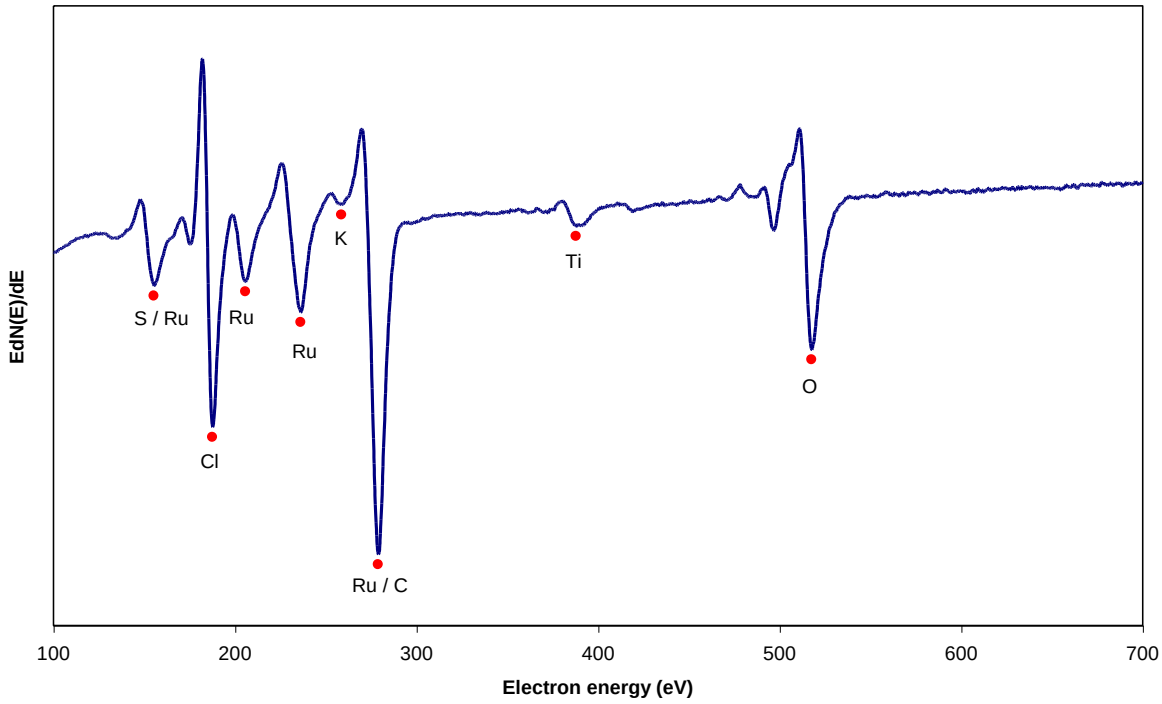

Figure 6.2: AES spectrum of the surface of an electroformed $RuO_x.nH_2O$ film on Ti, no calcination.

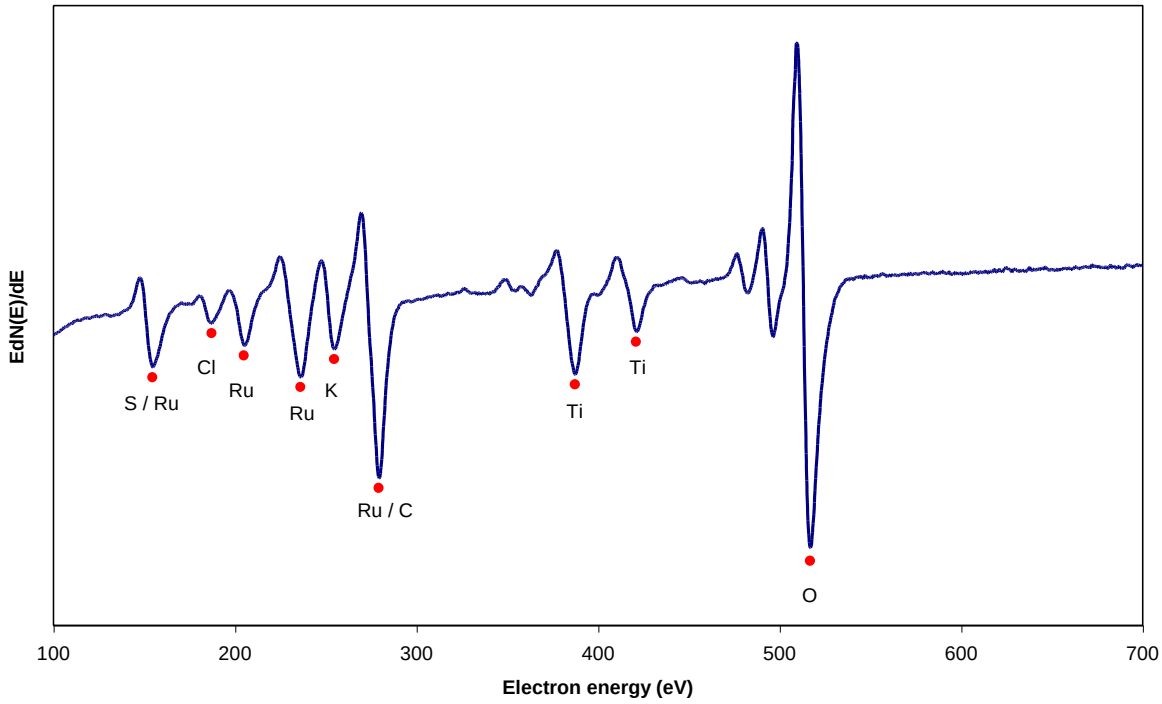

Figure 6.3: AES spectrum of a calcinated $RuO_x.nH_2O$ film, 240min, 600°C.

Although it appears that the Cl APPH further diminishes as a function of calcination time, no mathematical relation exists. The effect of annealing duration on the APPH of the Ti transitions at 390eV is plotted in figure 6.5.

Transition	Duration of calcination (minutes)					Hedberg [104]
	0	30	60	120	240	
	Measured energy (eV)					Energy (eV)
S (LVV)	155.5	156.2	154.8	155.2	154.8	153
Cl (LVV)	187.7	187.7	187.3	188.1	187.3	184
Ru (MNN)	205.9	206.2	205.2	205.5	205.2	-
Ru (MNN)	236.3	236.3	236.0	236.4	236.3	235
K (LMM)	258.7	255.9	254.9	254.4	254.9	252
Ru (MNN) / C (KLL)	279.0	279.0	278.7	278.6	279.4	277 / 275
Ti (LMM)	387.9	388.6	387.9	388.7	387.5	390
Ti (LMM)	-	421.8	421.1	422.0	421.1	421

Table 6.1: Energy positions of the relevant Auger transitions for the voltammetrically prepared samples.

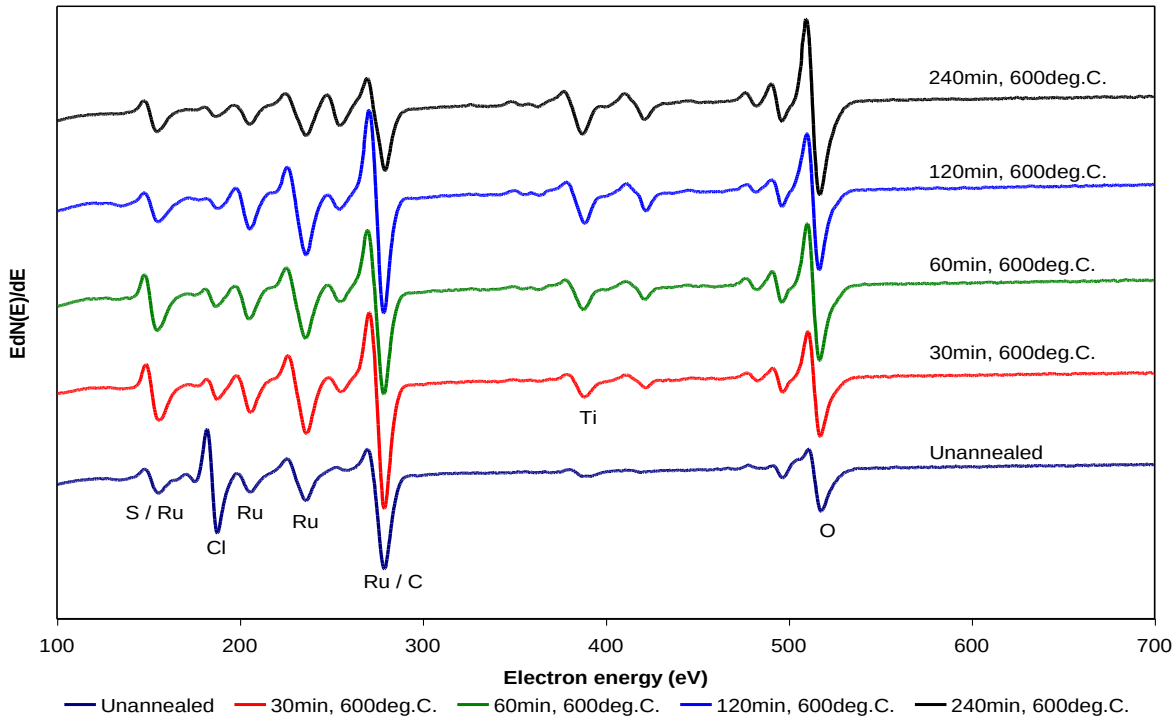

Figure 6.4: AES spectra on the surface of a $RuO_x.nH_2O$ film that was calcinated for different durations at 600°C.

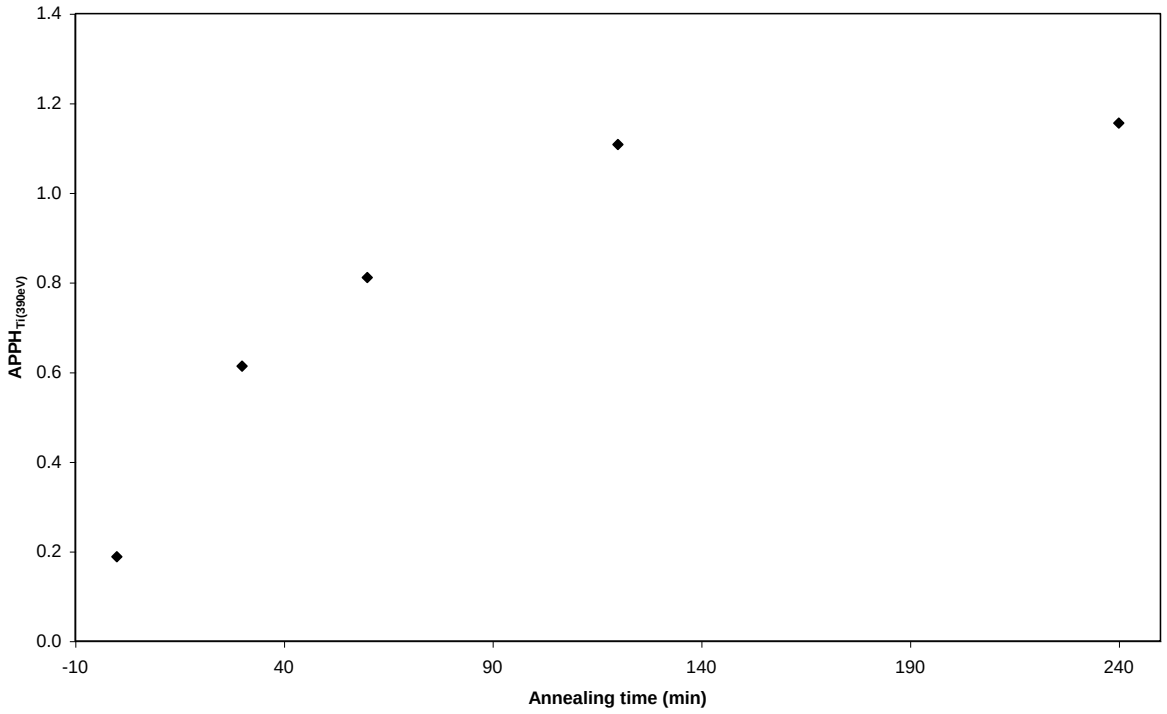

Figure 6.5: Graph of $APPH_{Ti(390eV)}$ *vs*. duration of calcination.

A distinct 2nd order polynomial (parabolic) relation between the APPH of the Ti (390eV) transition and calcination time is confirmed in figure 6.6. Another conclusion that follows

from figure 6.4 is that the unannealed surface tends to contain a higher concentration of C if the symmetry of the Ru (277eV) transitions of the calcinated samples is compared with the shape of the same transition of the unannealed $RuO_x.nH_2O$ film.

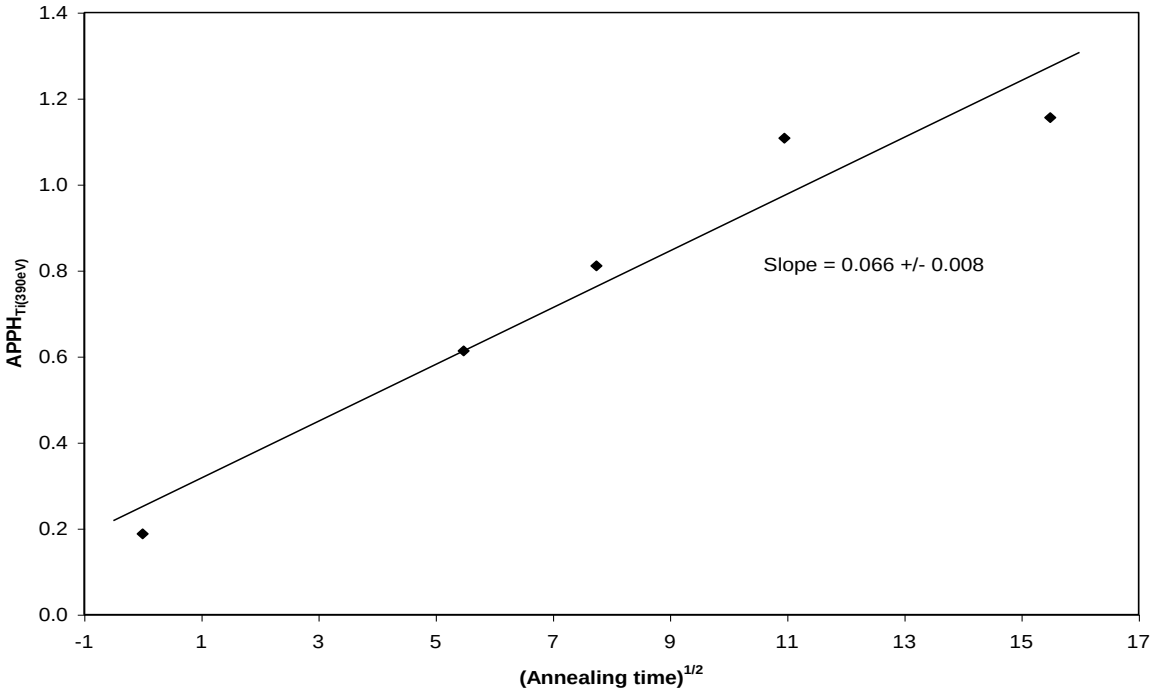

Figure 6.6: 2nd order polynomial relation between $APPH_{Ti(390eV)}$ and duration of calcination.

An example of the result of AES measurements at 5 different positions on the surface of a $RuO_x.nH_2O$ film is compared in figure 6.7. This served the purpose of evaluating the homogeneity of the films. From a mere visual inspection of figure 6.7, it is possible to deduce that the film can be regarded as homogeneous to a large degree. Equation 3.21 was used to calculate the average concentrations of the different elements for the 5 measurements on each sample's surface. The sensitivity factors (at 3keV) were taken from the book of Hedberg [104] and the values for the relevant transitions are presented in table 6.2. Note that the Ru (235eV) transition was used to represent Ru instead of the 277eV transition. This approach is followed to avoid complications caused by overlap of the C (275eV) and Ru transitions.

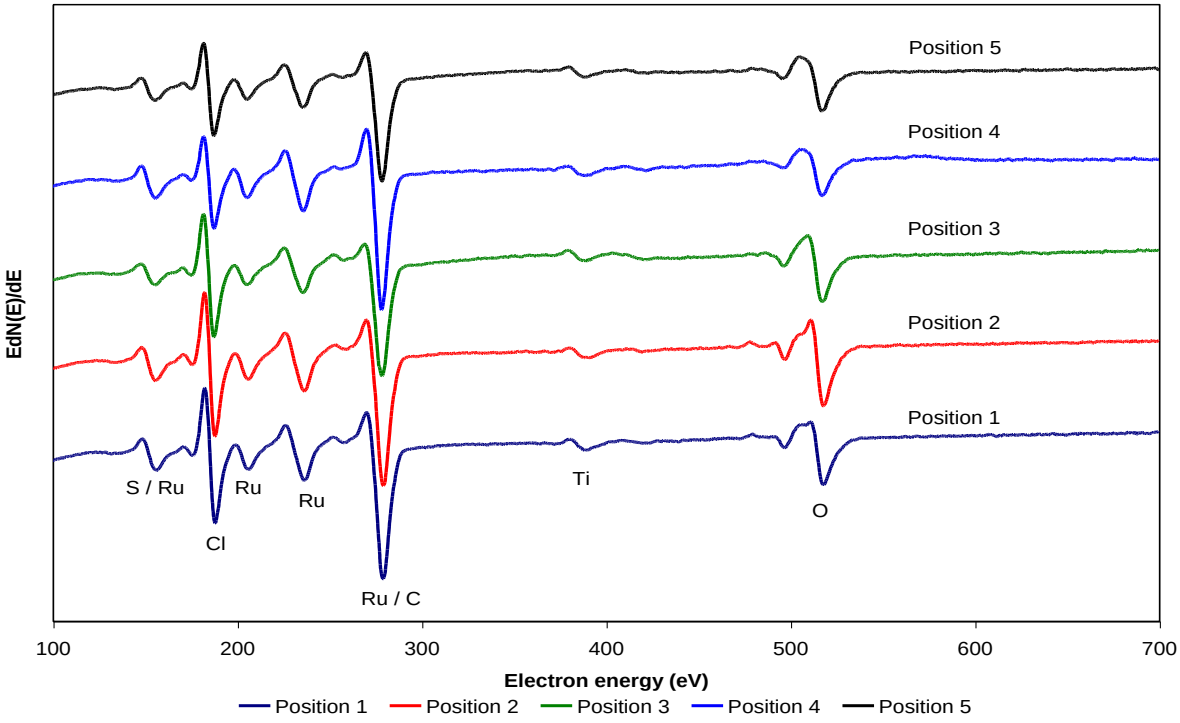

Figure 6.7: Comparison between AES spectra that were taken at different positions on the surface of a $RuO_x.nH_2O$ film, no calcination.

Transition	S_i (3keV)
S (153eV)	4.7575
Cl (184eV)	11.9182
Ru (235eV)	0.8042
K (252eV)	1.1177
Ti (390eV)	1.2155
O (510eV)	1.2571

Table 6.2: Sensitivity factors for the transitions used to calculate the relative atomic concentrations on the surface of $RuO_x.nH_2O$ samples.

It should be mentioned that the atomic concentration of C is completely ignored in the results presented and this approach impacts on the calculated concentrations of the other elements. The objective is therefore to obtain a relative indication of the concentration of the elements if the various samples are compared with one another and not to calculate analytical correct values. The omission of C is realised to be problematic should exact quantitative concentrations be required. It also follows from table 6.2 that the 390eV transition is used to

calculate the Ti concentration since the APPH of this transition is not as dependent on the oxidation state is as the case for the LMV and LVV transitions. A transition for Ru at ≈ 155eV is reported in reference [104]. The consequence is that an overlap with the S (153eV) transition takes place in the AES spectra. The contribution of S to the measured transition at 153eV was resolved by subtracting a fraction of the Ru (235eV) APPH from the measured APPH of the 153eV transition. In the absence of S and for a certain oxidation state of Ru, the following equation holds:

$$\frac{APPH_{Ru(155eV)}}{APPH_{Ru(235eV)}} = k \quad \text{.....(6.1),}$$

with k being a constant that is used as the factor with which the APPH of the 235eV transition is multiplied. This gives:

$$APPH_S = APPH_{153eV} - k.APPH_{Ru(235eV)} \quad \text{.....(6.2).}$$

The value of k was experimentally determined from a depth profile for each sample. The ratio in equation 6.1 becomes constant after a certain period of sputtering and it is assumed that S is completely removed from the surface at such point in a depth profile. Slight variation in k is observed between different samples with the result that a unique value of k is used to calculate $APPH_S$ for each sample. The values of k, as well as the average atomic concentrations of Ru, Ti and O (average of 5 measured APPH values) for the 5 samples under discussion, are condensed in table 6.3. The maximum and minimum concentration values for each element and each sample in table 6.3 originate from the different positions of which the average atomic concentrations are calculated. The atomic concentration of Ru and Ti is plotted in figure 6.8 *vs*. calcination time. Similar to figure 6.5, a parabolic relation between Ti atomic concentration and calcination time follows from figure 6.9. The diminution of Ru in figure 6.8 appears to follow a 2^{nd} order polynomial trend, but the correlation coefficient does not suffice to plot a strict linear relation between Ru atomic % (at%) and $t^{1/2}$. Although no relation exists between the surface concentration of Ru (with the limitations in its calculation) and the behaviour of the electrodes under anodic load in a

$MnSO_4$ medium, it is still worthwhile to take note of the concentration of Ru on the different sample surfaces.

Calcination time (min)	k	Ave. at% Ru	Max. (at%)	Min. (at%)
0	0.28	46	56	42
30	0.22	38	54	25
60	0.22	31	36	23
120	0.20	30	41	22
240	0.21	31	42	20
Calcination time (min)	k	Ave. at% Ti	Max. (at%)	Min. (at%)
0	0.28	6	7	5
30	0.22	8	10	6
60	0.22	10	11	9
120	0.20	12	13	11
240	0.21	15	18	12
Calcination time (min)	k	Ave. at% O	Max. (at%)	Min. (at%)
0	0.28	36	41	28
30	0.22	42	55	28
60	0.22	49	56	44
120	0.20	49	53	40
240	0.21	45	54	37

Table 6.3: Atomic concentrations of Ru, Ti and O on the surface of voltammetrically prepared samples.

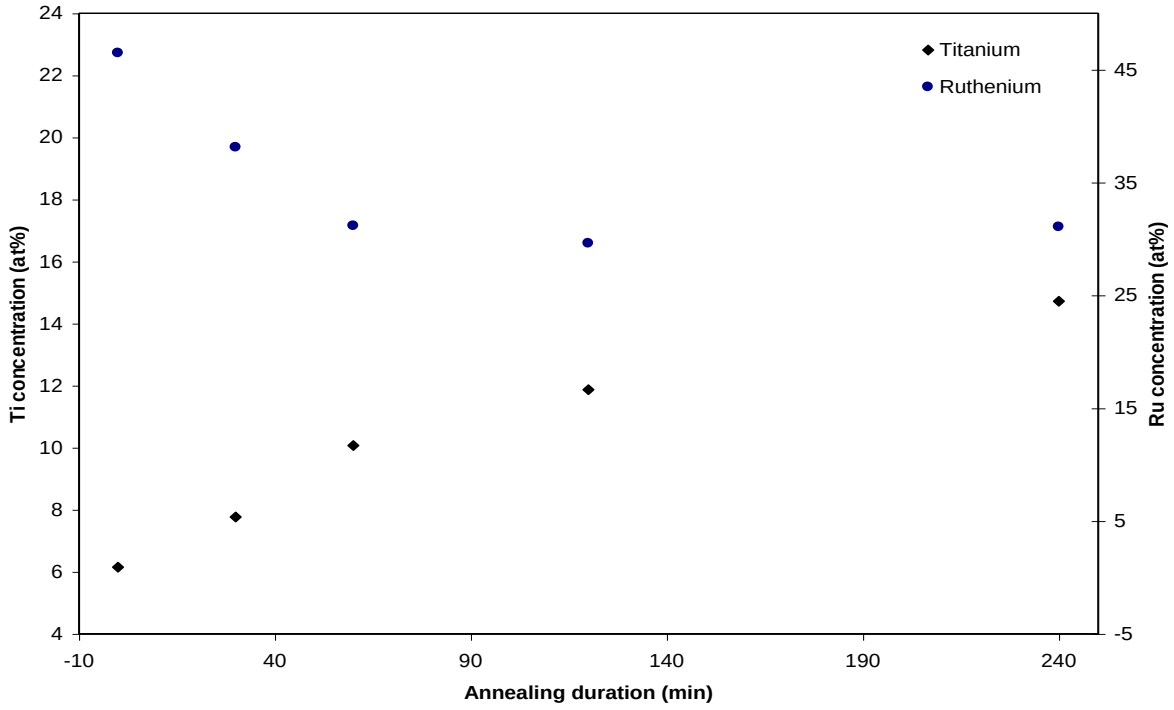

Figure 6.8: Graph of the atomic concentration of Ru and Ti on the surface of electroformed $RuO_x.nH_2O$ films as a function of calcination.

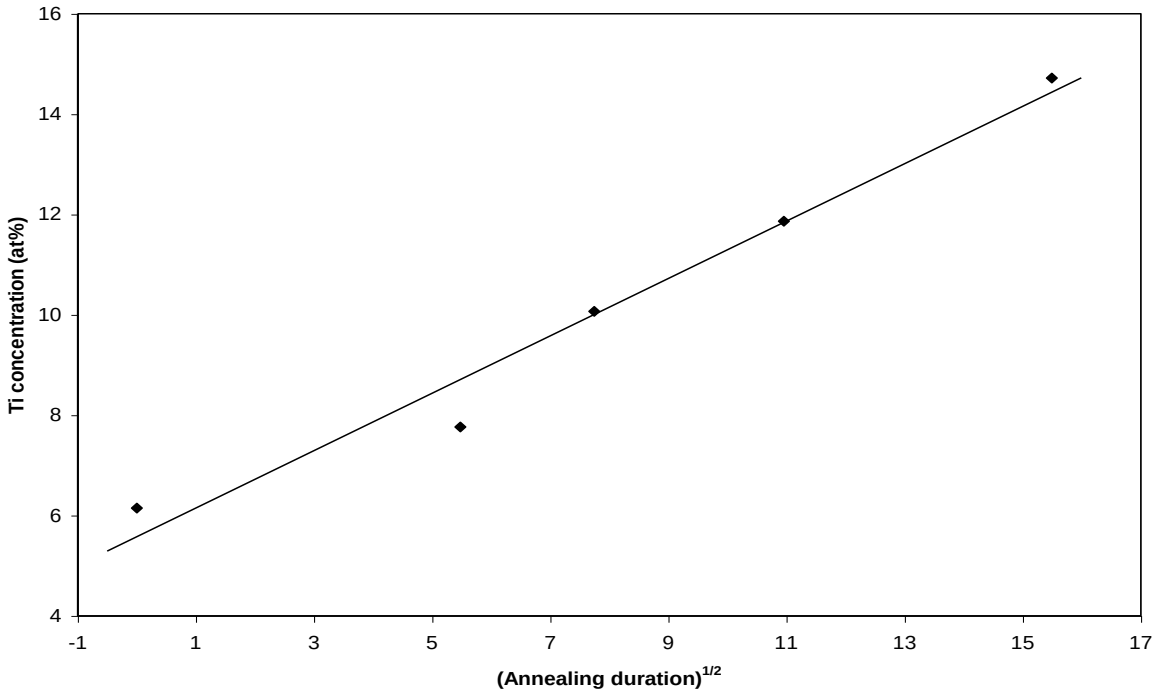

Figure 6.9: Confirmation of the parabolic relation between at% Ti and calcination time for electroformed electrocatalysts.

The fact that heat treatment has the tendency to cause a decrease in the surface concentration of Ru cannot be ignored and ≈ 46at% Ru on the surface in the absence of calcination furthermore proves that the method of cyclic voltammetry for the growth of a $RuO_x.nH_2O$ film is very effective in depositing a significant amount of RuO_x on a Ti substrate. A value of ≈ 38at% is calculated for the 30min annealed surface and cannot be regarded as significantly larger than the remaining samples if the minimum and maximum values of the 5 observations are taken into account. The lowest surface concentration of Ru in this series of samples is at ≈ 30at% for the 60min to 240min calcinated samples, a value that is still considerably high when compared to the surface concentration of Ti for these specific samples. These values for the surface concentration of Ru will become even more relevant once compared with the corresponding values of the thermally prepared electrocatalysts.

6.2 AES depth profiling on Ti/$RuO_x.nH_2O$ electrocatalysts.

Note that all depth profiles are presented in terms of normalised APPH while the sputter-scaling factor, as introduced in section 3.5.2, is also used to correct the x-axis of each profile. The sputter time through a Ti standard is taken from the time when the acceleration voltage was applied to the ion gun up to the point where the Ti APPH decreased to half of its maximum value. The latter is exemplified in figure 6.10. The length of the dotted horizontal line is 3458s to yield a sputter rate of 0.582Å.s^{-1} for a Ti film of 2014Å thickness. It should be realised that this rate is not completely reproducible between measurements. A sputter-scaling factor therefore serves the purpose of calibrating the time axis. The factor under discussion is calculated as follows:

$$\text{Sputter scaling factor} = \frac{\text{Measured rate}}{\text{Reference rate}} \quad \text{.....(6.3)}$$

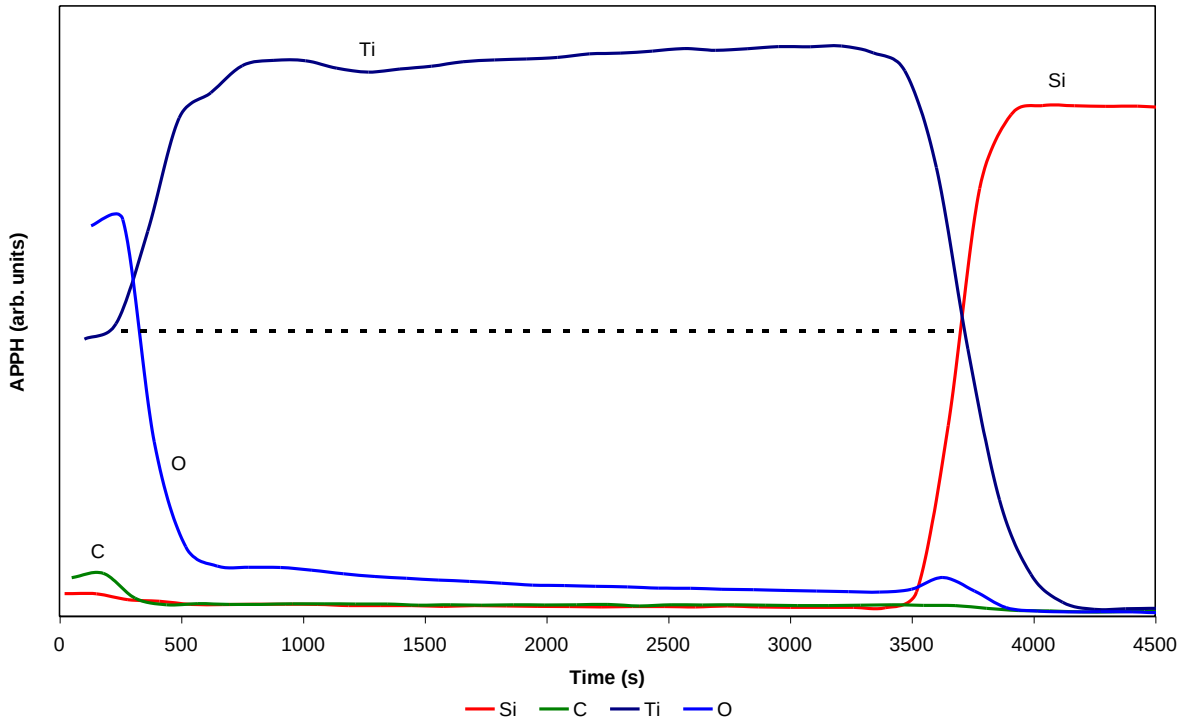

Figure 6.10: AES sputter depth profile through a 2014Å Ti film on a Si wafer to determine sputter rate.

The chosen value of the experimentally determined reference sputter rate is 0.607Å.s^{-1}. The contribution of S at each point in a profile was deconvoluted using equation 6.2. The first

part of each profile represents APPH measurements that were taken in the absence of Ar^+ sputtering, with the vertical line indicating the onset of sputtering. No further modifications are made to the measured profiles and observed differences can therefore be interpreted as being relative between the various samples. An indication of the repeatability of depth profiling on a certain sample can be appreciated from figures 6.11 and 6.12. The depth profiles for the extremes of an unannealed and a 240min-calcinated sample are compared in figures 6.11 or 6.12 and 6.13. Although the implication of figures 6.11 and 6.12 cannot be straightforwardly interpreted, it is readily deducible from figure 6.13 that heat treatment significantly affects the film's depth composition. It is again realised that heat treatment facilitates removal of Cl from the film's surface, but depth profiling also shows that Cl is removed from the film's inner structure. The graphs furthermore show how the relative positions of Ru, Ti and O profiles are influenced by thermal treatment. There appears to be a dramatic enrichment in O throughout the whole film after annealing and the position of the Ti profile is elevated relative to the Ru profile.

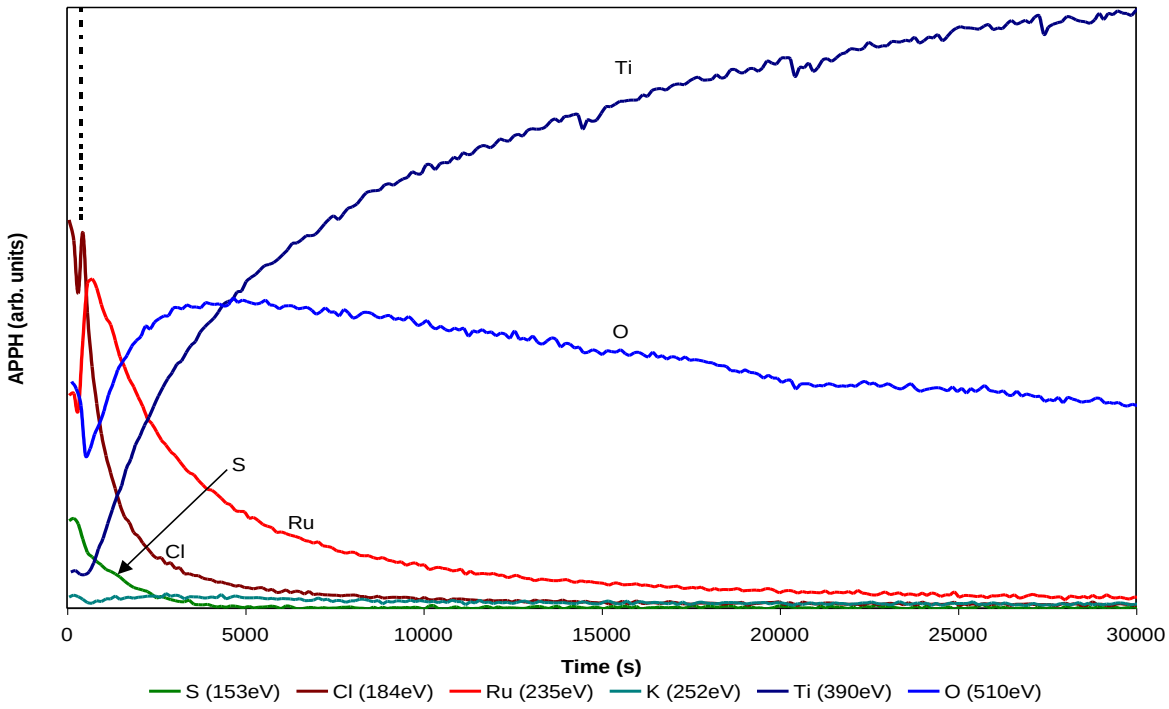

Figure 6.11: AES depth profile through an unannealed $RuO_x.nH_2O$ film.

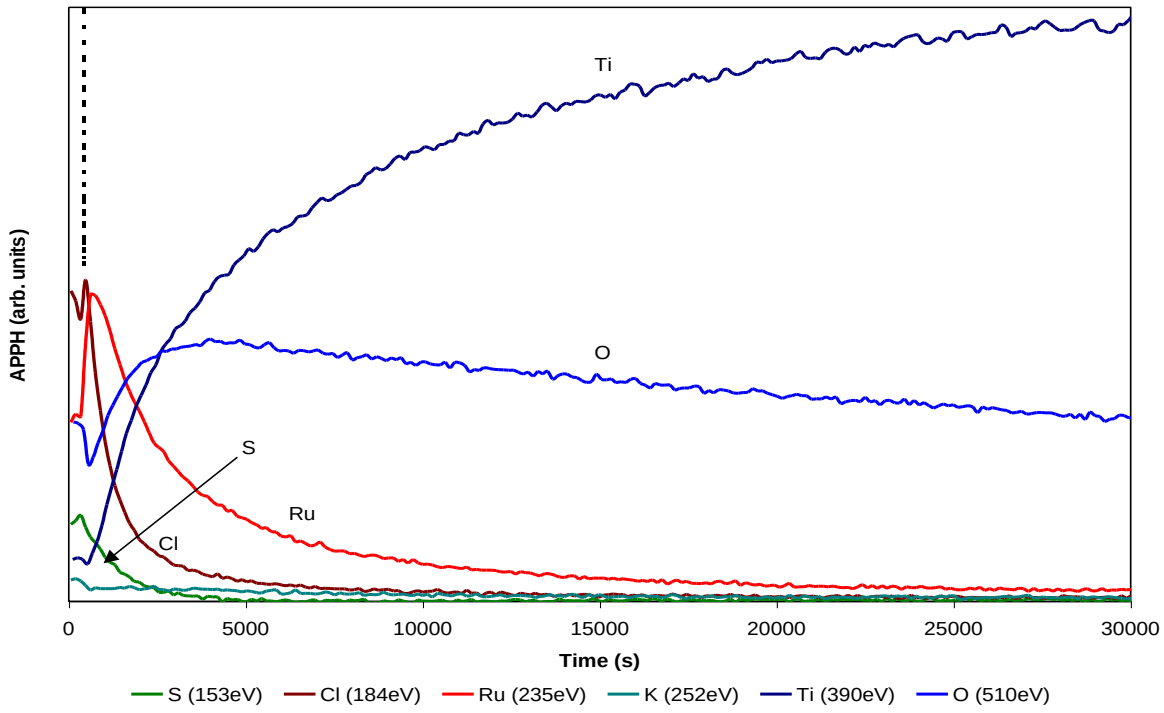

Figure 6.12: AES depth profile through an unannealed $RuO_x.nH_2O$ film. Repeat of the depth profile in figure 6.11.

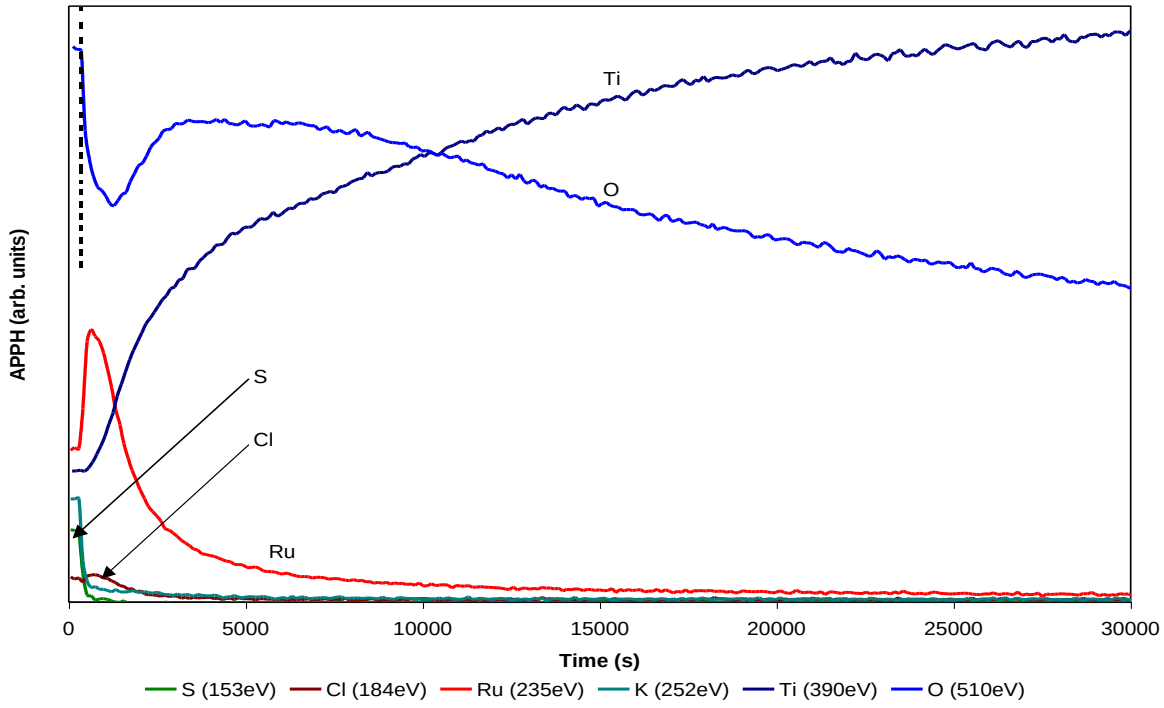

Figure 6.13: AES depth profile through a $RuO_x.nH_2O$ film, calcination at 600°C for 240min.

Another significant difference exists between the profiles in figures 6.11 and 6.13 in the form of the cross-over point between the Ti and O profiles. The Ti-O cross-over point for the sample that was subjected to thermal treatment is significantly retarded in terms of sputter time. Although the latter is again merely experimental evidence without mathematical substantiation, a phenomenon such as substrate oxidation and diffusion between relevant elements can be appreciated.

It follows from a number of discussions in the previous chapters of this study that the Ru content and / or compositional distribution in an electrocatalytic film can be regarded as being of significant importance in terms of the oxide electrode's physical and electrochemical characteristics. It is therefore appropriate to attempt a more in-depth analysis of the Ru profiles in the various films. As an extension of figures 6.11 and 6.12, the repeatability of the behaviour of Ru in the profiles for an unannealed and a 240min-calcinated sample is given in figures 6.14 and 6.15 respectively. These comparisons are deemed necessary to be able to confidently interpret the effect of calcination duration on the Ru profiles in figure 6.16. Note that the Ru profile for the unannealed specimen is omitted for the sake of illustrating the profiles of annealed samples to better effect.

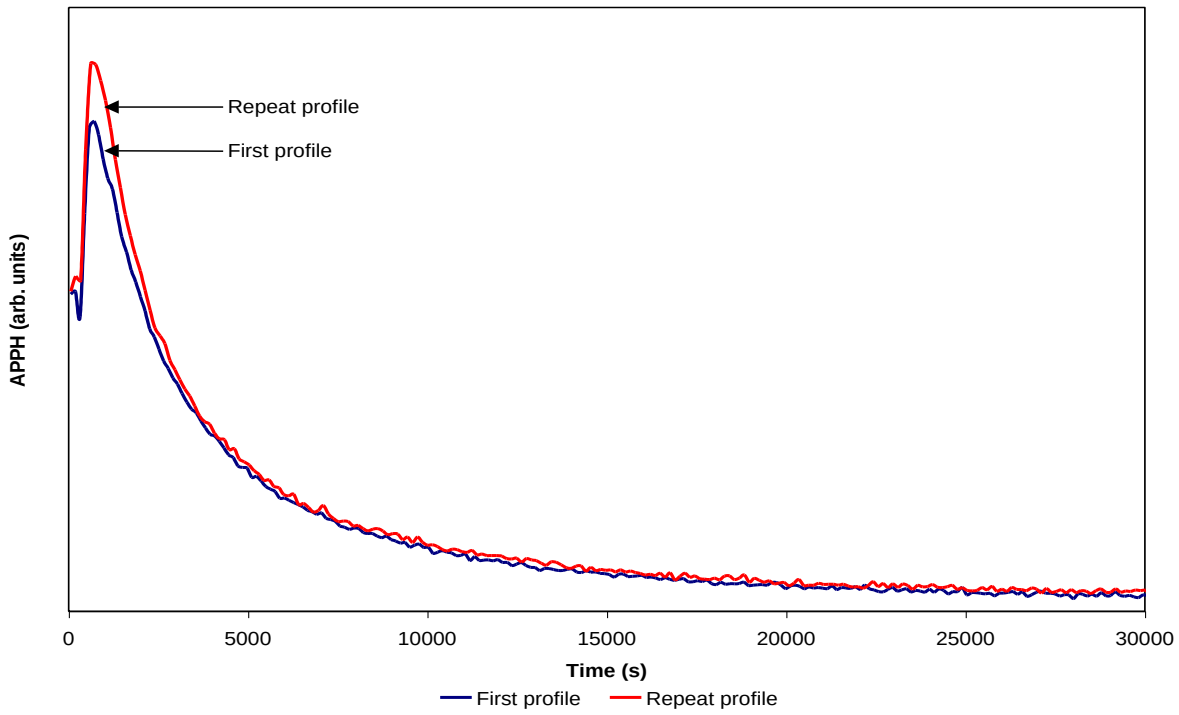

Figure 6.14: Duplicate depth profile traces of Ru in a film of $RuO_x.nH_2O$, no heat-treatment.

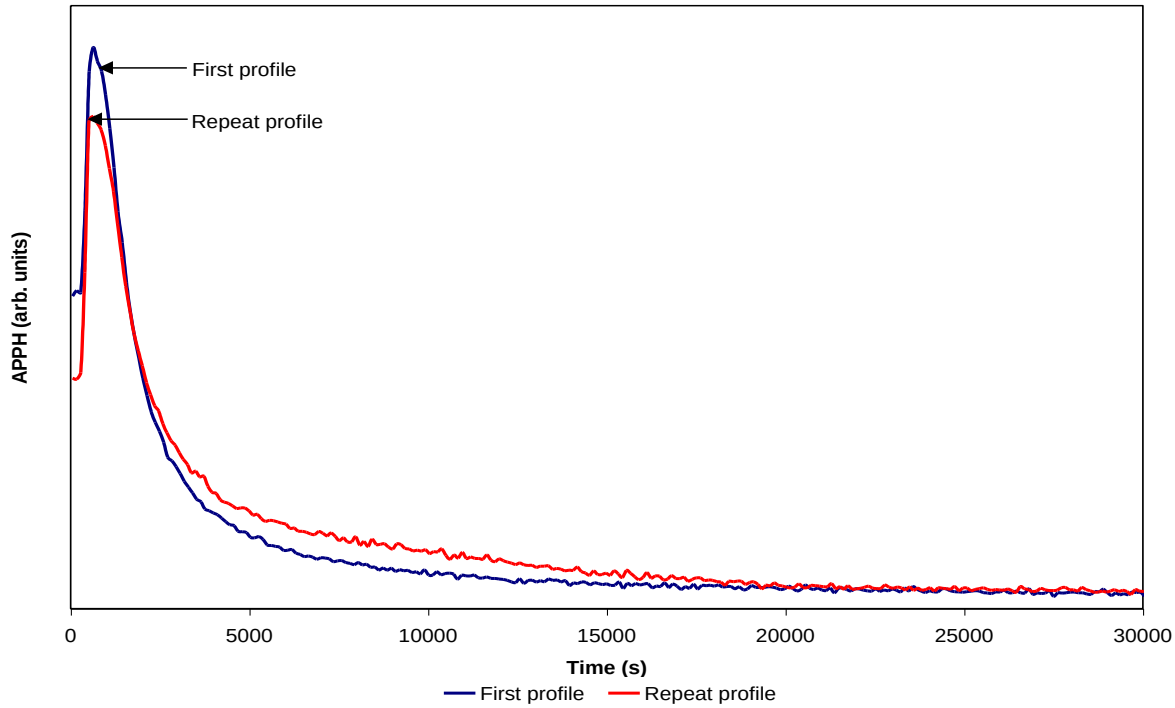

Figure 6.15: Duplicate depth profile traces of Ru in a $RuO_x.nH_2O$ film, calcination at 600°C for 240min.

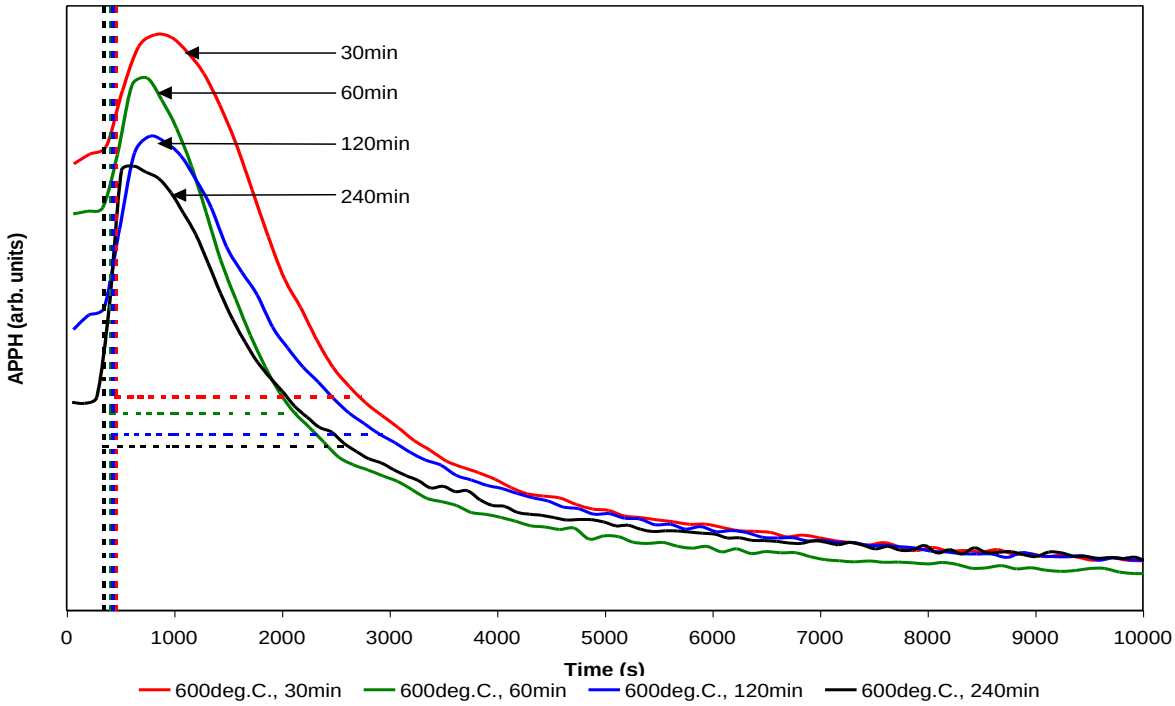

Figure 6.16: Depth distribution of Ru for the various electroformed samples. Relative thickness is determined by the time the APPH decreases to e^{-1} of the maximum.

The decrease in the surface concentration of Ru with calcination time was already discussed in section 6.1 and can again be observed in figure 6.16. Each profile goes through a maximum with a trend similar to the relative surface concentration of Ru. This however does not appear to impact on the electrodes' behaviour during MnO_2 electroplating. A relative measure of the Ru "thickness" is furthermore illustrated in figure 6.16. The unit of sputtering time, i.e. s, is used to represent thickness by calculating the time difference between the onset of sputtering and the point at which the measured APPH has decreased to a value of e^{-1} of the maximum APPH. These values are summarised in table 6.4.

Calcination time (min)	"Thickness" (s)
0	3465
30	2274
60	1710
120	2488
240	2266

Table 6.4: "Thickness" of Ru films on the various samples expressed as sputter time.

The "thickness" of the unannealed film calculates to the highest value. There is however evidence that confines the result for the unannealed film to a different category compared to the layers that underwent thermal treatment. Heat treatment is known to cause a decrease in the surface area of electrochemically prepared hydrous $RuO_x.nH_2O$ films [60]. It could consequently be readily realised that the unannealed film has a highly porous structure that collapses upon heat treatment. A thicker RuO_x film for the unannealed film is thus an aberration and since sputter rate is also not taken into account, it is very well possible for the porous layer to appear thicker than a heat treated film with the same initial oxide loading. A plot of Ru "thickness" *vs*. calcination time is overlaid on figure 5.21 in figure 6.17. With film porosity in mind, a tenable hypothesis can be presented regarding the relation between Ru "thickness" and polarization slope. The first point in figure 6.17 has been explained in section 5.2.3 (porosity and anodic corrosion). At 30min annealing, the porous structure has collapsed to an extent where anodic corrosion is eliminated, but the film still appears thicker than the 60min calcinated film, even though it could be expected that diffusion should have rendered a higher degree of depth distribution of Ru in this film (i.e. 60min should have a thicker Ru layer due to diffusion into Ti and/or TiO_x). At 60min annealing, all porosity has been eliminated and with substrate oxidation taking place, the behaviour of this electrocatalyst is as previously explained, i.e. oxidised Ti causes an increase in electrode

resistance at higher current densities and a higher polarization slope compared to the 30min sample transpires. The increase in measured "thickness" of Ru for the 120min and 240min calcinated films is assumed to be the result of diffusion and is within experimental repeatability. It was also mentioned in section 5.2.3 that binary mixed oxides are possibilities that furnish these electrodes its favourable properties. In terms of prolonged industrial applications, these oxides might also present improved stability over the 30min calcinated sample thus rendering a better option in terms of extensive use under anodic load.

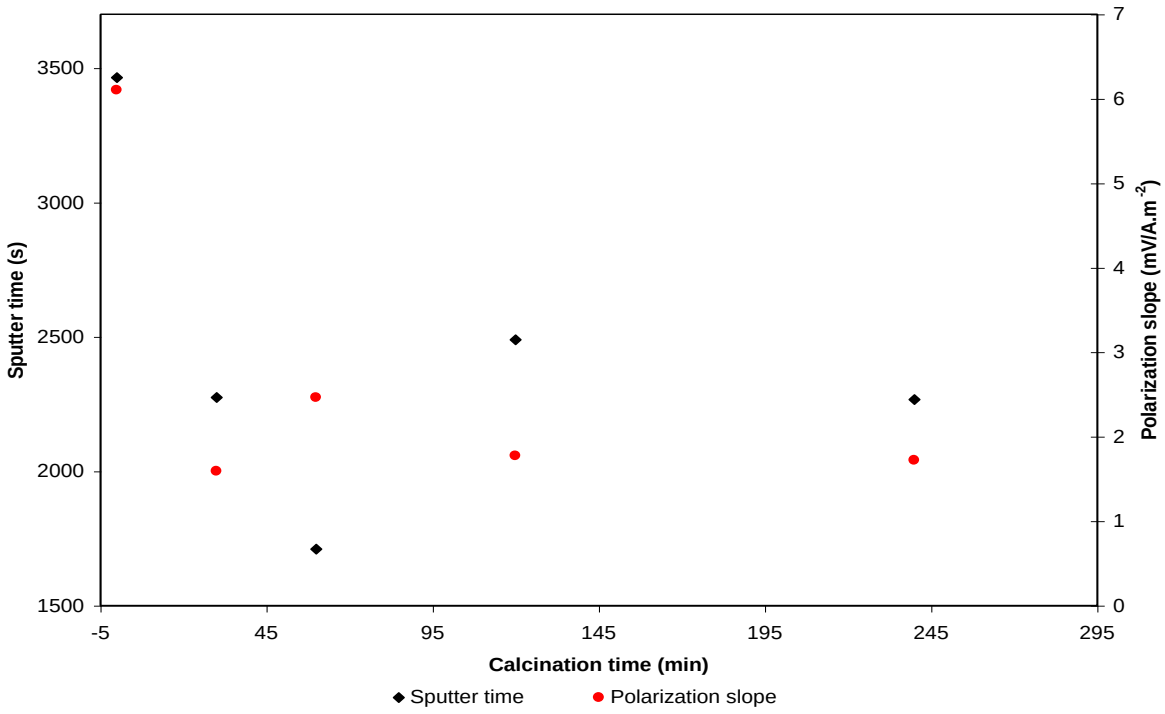

Figure 6.17: A comparison between Ru "thickness" and electrode performance under anodic load as a function of calcination time.

Data from the depth profiles are further exploited to probe the oxidation state of Ti as a function of the depth distribution of this metal. The significance of $\frac{APPH_{Ti(390eV)}}{APPH_{Ti(421eV)}}$ is described in section 2.5.1 (a value of 2 represents formal TiO_2 and the ratio will calculate to 0.7 for Ti metal). The extremes of an unannealed film and a $RuO_x.nH_2O$ film that was exposed for 240min at 600ºC are again used as prefatory examples in figures 6.18 and 6.19. A region of zero slope is present in figure 6.19 that is representative of a Ti compound which is absent from the unannealed sample. The compound is undoubtedly an oxide of Ti and the value of 1.4 represents Ti with an oxidation state $<4^+$, i.e. not formal TiO_2.

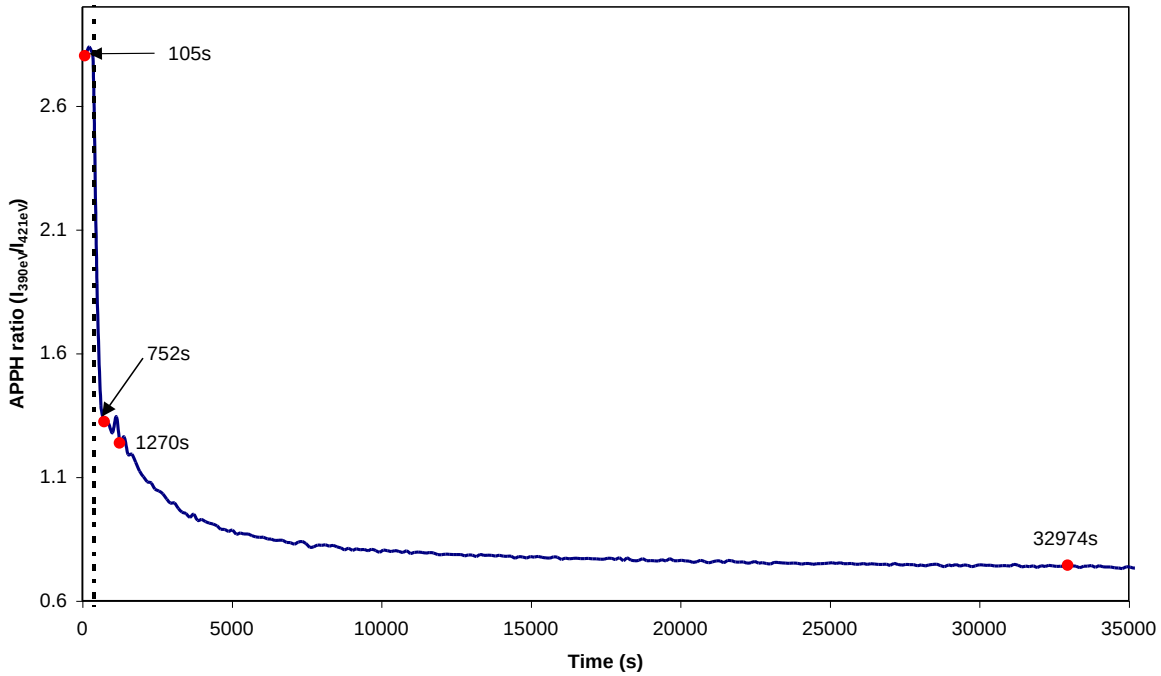

Figure 6.18: Graph of $\frac{APPH_{Ti(390eV)}}{APPH_{Ti(421eV)}}$ *vs*. sputter time for a $RuO_x.nH_2O$ film, no calcination.

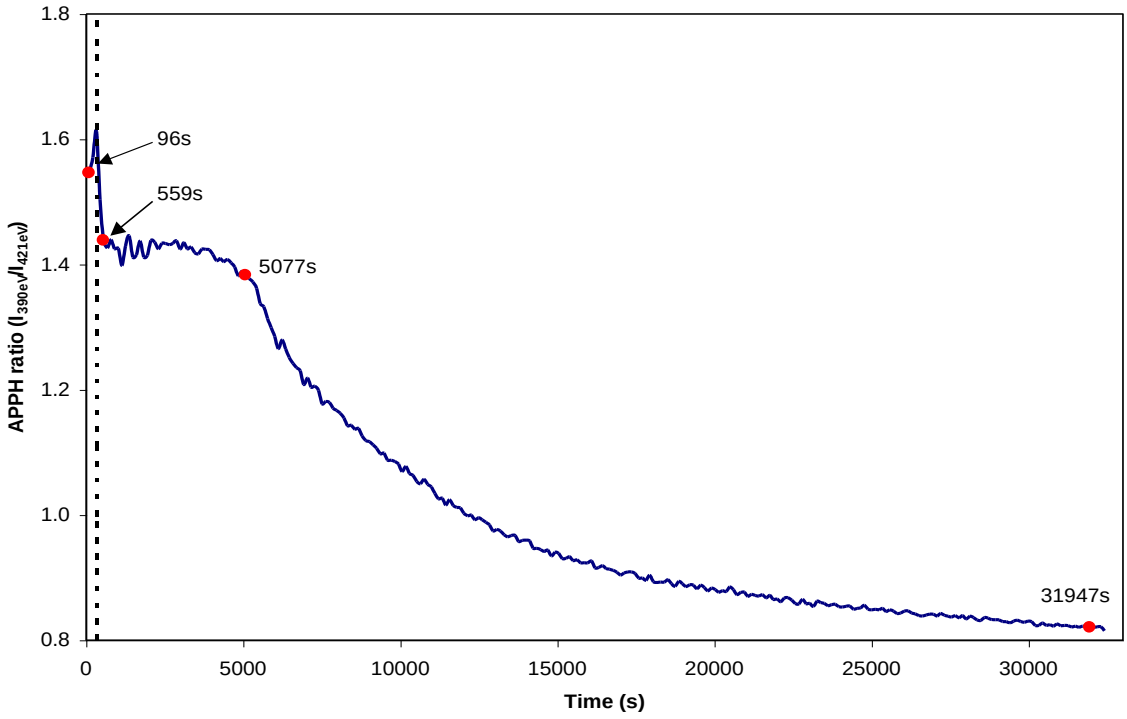

Figure 6.19: Graph of $\frac{APPH_{Ti(390eV)}}{APPH_{Ti(421eV)}}$ *vs*. sputter time for a $RuO_x.nH_2O$ film, heat-treatment at 600°C for 240min.

Indicated in figures 6.18 and 6.19 are points of which the differentiated Auger spectra are revealed in figures 6.20 and 6.21.

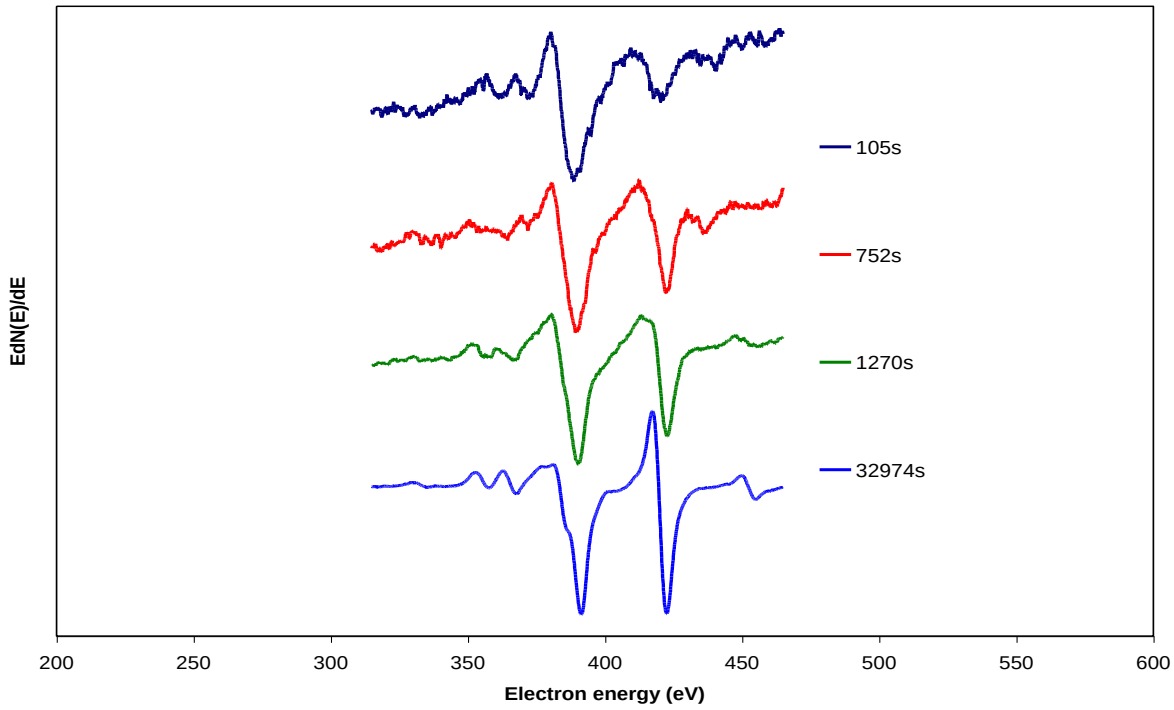

Figure 6.20: AES spectra of the points that are indicated in figure 6.18.

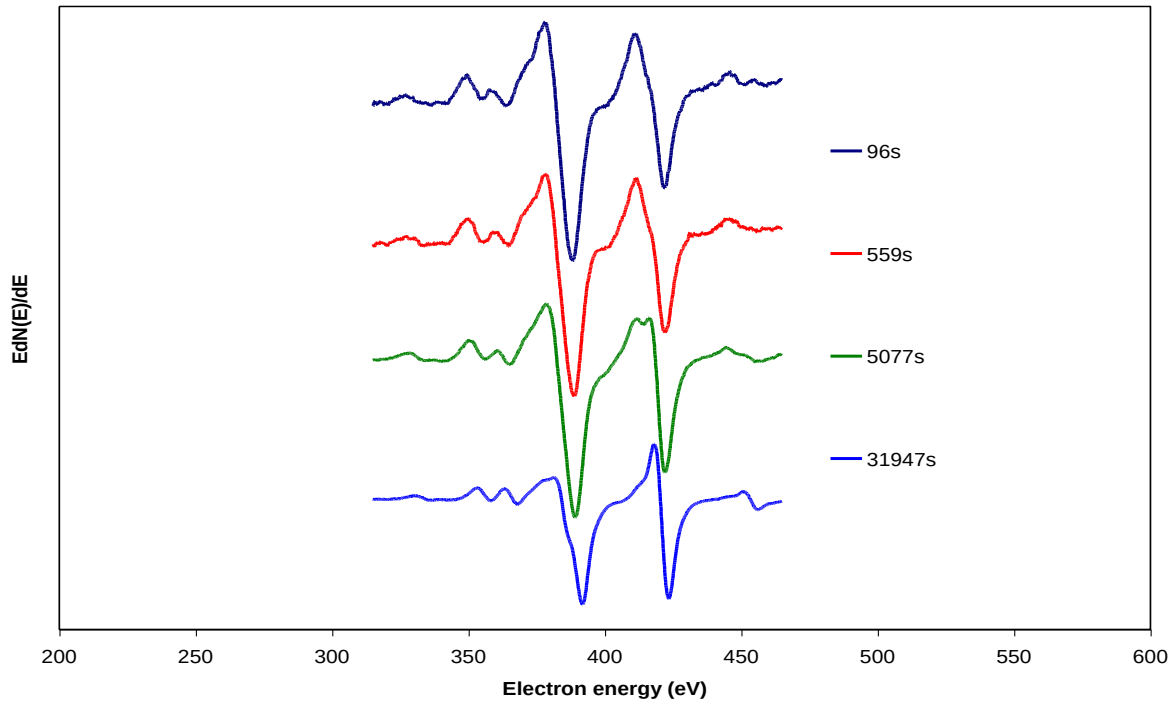

Figure 6.21: AES spectra of the points that are indicated in figure 6.19.

The peaks for the first two spectra in figure 6.20 are not well defined and comment regarding the significance of these peaks in terms of Ti oxidation state will be omitted. The “flat” shape of the maximum of the 421eV transition suggests that octahedral crystal field splitting is present and the existence of TiO is possible. The spectrum at the end of the depth profile has well defined peaks for all Ti transitions in the measured energy range and the most typical feature that confirms the existence of Ti metal is the edge between the minimum and maximum of the 390eV transition. The latter phenomenon in the Auger fine structure was described in section 2.5.1 as a shake-up line originating from the LMV (421eV) transition. Octahedral crystal field splitting is very prominent in the third spectrum in figure 6.21 as can be gathered from the resolved splitting of the maximum of the 421eV transition. TiO therefore definitely exists in the region of zero slope in figure 6.19.

6.3 Surface composition of thermally prepared binary mixed oxides.

The *modus operandi* regarding mathematical calculations to evaluate the surface composition of the thermally prepared samples is similar to the detail described in section 6.1. Examples of Auger transition identification are depicted in figures 6.22 and 6.23 for samples prepared with single and mixed precursor solutions respectively. These graphs immediately show a significantly higher Ru : Ti ratio for the surface that originates from the single component precursor compared to the film that was precipitated from the Ru/Ti mixed precursor solution. This is comprehensible from the fact that $TiCl_3$ makes part of the latter precursor and the formation of TiO_x is promoted. A summary of the measured Auger energies for the relevant transitions is given in table 6.5 for all the applicable samples. A direct comparison between the measured surface spectra at single points on the different sample surfaces is plotted in figures 6.24 and 6.25 for the samples originating from the respective precursor solutions. Inspection of these spectra reveals two facts. Firstly, there appears to be a significant quantity of C on all the measured points if the shape of the transition at 279eV is considered. A second ascertainable fact that follows from these graphs is that there are no definite trends and consequently no readily observable difference in the Ru and Ti quantities on samples that are prepared with the same precursor solution (i.e. single or mixed component) with different concentrations of Ru in these solutions.

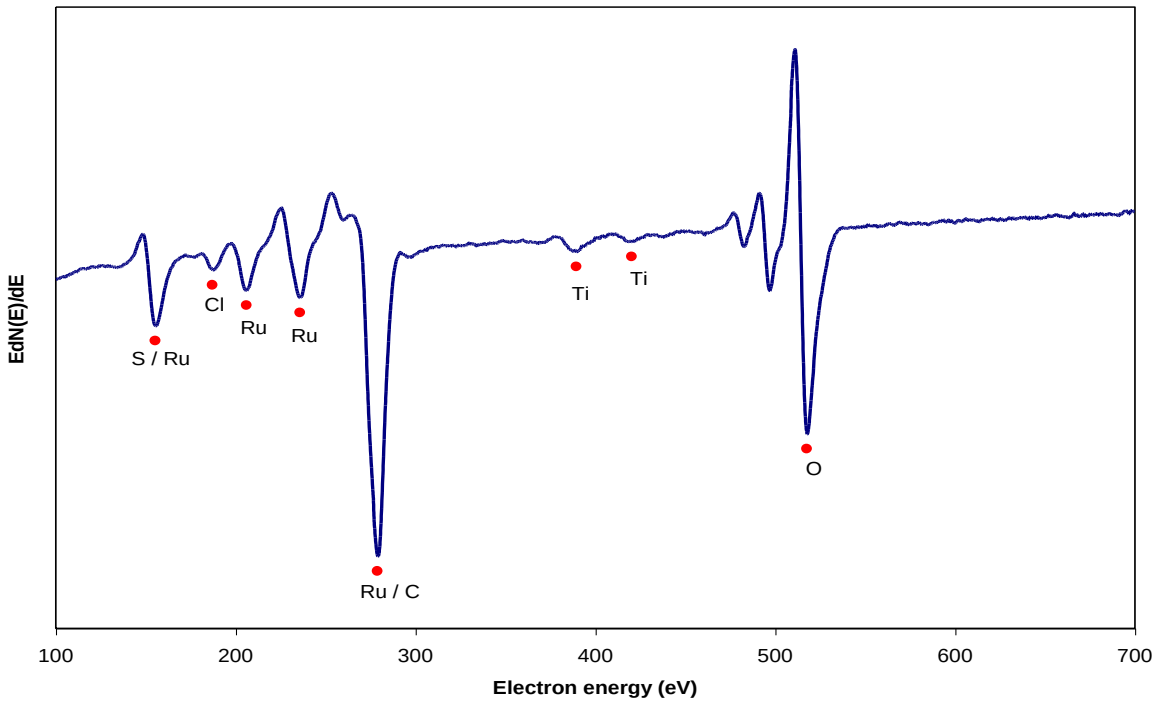

Figure 6.22: AES spectrum of the surface of an oxide film as prepared *via* thermal decomposition of a 3.21wt/wt% Ru precursor solution.

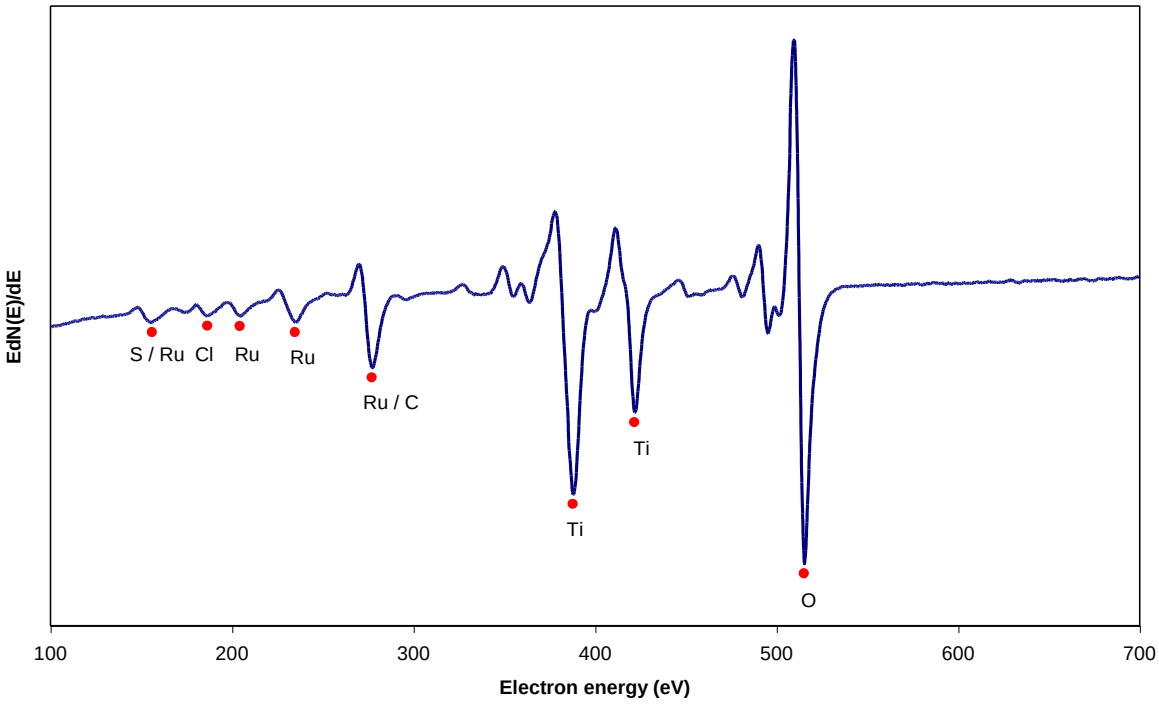

Figure 6.23: AES spectrum of the surface of an oxide film as prepared *via* thermal decomposition of a precursor solution containing 3.75wt/wt% Ru and 3.75wt/wt% Ti.

Transition	% Ru in precursor						Hedberg [104]
	Single component (wt/wt% Ru)			Ru / Ti mixed precursor (wt/wt% Ru)			
	0.8	3.21	10	2.25	3.75	5.25	
	Measured energy (eV)						Energy (eV)
S (LVV)	155.8	155.5	155.1	154.1	156.2	156.2	153
Cl (LVV)	187.7	187.3	187.7	185.8	186.6	186.3	184
Ru (MNN)	206.2	206.2	205.5	203.8	204.5	204.8	-
Ru (MNN)	236.0	236.0	236.3	234.4	234.9	234.2	235
Ru (MNN) / C (KLL)	279.7	279.0	279.0	276.5	277.3	276.6	277 / 275
Ti (LMM)	387.5	389.6	387.2	387.7	387.9	387.5	390
Ti (LMM)	421.1	420.4	421.1	421.7	421.8	421.5	421
O (KLL)	518.1	517.7	517.7	514.9	515.3	514.6	510

Table 6.5: Energy positions of Auger transitions for the thermally prepared samples.

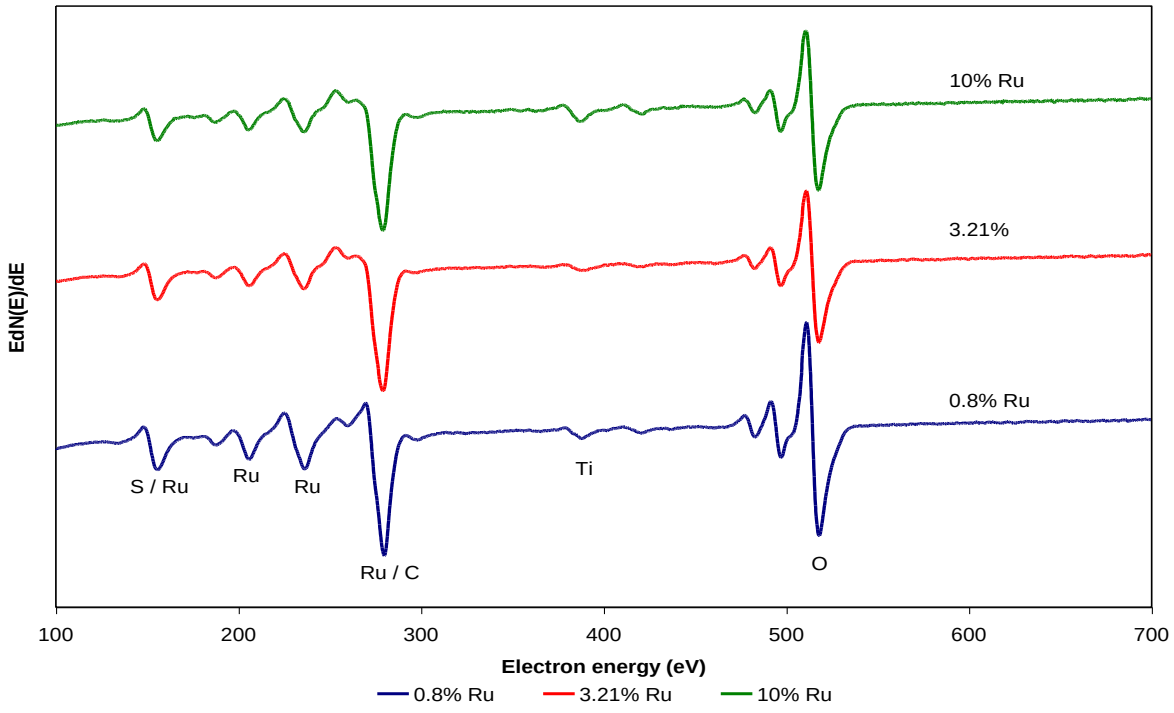

Figure 6.24: AES spectra of the surface of films from the single component precursor solutions using different Ru concentrations.

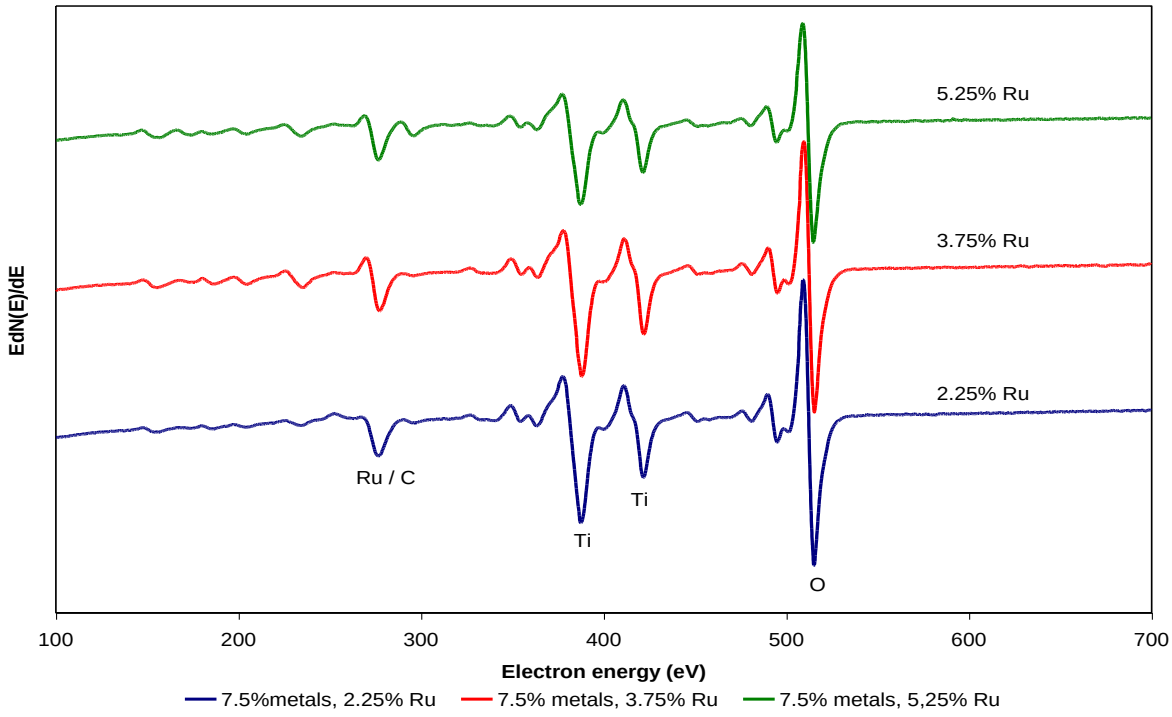

Figure 6.25: AES spectra of the surface of films from the mixed precursor solutions using different Ru concentrations (total metal concentration is constant at 7.5wt/wt%).

With the omission of the K (252eV) transition, an indication of the atomic concentrations of Ru, Ti and O was obtained with the use of equation 3.21 and the published values for S_i (3keV) as given in table 6.2. The contribution of C were again not included in equation 3.21 and precise values are therefore not expected, but a relative indication of the concentrations is nonetheless of value. The contribution of S to the transition at 155eV were again deconvoluted using equation 6.2 as described in section 6.1 with the k values summarised in table 6.6. The average concentration values in table 6.6 were again calculated from 5 different measurements on each sample's surface. Two examples of the homogeneous nature of thermally prepared oxide films can be inspected in figures 6.26 and 6.27.

Precursor	k	Ave. at% Ru	Max. (at%)	Min. (at%)
0.8wt/wt% Ru	0.28	24	29	13
3.21wt/wt% Ru	0.26	26	26	25
10wt/wt% Ru	0.28	21	23	17
2.25wt/wt% Ru & 5.25wt/wt% Ti	0.26	2	3	1
3.75wt/wt% Ru & 3.75wt/wt% Ti	0.27	6	6	5
5.25wt/wt% Ru & 2.25wt/wt% Ti	0.25	6	7	5
Precursor	**k**	**Ave. at% Ti**	**Max. (at%)**	**Min. (at%)**
0.8wt/wt% Ru	0.28	7	19	3
3.21wt/wt% Ru	0.26	3	4	3
10wt/wt% Ru	0.28	10	15	7
2.25wt/wt% Ru & 5.25wt/wt% Ti	0.26	34	36	32
3.75wt/wt% Ru & 3.75wt/wt% Ti	0.27	34	35	33
5.25wt/wt% Ru & 2.25wt/wt% Ti	0.25	32	32	31
Precursor	**k**	**Ave. at% O**	**Max. (at%)**	**Min. (at%)**
0.8wt/wt% Ru	0.28	67	68	65
3.21wt/wt% Ru	0.26	67	69	67
10wt/wt% Ru	0.28	67	68	66
2.25wt/wt% Ru & 5.25wt/wt% Ti	0.26	64	67	61
3.75wt/wt% Ru & 3.75wt/wt% Ti	0.27	60	61	58
5.25wt/wt% Ru & 2.25wt/wt% Ti	0.25	62	62	61

Table 6.6: Atomic concentrations of Ru, Ti and O on the surface of thermal samples.

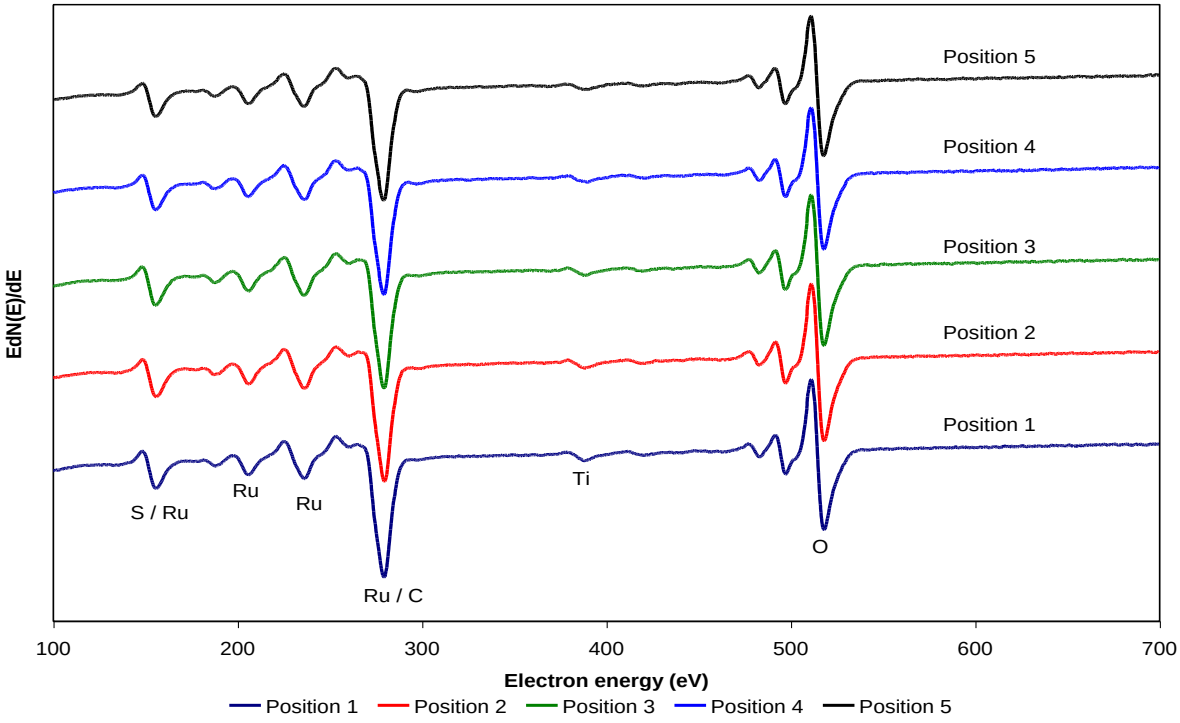

Figure 6.26: Graph of the comparison between AES spectra that were taken at different positions on the same sample, precursor solution: 3.21wt/wt% Ru.

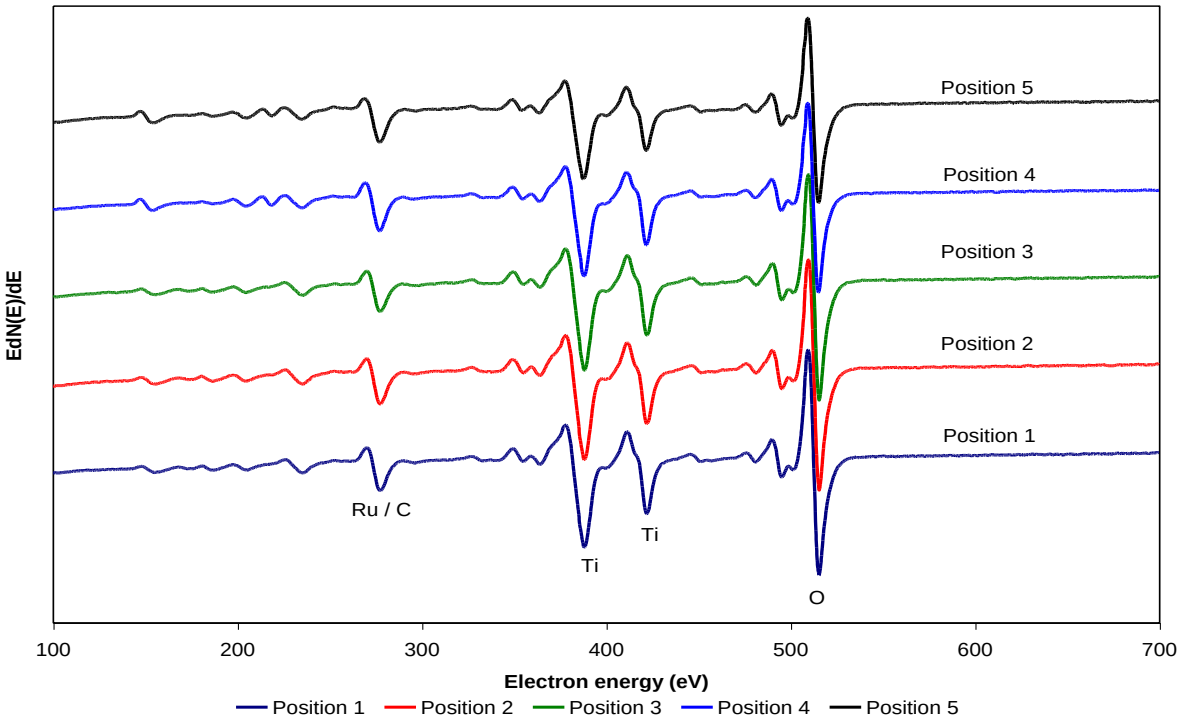

Figure 6.27: Graph of the comparison between AES spectra that were taken at different positions on the same sample, precursor solution: 3.75wt/wt% Ru & 3.75wt/wt% Ti.

It was concluded from chapter 5 that electrode polarization at 100.5A.m^{-2} is independent of Ru content in the precursor solution within the range of experimentation. This can be regarded as somewhat of a counter-intuitive result if the differences in Ru concentration in the precursors are considered. Moreover, this observation presents an even greater challenge to convention if the Ru concentration on the electrodes' surfaces is evaluated from table 6.6. The at% Ru on the outermost surface of the samples from the single component precursor solutions is taken as indistinguishable between 21at% and 26at% (a result that is also informative if the range of Ru concentrations in the precursors is taken into consideration) as suggested by the elementary calculations applied here. The surface concentration of Ru on the electrocatalysts from the Ru/Ti mixed solutions is calculated at 2at% Ru for the 2.25wt/wt% Ru precursor and 6at% Ru for samples that were produced with the 3.75wt/wt% and 5.25wt/wt% Ru solutions. With the latter variation set aside, there remains a definite difference of roughly 20at% Ru in the surface composition of films created with the two groups of precursor solutions. This difference in surface concentration of Ru corresponds with the prediction that was made using figures 6.22 and 6.23 at the beginning of this section, yet the 100.5A.m^{-2} polarization remains unaffected.

The surface concentration of Ru on electrochemically prepared samples can now also be put into perspective. The applicable values are mentioned below to have a direct comparison between differently prepared samples:

(a) Cyclic voltammetry: 30at% to 46at% Ru,
(b) Thermal decomposition of single component precursor: 21at% to 26at% Ru,
(c) Thermal decomposition of Ru/Ti mixed component precursor: 2at% to 6at% Ru.

Although the surface concentration of Ru does not control electrode polarization at 100.5A.m^{-2}, it is apparent from tables 5.1 and 5.3 in conjunction with points (b) and (c) that the rate of change in polarization at higher current densities (155A.m^{-2} to 170A.m^{-2}) could be influenced by the surface concentration of Ru (for thermally prepared electrocatalysts). The following section will evaluate the significance of the depth distribution of Ru on the polarization resistance of the thermally prepared DSA samples.

6.4 AES depth profiling on thermally prepared binary mixed oxides.

APPH values and sputter times in all depth profiles in this section are again normalised as previously described. Deconvolution of S was also done according to the discussed method. Duplicate depth profiles on a sample prepared from 2.25wt/wt% Ru (Ru/Ti mixed precursor) is revealed in figures 6.28 and 6.29. Homogeneity of the electrocatalytic layer is verifiable if the elemental traces in figures 6.30 and 6.31 are compared with figures 6.28 and 6.29. The depth distribution of Ru, Ti and O in figure 6.30 (sample prepared with 3.75wt/wt% Ru) was confirmed with a second profile and the pattern in this profile could be elucidated if the method of preparation is considered. Although not very prominent, three regions in the Ru distribution are identifiable and indicated in figure 6.30. It is proposed that each region correspond with a $RuCl_3$ / $TiCl_3$ application and annealing step. The layer nearest to the surface has a definite peak in terms of Ru concentration compared to the other layers. This gives further evidence of the proposed hypothesis since the first two layers were exposed to duplicate and triplicate heat treatments and diffusion is therefore a possibility to cause broadening of the Ru peaks.

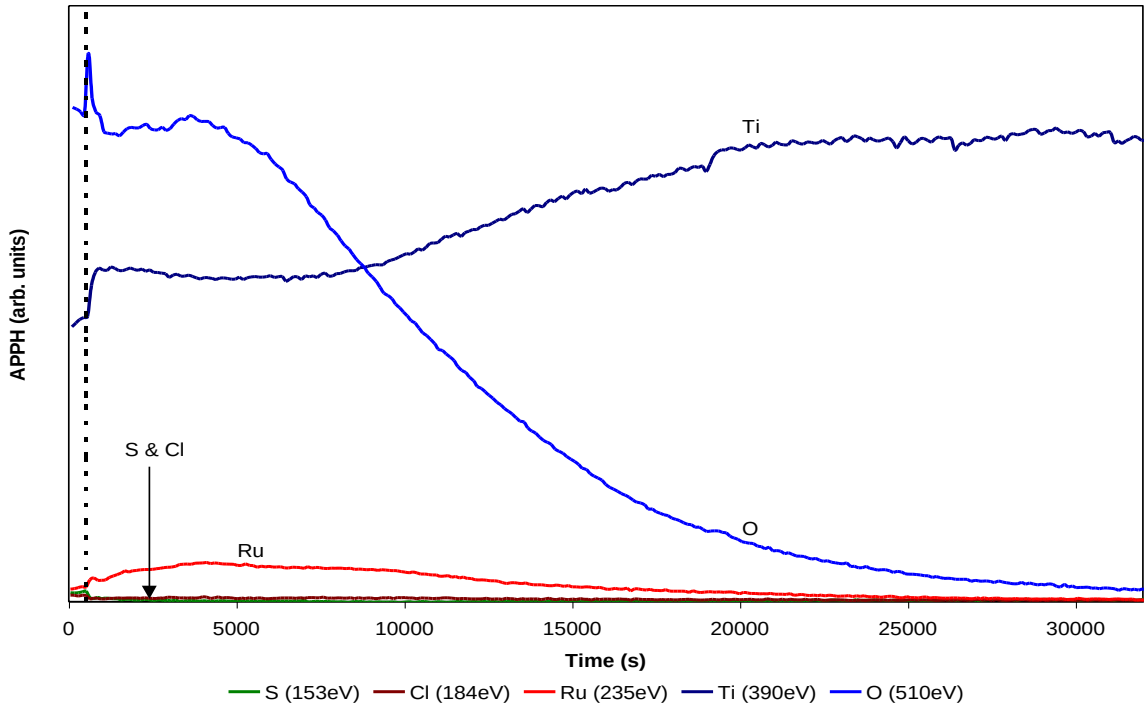

Figure 6.28: AES depth profile through an oxide film that was precipitated from a 2.25wt/wt% Ru & 5.25wt/wt% Ti precursor.

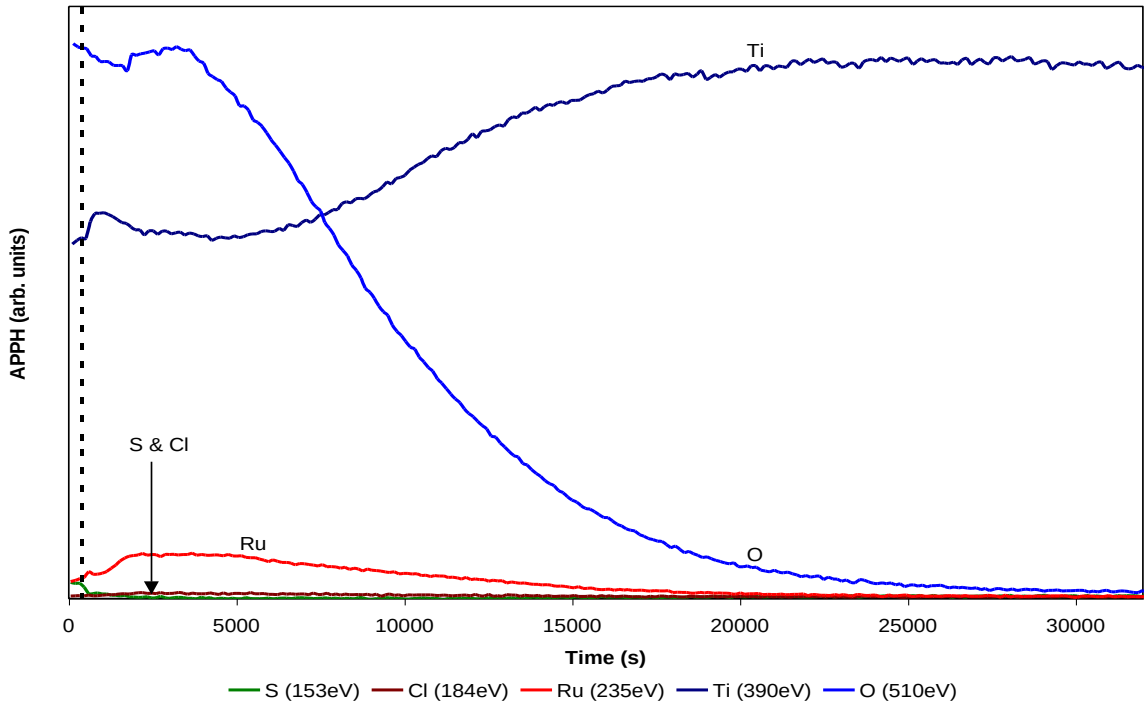

Figure 6.29: AES depth profile through an oxide film that was precipitated from a 2.25wt/wt% Ru & 5.25wt/wt% Ti precursor, repeat analysis of depth profile in figure 6.28.

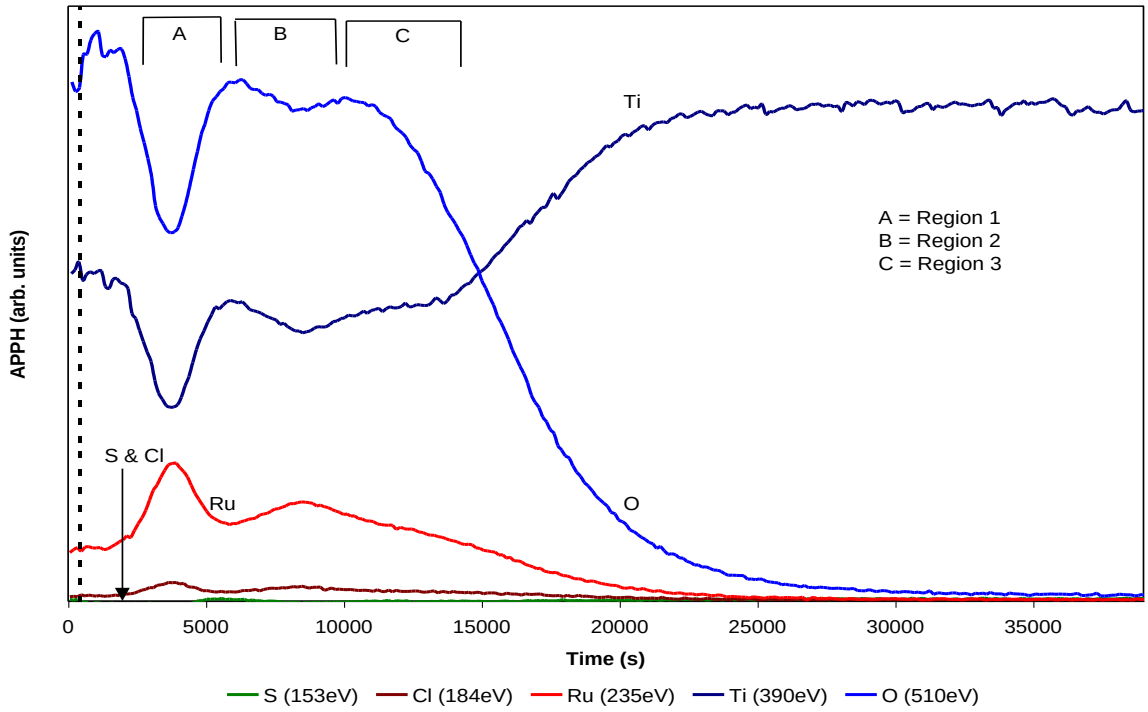

Figure 6.30: AES depth profile through an oxide film that was precipitated from a 3.75wt/wt% Ru & 3.75wt/wt% Ti precursor.

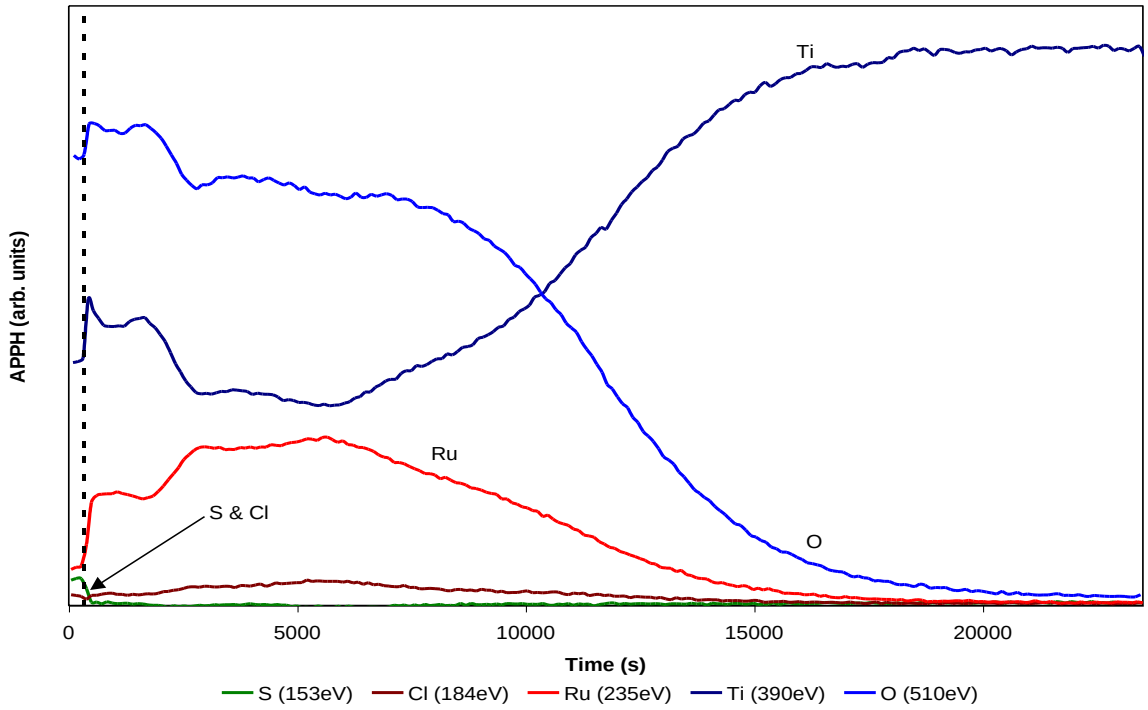

Figure 6.31: AES depth profile through an oxide film that was precipitated from a 5.25wt/wt% Ru & 2.25wt/wt% Ti precursor.

Interfacing in the Ru profile for the sample from the 5.25wt/wt% Ru precursor is also evident to some degree. The only way to explain the absence of layer formation on the sample from the 2.25wt/wt% Ru precursor solution is to assume variation in preparation between samples.

A direct comparison between the Ru profiles for the samples prepared with the Ru/Ti mixed precursor solutions in figure 6.32 is yet another attempt to evaluate differences in film composition. Visual inspection of the curves immediately suggests that a higher concentration of Ru in the precursor solution causes an increase in the quantity of Ru in the oxide film. The areas under the curves are presented as a function of polarization slope (from table 5.1) in figure 6.33. A linear relation in this figure is in agreement with the result in figure 5.4 where the polarization slope shows a linear decrease with respect to an increasing intensity of the diffraction signal from the (1 1 0) plane. Thus, a higher intensity diffraction peak indicates more RuO_2, just as a larger area under the Ru profile is indicative of a thicker distribution of Ru in the RuO_2 film and both these measured quantities are linked to the electrodes' polarization slopes.

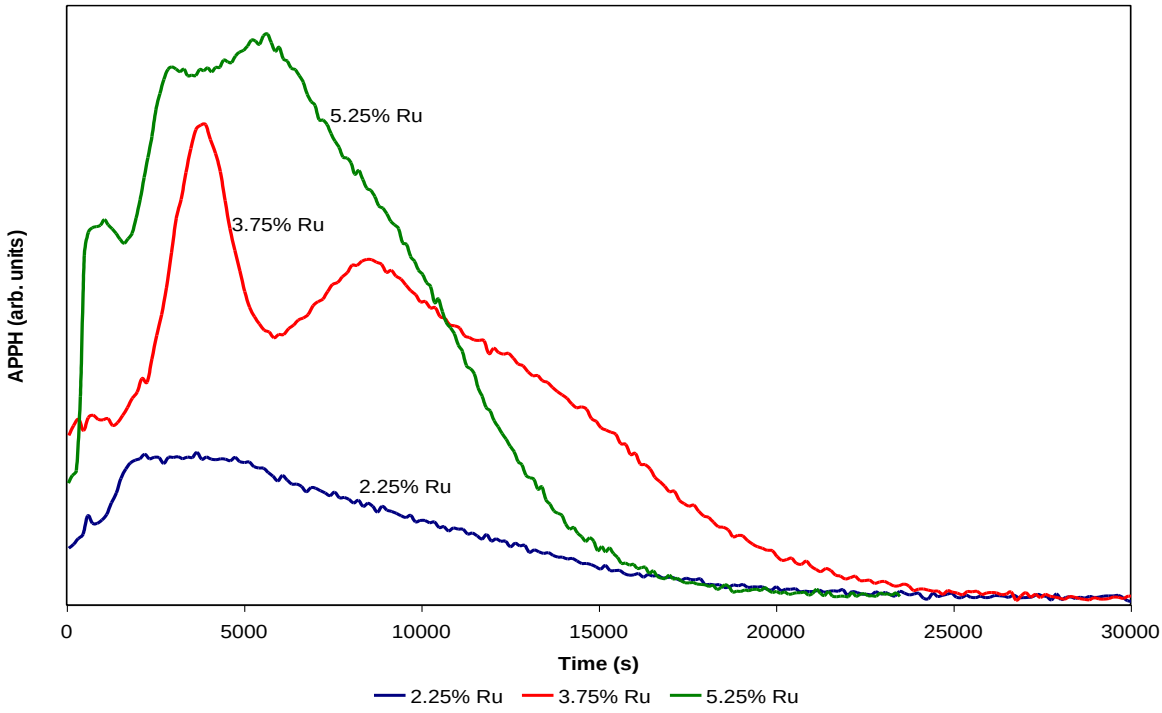

Figure 6.32: Graph to illustrate the difference in the Ru traces from the depth profiles on samples that were prepared with different Ru/Ti mixed precursor solutions.

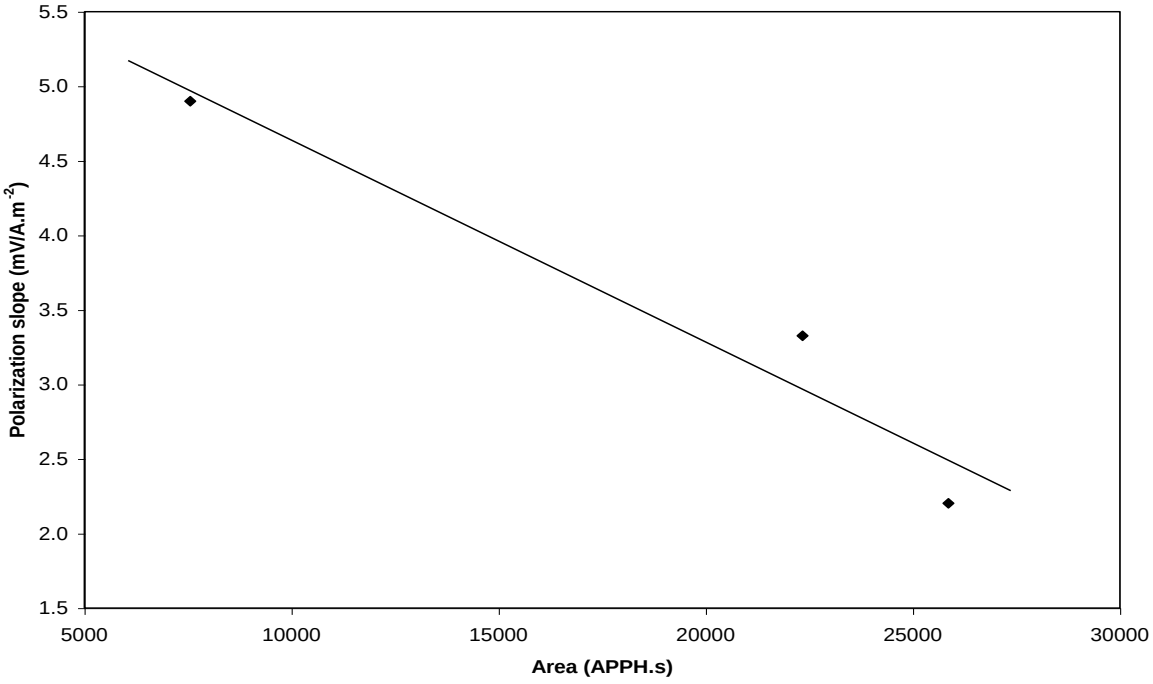

Figure 6.33: Graph of the area under the Ru profiles in figure 6.32 *vs*. polarization slope.

A plot of $\frac{APPH_{Ti(390eV)}}{APPH_{Ti(421eV)}}$ *vs.* sputter time in figure 6.34 evaluates the oxidation state of Ti in the oxide film. The region of zero slope at a value of 1.4 gives evidence of Ti with an oxidation state that is intermediate between formal TiO_2 and TiO. The Auger spectrum at 15307s in figure 6.35 is the best representation of TiO at a ratio of 1.17. Splitting of the positive excursion of the LMV transition (421eV) also shows the existence of octahedral crystal field splitting. Formal Ti metal can be recognised at 34997s *via* interpretation of the shape of the Ti transitions at 390eV and 421eV as well as the existence of the Ti (LVV) transition at 451eV. Although differences can be observed, the $\frac{APPH_{Ti(390eV)}}{APPH_{Ti(421eV)}}$ depth ratios for the three samples from the different mixed precursor solutions are very similar and no further discussion can be presented on its significance.

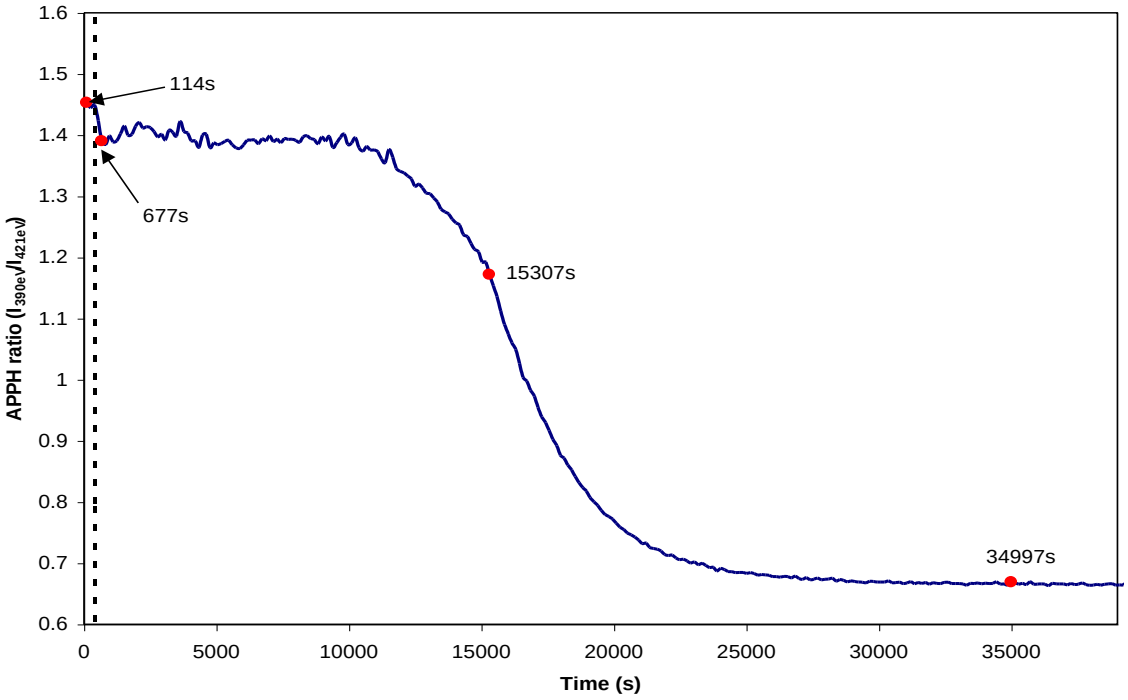

Figure 6.34: Graph of $\frac{APPH_{Ti(390eV)}}{APPH_{Ti(421eV)}}$ *vs.* sputter time for the oxide film from the 3.75wt/wt% Ru and 3.75wt/wt% Ti mixed precursor.

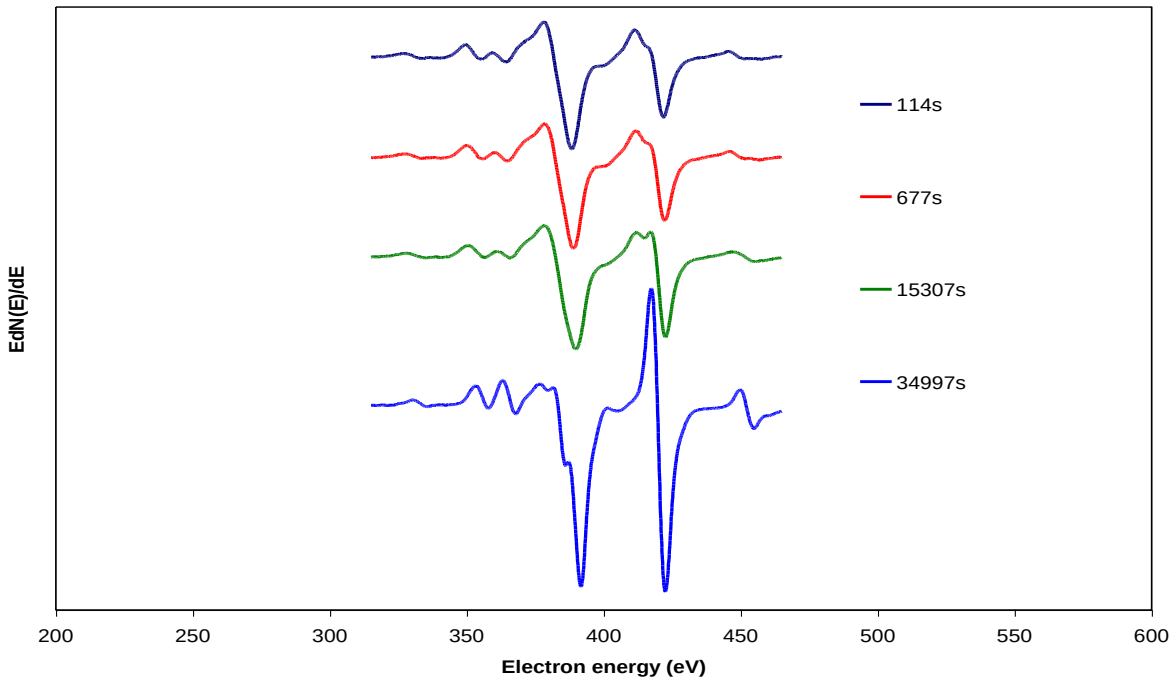

Figure 6.35: AES spectra at the different points as identified in figure 6.34, 3.75wt/wt% Ru and 3.75wt/wt% Ti mixed precursor.

A depth profile through a film prepared with 0.8wt/wt% Ru single precursor in figure 6.36 is given more attention in figure 6.37 in terms of the homogeneity and/or repeatability of the depth distribution of Ru. It is deduced from this result that the film can be regarded as being remarkably homogeneous given the robust nature of the preparation technique. A direct comparison between the Ru traces for DSA samples that were prepared with the different concentrations of single component precursor solutions is plotted in figure 6.38 together with the Ru profile of a sample that was prepared with 5.25wt/wt% Ru in a mixed precursor solution. This result is very informative and it reveals a very important finding regarding the use of RuO_2 containing oxide electrodes for MnO_2 electroplating. It has already been mentioned in the final paragraph of section 6.3 that the surface concentration of Ru in thermally prepared films could be the controlling factor in terms of electrode polarization at $155A.m^{-2}$ to $170A.m^{-2}$. Depth profiling has now conclusively shown that the depth distribution of Ru is far greater for a film from a mixed precursor solution. The films from single component precursor solutions however remains the best at lowering electrode polarization at higher current densities. Thus, the ability of an oxide electrode to retard passivation is enhanced by the outer concentration of Ru in the film to a much greater extent than by the overall thickness of the RuO_2 layer.

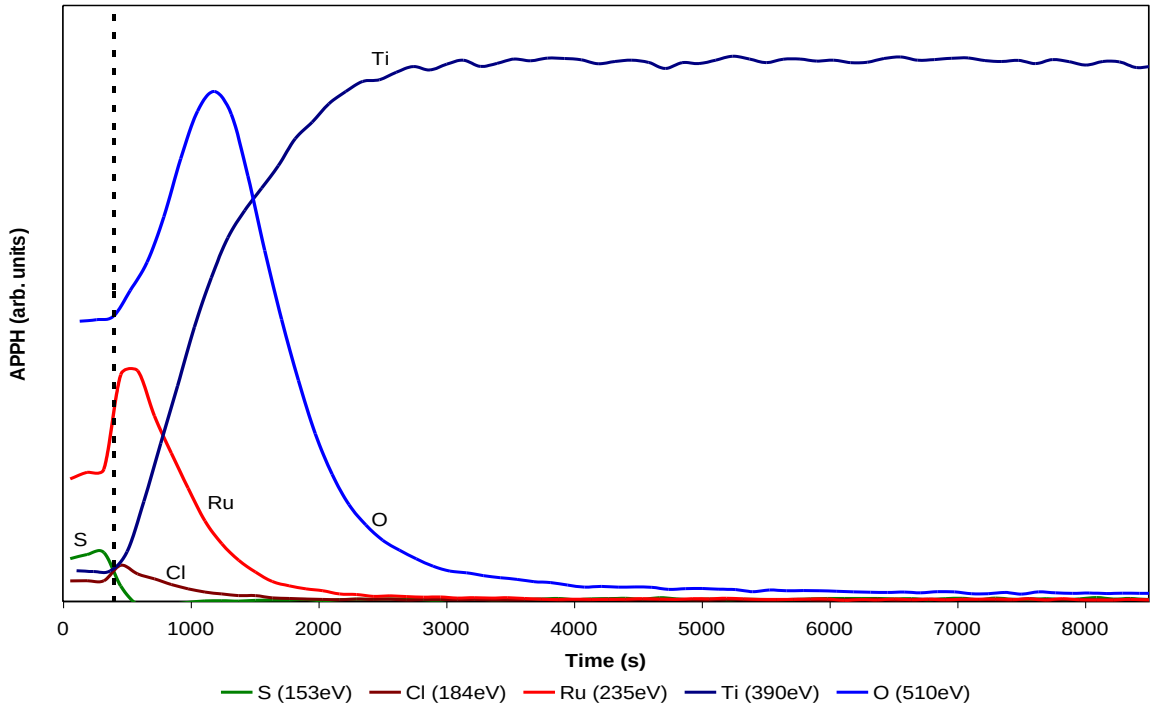

Figure 6.36: AES depth profile through an oxide film as prepared *via* thermal decomposition of a 0.8wt/wt% Ru solution.

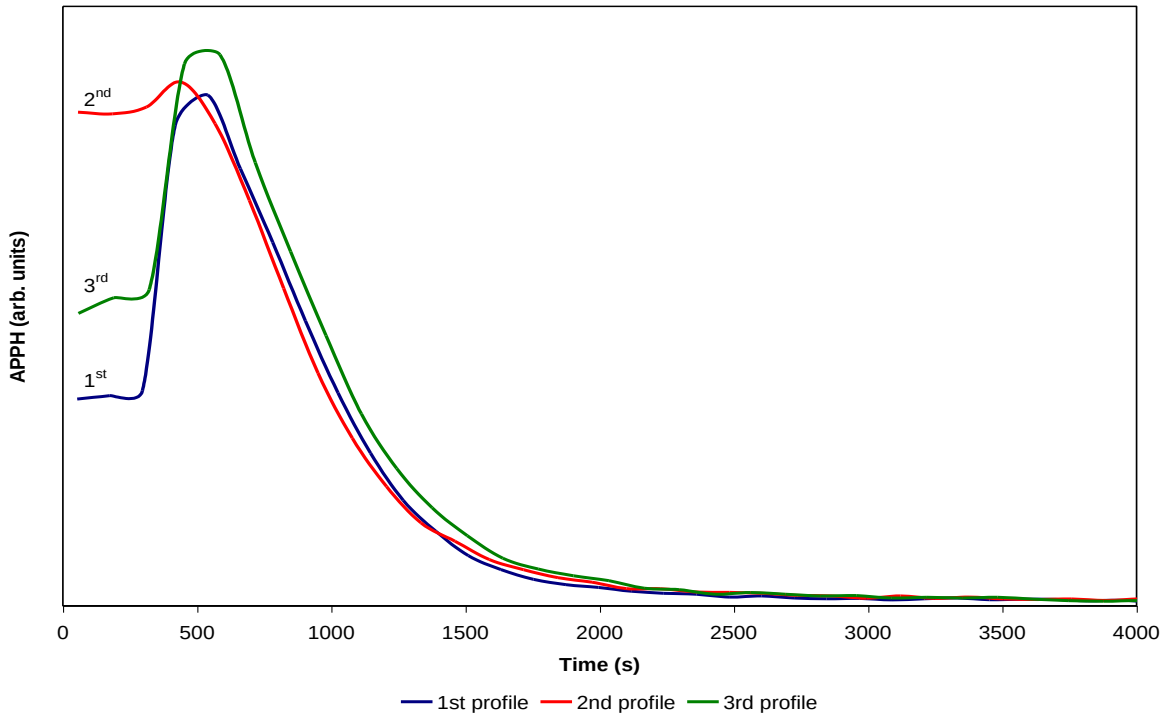

Figure 6.37: Ru traces of three repeated depth profiles on a sample as prepared with a 0.8wt/wt% Ru solution.

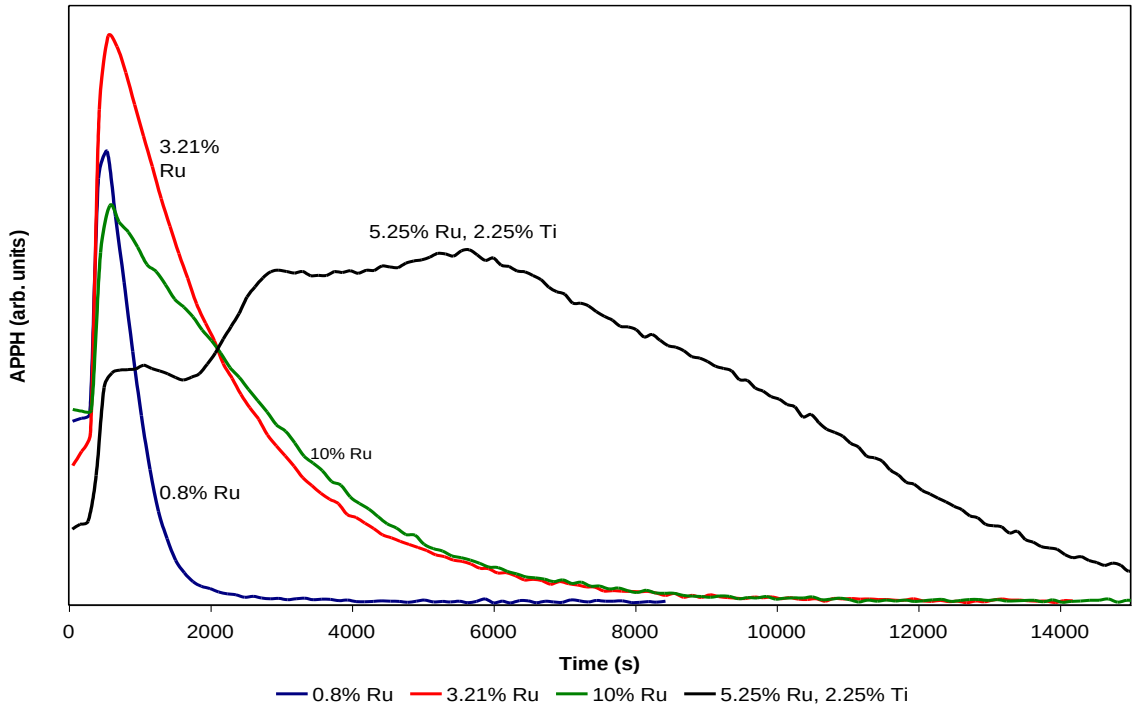

Figure 6.38: Illustration of the difference in the depth distribution of Ru between samples from the single component precursor solutions as well as a comparison with an oxide film from the 5.25wt/wt% Ru & 2.25wt/wt% Ti solution.

The Ti oxidation state was again obtained by evaluating the $\frac{APPH_{Ti(390eV)}}{APPH_{Ti(421eV)}}$ ratio as a function of sputter time. The example in figure 6.39 represents the film from the 0.8wt/wt% Ru solution. The existence of TiO is confirmed by the fine structure of the spectrum at 1070s in figure 6.40, while the value of the ratio denies the presence of any TiO_2. The oxidation curves for the other two thermal oxide films (3.21wt/wt% and 10wt/wt% Ru precursor solutions) have a similar form than the latter. These curves have a definite different shape in compared to the films from the mixed oxides and voltammetrically grown films. A possible reason for this is sensitivity towards electron and ion radiation of the oxide films from the single component precursor solutions.

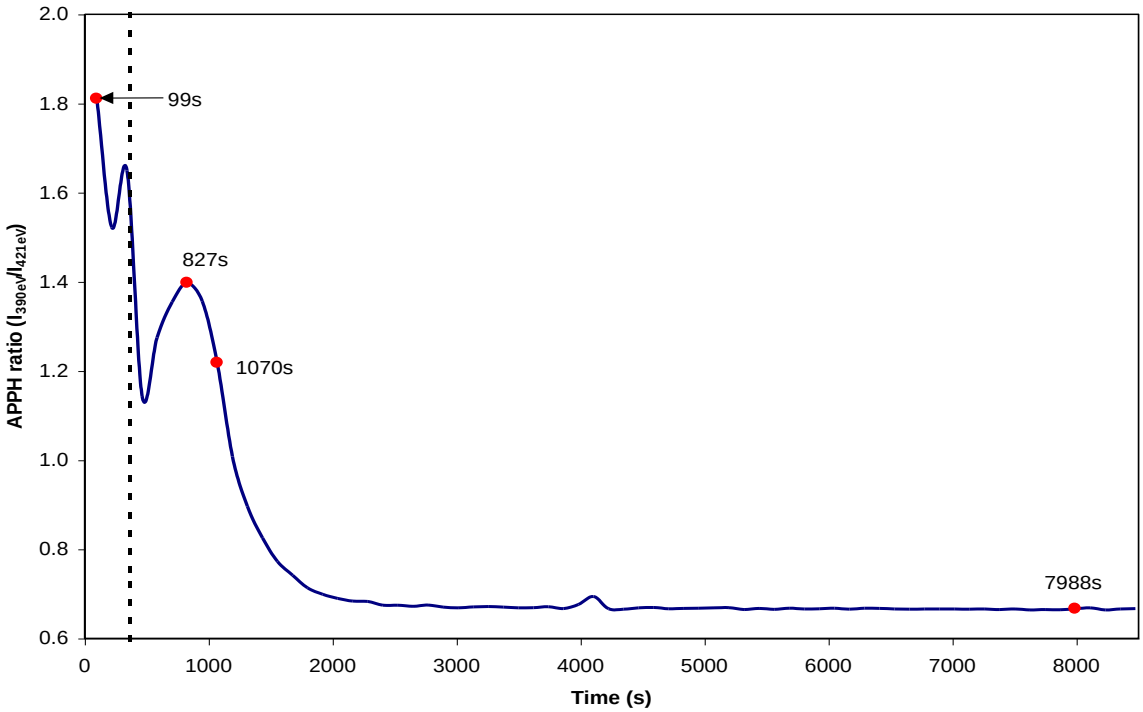

Figure 6.39: $\frac{\text{APPH}_{\text{Ti(390eV)}}}{\text{APPH}_{\text{Ti(421eV)}}}$ *vs.* sputter time for the oxide film from the 0.8wt/wt% Ru precursor. Dotted line indicates the onset of sputtering.

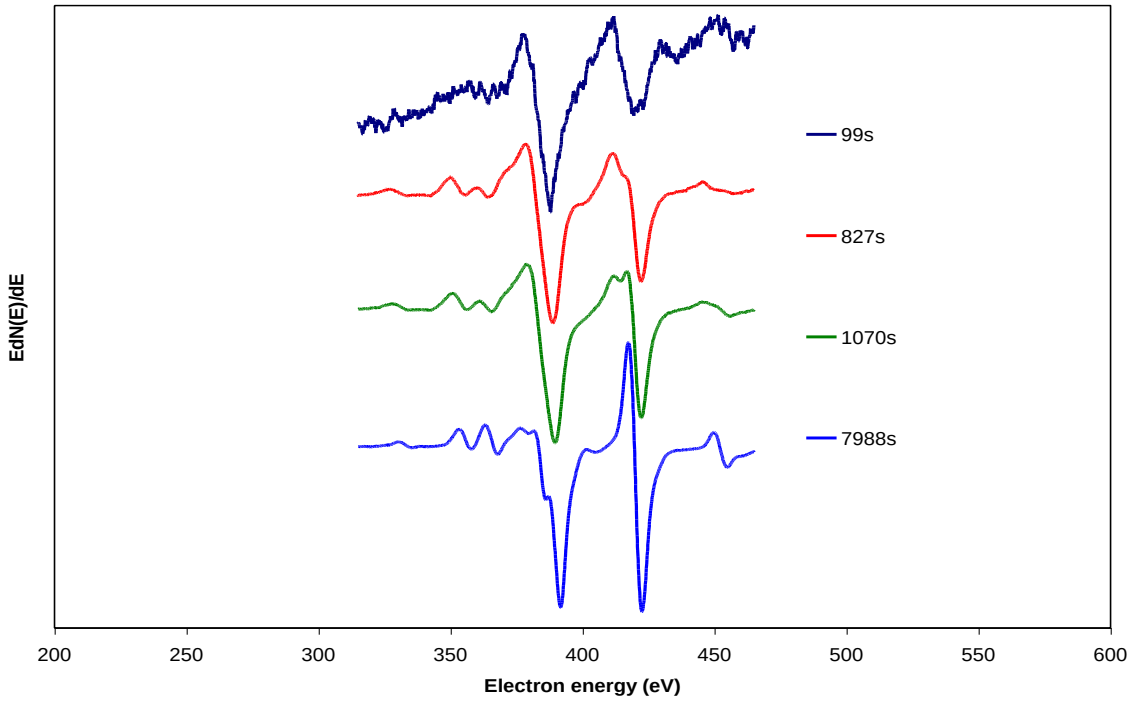

Figure 6.40: AES spectra at the different points as identified in figure 6.39.

6.5 AES measurements on TiC and Ti-Mn composite electrodes.

The surface composition of the Ti-Mn composite sample can be identified in figure 6.41. The peaks of relevance are identified and evaluated in table 6.7 in terms of its exact measured energies.

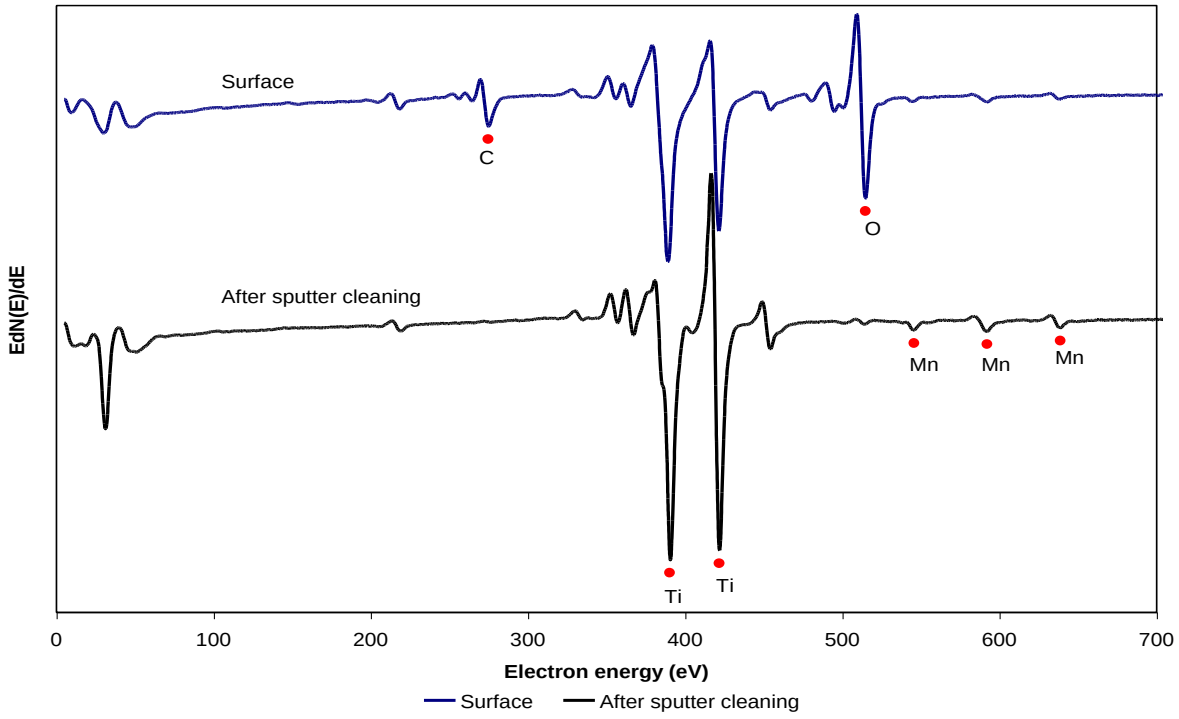

Figure 6.41: AES spectra of the surface of the Ti-Mn composite metal.

Transition	Measured energy (eV)	Energy (eV), [104]
C (KLL)	275	275
Ti (LMM)	390.5	390
Ti (LMM)	422	421
O (KLL)	515	510
Mn (MNN)	546	545
Mn (MNN)	592.5	592
Mn (MNN)	639	638

Table 6.7: Energy positions of transitions from the surface of a polished and sputter-cleaned surface of Ti-Mn.

AES measurements on the Ti-Mn composite sample served the purpose of quantitative evaluation of the metal's composition. Sensitivity factors for Ti, (S_{Ti}) and Mn (S_{Mn}) were experimentally determined for the specific AES system. Equations 6.4 and 6.5 are used to determine the applicable sensitivity factors and Cu can be recognised as the reference sensitivity factor according to equation 3.20.

$$S_{Ti} = \left(\frac{\rho_{Cu}}{\rho_{Ti}}\right)\left(\frac{APPH_{Ti(390eV)}}{APPH_{Cu(922eV)}}\right)1 \quad \text{.....(6.4)}$$

$$S_{Mn} = \left(\frac{\rho_{Cu}}{\rho_{Mn}}\right)\left(\frac{APPH_{Mn(592eV)}}{APPH_{Cu(922eV)}}\right)1 \quad \text{.....(6.5)}$$

The atomic density, ρ_i, for each element is calculated with equation 6.6.

$$\rho_i = \frac{(D_i)(\text{Avogadro's number})}{M_r(i)} \quad \text{.....(6.6)}$$

All variables for the calculation of ρ_i are summarised in table 6.8. Values for density, D_i, and atomic masses, $M_r(i)$ were taken from reference [128]. All APPH values were determined from sputter-cleaned surfaces.

Transition	APPH	D_i (g.cm^{-3})	$M_r(i)$ (g.mol^{-1})	ρ_i (atoms.cm^{-3})
Cu (922eV)	6.336	8.93	63.54	8.464 x 10^{22}
Ti (390eV)	6.926	4.507	47.9	5.666 x 10^{22}
Mn (592eV)	6.088	7.47	54.938	8.188 x 10^{22}
S_{Ti} = 1.633; S_{Mn} = 0.993				

Table 6.8: Summary of variables for the calculation of ρ_i.

The atomic fractions of Ti (X_{Ti}) and Mn (X_{Mn}) were determined at four arbitrary positions on the sample. Calculations were done using equation 3.21. The results in table 6.9 show that the Ti-Mn sample contains an average of 90at% Ti and 10at% Mn.

$APPH_{Ti(390eV)}$	$APPH_{Mn(592eV)}$	X_{Ti}	X_{Mn}
5.780	0.426	0.89	0.11
6.207	0.333	0.92	0.08
6.207	0.402	0.90	0.10
6.021	0.385	0.90	0.10

Table 6.9: Results on the elemental composition of the Ti-Mn composite.

Depth profiling on the Ti/TiC sample served the purpose of identifying C as carbide in the C-Ti bonding state. The depth distribution of O is overlaid on the $\frac{APPH_{Ti(390eV)}}{APPH_{Ti(421eV)}}$ ratio behaviour in figure 6.42. The O void between 600s and 5500s is the result of the presence of evaporated C. The increase in $APPH_{O(510eV)}$ at 5500s is regarded as an oxide on the metal surface prior to C coating. The $\frac{APPH_{Ti(390eV)}}{APPH_{Ti(421eV)}}$ ratio in the absence of O serves as proof of Ti existing in a chemical state that differs from Ti metal, i.e. the ratio $\neq 0.7$. The Auger spectra of C on the surface and at point A in the profile is compared in figure 6.43. The fine structure of the two spectra reveals the desired information, i.e. there exists two chemical states of C on the sample. The surface spectrum represents C in the C-C bonding state (graphite) and C in the C-Ti bonding state (carbide) takes the form of the spectrum at point A. A change in energy of the C KVV transition going from graphite to carbide is found to be 1eV. This correlates with the findings of M. Maline *et. al.* [129] who illustrated that the C KVV non-differentiated peak shifts from 267eV for the C-C bonding state to 269eV for C in the C-Ti bonding state. This change in the Auger fine structure and energy position follows from the fact that C in the C-C bonding state is sp^2 hybridised, while C is sp^3 hybridised in the C-Ti state.

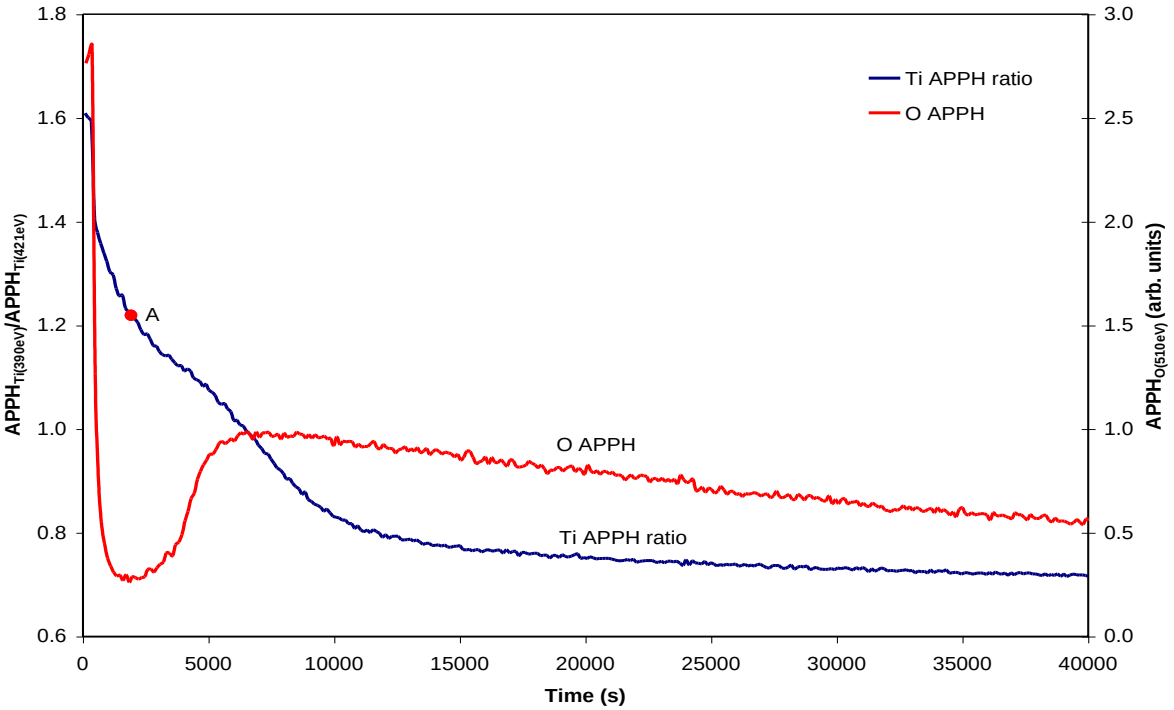

Figure 6.42: AES profile of O on a Ti/TiC sample. Included is an indication of the oxidation state of Ti as can be evaluated from the value of $\frac{\mathrm{APPH}_{\mathrm{Ti(390eV)}}}{\mathrm{APPH}_{\mathrm{Ti(421eV)}}}$.

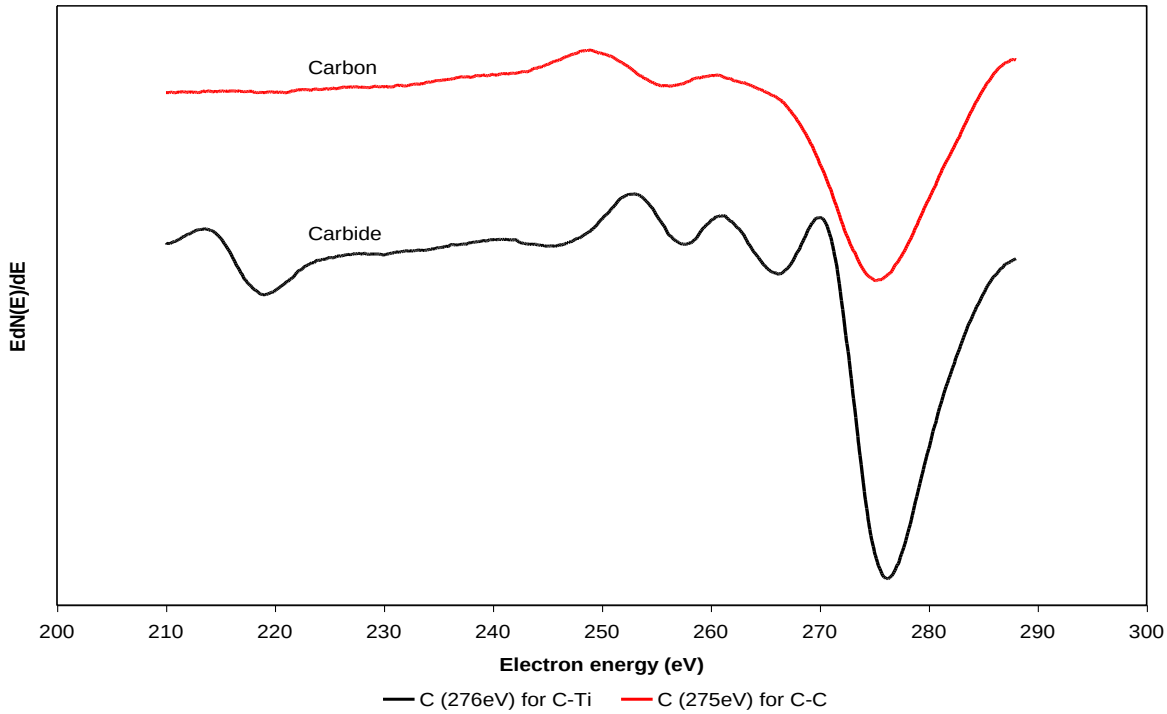

Figure 6.43: Auger spectra at different points in a depth profile on the TiC sample to illustrate the difference in the C bonding state.

6.6 Conclusion.

AES measurements have shown that cyclic voltammetry is capable of homogeneously depositing a significant amount of Ru on the surface of Ti. An average value of 46at% Ru was reported. Cl was found to be present on the surface as well as incorporated into the film structure of an electroformed $RuO_x.nH_2O$ film, but is effectively removed by calcination at 600°C. Although it has no direct implication for the use of an electroformed DSA, a 2nd order polynomial relation between the at% Ti on the surface and calcination time presented itself in the range of experimentation. Depth profiling on the $RuO_x.nH_2O$ films justified phenomena like substrate oxidation and diffusion suggested by oxygen enrichment observed in the various films. Evaluation of the depth distribution of Ru was used to prove a hypothesis of a highly porous structure of $RuO_x.nH_2O$ in the absence of calcination. A theory was presented to explain the polarization behaviour of said electrocatalysts as a function of the "thickness" of the depth distribution of Ru. A 30min-calcinated sample has proven to behave the best at high current densities in chapter 5. This is due to the presence of a certain degree of porosity, while the 60min annealed film was the worst due to substrate oxidation and the complete absence of porosity as proven by a small value for the Ru "thickness". The improved "thickness" of the Ru distribution in the 120min and 240min samples agrees with the assumption of solid state diffusion. Although extended annealing proved to result in slightly less favourable polarization behaviour, the structural characteristics of such materials are expected to potentially improve the life expectancy of these DSA's compared to that of 30min annealed materials. The oxidation state of Ti as a function of sputter time was also studied and octahedral crystal field splitting as relevant to TiO was recognised from the AES fine structure.

AES measurements on $Ti/TiO_y/RuO_x$ electrode surfaces suggest an average of roughly 20at% Ru that forms on a Ti surface during thermal decomposition of a single component precursor solution compared to 2at% - 6at% Ru when applying mixed precursor solutions. This gives immediate evidence for the lower rate of increased electrode polarization during MnO_2 electroplating on electrodes originating from single component precursors. It is conclusive from depth profiling on these single component precursor films that the concentration of Ru on the surface probably dictates electrode passivation behaviour to a much greater extent than does the thickness or depth distribution of Ru in the oxide structure. A linear relation

was obtained between the Ru quantity (represented by the area under the Ru trace in the depth profile) and polarization slope from 155A.m^{-2} to 170A.m^{-2} for Ru/Ti mixed component precursor films. This implies that the RuO_x film thickness does influence the polarization slope. TiO was again confirmed to be present in all the various types of thermally prepared oxide structures. In terms of potential capacity to retard passivation of the substrate under anodic load, the following general improving order was established: thermally prepared DSA's from single component precursors > annealed electroformed DSA's > thermally prepared DSA's from mixed component precursors. Although this general guideline can be presented, specific outstanding performances were identified within each category. It should also be mentioned that although no specific evaluation of performance over prolonged application periods was done, specific predictions in this regard can be attempted by considering the structural composition of the films as extensively described in this work.

Analyses of the Ti-Mn composite samples revealed a composition of 90at% Ti and 10at% Mn. The fine structure of the C KVV Auger transition confirmed the existence C in the C-Ti bonding state on the Ti/TiC electrode.

Conclusive summary

A literature survey as presented in chapter 2 is illustrative of the vast amount of available knowledge on DSA's in terms of its properties, preparation methods, applications and characterisation techniques. Although the study on the effect of H_2 evolution on Ti metal does not form part of the development of new materials for MnO_2 electroplating, it does present valuable information on the application of unmodified Ti metal in an acidic $MnSO_4$ solution. Ti activation takes place at 52°C at a rest potential of –0.67 ± 0.01V *vs*. Ag/AgCl. Activation is accompanied by spontaneous H_2 evolution on the metal and exposure to the gas causes an increase in electrode potential of 0.188 ± 0.02V.hr^{-1} *vs*. Ag/AgCl during MnO_2 electroplating at 100.5A.m^{-2}. Neither open circuit decay nor cathodic treatment is therefore regarded as desired methods in industrial electroplating facilities to rejuvenate passivated electrodes.

The primary objective of preparing and evaluating different oxide electrode materials was proven possible. XRD has illustrated the possibility of increasing the total RuO_2 content on thermally prepared Ti/TiO_y/RuO_x films by increasing the Ru concentration in the precursor solution. This was confirmed for oxides as precipitated from the mixed precursor solutions by AES depth profiling. Note that the total RuO_2 content (this includes the total thickness of the Ru distribution) is relevant in last mentioned findings. AES measurements has shown, in conjunction with electrolysis of acidic $MnSO_4$, that it is actually the Ru concentration of the outer most surface layer, i.e. the solid state that is directly in contact with the electrolysis solution, that enhances electrocatalytic behaviour and increased resistance to passivation in the current density range of 155A.m^{-2} to 170A.m^{-2}. This can again be exemplified by reassessing the following: an electrode from the 0.8wt/wt% Ru solution contains roughly 24at% Ru on its surface, while a 5.25wt/wt% Ru solution (mixed precursor) results in 6at% Ru on a Ti surface. However, the latter electrode has a considerably higher total RuO_2 content as can be gathered from the (1 1 0) XRD reflection at 28° 2θ as well as from AES depth profiling. Nonetheless, it is the electrode from the single component precursor that performs the better at high current densities during electroplating.

Visual assessment of an unannealed Ti/$RuO_x.nH_2O$ electrode revealed anodic corrosion during MnO_2 electrodeposition and is therefore insufficient as an anode. A parameter was derived from AES depth profiling to provide a measure of the thickness of the Ru distribution in calcinated $RuO_x.nH_2O$ films on Ti. A hypothesis based on these findings was used to explain the advantage of a 30min annealed Ti/$RuO_x.nH_2O$ electrode under anodic load.

After expatiatory discussions on possible modifications of Ti metal for MnO_2 electroplating, the most compelling result in the interest of an EMD electroplating facility is the advantage that a 0.8wt/wt% Ru precusor-DSA possesses in terms of preparation cost and electrocatalytic properties. Electrochemically prepared $RuO_x.nH_2O$ films followed by appropriate thermal treatment yielded electrocatalytic electrodes with ability that is on par with the best thermally prepared electrocatalyst in this study. Indications also exist that the process cost for industrial production of these Ti/$RuO_x.nH_2O$ electrodes could possibly be lower than any of the studied oxides from the aqueous precursors due to the quantities of $RuCl_3$ involved.

Future work

By further varying the Ru : Ti ratio in precursor solutions, together with the use of additives such as Sn, Ir and Zr, the possibilities for preparing different anode materials for MnO_2 electroplating *via* thermal decomposition appear infinite. Measurement of electrochemical spectra has the prospect of a fast and repeatable test to evaluate DSA samples. Application of potentiostatic polarization curves (Tafel slopes) in the presence of Mn(II) to Mn(IV) oxidation might also prove to be an elegant method to study electrocatalytic capacity towards this specific reaction. Electrochemical measurements could furthermore be employed to probe the validity of the proposed hypothesis of porosity in $RuO_x.nH_2O$ films. By again combining any of the above electrochemical techniques with solid state measurements, the true nature of an electrocatalyst under investigation could be exposed with greater certainty.

References

[1] M.M. Thackeray, M.H. Rossouw, R.J. Gummow, D.C. Liles, K. Pearce, A. de Kock, W.I.F. David and S. Hull, *Electrochim. Acta* **38** (1993) 1259

[2] D. Balachandran, D. Morgan and G. Ceder, *J. Solid State Chem*. **166** (2002) 91

[3] A Ferdman, U.S. Patent 6,129,822 (2000)

[4] S. Nijjer, J. Thonstad and G.M. Haarberg, *Electrochim. Acta* **46** (2000) 395

[5] S. Bodoardo, J. Brenet, M. Maja and P. Spinelli, *Electrochim. Acta* **39** (1999) 1994

[6] S. Rodrigues, N. Munichandraiah and A.K. Shukla, *J. Appl. Electrochem*. **28** (1998) 1235

[7] D. Velayutham, M. Noel and S. Chidambaram, *Bull. Electrochem.* **9** (1993) 99

[8] G. Davies, *Coord. Chem. Rev.* **4** (1969) 199

[9] J.P. Petitpeirre, C. Comninellis and E. Plattner, *Electrochim. Acta* **35** (1990) 281

[10] W.H. Kao and V.J. Weibel, *J. Appl. Electrochem.* **22** (1992) 21

[11] R.L. Paul and A. Cartwright, Counsil of Materials Technology, *Mintek Report 50*, South Africa, 1985

[12] M.M.E. Duarte, A.S. Pilla and C.E. Mayer, *J. Appl. Electrochem*. **33** (2003) 387

[13] A. Urfer, G.A. Lawrance and D.A.J. Swinkels, *J. Appl. Electrochem*. **27** (1997) 667

[14] A. Urfer, G.A. Lawrance and D.A.J. Swinkels, *J. Appl. Electrochem*. **31** (2001) 341

[15] S. Rodrigues, N. Munichandraiah and A.K. Shukla, *J. Appl. Electrochem*. **30** (2000) 371

[16] W.C. Vosburgh, *J. Electrochem. Soc*. **106** (1959) 839

[17] D. Boden, C.J. Venuto, D. Wisler and R.B. Wylie, *J. Electrochem. Soc*. **115** (1968) 333

[18] C. Mondoloni, M. Laborde, J. Rioux, E. Andoni and C. Levy-Clement, *J. Electrochem. Soc*. **139** (1992) 954

[19] D. Qu, *J. Appl. Electrochem*. **29** (1999) 511

[20] F. Jean, C. Cachet, L.T. Yu, A. Lecerf and A. Quivy, *J. Appl. Electrochem*. **27** (1997) 635

[21] P. Brouillet, A. Grund, F. Jolas and R. Mellet, *C.R. Acad. Sci. Paris* **257** (1963) 3390

[22] C.L.P.S. Zanta, A.R. de Andrade and J.F.C. Boodts, *Electrochim. Acta* **44** (1999) 3333

[23] L.N. Dzhaparidze, Y.M. Dubov, E.A. Bogdanov, T.A. Chakhunashvili, G.T. Gogoladze, A.A. Teisheva, G.N. Ryzygraeva, M.A. Melnikov-Eichenvald and T.V. Rokva, U.S. Patent 4,140,617 (1979)

[24] C.E.B. Marino, E.M. de Oliveira, R.C. Rocha-Filho and S.R. Biaggo, *Corros. Sci.* **43** (2001) 1465

[25] L. Zhang, D.D. Macdonald, E. Sikora and J. Sikora, *J. Electrochem. Soc*. **145** (1998) 898

[26] E.M. Oliveira, C.E.B. Marino, S.R. Biaggio and R.C. Rocha-Filho, *Electrochem. Comm.* **2** (2000) 254

[27] M.A. Abdel Rahim, *J. Appl. Electrochem.* **25** (1995) 881

[28] A.L. Bacarella, H.S. Gadiyar and A.L. Sutton, *J. Electrochem. Soc.* **128** (1981) 1531

[29] N.R. Armstrong and R.K. Quinn, *Surf. Sci*. **67** (1977) 451

[30] F. Climent and R. Capellades, *Electrochim. Acta* **33** (1988) 433

[31] H. Habazaki, K. Shimizu, S. Nagata, P. Skeldon, G.E. Thompson and G.C. Wood, *J. Electrochem. Soc.* **149** (2002) B70

[32] J.A. Harrison and D.E. Williams, *Electrochim. Acta* **27** (1982) 891

[33] T. Shibata and Y.C. Zhu, *Corros. Sci.* **37** (1995) 133

[34] D.J. Blackwood, L.M. Peter and D.E. Williams, *Electrochim. Acta* **33** (1988) 1143

[35] D.J. Blackwood and L.M. Peter, *Electrochim. Acta* **34** (1989) 1505

[36] Y. Massiani, A. Medjahed, P. Gravier, L. Argeme and L. Fedrizzi, *Thin Solid Films* **191** (1990) 305

[37] M. Lakatos-Varsanyi and D. Hanzel, *Corros. Sci.* **41** (1999) 1585

[38] S. Rudenja, J. Pan, I.O. Wallinder, C. Leygraf and P. Kulu, *J. Electrochem. Soc.* **146** (1999) 4082

[39] J.C. Francois, Y. Massiani, P. Gravier, J. Grimblot and L. Gengembre, *Thin Solid Films* **223** (1993) 223

[40] J.P.S. Pringle, *Electrochim. Acta.* **25** (1980) 1420

[41] F. Brown and W.D. Mackintosh, *J. Electrochem. Soc.* **120** (1973) 1096

[42] K. Shimizu, K. Kobayashi, P.Skeldon, G.E. Thompson and G.C. Wood, *Corros. Sci.* **38** (1996) 431

[43] J.P.S. Pringle, *J. Electrochem. Soc.* **120** (1973) 398

[44] G.C. Wood, P. Skeldon, G.E. Thompson and K. Shimizu, *J. Electrochem. Soc*. **143** (1996) 74

[45] C.K. Dyer and J.S.L. Leach, *J. Electrochem. Soc.* **125** (1978) 1032

[46] J. Mizuguchi, *J. Electrochem. Soc.* **148** (2001) J55

[47] *Terra – Femto* [online], available from http:/www.chem.yale.edu/~cas/tio2.html [Accessed 2002]

[48] M.E. Armacanqui and R.J. Ekern, *J. Appl. Electrochem.* **22** (1992) 722

[49] Dom Swinkels, "Production, Characterisation and Utilisation of Manganese Oxides in Batteries", An electronic document published by D&W Informatechs Pty Ltd, PO Box 578, Raymond Terrace, 2324, AUSTRALIA, 1998. E-mail: DOMS@paracelsus.newcastle.edu.au

[50] K. Matsuki and M. Sugawara, *Progress in Batteries & Solar Cells* **8** (1989) 28

[51] E. Preisler, *Progress in Batteries and Battery Materials* **10** (1991) 1

[52] K. Miyazaki, T. Kato and S. Kumamoto, *The Electrochemical Society Meeting Abstract* **98-2** (1998) No. 41

[53] K. Miyazaki, T. Kato and S. Kumamoto, *The Electrochemical Society Proceedings* **98-15**

[54] M.A. Omar, *Elementary Solid State Physics*, Addison-Wesley Publishing Company (1975) Chapter 6

[55] *Formation and characteristics of Anodized Aluminum* [online], available from http://www.sic.shibaura-it.ac.jp/~sato/lab/plaza/chap218.html [Accessed August 2002]

[56] E.K. Rideal and H.S. Taylor, *Catalysis in Theory and Practice*, Macmillian & Co. (1926) Chapter 15

[57] B. Borresen, G. Hagen and R. Tunold, *Electrochim. Acta* **47** (2002) 1819

[58] I.M. Campbell, *Catalysis at Surfaces*, Chapman & Hall (1988)

[59] S. Trasatti, *The Electrochemistry of Novel Materials,* ed. J. Lipkowski and P.N. Ross

[60] M. Vukovic, *Electrochim. Acta* **34** (1989) 287

[61] Y. Takasu and Y. Murakami, *Electrochim. Acta* **45** (2000) 4135

[62] I. Zhitomirsky, *Materials Letters* **33** (1998) 305

[63] C. Chabanier, E. Irissou, D. Guay, J.F. Pelletier, M. Sutton and L.B. Lurio, *Electrochem. Solid State Letters* **5** (2002) E40

[64] J.L. Fernandez, M.R. Gennero De Chialvo and A.C. Chialvo, *J. Appl. Electrochem.* **32** (2002) 513

[65] L. Ouattara, T. Diaco, I. Duo, M. Panizza, G. Foti and C. Comninellis, *J. Electrochem. Soc.* **150** (2002) D41

[66] K. Kim, E. Lee, J. Kim, K. Shin and B. Jung, *J. Electrochem. Soc.* **149** (2002) D187

[67] S. Trasatti, *Electrodes of Conductive Metallic Oxides*, Elsevier Amsterdam (1980)

[68] Q.L. Fang, D.A. Evans, S.L. Roberson and J.P. Zheng, *J. Electrochem. Soc.* **148** (2001) A833

[69] W.A. Gerrard and B.C.H. Steele, *J. Appl. Electrochem.* **8** (1978) 417

[70] Y.E. Roginskaya, B.S. Galyamov, V.M. Lebedev, I.D. Belova and Y.N. Venevtsev, *Zh. Neorg. Khim*. **22** (1977) 499

[71] V.K. Spynu, V.V. Shalaginov, N.V. Kozlova, I.A. Groza and D.M. Shub, *Elektrokhimiya* **22** (1986) 709

[72] S. Pizzini, G. Buzzanca, C.M. Mari, L. Rossi and S. Torchio, *Mat. Res. Bull*. **7** (1971) 449

[73] S. Ardizzone, M. Falciola and S. Trassati, *J. Electrochem. Soc.* **136** (1989) 1545

[74] R. Kotz and S. Stucki, *Electrochim.* Acta **31** (1986) 1311

[75] Y.J. Kim, Y. Gao and S.A. Chambers, *Appl. Surf. Sci.* **120** (1997) 250

[76] C. Hu and Y. Huang, *J. Electrochem. Soc.* **146** (1999) 2465

[77] Y. Mo, W. Cai, J. Dong, P.R. Carey and D.A. Scherson, *Electrochem. Solid State Letters* **5** (2002) E40

[78] I.D. Belova, R.R. Shifrina, Y. E. Roginskaya, A.V. Popov and T.V. Varlamova, *Elektrokhimiya* **23** (1987) 1208

[79] Y.E. Roginskaya, I.D. Belova, B.S. Galyamov, Y.M. Popkov and D.S. Zakharin, *Elektrokhimiya* **23** (1987) 1215

[80] P.H. Duvigneaud and A. Coussment, *J. Solid State Chem*. **52** (1984) 22

[81] B.S. Galyamov, Y.E. Roginskaya, R.M. Lozorenko-Manevich, V.B. Kozhevnokov, M.I. Yanovskaya and Y.A.M. Kolotyrkin, *Mat. Chem. Phys*. **11** (1984) 525

[82] S. Trasatti, *Electrochim.* Acta **36** (1991) 225

[83] G. Lodi, C. De Asmundis, S. Ardizzone, E. Sivieri and S. Trasatti, *Surf. Technol*. **14** (1981) 335

[84] M. Del Arco and V. Rives, *J. Mat. Sci*. **21** (1986) 2938

[85] B.V. Tilak, *J. Electrochem. Soc.* **126** (1979) 1343

[86] C. Iwakura, K. Hirao and H. Tamura, *Electrochim.* Acta **22** (1977) 329

[87] R. Kotz, H.J. Lewerenz and S. Stucki, *J. Electrochem. Soc.* **130** (1983) 825

[88] C. Iwakura and K. Sakamoto, *J. Electrochem. Soc.* **132** (1985) 2420

[89] L.D. Burke and M. McCarthy, *Electrochim. Acta* **29** (1984) 211

[90] G. Lodi, G.L. Zucchini, A. De Battisti, A. Giatti, G. Battaglin and G. Della Mea, *Surf. Sci*. **251** (1991) 836

[91] S. Ardizzone, G. Fregonara and S. Trasatti, *Electrochim. Acta* **35** (1990) 263

[92] J. O'M. Bockris and T. Otagawa, *J. Electrochem. Soc*. **131** (1984) 290

[93] Lj. Atanasoska, R.T. Atanasoski, F.H. Pollak and W.E. O'Grady, *Surf. Sci.* **230** (1990) 95

[94] J.S. Solomon and W.L Baun, *Surf. Sci*. **51** (1975) 228

[95] S. Thomas, *Surf. Sci.* **55** (1976) 754

[96] P.J. Basset and T.E. Gallon, *J. Electron Spectrosc. Related Phenom.* **2** (1973) 101

[97] J.P. Coad and J.C. Riviere, *Proc. Roy. Soc.* **A331** (1972) 403

[98] K. Siegbahn et. al., ESCA – *Atomic, Molecular and Solid State Structure Studied by Means of Electron Spectroscopy*, Almquist and Wicksell, Uppsala, 1967

[99] D.W. Fischer, *J. Phys. Chem. Solids* **32** (1971) 2455

[100] D.W. Fischer, *Phys. Rev*. **B5** (1972) 4219

[101] X. Tian, R.K.Y. Fu and P.K. Chu, *J. Vac. Sci. Technol. A* **20** (2002) 160

[102] Lj. Atanasoska, W.E. O'Grady, R.T. Atanasoski and F.H. Pollak, *Surf. Sci*. **202** (1988) 142

[103] H.P. Myers, *Introductory Solid State Physics*, 2nd edition, Taylor & Francis (1997) Chapter 3.

[104] *Handbook of Auger Electron Spectroscopy*, ed. C.L. Hedberg, Physical Electronics Inc. (1995)

[105] K. Muller, *Surface Physics*, Springer-Verlag (1975)

[106] M.P. Seah, *Surf. Sci*., **32** (1972) 703

[107] J.M. Walsh and N.P. Anderson, *Surface Analysis Techniques for Metallurgical Applications*, ed. R.S. Carbonara and J.R. Cuthill, ASTM Special Technical Publication (1975)

[108] H. An, S. Chen, H. Cui and X. Yang, *J. Electrochem. Soc.* **149** (2002) B174

[109] H.C. Swart, A.J. Jonker, C.H. Claassens, R. Chen, L.A. Venter, P. Ramoshebe, E.Wurth, J.J. Terblans and W.D. Roos, *Appl. Surf. Sci.* **205** (2003) 231

[110] C.P. De Pauli, M.C. Giordana and J.O. Zerbino, *Electrochim. Acta* **28** (1983) 1781

[111] O.R. Camara, C.P. De Pauli and M.C. Giordana, *Electrochim. Acta* **29** (1984) 111

[112] S.J. Botha, *Surface Properties and Bio-acceptability of Ti_2O_3 Surfaces*, International Symposium of Thermomechanical Processing & Metallurgy of Titanium Alloys, Thermex'97, **41**, July 7-11 (1997)

[113] C.W. Louw, *The Oxidation of Titanium and its Alloys*, Ph.D. thesis (1997)

[114] V. Brusic, *Oxides and oxide films*, ed. J.W. Diggle, Marcel Dekker Inc. (1972) Chapter 1

[115] S. Tanaka, M. Aonuma, N. Hirose and T. Tanaki, *J. Electrochem. Soc.* **149** (2002) D167

[116] S. Tanaka, T. Iwatani, N. Hirose and T. Tanaki, *J. Electrochem. Soc.* **149** (2002) F186

[117] M.E. Armacanqui and R.J. Ekern, *J. Appl. Electrochem*. **22** (1992) 593

[118] D. Bartlett, V. Ashworth, F.L. Bowden and J.R.B. Gilbert, in Titanium 80: Proceedings of the international conference on titanium, Kyoto, ed. H. Kimura and O. Izumi, Metallurgical society AIME, Warrendale, Philadelphia (1980)

[119] K.D. Allard, M. Ahrens and K.E. Heusler, *Werkstoff. Korros*. **9** (1975) 694

[120] W.D. Roos, *personal communication*, University of the Free State

[121] R. N. Goldberger and L.G. Hepler, *Thermochemistry and oxidation potentials of the platinum group metals and their compounds*, (1967)

[122] A Jonker, *unpublished results*, Delta EMD (Pty) Limited

[123] G. Lodi, C. Bighi and C. De Asmundis, *Mat. Chem*. **1** (1976) 177

[124] Y.S. Huang, H.L. Park and F.H. Pollak, *Mat. Res. Bull*. **17** (1982) 241

[125] M. Vukovic, H. Angerstein-Kozlowska and B.E. Conway, *J. Appl. Electrochem.* **12** (1982) 193

[126] L.D. Burke, O.J. Murphy, J.F. O'Neill and S. Venkatesan, *J. Chem. Soc. Faraday Trans*. **73** (1977) 1659

[127] A.C.C. Tseung and S. Jasem, *Electrochim. Acta* **22** (1977) 31

[128] D.R. Askeland, *The Science and Engineering of Materials*, 3rd edition, Stanley Thornes Publishers (1998) Appendix A

[129] M. Maline, M. Ducarroir, F. Teyssandier, R. Hillel, R. Berjoan, F.J.J. Van Loo and W. Wakelkamp, *Surf. Sci*. **286** (1993) 82